

**DEVELOPMENT AND APPLICATION OF A MOMENTUM DISPERSIVE
MULTICHANNEL ELECTRON MOMENTUM SPECTROMETER**

by

Noah Lerner

B. Sc., University of Lethbridge, 1989

A THESIS SUBMITTED IN PARTIAL FULFILLMENT OF
THE REQUIREMENTS FOR THE DEGREE OF
DOCTOR OF PHILOSOPHY

in

THE FACULTY OF GRADUATE STUDIES
DEPARTMENT OF CHEMISTRY

We accept this thesis as conforming
to the required standard

THE UNIVERSITY OF BRITISH COLUMBIA

March 1995

© Noah Lerner, 1995

In presenting this thesis in partial fulfilment of the requirements for an advanced degree at the University of British Columbia, I agree that the Library shall make it freely available for reference and study. I further agree that permission for extensive copying of this thesis for scholarly purposes may be granted by the head of my department or by his or her representatives. It is understood that copying or publication of this thesis for financial gain shall not be allowed without my written permission.

(Signature)

Department of Chemistry

The University of British Columbia
Vancouver, Canada

Date March 24, 1995

Abstract

The design, evaluation, and application of a momentum dispersive multichannel spectrometer for electron momentum spectroscopy (EMS) is reported. The spectrometer employs a microchannel plate/resistive anode position sensitive detector and a channel electron multiplier, situated on the exit circle of a cylindrical mirror electron energy analyzer, to simultaneously measure (e,2e) coincidence events over a $\pm 30^\circ$ range of azimuthal angle. A novel coincidence detection system based on the 'pile-up' of pulses from the detectors has been developed to provide prompt detection of coincidence events. This spectrometer provides an improvement of one to two orders of magnitude in sensitivity over typical single channel instruments.

The performance of the new spectrometer has been characterized through measurements of the binding energy spectra and experimental momentum profiles (XMPs) of the valence electrons of Ne, Ar, Kr, Xe, CH₄ and SiH₄. These measurements show significantly higher statistical precision than any previously reported EMS work. Consistent with earlier studies, the present multichannel XMPs exhibit very good agreement with theoretical momentum profiles calculated using high quality wavefunctions.

The momentum profiles of the helium atom for the transitions to the ground (n=1) and the excited (n=2, n=3) He⁺ final ion states have been obtained with considerably greater

precision than previously reported. The experimental momentum profiles of H_2 and D_2 for transitions to the ground and excited ($2p\sigma_u$, $2s\sigma_g$) ion states have also been measured to high precision. While the XMPs for the transitions to the ground ion states of each system are found to be in good agreement with theory, the XMPs for the transitions to the excited ion states show significant deviations from theoretical profiles calculated with very accurate correlated wavefunctions. It is suggested that these discrepancies arise from contributions of higher order collision processes neglected in the plane wave impulse description of the (e,2e) scattering event normally used in the theoretical interpretation of EMS experiments. While these additional processes have been discussed with regard to other photon, electron and proton impact studies of two-electron transitions (i.e. ionization plus excitation, double ionization), they have not been previously considered in the context of EMS studies.

Table of Contents

Abstract	ii
Table of Contents	iv
List of Figures	viii
List of Abbreviations	xii
Acknowledgments	xiii
Chapter 1 Introduction	1
1.1 Electron Momentum Spectroscopy.....	2
1.2 Early Instrumental Developments	6
1.3 Experimental Studies by EMS	9
1.4 Multichannel Instrumental Developments	14
1.5 Context and Organization of this Work	17
Chapter 2 Theoretical Background	22
2.1 The EMS Scattering Cross Section	22
2.2 The Calculation of Electronic Wavefunctions	32
2.2.1 The Hartree-Fock Method.....	34
2.2.2 The Method of Configuration Interaction	37

Chapter 3	The Momentum Dispersive Multichannel EMS Spectrometer	40
3.1	The Electron Source and Analyzer	41
3.1.1	The Electron Beam Assembly	45
3.1.2	The CMA Baseplate	46
3.1.3	The Collision Chamber	46
3.1.4	The Conical Lenses	47
3.1.5	The Cylindrical Mirror Analyzer	48
3.1.6	Preliminary Results	51
3.2	The Detector Assembly	53
3.2.1	The Channel Electron Multiplier	54
3.2.2	The Microchannel Plate/Resistive Anode Assembly	55
3.3	Coincidence Timing and Data Acquisition Electronics	61
3.3.1	Signal Processing	61
3.3.2	The Spectrometer Time Response	62
3.3.3	The Coincidence Detection System.....	66
3.3.4	The Pulse-Pile-Up Coincidence Circuitry	71
3.3.5	The Accidental Flag Circuitry	79
3.3.6	Data Acquisition.....	80
3.4	Characterization of the Instrument.....	84
3.4.1	The CMA.....	85
3.4.2	The Channel Electron Multiplier	87
3.4.3	The Microchannel Plate/Resistive Anode Operating Voltages	92

3.4.4	The MCP/RAE Position Calibration and Uniformity	95
3.4.5	Linearity of the Detectors	100
3.4.6	The Coincidence Timing Windows	102
3.5	Experimental Results.....	105
Chapter 4	Momentum Dispersive Multichannel EMS Measurements	114
4.1	Neon.....	116
4.2	Krypton	122
4.3	Xenon	125
4.4	A Summary of the Noble Gas Measurements.....	128
4.5	Multichannel EMS of Methane and Silane	130
4.6	Conclusions	137
Chapter 5	EMS of Two Electron Systems: Helium	138
5.1	Background	138
5.2	A Momentum Dispersive Multichannel EMS Investigation of Helium.....	147
5.2.1	Theoretical Momentum Profiles.....	148
5.2.2	Multichannel Binding Energy Spectra and Momentum Distributions	151
5.3	Discussion.....	161
5.4	Conclusions	170

Chapter 6	EMS of Two Electron Systems: Molecular Hydrogen and Deuterium	172
6.1	Background	172
6.2	Theoretical Momentum Profiles of Molecular Hydrogen.....	174
6.3	Multichannel BES Spectra and Momentum Profiles of H ₂	176
6.4	Multichannel BES Spectra and Momentum Profiles of D ₂	187
6.5	Discussion.....	192
6.6	Conclusions	195
Chapter 7	Closing Remarks	197
Bibliography		202

List of Figures

1.1	The symmetric non-coplanar (e,2e) scattering geometry	4
1.2	A schematic of a single channel symmetric non-coplanar (e,2e) spectrometer	8
2.1	The Mott scattering cross section	25
3.1	Photographs of the multichannel spectrometer	42
3.2	A break-away schematic of the spectrometer	43
3.3	A schematic of the momentum dispersive spectrometer	44
3.4	A schematic of the collision chamber and conical lenses	49
3.5	Preliminary single channel EMS measurements	52
3.6	The CEM signal coupling circuitry	56
3.7	A typical CEM timing pulse	56
3.8	The MCP/RAE assembly	60
3.9	A typical MCP timing pulse	60
3.10	CEM pulse distribution and bipolar CFD pulses	63
3.11	Multichannel spectrometer timing spectrum	64
3.12	The PPU coincidence detection method	67
3.13	A block diagram of the coincidence detection system	70
3.14	A schematic of the coincidence detection circuit board	73
3.15	The PPU coincidence detection and gating circuit diagram	74
3.16	Waveform sequence through the coincidence circuitry	75

3.17	Position computer gating pulses	76
3.18	The accidental flag circuit diagram	81
3.19	Waveform sequence for the accidental flag signal	82
3.20	Characterization of the CMA energy resolution	86
3.21	CEM saturation.....	88
3.22	CEM and coincidence count rate variation with CEM front bias potential.....	89
3.23	Simulation of electron trajectory in the CEM.....	91
3.24	MCP and coincidence count rate variation with MCP back bias potential.....	94
3.25	Calibration of the MCP/RAE angle information	97
3.26	Angular distribution of electrons at the MCP/RAE	99
3.27	Variation of CEM / MCP / (e,2e) count rates with incident beam current.....	101
3.28	The coincidence timing window	104
3.29	The coincidence count rate variation with MCP / CEM signal delay.....	104
3.30	A 15-minute multichannel binding energy spectrum of argon	106
3.31	A 15-minute multichannel Ar 3 <i>p</i> ϕ -distribution.....	107
3.32	A 46.5 hour single channel Ar 3 <i>p</i> ϕ -distribution	107
3.33	A high precision multichannel BES of the argon valence region	109
3.34	A high precision multichannel ϕ -distribution and <i>p</i> -distribution of argon.....	110
3.35	An impact energy / ϕ -distribution surface — 2D-EMS	113
4.1	A binding energy spectrum of the valence region of neon.....	117
4.2	Experimental and theoretical momentum profiles of the neon 2 <i>p</i> electron	119

4.3	XMPs of the neon $2p$ and $2s$ electrons with DWIA and PWIA theoretical profiles.	121
4.4	A binding energy spectrum of the valence region of krypton.....	123
4.5	Experimental and theoretical momentum profiles of the $4p$ and $4s$ electrons of krypton.	124
4.6	A binding energy spectrum of the valence region of xenon.....	126
4.7	Experimental and theoretical momentum profiles of the $5p$ and $5s$ electrons of krypton.	127
4.8	ϕ - and p -distributions of the noble gases Ne, Ar, Kr, and Xe	129
4.9	A binding energy spectrum of the valence region of methane	132
4.10	Experimental and theoretical momentum profiles of the $1t_2$ and $2a_1$ electrons of methane.	133
4.11	A binding energy spectrum of the valence region of silane	135
4.12	Experimental and theoretical momentum profiles of the $2t_2$ and $3a_1$ electron of methane.	136
5.1	Experimental and theoretical momentum profiles of helium reported..... by Cook <i>et al.</i> [26].	141
5.2	Experimental and theoretical $n=2$ to $n=1$ cross section ratios reported by Lahmam-Bennani <i>et al.</i> [74]	145
5.3	Theoretical momentum profiles for helium.....	149
5.4	A binding energy spectrum of helium showing double scattering effects.....	151
5.5	A binding energy spectrum of helium measured following the modification of the collision chamber.	156
5.6	XMPs and TMPs for the $(e,2e)$ ionization of helium to the $n=1$, $n=2$ and $n=3$ final ion states.	158
6.1	TMPs for the $(e,2e)$ ionization of molecular hydrogen to the $1s\sigma_g$, $2p\sigma_u$, $2p\pi_u$, and $2s\sigma_g$ final ion states.	174

6.2	The potential energy curves of the H_2 ground state and the H_2^+ ion states	161
6.3	A binding energy spectrum of molecular hydrogen.....	178
6.4	The H_2 BES in the region of the transitions to the excited ion states	179
6.5	XMPs and TMPs for the (e,2e) ionization of H_2 to the $1s\sigma_g$, $2p\sigma_u$,..... and $2s\sigma_g$ final ion states.	184
6.6	XMPs -- corrected for the overlap of neighbouring transitions -- and TMPs ... for the (e,2e) ionization of H_2 to the $1s\sigma_g$, $2p\sigma_u$, and $2s\sigma_g$ final ion states.	185
6.7	A binding energy spectrum of deuterium	189
6.8	The comparison of XMPs for H_2 and D_2	190

List of Abbreviations

BES	binding energy spectrum
CEM	channel electron multiplier or channeltron
CFD	constant fraction discriminator
CI	configuration interaction
CMA	cylindrical mirror analyzer
DAC	digital-to-analog converter
DWIA	distorted wave impulse approximation
DWBA	distorted wave Born approximation
ECL	emitter coupled logic
EMS	electron momentum spectroscopy
FWHM	full width at half maximum
IP	ionization potential
GTO	Gaussian type orbital
GW-PG	Gaussian-weighted planar grid
MCP	microchannel plate
MR-SDCI	multireference singles and doubles CI
OVD	overlap distribution
PES	photoelectron spectroscopy
PPU	pulse-pile-up
PWIA	plane wave impulse approximation
PWBA	plane wave Born approximation
RAE	resistive anode encoder
SCF	self-consistent-field
TAC	time-to-amplitude converter
TMP	theoretical momentum profile
TS	two-step collision process
TTL	transistor-transistor logic
XMP	experimental momentum profile

Acknowledgments

The research presented in this thesis would not be complete were it not for the contributions of a number of individuals whose efforts I would like to acknowledge.

It was the vision of Dr. Chris Brion, my research supervisor, that initiated, fueled and advanced the development of the new momentum dispersive multichannel spectrometer. A special note of gratitude is given to Dr. Brion for his advice, support, assistance, and patience throughout the study.

The contributions of Dr. Bruce Todd, a post-doctoral fellow with whom I worked on the development of the spectrometer, are recognized and very much appreciated. Dr. Todd's electrical and mechanical expertise were of paramount importance to the success of the project. Specific note should be made of his introduction of the pulse-pile-up technique for coincidence detection. My heartfelt gratitude is expressed to Dr. Todd for his assistance, guidance and friendship during the course of the project.

Dr. Natalie Cann provided calculations of the theoretical momentum profiles for helium using a very accurate explicitly correlated wavefunction. Additionally, I would like to thank Dr. Cann for discussions regarding the He and H₂ measurements and for her friendship and advice during the latter stages of my research. Dr. E. R. Davidson and S. Chakravorty of Indiana University also provided theoretical profiles for helium, calculated with a very high quality correlated wavefunction.

Ed Gomm, from the Department of Chemistry machine shop, skillfully fabricated many of the individual components of the spectrometer. The care and exacting standards of Mr. Gomm are reflected in the successful operation of the instrument. Brian Greene, from the Department of Chemistry electronics division, constructed many of the supporting electronic components of the instrument including the electrometers, the vacuum safety system, and the CEM amplifier. Additionally Mr. Greene freely offered advice and promptly executed emergency repairs when necessary.

The assistance of every member of the electronic and the mechanical divisions of the chemistry department was called upon at one point or another during the project, and I express my warmest thanks to Brian Greene, Joseph Sallos, Mike Hatton, Milan Cocshizza, David Tonkin, Zoltan German, Tom Markus, Ed Gomm, Bill Henderson, Ron Marwick, Brian Snapkauskas, Brin Powell, Oscar Greiner and Des Lovrity. As well, the friendly aid of the front office personnel is affectionately acknowledged. In particular, I am grateful to Carolyn C. Joyce for proofreading this manuscript.

Thanks are also due to Prof. N. Jaeger, Dr. Hiroshi Kato and Ken Madore of the Centre for Advanced Technology in Microelectronics of the Department of Electrical Engineering, UBC, who kindly offered their services in the photolithographic etching of the MCP/RAE resolution mask.

Helpful discussions with Mike Mellon of Quantar Technologies, Lorenzo Avaldi of the IMAI Institute of CNDR (Italy), and Prof. I. E. McCarthy of Flinders University of South Australia are gratefully acknowledged.

The photographs of the spectrometer presented in chapter 3 were kindly provided by Mankee Mah.

I am also grateful for the many people who offered advice and support, and who together created a challenging, dynamic and entertaining research environment. These include Bruce Hollebone, Patrick Duffy, Mark Casida, Terry Olney, Glyn Cooper, Gord Burton, Wing Fat Chan, John Neville, Steve Clark, Jennifer Au, Jim Rolke, Prof. D.P. Chong, and Dr. Y Zheng.

The Natural Sciences and Energy Research Council and the Alberta Heritage Trust for providing financial assistance during the course of the study is gratefully acknowledged.

Finally, I would like to thank my family and friends for their support throughout my graduate studies.

Chapter One

Introduction

Advances in our understanding of nature are often gained through the development of new and creative instrumental techniques. Experimental tools have ‘made it possible to observe, in unprecedented detail, a whole new world of small dimensions.’¹ An appropriate example of this is provided in the first unambiguous experimental measurements of the distribution of momenta of electrons in atoms, obtained by DuMond and Kirkpatrick over 60 years ago [1,2]. Their measurements showed that the linewidth of inelastically scattered X-rays, i.e. the Compton profile, originates from the Doppler broadening of the X-rays by the motion of the electrons in the target [3]. Difficulties arising from the weakness of the Compton signal were overcome through the development of a multicrystal spectrograph [4] that used 50 calcite crystals to analyze the wavelengths of X-rays scattered from a target at a well defined angle. In the late 1960s and early 1970s a new experimental technique for the measurement of momentum distributions of electrons was proposed and developed. The technique, originally known as binary (e,2e) spectroscopy, is now more commonly referred to as electron momentum spectroscopy or EMS. Unlike Compton scattering, in which the total

¹Professor Sture Forsén, discussing the invention of the microscope, on the occasion of the awarding of the Nobel prize in Chemistry to Dr. R. Ernst, 1991 [175].

momentum distribution of all the electrons in the target is measured, EMS allows the momentum distribution of electrons associated with well defined energy states (i.e. orbitals in the language of the independent particle model) to be determined. However, energy specificity is not achieved without a commensurate loss of signal and increased difficulty of measurement. This dissertation describes the development and application of a new spectrometer for the measurement of momentum distributions using electron momentum spectroscopy. As in the developments of DuMond and Kirkpatrick, this project attempted to mitigate the difficulties imposed by low signal rates through improved efficiency of instrumentation. The new spectrometer employs multichannel electron detection and novel timing circuitry to enhance the collection efficiency by approximately two orders of magnitude over conventional single channel EMS spectrometers.

1.1 Electron Momentum Spectroscopy

The method of electron momentum spectroscopy is conceptually quite simple. It is based on the idea that the momentum \mathbf{p}_t of a target object can be determined by a collision with another object of known momentum \mathbf{p}_o and observation of the direction and speed, that is the momenta (labeled \mathbf{p}_e and \mathbf{p}_s for ejected and scattered), of both objects following the collision. Conservation of momentum requires that

$$\mathbf{p}_t = \mathbf{p}_e + \mathbf{p}_s - \mathbf{p}_o. \quad (1.1)$$

In an EMS experiment, a beam of high energy electrons (typically 1200 eV) is directed into a gas cell. The vast majority of the electrons passes through the region with no interaction with the target species. Occasionally, an electron will “collide” with an electron in a bound state of the target atom or molecule in such a way that both electrons are scattered into large polar angles θ , relative to the direction of the incident electron. These large momentum transfer collisions are the events of interest in EMS. The large polar angle and high (equal) energies of the outgoing electrons observed ensure that the collision can be modeled by the direct collision of the two electrons with trajectories that can be well described classically. As shown by equation (1.1), the direction and speed of the two outgoing electrons should reflect the initial momentum of the bound target electron.

A favorable experimental configuration for the detection of these (e,2e) scattering events (i.e. one electron in, two electrons out) is the symmetric non-coplanar geometry [5,6,7], presented in figure 1.1. In this geometry, only those events in which both outgoing electrons have equal energies $E_s = E_e$ and polar angles of $\theta_s = \theta_e = 45^\circ$ are detected. The collision process can be summarized by

$$\begin{array}{rcll}
 & e_0^- + [e_t^- + M_t^+] & \rightarrow & e_s^- + e_e^- + M^+ \\
 \text{Energy} & E_0 & & E_s \quad E_e & (1.2) \\
 \text{Momentum} & \mathbf{p}_0 & [\mathbf{p}_t, \mathbf{q}] & \mathbf{p}_s \quad \mathbf{p}_e \quad \mathbf{q}
 \end{array}$$

where e_0^- , e_s^- and e_e^- represent the incident, scattered and ejected electron respectively, e_t^- represents the target electron prior to the collision event, and M^+ represents the final ion.

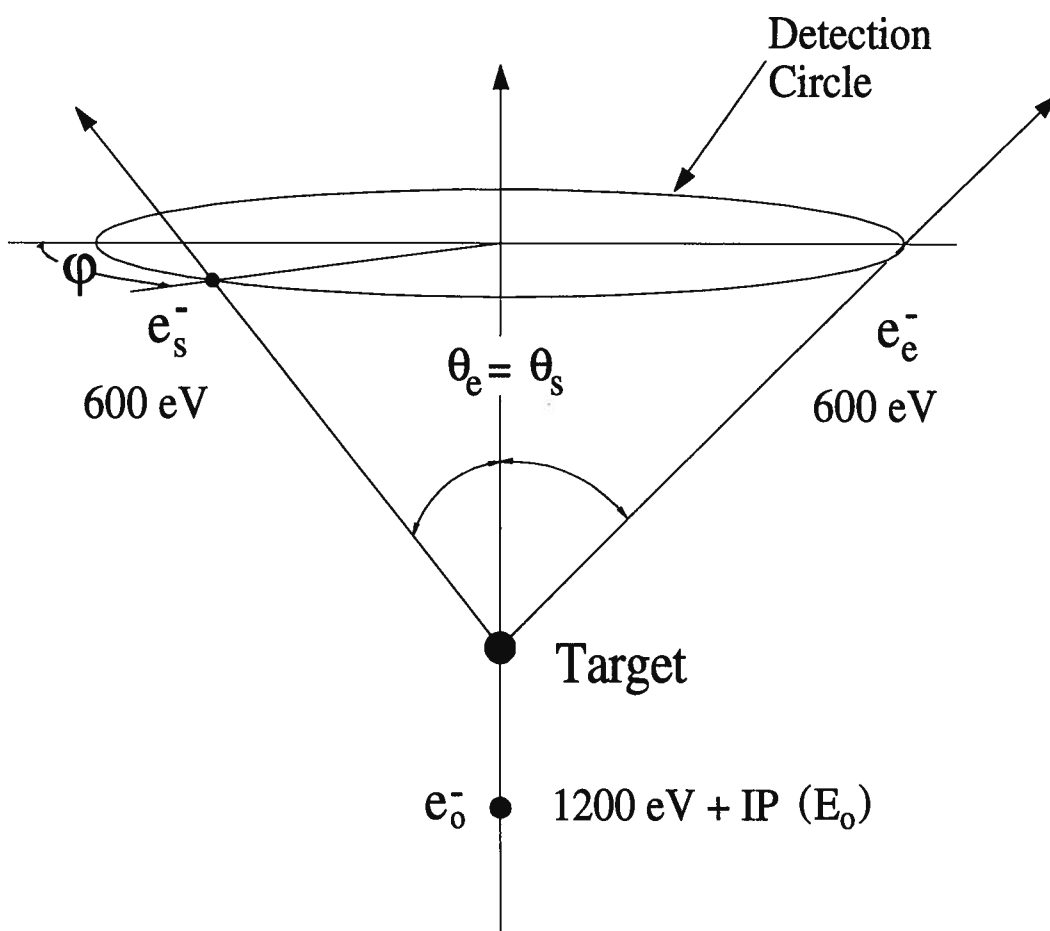


Figure 1.1: The symmetric non-coplanar (e,2e) scattering geometry.

Under the conditions typically used in EMS, the target species, depicted by the terms in square brackets, may be assumed to be at rest. As well, the ion can be thought to be spectator of the collision event, having a recoil momentum q equal in magnitude and opposite in direction to the momentum of the target electron. If the very small recoil energy of the ion is neglected, the binding energy or ionization potential (IP) of the target electron is given by the energy difference of the neutral target and the final ion species. This energy must be equal to the difference of the incident and outgoing electron energies in an ionizing collision

$$IP = E_0 - E_s - E_e. \quad (1.3)$$

The momentum of the ejected electron prior to the collision is given by equation (1.1) which, in the non-coplanar symmetric geometry at $\theta_e = \theta_s = 45^\circ$, can be expressed as

$$p_t = \sqrt{(2p_e - p_0)^2 + 2p_e^2 \sin^2(\varphi/2)}. \quad (1.4)$$

The probability of detecting two outgoing electrons of equal energy from an ionization event, at polar angles of 45° and relative azimuthal angle φ , is directly proportional to the probability of the target electron having the initial momentum given by equation (1.4). By measuring this probability at a number of relative azimuthal angles and at the appropriate impact energy, the momentum distribution of a binding energy selected electron in the target is obtained.

The distributions measured in EMS are often referred to as experimental momentum profiles (XMPs). The strength of EMS lies in the fact that the XMPs of valence electrons are,

to a very good approximation, proportional to the square of the momentum space wavefunction of the respective target electrons. In a more rigorous treatment, the momentum profile is calculated by the overlap of the total electronic wavefunctions of the ion and neutral species. Thus the measurement of the experimental momentum profiles gives a unique means with which to examine and evaluate theoretical electronic wavefunctions of atomic and molecular systems and their ions.

1.2 Early Instrumental Developments

The first instrument developed to measure (e,2e) scattering was reported by Ehrhardt *et al.* [8] in 1969. This instrument was designed to observe the scattering of slow (~ 100 eV) electrons from a gas in a coplanar geometry, to provide a test for theories of low energy electron impact ionization. In the same year, Amaldi *et al.* [9] reported the development of a high impact energy (14.6 keV) symmetric coplanar instrument designed to measure the momentum distributions of electrons in thin film targets, via the (e,2e) reaction. This work [9] presented binding energy spectra of the carbon 1s electron, obtained at $\theta = \theta_e = \theta_s = 45^\circ$ and $\theta = 41^\circ$ corresponding to two values of initial target electron momentum. These initial studies were followed by measurements of the angular distributions (i.e. momentum profiles) of the carbon K shell (1s orbital) and L shell (2s and 2p orbitals) by Camilloni *et al.* [10]. The experimental energy resolution in the studies by Amaldi *et al.* and Camilloni *et al.*, (135 and 64 eV FWHM respectively) was not sufficient to permit the valence structure of the target species to be resolved. In 1973, Weigold *et al.* [11] reported the development of an

instrument configured to observe symmetric non-coplanar scattering on gas phase targets. With an energy resolution of 4.3 eV [12], the momentum profiles of the outer valence region could be measured for the first time. A similar instrument to that of Weigold *et al.* was developed shortly thereafter at the University of British Columbia [13].

The design of the ‘first generation’ of symmetric non-coplanar spectrometers is presented schematically in figure 1.2. The polar (θ) and azimuthal (ϕ) angles of observed (e,2e) scattering events are selected by apertures positioned at the entrance of each of a pair of energy analyzers. The analyzers disperse the electrons on the basis of their energies by means of a potential difference applied across the inner and outer surfaces. An aperture at the exit of each analyzer passes only those electrons having energies within a narrow range. The energy and angle selected electrons are detected by single channel electron multipliers (CEMs). With the appropriate circuitry, these devices permit individual electron detection [14,15] via an electron cascade initiated by the impact of an electron having sufficient energy. In these ‘first generation’ instruments, one of the assemblies consisting of entrance and exit apertures, energy analyzer, and detector, is able to rotate about the azimuth while the other is fixed in position.

Coincidence timing is used to identify an (e,2e) collision event. In all EMS experiments to date, timing information has been provided by a time-to-amplitude converter (TAC), which gives an output voltage signal proportional to the time delay between two pulses. A single channel analyzer is typically employed in conjunction with a TAC to detect coincidence events

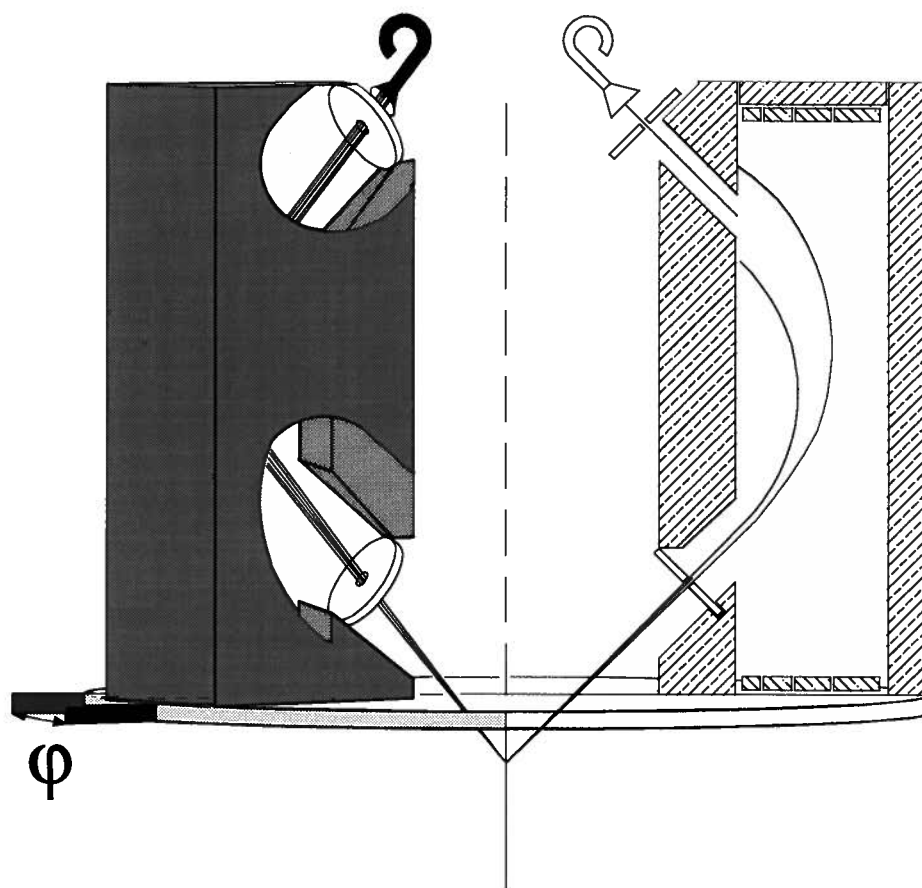


Figure 1.2: A schematic of a single channel symmetric non-coplanar (e,2e) spectrometer. The right side shows a cross sectional view of a stationary analyzer, while the left side displays a three-dimensional outline of a movable analyzer at a relative azimuthal angle ϕ . The polar (θ) and azimuthal (ϕ) angles of electrons scattered from the collision region are selected by the lower circular apertures of the analyzers. Electrons in the analyzers are deflected by the applied potential, and those having the appropriate energy will pass through the upper apertures, where they may be detected by the CEMs.

occurring within a set time window. The instruments are operated in two modes. A binding energy spectrum is obtained at a fixed position of the analyzers by accumulating coincidence events while the incident electron energy E_0 is scanned. The measurement of a momentum profile of electrons having a particular IP is performed by counting coincidence events at the appropriate impact energy while sequentially stepping the movable detector assembly through a range of azimuthal angles (typically 0° to $\pm 30^\circ$ at $E_0 = (1200 \text{ eV} + \text{IP})$).

1.3 Experimental Studies by EMS

The application of the fully kinematically determined (e,2e) scattering experiment to the investigation of electron momentum distributions was first explored theoretically by Neudachin *et al.* [16,17] and these ideas were developed further by Glasgold and Ialongo [18]¹. Following the thin film measurements of Amaldi *et al.* [9] and Camilloni *et al.* [10], the first measurements of the valence orbitals of gas phase atoms (Argon 3*p*,3*s*) [11] and molecules (H₂ 1*s*σ_g [19], CH₄ 1*t*₂ and 2*a*₁ [12]) were reported in 1973. In the two decades since these landmark measurements, EMS has developed into a sensitive technique with which to investigate electronic structure. Recent reviews [7,20,21,22] give a good overview of the measurements of the more than 70 atomic and molecular species that have been investigated with EMS. A brief discussion of a few particularly significant EMS studies is given below.

¹ It should be noted that an earlier reference to the extension of the (p,2p) scattering technique to atomic and molecular systems was made by Baker, McCarthy, and Porter in 1960 [176]

Perhaps the most fundamental EMS investigation is the study of the hydrogen atom by Lohmann and Weigold [23]. Atomic hydrogen was formed by the dissociation of H_2 in a dc discharge tube. As the ground state of atomic hydrogen has an ionization potential (13.6 eV) well separated from that of molecular hydrogen (~ 16 eV), its momentum profile could be measured despite the abundance of H_2 in the collision region. The wavefunction of the hydrogen atom is known exactly, and the experimental momentum profile should be directly proportional to the square of the $1s$ orbital momentum space wavefunction given by

$$|\psi_{1s}(p)|^2 = 8\pi^{-2}(1+p^2)^{-4}. \quad (1.5)$$

Excellent agreement between theory and experiment was observed, providing a direct experimental verification of the solution of the Schrödinger equation for the ground state of the hydrogen atom.

As the simplest system in which electron correlation is present, helium is an interesting system for study by EMS. The transition of the helium atom to the ground state of the ion corresponds to an ionization potential of 24.6 eV. The momentum profile measured at this binding energy is well described by the theoretical profile using a near SCF limit wavefunction¹ [5,24,25,26]. The transition from the ground state of helium to the first excited ion state (IP = 65.4 eV) is experimentally and theoretically more complex. Early studies [5,27] of the momentum profiles for this transition indicated that the inclusion of electron correlation in the wavefunction of the atom was required in the calculation of theoretical momentum profiles. A

¹ A description of SCF and CI wavefunctions is given in chapter 2.

number of theoretical profiles for this transition have been calculated using very accurate CI wavefunctions [26,28,29] and have exhibited a significant variation, reflecting the sensitivity of the EMS scattering process to initial state electron correlation and to wavefunction quality. However, the transition to the excited ion state has a much lower cross section than the transition to the ground ion state, and accurate measurement of the shapes and relative intensities of the momentum profiles for these transitions is difficult. The statistical precision of the experimental momentum profiles of the initial and subsequent investigations [26,30,31], is insufficient to clearly distinguish amongst the various theoretical profiles, calculated with different correlated wavefunctions.

The momentum profiles of the molecular hydrides of second and third row heavy atoms (CH_4 , NH_3 , H_2O , HF ; SiH_4 , PH_3 , H_2S , HCl) have been the subject of extensive investigation by EMS [13,32-45]. Experimental momentum profiles (XMPs) for the outer valence orbitals of water, reported by Bawagan *et al.* in 1985 [36], showed a remarkable discrepancy with theoretical profiles obtained using what were considered to be high quality SCF calculations. In particular, the XMPs of the $1b_1$ and $3a_1$ orbitals exhibited increased intensity at low momentum relative to the theoretical momentum profiles. Interestingly, results for the other highly polar second-row hydrides, HF [42] and NH_3 [13], showed similar discrepancies with theoretical momentum profiles using SCF wavefunctions, while the corresponding third row hydrides HCl [42], H_2S [46], and PH_3 [47], were well described by theoretical profiles at this level of theory. One suggestion for the observed discrepancy in water [36] was the

inadequacy of the variationally determined wavefunction to describe the long range behaviour of the molecular systems. The momentum profiles obtained by EMS investigate the low momentum region of molecules which corresponds to larger distances from the nuclei. Indeed, further investigations involving the addition of extra diffuse and polarization functions to the basis set of the SCF calculations produced theoretical momentum profiles exhibiting significantly improved agreement with the XMPs of water [37]. Importantly, very little change in the total electronic energy of the SCF wavefunction was observed with this enhancement of the basis set. The inclusion of electron correlation and relaxation effects by using CI wavefunctions for the ion and neutral species, built with the diffuse and saturated Gaussian basis sets developed in the SCF calculations, was also found to have a significant effect on the shape of the theoretical momentum profile, and adequate treatment of these effects was required to obtain good agreement with experimental EMS results. Additionally, these studies have revealed the need for an accurate accounting of momentum (angular) resolution effects in comparing theory and experiment. Small discrepancies were still observed at low momentum when the high quality theoretical momentum profiles were folded with a single Gaussian momentum resolution function. These discrepancies were eliminated [20] when the experimental resolutions in the polar and azimuthal angles ($\Delta\theta$ and $\Delta\phi$) were taken into account separately [48,49].

With a recent reinvestigation of HF [44] and HCl [45], the disagreement between the theoretical and experimental momentum profiles has been resolved for the row two and three

hydrides. The studies indicate that the highly polar second row hydrides HF, H₂O and NH₃ each require a large degree of polarization and extremely diffuse functions in highly saturated basis sets to properly describe the low momentum (outer spatial regions) of the molecule. Furthermore, the use of highly correlated wavefunctions for both the neutral and ion species is required in the theoretical calculation of momentum profiles. The EMS study of water and other second row hydrides revealed the power of EMS to provide information on the chemically important outer spatial regions of molecular charge distributions, where changes in electron density have little effect on the variationally determined electronic energies. These studies have also aided in the development of improved molecular wavefunctions that yield extremely accurate one-electron properties [20,37,50,51].

The first EMS study of an oriented and excited target was recently reported by Zheng *et al.* [52]. In this experiment sodium atoms were excited by circularly polarized light. With the *z* axis selected to be along the direction of the incident electron beam, the 3*p* (*m_l* = +1) state, was populated while the 3*p* (*m_l* = 0) state (i.e. 3*p_z*) remained unoccupied. The binding energy of the 3*p* electron is sufficiently less than that of the Na 3*s* electron to enable the ionization of the 3*p* electrons of the excited atoms to be distinguished from ionization of the ground state atoms, and momentum profile of these electrons was obtained. Good agreement was found between the Na 3*p* XMP and the theoretical momentum profile using the Hartree-Fock 3*p* (*m_l* = +1) wavefunction. Momentum profiles calculated for the unoriented Na 3*p* (*m_l* = 0, ±1) states gave significantly poorer agreement with the experimental data. While this study

involves a relatively simple system, it portends the likely direction of future EMS studies towards prepared and more well defined target species.

1.4 Multichannel Instrumental Developments

The modern architecture of EMS spectrometers has evolved from ‘first generation’ instrumental designs. The early EMS instruments described above are termed single channel, as they measure (within experimental resolution) scattering events for a single binding energy and a single relative azimuthal angle ($\pi - \phi$) between the outgoing electrons. However, valid (e,2e) collision events from all the target valence electrons occur at all angles of full 2π azimuth. The vast majority of these scattering events is not measured with a single channel instrument. The natural progression from the first generation instrumentation was the application of multichannel or multiparameter techniques to observe simultaneously as many (e,2e) events as possible. Two approaches were taken: one to sample a range of energies, the other to sample a range of azimuthal angles.

The first momentum (azimuthal angle) dispersive multichannel spectrometer was developed by Moore *et al.* [53]. This instrument uses a single truncated spherical analyzer to provide energy analysis over a large range of azimuthal angles. Detection of electrons at a number of angles is achieved by 14 channel electron multipliers [54] (increased from the original 10 CEMs [53]) that are dispersed in two banks of seven; one bank in a narrow angular spread, the other more widely dispersed on the opposite side of the detection circle.

Coincidence events are determined via a TAC using the start pulse from any one of the channeltrons in one bank, while the stop is given by any one of the channeltrons of the opposing bank. With the appropriate signal processing, this arrangement gives the simultaneous measurement of 49 relative azimuthal angles, and hence a possible enhancement of 49 in collection rate. In practice however, the use of an array of channeltrons for multichannel detection has limited the effectiveness of this instrumental design, since the gains of individual CEMs are different from device to device and are subject to variation with time and experimental conditions [54,55,56]. Frequent calibration of the instrument to a single channel measurement of the argon $3p$ orbital is required to circumvent this difficulty [54]. In practice, the statistical precision of the data obtained with this multichannel instrument [54] has been little different from that achieved in single channel instruments.

The energy dispersive multichannel approach has been pioneered and developed by Weigold *et al.* [7,26,57]. An improvement of approximately an order of magnitude in collection efficiency is achieved by the simultaneous measurement of a range of outgoing electron energies. The general design is similar to that of single channel instruments, shown in figure 1.2. A pair of hemispherical analyzers is used to disperse the outgoing electrons, and a slit aperture is used in place of the typical circular aperture in the exit plane of the analyzer. A microchannel plate/resistive anode encoder (MCP/RAE) assembly provides electron multiplication and positional determination of the electrons in the exit plane of the analyzers. The radial position of an electron at the exit plane of the analyzer is approximately a linear

function of the electron energy [57]. Thus a spread of outgoing energies can be measured simultaneously while maintaining the required energy resolution. As in single channel instruments, a complete binding energy spectrum is obtained by sweeping the energy of the incident electrons through the desired range of binding energies, and a momentum profile is measured by scanning one hemispherical analyzer about the azimuthal detection circle. A TAC is used for the determination of coincidence events, and improved timing is provided by software correction for the variation in transit times of different electron paths through the analyzers [57].

Following the initial (e,2e) measurements on solid targets [9,10], the attention of EMS studies in the past 20 years has been primarily directed towards gas phase systems. EMS measurements on solid targets are obviously of great interest, but such studies are hampered by the often high (background) accidental coincidence count rate, and by the necessity for much larger (~20-25 keV) electron impact energies to minimize multiple scattering effects. This significantly reduces the (e,2e) coincidence count rate, and increases the experimental demands on energy and momentum resolution [58,59]. A new spectrometer for the study of thin (<100 Å) solid films has recently been developed by Storer *et al.* [60], that combines limited ranges of both energy and momentum dispersive multichannel operation. This instrument [60] employs a toroidal analyzer and a hemispherical analyzer in an asymmetric geometry, with both analyzers designed to accept electrons from a range of azimuthal angles. Two-dimensional MCP/RAE detectors positioned at the exit plane of each analyzer provide

energy and angular information. An asymmetric geometry was chosen to take advantage of the higher cross section of asymmetric (e,2e) scattering over the symmetric case [61]. Binding energy spectra of the valence region of carbon have been presented as a function of momentum [60] and illustrate the potential of the new instrument to study the electronic structure of thin films.

1.5 Context and Organization of this Work

Electron momentum spectroscopy provides unique insight into the electronic structure of atomic and molecular systems, and fruitful collaborations with theoretical groups have developed in recent years. Future directions in EMS will involve the study of more interesting and complex target systems. Larger molecules of chemical and biochemical importance, van der Waals complexes, oriented molecules [62], molecules oriented on a surface [63], as well as excited molecules, free radicals and ions are all on the EMS ‘wish list’. However, relative to small atoms and molecules, many of these systems have more closely spaced valence energy levels, and can only be produced with low number densities (three to five orders of magnitude less than common gas targets). Both the required improvement of energy resolution and the necessarily low target densities will dramatically reduce the count rate of EMS coincidence events. Significant improvements in the detection efficiency of (e,2e) spectrometers are therefore required before measurements for these systems become feasible.

The earlier multichannel developments offer some insight into potential avenues for the improvement of EMS detection capabilities. The energy dispersive multichannel EMS spectrometer [26] has effected an order of magnitude improvement in sensitivity (i.e. detection efficiency), and has been quite successful in the measurement of relatively small, gas phase targets. However, the design suffers from the complexity involved in physically rotating and reproducibly positioning one of the energy analyzers to scan a range of momentum. The sequential scanning requires that experimental conditions (i.e. the incident electron gun current and target number density) remain constant during a measurement period, and additionally, necessitates significant analysis and reassembly of the experimental data to extract the individual orbital momentum profiles of the target. As well, only a relatively narrow range of binding energies can be sampled simultaneously, and the potential for further development of the instrumentation to improve sensitivity is limited. The momentum dispersive approach offers the advantage of using a single analyzer with no moving parts. The relatively simple design allows for greater precision in the construction and alignment of the spectrometer. Furthermore, such an instrument can be designed to simultaneously detect events over a wide range of azimuthal angles, permitting the complete XMP (i.e. ~ 0 - 2.5 a.u.) to be measured for any selected binding energy. Accordingly, the XMP measurements are relatively insensitive to fluctuations in experimental conditions. However, the instrumental design requires uniform detection efficiency of electrons over the observed azimuthal range. In this respect, the use of individual channeltrons to provide detection about the azimuth has proven to be problematic [54].

This thesis presents the development and application of a new momentum dispersive multichannel electron momentum spectrometer incorporating several new design features in both the spectrometer hardware and the coincidence detection electronics. The spectrometer employs a single cylindrical mirror analyzer (CMA) to provide energy analysis of (e,2e) electrons over a wide range of azimuthal angle. A two-dimensional microchannel plate/resistive anode encoder position sensitive detector and a single channel electron multiplier at the exit of the CMA gives parallel detection of electrons over a $\pm 30^\circ$ range of azimuth. Furthermore, a novel technique for the determination of (e,2e) coincidence events has been implemented. Based on the discrimination of pulse-pile-up of pairs of detector timing pulses, this coincidence detection scheme possesses distinct advantages over conventional TAC-based coincidence timing techniques. With such a design, the spectrometer should provide an improvement of one to two orders of magnitude in sensitivity relative to single channel instrumentation.

The development of the new multichannel spectrometer is the focus of chapter 3. The design, operation and testing of the electron source, collision region, lens system, cylindrical mirror analyzer, CEM and MCP/RAE detectors, coincidence timing electronics, and the data acquisition system are discussed in some detail. Proof-of-concept test measurements of argon, exhibiting the enhanced performance of the new spectrometer, are presented. Additionally, the two-dimensional surface displaying the angular (momentum) intensity as a function of

binding energy for the valence electrons of argon is presented. A description of the new instrument and some proof-of-concept results have appeared in the literature as:

B.R. Todd, N. Lerner, and C. E. Brion, *Rev. Sci. Instrum.* **65** (1994) 349.

Prior to the description of the spectrometer in chapter 3, the theoretical analysis of the (e,2e) cross sections measured in EMS is briefly discussed in chapter 2. Since detailed reviews of the scattering theory and the approximations used in the development of the theoretical momentum profiles have been published [64,65], only a summary is provided here. Additionally, a short comment on the more common approaches to calculating the electronic wavefunction of atoms and molecules is presented.

In chapter 4, binding energy spectra and experimental momentum profiles of the outer valence orbitals of Ne, Ar, Kr, and Xe, and of the molecular systems of CH₄ and SiH₄ are shown. These measurements provide a thorough examination of the performance and angular resolution of the new instrument. As well, the XMPs represent the most statistically precise measurements of these systems to date. The profiles are compared to earlier EMS measurements and to theoretical momentum profiles calculated using wavefunctions of various levels of quality.

Measurements of the (e,2e) ionization of helium and molecular hydrogen are presented in chapters 5 and 6 respectively. Momentum profiles are presented for the ionization of the

ground state neutral target to the ground state of the ion, as well as for ionization to excited ion states. As the final states of each of these systems have only one electron, the ion wavefunctions can be expressed exactly (within the Born-Oppenheimer approximation in the case of H_2). Hence, these systems are ideal for the detailed study of ground state electronic wavefunctions, and in particular, electron correlation effects. Previous investigations of He and H_2 have been hampered by the extremely low cross sections for ionization to the excited ion states. The improved detection efficiency of the new multichannel instrument has permitted detailed measurements of these systems. The experimental profiles of He are compared with momentum profiles based on extremely high quality correlated wavefunctions, including an explicitly correlated calculation by N. Cann here at UBC, and very large CI calculations performed by E.R. Davidson of Indiana University. The XMPs of H_2 are compared to ground and excited state momentum profiles calculated by J.W. Liu and V.J. Smith Jr. [66]. To examine the influence of molecular vibration, the multichannel XMPs of D_2 for the transitions to the excited ion states are compared to the H_2 measurements. Differences observed between the experimental and theoretical results are discussed.

It should be noted that throughout this thesis experimental momentum profiles are presented in atomic units (a.u.) where 1 a.u. of momentum is equivalent to 1.9929×10^{-24} Kg m/s. Additionally, the total electronic energies associated with the wavefunctions used in the calculation of theoretical profiles are presented in atomic units of energy, where 1 a.u. is equivalent to 27.212 eV.

Chapter Two

Theoretical Background

2.1 The EMS Scattering Cross Section

The ionization of atoms and molecules by electron impact is an important physical process that continues to be an area of considerable interest and investigation both experimentally and theoretically [65,67,68]. The probability of a given outcome of an electron impact ionization is expressed by the scattering cross section, which, ideally, accounts for the interaction of an incoming electron with all of the electrons and nuclei of the target system. However, approximations are required to describe this many-body interaction. The particular approach used to simplify the cross section calculation is dependent on the scattering kinematics: principally the energies of the incident and outgoing electrons, and the momentum transfer. The momentum transfer, $\mathbf{K} = \mathbf{p}_0 - \mathbf{p}_s$, is related to the classical concept of the impact parameter, with a small momentum transfer suggesting a soft or glancing collision, while a large momentum transfer suggests a hard or direct collision [69]. In electron momentum spectroscopy, the experiment is designed to observe ionizing collisions having high momentum transfer and high kinetic energies such that the description of the complex scattering process is greatly simplified. Ideally, measurements in EMS are a direct reflection of the target

properties rather than the scattering physics. The theoretical treatment of the EMS scattering cross section has been investigated in detail by McCarthy and Weigold [5,7,64,70]. A brief overview is given below.

The triple differential cross section for an (e,2e) reaction can be written as [7,71]

$$\frac{d^3\sigma}{dE d\Omega_s d\Omega_e} = (2\pi)^4 \frac{p_e p_s}{p_o} \sum_{ave} |M_f|^2 \quad (2.1)$$

where E is the energy of the ejected (or scattered) electron, Ω_s and Ω_e are the outgoing electron solid angles, and M_f is the scattering amplitude, given by

$$M_f = \langle \chi_e^{(-)} \chi_s^{(-)} \Psi_f^{N-1} | T(E) | \Psi_o^N \chi_o^{(+)} \rangle. \quad (2.2)$$

In this equation, $\chi^{(\pm)}$ represent wavefunctions of the incident (+) and outgoing (-) electrons in the target scattering potential, T is the transition operator, and Ψ_f^{N-1} and Ψ_o^N represent the total wavefunctions of the ion and neutral species respectively. The high electron energies and large momentum transfer permit the scattering process to be viewed as an impulsive, binary collision of the incident and target electrons. A nice physical picture of the impulse approximation has been recently given by Hall, Reading and Ford [72]:

During the collision the (*target*) electron does not move very far, if at all. It therefore has no time to sense the forces binding it to the target nucleus; they merely determine some distribution of electronic momenta and position. During the collision the electron can be considered as recoiling freely. The simplifying nature of this assumption is that this problem now reduces to a two-body collision, which is soluble if we know the projectile-electron *t*-matrix.

In the binary encounter approximation, the operator T depends only on the coordinates of the incident and target electron, and commutes with the ion wavefunction to give

$$M_f = \langle \chi_e^{(-)} \chi_s^{(-)} | T(E) | (\Psi_f^{N-1} | \Psi_o^N) \chi_o^{(+)} \rangle. \quad (2.3)$$

If the wavefunctions of the incident and outgoing electrons are represented as distorted waves, the cross section using equation (2.3) is referred to as the distorted wave impulse approximation (DWIA); however, the calculation of the transition amplitude using this equation is prohibitively difficult [73]. At sufficiently high impact energies, plane waves may be used to represent the incident and outgoing electrons. In the plane wave impulse approximation (PWIA), the scattering amplitude may be factorized into a collision term and a structure term, to give

$$M_f = \langle \mathbf{k}' | t(E) | \mathbf{k} \rangle \langle \chi_e^{(-)} \chi_s^{(-)} | (\Psi_f^{N-1} | \Psi_o^N) \chi_o^{(+)} \rangle \quad (2.4)$$

where $t(E)$ is the two electron t -matrix, and $\mathbf{k} = \frac{1}{2}(\mathbf{p}_0 - \mathbf{p}_t)$ and $\mathbf{k}' = \frac{1}{2}(\mathbf{p}_s - \mathbf{p}_e)$ are the relative momenta of the two electrons before and after the collision.

The square of the first term in equation (2.4) is the (half-off-shell) Mott scattering cross section σ_{Mott} , which describes the Coulomb scattering of two electrons including the possibility of exchange. This term can be expressed exactly, and has a simple form in the symmetric non-coplanar geometry [25]. In figure 2.1, the variation of the Mott cross section with azimuthal angle, using typical values of $\theta = 45^\circ$ and $E_s = E_e = 600$ eV, is presented for impact energies of

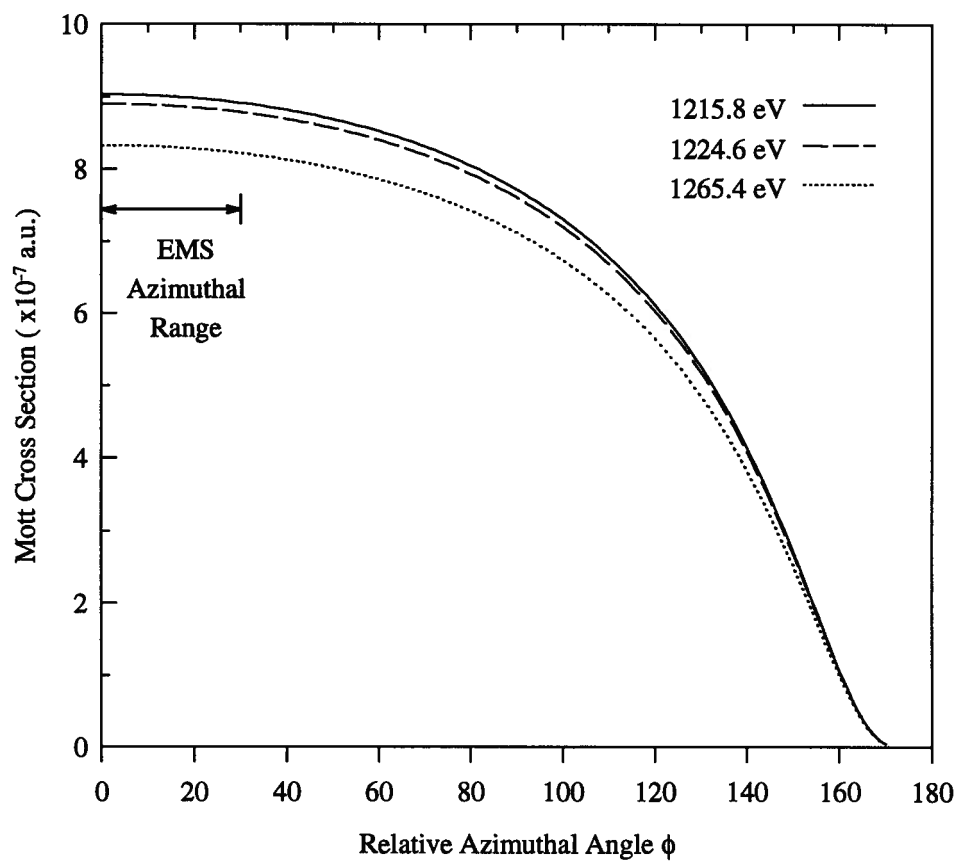


Figure 2.1: The Mott scattering cross section for symmetric non-coplanar kinematics with $\theta = 45^\circ$, $E_1 = E_2 = 600$ eV, for three values of impact energy.

1215.8, 1224.6 and 1265.4 eV. These energies (less 1200 eV) correspond to the ionization of an electron from the argon 3*p* orbital, and to the transitions from the ground state of He to the ground and first excited states of the He⁺ ion. While the decrease in cross section is small for measurement over the outer valence region of atoms and molecules, the change must be considered when, as for some experiments in the present work (chapter 5), a large range of binding energies is investigated. It is most important to note that, for a given impact energy, the Mott cross section is essentially constant over the range of φ angles at which observations are made in an EMS experiment. This is in contrast with the large variation of the Mott cross section inherent to the symmetric coplanar geometry ($\varphi = 0^\circ$, $\theta_e = \theta_s$) [74].

The plane waves in the structure term of equation (2.4) are given by $\chi_a^{(\pm)} = e^{\pm i\mathbf{p}_a \cdot \mathbf{r}}$ and since $\mathbf{p}_t = \mathbf{p}_e + \mathbf{p}_s - \mathbf{p}_o$ (eqn. 1.1), the equation can be rewritten as

$$|M_f|^2 = \sigma_{\text{Mott}} \left| \left\langle e^{i\mathbf{p}_t \cdot \mathbf{r}} \Psi_f^{N-1} \middle| \Psi_o^N \right\rangle \right|^2 \quad (2.5)$$

such that the (e,2e) scattering cross section in the PWIA is:

$$\sigma_{\text{EMS}} = \frac{d^3\sigma}{dE d\Omega_s d\Omega_e} = (2\pi)^4 \frac{p_e p_s}{p_o} \sigma_{\text{Mott}} \sum_{\text{ave}} \left| \left\langle e^{i\mathbf{p}_t \cdot \mathbf{r}} \Psi_f^{N-1} \middle| \Psi_o^N \right\rangle \right|^2. \quad (2.6)$$

The term \sum_{ave} denotes the average over degenerate initial states and the sum over unresolved final ion states. Thus, as σ_{Mott} is effectively constant at a given impact energy, the cross section observed in an EMS experiment is explicitly dependent on the overlap of the initial

target and final ion wavefunctions. A theoretical momentum profile evaluated using the cross section expression of equation (2.6) is often referred to as an overlap distribution (OVD).

In the case of molecular targets, the molecular and ionic wavefunctions are expressed (using the Born-Oppenheimer approximation) as products of electronic, vibrational and rotational functions. Since vibrational and rotational states are not resolved in typical EMS experiments, the cross section is summed over the final rotational and vibrational states, and the final rotational and vibrational wavefunctions are removed from the cross section expression (via a closure relation) [7,64]. The rotation of the (randomly oriented) gaseous target species is accounted for by spherically averaging over the nuclear coordinates (Ω) or equivalently by spherically averaging over the direction of the target electron momentum. The vibrational motion of the target molecule requires that the cross section be integrated over the vibrational coordinates, with the electronic terms evaluated at each nuclear geometry and weighted by the absolute square of the vibrational wavefunction [7]. However, the influence of vibrational motion on the cross section is commonly approximated by evaluating the electronic overlap at the equilibrium geometry of the target molecule (see section 6.4). The PWIA EMS cross section for molecular species is now given as

$$\sigma_{\text{EMS}} = (2\pi)^4 \frac{p_e p_s}{p_o} \sigma_{\text{Mott}} \sum_{\text{ave}} \int d\Omega \left| \langle e^{i\mathbf{p}_i \cdot \mathbf{r}} \Psi_f^{N-1} | \Psi_o^N \rangle \right|^2 \quad (2.7)$$

where Ψ_f^{N-1} and Ψ_o^N are the ion and neutral electronic wavefunctions.

Often the target Hartree-Fock approximation (THFA) is employed, which permits a simplification of the form of the ion-neutral overlap $\langle e^{i\mathbf{p}_i \cdot \mathbf{r}} \Psi_f^{N-1} | \Psi_o^N \rangle$. If the target wavefunction is approximated by an antisymmetrized product of one-electron wavefunctions (i.e. canonical Hartree-Fock orbitals), the integral over the coordinates of the target electron can be separated from the integral over the coordinates of the remaining electrons. This gives

$$\langle e^{i\mathbf{p}_i \cdot \mathbf{r}} \Psi_f^{N-1} | \Psi_o^N \rangle = \langle \Psi_f^{N-1} | \Phi_o^{N-1} \rangle \int e^{i\mathbf{p}_i \cdot \mathbf{r}} \phi_t(\mathbf{r}) d\mathbf{r} \quad (2.8)$$

where Φ_o^{N-1} is the Hartree-Fock wavefunction of the target, with an electron removed from the orbital ϕ_t . The square of the overlap $\langle \Psi_f^{N-1} | \Phi_o^{N-1} \rangle$ is termed the spectroscopic factor S_f^t . The integral on the right hand side of equation (2.8) is just the Fourier transform of the position space canonical Hartree-Fock orbital ϕ_t . Thus, in the THFA, the EMS cross section is expressed as

$$\sigma_{EMS} = \text{constant } S_f^t \int d\mathbf{p} |\phi_t(\mathbf{p})|^2. \quad (2.9)$$

Within the framework of the PWIA and THFA, the experimental momentum profile is directly proportional to the spherically averaged square of the momentum space orbital occupied by the target electron before the ionization process.

The experimental (e,2e) coincidence count rate is related to the atomic or molecular (e,2e) cross section (equation 2.6 or 2.7) by

$$N_t = n I \sigma_{EMS} \Delta\Omega_a \Delta\Omega_b \Delta E_a \Delta E_b \delta(E_o - E_a - E_b - IP) \quad (2.10)$$

where $\Delta\Omega$ and ΔE are the solid angles and resolution of the energy analyzers labeled a and b, n is the number of target species in the collision region, and I is the rate of incident electrons through the collision region [5]. Typically in EMS studies the measured cross sections are not absolute, since neither n nor I are usually determined. However, the experimental parameters of equation (2.10) are (essentially) constant over the valence region of the target species, and the EMS momentum profiles are measured with the correct relative intensities. Only one normalization of theory and experiment is required for the valence region of a given species. Hence, the normalization of an XMP of one orbital to a corresponding theoretical profile determines the relative intensities of the XMPs of other valence electrons.

The comparison of the theoretical and experimental momentum profiles for inner valence electrons may be complicated by the often significant splitting of the main peak intensity to the satellite peaks that arises from electron correlation effects (primarily final state correlation). However, the sum of the spectroscopic factors is governed by the sum rule

$$\sum_f S_f^t = 1 \quad (2.11)$$

where the summation is over the final ion states associated with the ionization of an electron from orbital ϕ_t (i.e. over the symmetry manifold t). As the spectroscopic factors are reflected in the relative peak areas of the binding energy spectra, the sum of the peak areas over main and satellite transitions permits a direct comparison to the theoretical cross sections, using a spectroscopic value of unity (see chapter 4).

The viability of the plane wave impulse approximation is crucial for the application of EMS to investigations of electronic structure. As the approximation is based on the neglect of the interactions of the free (incoming and outgoing) electrons with the neutral target and final ion, the PWIA is expected to be increasingly valid at higher impact energies. A convincing test of the approximation is given in the EMS measurements of atomic hydrogen [23] discussed in chapter 1. The XMP measurements at impact energies of 400, 800 and 1200 eV show very good agreement with each other as well as with the theoretical momentum profile calculated in the PWIA using the exact wavefunction of the hydrogen atom. Experience has indicated that the PWIA analysis is valid for the EMS investigation of the outer valence regions of atoms and molecules in the momentum region from 0 a.u. to ~ 1.5 a.u., provided the electron impact energy is greater than 1000 eV [6,64,75]. This range covers the majority of the momentum region typically observed in an EMS experiment.

At higher values of momenta (≥ 1.5 eV) the PWIA often underestimates the experimental intensity. This effect is not unreasonable, since the higher momentum region corresponds to ionization from regions closer to the nuclei, where distortion of the incident and outgoing electron waves by the target and ion potentials is expected to be larger [30]. In the case of atoms, the influence of the ion/target potentials on the (e,2e) cross sections can be partially restored by the use of the factorized distorted wave impulse approximation (DWIA) [27,73]. In this approximation, the factorized form of the scattering amplitude shown in

equation (2.3) is retained, and distorted waves $\chi^{(\pm)}$, calculated in the static potential of the target and the ion, represent the incoming and outgoing electrons. Although the factorization of the scattering amplitude is not exact in this approximation, it has been shown to be valid for scattering in the symmetric non-coplanar geometry [73]. In studies of the noble gas atoms, the theoretical cross sections evaluated in the (factorized) DWIA have shown improved agreement with experimental momentum profiles, in the higher momentum region [27,76].

The direct comparison of experimental and theoretical momentum requires a consideration of the necessarily finite experimental angular resolution. This is achieved by ‘folding’ the estimated experimental resolution into the theoretical profile. The Δp method is a procedure that has been used to account for the instrumental resolution by folding the theoretical cross section with a single Gaussian momentum resolution function. However, such a resolution function is unphysical [48,49] as the experimental resolution originates from the uncertainty (experimental spread) in angular coordinates, rather than in momentum coordinates. An improved resolution-folding procedure, titled the Gaussian-weighted planar grid (GW-PG) method, has recently been reported by Duffy *et al.* [49]. This method is an extension of the momentum-averaged Gaussian-weighted (MAGW) formalism [48], which is itself a modification of the uniformly weighted planar grid (UW-PG) technique [35,77]. In contrast to the Δp method, the GW-PG method uses individual Gaussian resolution functions for the azimuthal (ϕ) and polar (θ) coordinates in the calculation of p-dependent momentum resolution functions. At low values of p, the GW-PG momentum resolution function is non-

symmetric and has a tail extending to higher momenta. At higher values of momentum, a more symmetric, Gaussian-shaped function is generated (see fig. 3 of ref. [49]). Theoretical momentum profiles folded with such a procedure show an increase in the intensity at low momentum relative to the Δp method, and comparison of GW-PG folded TMPs calculated using very accurate wavefunctions, have exhibited significantly improved agreement with experimental measurements for a wide range of systems. [20,49]. With a few noted exceptions, the TMPs presented throughout this thesis have been folded with the GW-PG procedure.

2.2 The Calculation of Electronic Wavefunctions

In 1959, Professor Charles Coulson² gave the closing address to participants of the Conference on Molecular Quantum Mechanics held in Boulder, Colorado. Commenting on clues into the direction of future work, he suggested that “the most important clue seems to me to be the recognition that the energy is not the only criterion of goodness of a wave function. In the past we have been preoccupied with energy”. The preceding section has shown the EMS cross section to be directly proportional to the overlap of the ion and neutral electronic wavefunctions, which, in the THFA, is proportional to the square of the momentum space orbital of the target electron. As the EMS momentum profiles investigate the low momentum, spatially diffuse regions of a wavefunction that have only small influence on the

² It should be noted that C.A. Coulson, along with W.E. Duncanson, wrote a series of landmark papers[177-182] in the early 1940's, pioneering the investigation of the chemical bond from the perspective of momentum space, rather than position space.

total electronic energy, EMS measurements are able to provide an additional “criterion of goodness” [78] for the assessment of an atomic or molecular wavefunction.

The most common techniques for the calculation of wavefunctions are based on the variational principle. Given the equation $\mathcal{H}|\Phi_0\rangle = \varepsilon_0 \Phi_0$ where \mathcal{H} is the Hamiltonian, Φ_0 is the exact ground state wavefunction, and ε_0 is the corresponding energy, then the expectation value of the Hamiltonian of a normalized wavefunction $|\Psi_0\rangle$ is an upper bound to the exact ground state energy

$$\langle \Psi_0 | \mathcal{H} | \Psi_0 \rangle \geq \varepsilon_0. \quad (2.11)$$

Thus in the variational method, the wavefunction that is assumed to be the best approximation to the exact wavefunction is the one calculated to have the lowest energy. The capability of the wavefunction to yield accurate atomic or molecular properties, including the momentum distribution, depends on both the computational technique, as well as the quality of building blocks, or basis set, used in the calculation. As suggested by Shavitt [79], “it is a truism that no calculated wave function can be better than the basis set from which it is constructed.”

In the following sections the computational methods of Hartree-Fock and Configuration Interaction, which are referred to throughout the thesis, are discussed. Only brief outlines are given as these computational techniques are well described in most modern quantum chemistry texts (see for example Levine [51], or Szabo and Ostlund [80]).

2.2.1 The Hartree-Fock Method

The (non-relativistic) electronic Hamiltonian operator for an N-electron system with M nuclei can be written in atomic units as

$$\mathcal{H} = - \sum_{i=1}^N \frac{1}{2} \nabla_i^2 - \sum_{i=1}^N \sum_{A=1}^M \frac{Z_A}{r_{iA}} + \sum_{i=1}^N \sum_{j>i}^N \frac{1}{r_{ij}} \quad (2.12)$$

where the first term represents the kinetic energy operator, the second the attraction between electrons and nuclei, and the third the mutual repulsion of electrons. The difficulty of solving for the eigenfunctions of the Hamiltonian arises from the term r_{ij}^{-1} , since as a result of this term the Schrödinger equation is non-separable. The Hartree-Fock approach circumvents this difficulty by averaging over the individual electron-electron interactions.

In the Hartree-Fock approximation, the wavefunction of an N-electron system is described by a single Slater determinant.

$$|\Psi_0\rangle = |\chi_1 \chi_2 \dots \chi_N\rangle \quad (2.13)$$

where the spin-orbitals χ_i are functions of the coordinates and spin of electron i. It can be shown that the wavefunction of this form that minimizes the energy given by $\langle \Psi_0 | \mathcal{H} | \Psi_0 \rangle$ is the Slater determinant composed of one-electron functions that are eigenfunctions of the Hartree-Fock equation

$$f(1) |\chi_i(1)\rangle = \epsilon_i |\chi_i(1)\rangle \quad (2.14)$$

where f is the one-electron Fock operator. The Fock operator can be written as

$$f(1) = -\frac{1}{2} \nabla_1^2 - \sum_A \frac{Z_A}{r_{1A}} + v^{\text{HF}}(1) \quad (2.15)$$

to emphasize the treatment of the electron interaction by an average potential of the other electrons of the systems, v^{HF} . This potential is written more explicitly as

$$v^{\text{HF}}(1) = \sum_j \ell_j(1) - \mathcal{X}_j(1) \quad (2.16)$$

where ℓ_j is the coulomb operator given by

$$\ell_j(1) = \int d\mathbf{x}_2 |\chi_j(2)|^2 r_{12}^{-1}, \quad (2.17)$$

\mathcal{X}_j is the exchange operator defined by

$$\mathcal{X}_j(1) \chi_i(1) = \left[\int d\mathbf{x}_2 \chi_j^*(2) r_{12}^{-1} \chi_i(2) \right] \chi_j(1) \quad (2.18)$$

and where \mathbf{x}_2 represents the space and spin coordinates of an electron, labeled here as electron 2.

The Hartree-Fock orbitals are expressed as the sum of a set of basis functions, each scaled by a coefficient:

$$\chi_i = \sum_v C_{vi} \phi_v. \quad (2.19)$$

As the Fock operator itself is dependent on the one-electron functions, the solution of the Hartree-Fock equation involves the iterative calculation of the basis function coefficients. An initial set of orbitals is used to evaluate a new set of orbitals, and the process repeated until the orbital coefficients no longer change, a procedure referred to as the self-consistent-field (SCF) method. The energy obtained from this procedure is dependent on the size and nature of the set of basis functions, or basis set, and as the basis size is increased, the wavefunction and energy will approach the Hartree-Fock limit.

Two types of basis functions are common: Gaussian-type and Slater-type orbitals.

Slater-type orbitals (STOs) are written in spherical polar coordinates as

$$\phi_{nlm} = N r^{n-1} e^{-\zeta r} Y_{lm}(\theta, \phi) \quad (2.20)$$

where N is the normalization constant, n is a positive integer, l and m are angular momentum quantum numbers, and ζ , the orbital exponent, determines the diffuseness of the basis function. A collection of atomic near-Hartree-Fock limit wavefunctions has been tabulated by Clementi and Roetti [81]. Theoretical momentum profiles of noble gas atoms, calculated using these wavefunctions, are presented in chapter 5. Cartesian Gaussian-type orbitals (GTOs) are very popular for molecular calculations as the integrals required in the wavefunction calculation are easily evaluated. The Cartesian GTOs are defined by

$$\phi_{kmn} = N x^k y^m z^n e^{-\zeta r^2}. \quad (2.21)$$

where N and ζ are as above, and k, m, n are (nonnegative) indices. A good overview of basis sets and techniques used to ensure the efficient calculation of atomic and molecular wavefunctions is provided by Davidson and Feller [82].

As shown in the previous section, in the target Hartree-Fock approximation the EMS cross section is proportional to the spherically averaged square of the momentum space orbital of the target electron. Since a Hartree-Fock calculation generally gives position space orbitals, the Fourier transform of these orbitals

$$\phi(\mathbf{p}) = (2\pi)^{-3/2} \int e^{-i\mathbf{p}\cdot\mathbf{r}} \phi(\mathbf{r}) d\mathbf{r} \quad (2.22)$$

must be calculated. A FORTRAN program (HEMS), developed in this laboratory and based on equations reported by Kaijser and Smith Jr.[83], performs the necessary transformations and evaluates the spherically averaged momentum profiles from a Hartree-Fock wavefunction. Originally written and revised by A. Hamnett, J. Cook, K.T. Leung, and A.O. Bawagan, this program was extensively modified during the course of the present study, and has recently been further expanded by N.M. Cann.

2.2.2 The Method of Configuration Interaction

The mutual repulsion of electrons gives rise to the correlation of their motion in an atomic or molecular system. Accordingly, the probability of finding two electrons very close together should be small. The Hartree-Fock method neglects this Coulombic correlation, and

the difference between the exact non-relativistic energy of a system and the Hartree-Fock limit energy is termed the correlation energy. Many theoretical techniques have been developed to calculate correlated wavefunctions. On small systems the correlation of electrons may be introduced by explicitly expressing the interparticle coordinates r_{ij} in the wavefunction [84]. Indeed, explicitly correlated wavefunctions for helium are used in the calculation of OVDs presented in chapter 5. Larger systems require the use of other methods, the most general and conceptually straightforward being that of Configuration Interaction (CI) [79].

Any many-electron wavefunction, including the exact wavefunction, can be written as the sum of a series of Slater determinants constructed from a complete set of one-electron functions [84]. This is the foundation of the CI method, in which the exact wavefunction is approximated by

$$\Psi_{\text{CI}} = \sum_i c_i |\Phi_i\rangle \quad (2.23)$$

where $|\Phi_i\rangle$ are Slater determinants representing the ground state, and the singly and multiply excited configurations. The expansion coefficients c_i are chosen such that the expectation value given by $\langle \Psi_{\text{CI}} | \mathcal{H} | \Psi_{\text{CI}} \rangle$ is a minimum. Singles and doubles CI (SDCI) is a common technique in which the CI expansion is restricted to include only singly and doubly excited configurations. Doubly excited configurations are particularly important as they mix directly with the ground state configuration; that is the CI matrix element given by $\langle \Phi_0 | \mathcal{H} | \Phi_D \rangle$, where Φ_D is a doubly excited configuration, is not zero. Singly excited configurations do not couple

with the ground state; however they enter the CI expansion through the indirect coupling with the doubly excited configurations. Additionally, the inclusion of singly excited configurations is important in the description of the one-electron properties of the system [79,80].

An extension of the SDCI method is the multireference singles and doubles CI (MR-SDCI) technique. In this approach, a SDCI calculation is performed first, and the significant configurations are used as the initial reference of a further calculation involving single and double excitations of each of the reference configurations. In this manner, the MR-SDCI wavefunction includes some triply and quadruply excited configurations [51]. A good example is provided in the MR-SDCI wavefunction for the ground state of water [36,50], calculated to investigate the outer valence momentum profiles as discussed in chapter 1. A basis of 109-GTOs, designed to give both a good energy (the lowest SCF energy reported at the time) and to saturate the diffuse basis function limit, was used in the calculation of the Hartree-Fock wavefunction. From a SDCI calculation, a reference wavefunction of 15 configurations was obtained. In the subsequent MR-SDCI calculation, 11011 configurations were used in the description of the final CI wavefunction. This wavefunction was estimated to recover 83% of the correlation energy of H₂O [36].

Chapter Three

The Momentum Dispersive Multichannel EMS Spectrometer

The new momentum dispersive multichannel electron momentum spectrometer is described in considerable detail in the following sections. The development of the instrument, incorporating a microchannel plate/resistive anode (MCP/RAE) position sensitive detector along with a conventional channel electron multiplier (CEM) detector, has provided the ability to simultaneously detect (e,2e) events occurring over an azimuthal range of $\pm 30^\circ$. The realization of the full gain in sensitivity offered by such an instrumental design demanded great care in the construction and evaluation of the instrument. Particular attention was given to the alignment and symmetry of the analyzer, the implementation of the detectors for time and position information, and the detection of coincidence events.

The description of the spectrometer is separated into five sections encompassing i) the vacuum system, electron gun, and analyzer assembly; ii) the detectors; iii) the coincidence electronics and data acquisition; iv) the characterization and operation of the instrument, and v) proof-of-concept (e,2e) measurements of the valence region of argon.

3.1 The Electron Source and Analyzer

In order to offer a sufficiently complete picture of the design of the spectrometer, three different views are presented in the following figures. Figures 3.1a and 3.1b are photographs of the instrument showing (from the bottom up) the spectrometer mounting plate (with one of the pumping apertures visible on the right hand side), the analyzer base plate and support pillars, the analyzer end corrector rings, and the inner and outer cylinder of the cylindrical mirror analyzer (CMA). An aluminum vacuum chamber rests on the O-ring in the spectrometer mounting plate. The chamber is evacuated by two 360 l/sec turbomolecular pumps (Leybold-Heraeus) to a base pressure of 2×10^{-7} torr. Differential pumping of the electron gun chamber is provided by a 150 l/sec turbomolecular pump (LH-150). As the motion of an electron is affected by a magnetic field, the stray magnetic field strength within the spectrometer is reduced by a hydrogen annealed mu-metal enclosure surrounding the vacuum chamber. Also out of consideration of magnetic fields, the components of the spectrometer are constructed primarily of aluminum or brass. To reduce the backscatter of electrons, the inner surfaces of the gun and analyzer assemblies are coated with benzene soot.

Figure 3.2 is a schematic showing the principal components of the spectrometer. The general order of assembly of the collision region, retarding lenses, CMA, and detector is displayed. A cross sectional schematic of the spectrometer is presented in figure 3.3. Each of the components presented in these figures is described in the following sections.

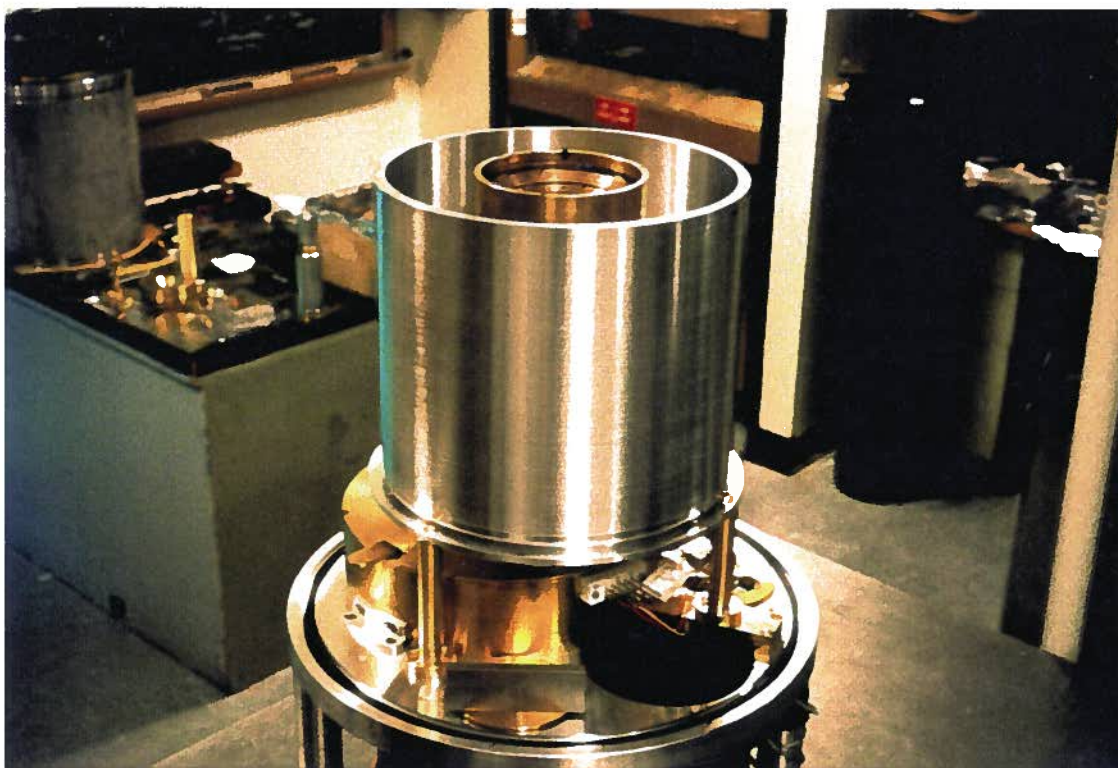


Figure 3.1: Photographs of the spectrometer. The spectrometer base, CMA base plate, end correctors and inner cylinder are displayed in the top photograph. The outer cylinder is in place in the lower photograph.

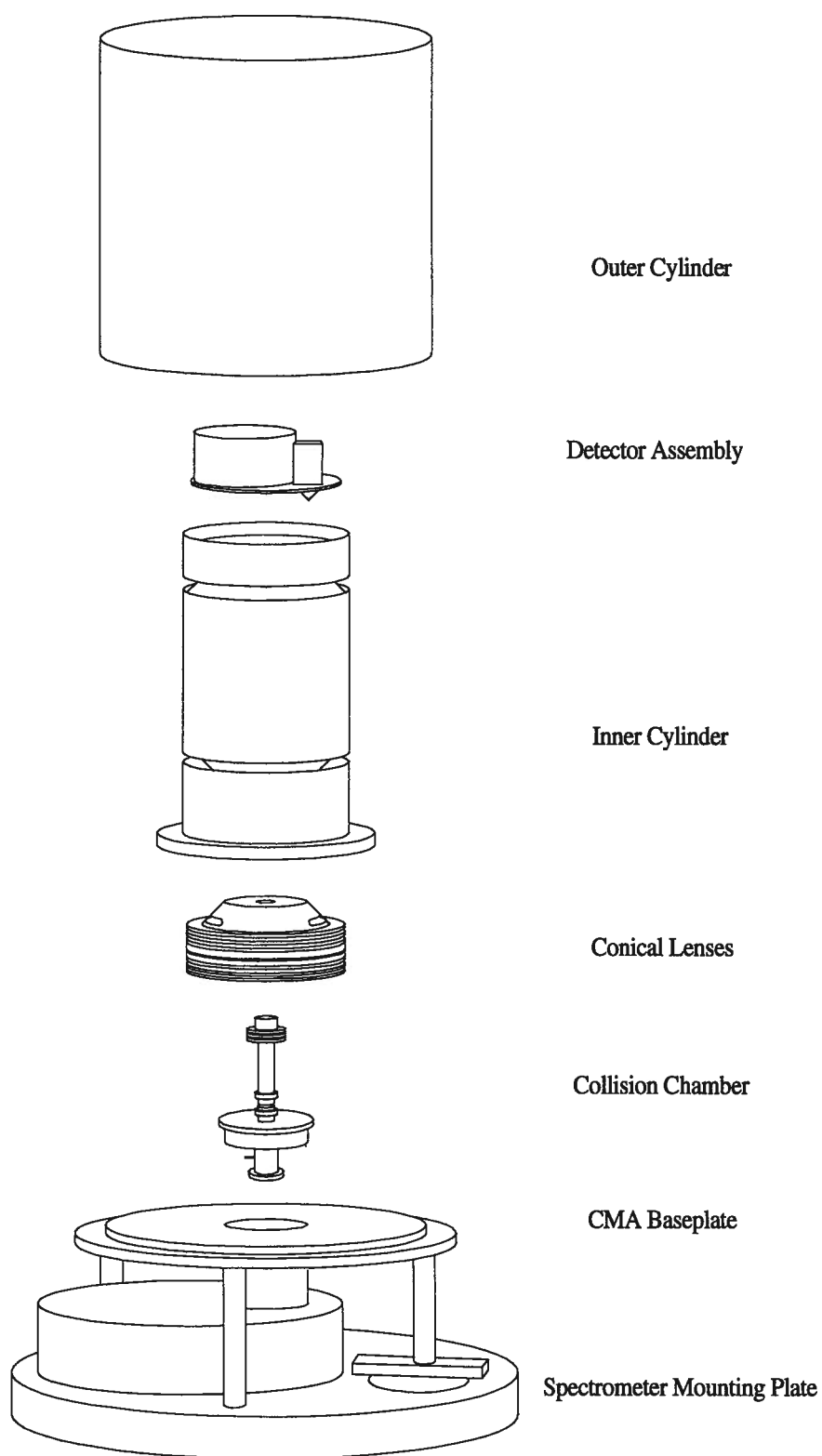


Figure 3.2: A break-away schematic of the spectrometer.

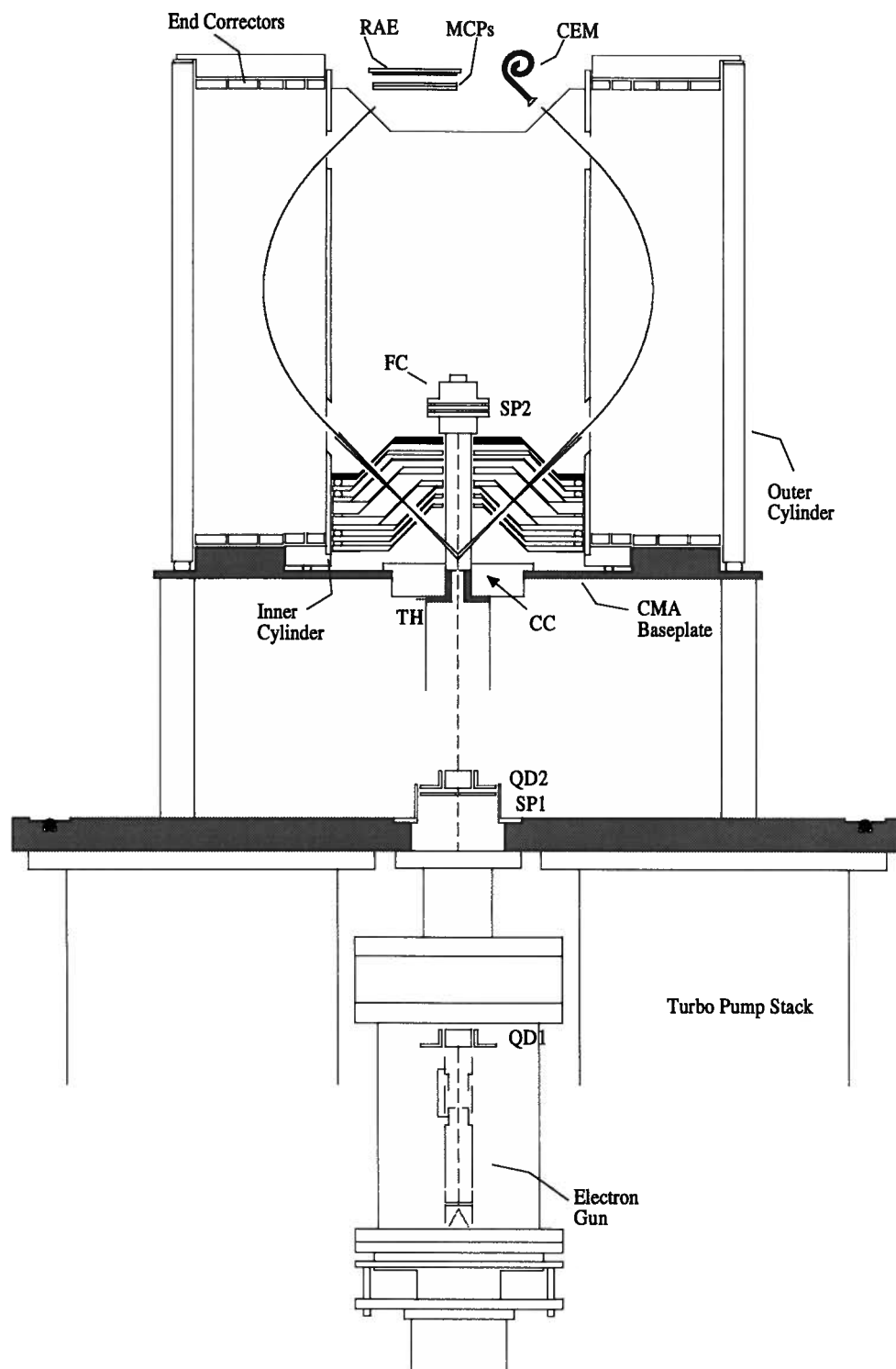


Figure 3.3: A schematic of the momentum dispersive spectrometer. QD=quadrupole plate deflector, SP=spray plate aperture, FC=Faraday cup, MCP=microchannel plate, RAE=resistive anode encoder, CEM=channel electron multiplier, CC=collision chamber, TH=top hat of CC.

3.1.1 The Electron Beam Assembly

A 0.125-mm thoriated tungsten (Goodfellow Metals W055300) "hairpin" filament, heated by a regulated (constant current) power supply (Lambda LK341) provides a stable source of electrons. The filament is maintained at a negative potential (~ -1200 V with respect to ground) with a DC power supply (Fluke 415B) that has been modified to allow computer control. The electron beam from the filament is accelerated and focused with a commercially available electron gun body (Cliftronic CE5AH) consisting of a grid, anode, and three-element electrostatic lens (see figure 3.3). As the third lens element and the collision chamber are at ground potential, the energy of the electron beam is determined by the potential applied to the filament. The electron gun assembly is mounted below and aligned with the central hole in the spectrometer mounting plate. The position of the filament mount may be manually adjusted, while under vacuum, to center the filament tip with respect to the grid aperture. Two pairs of parallel plate deflectors, provide additional control over the alignment of the electron beam. The collimation and alignment of the beam are monitored using microammeters that measure the current from molybdenum "spray plate" apertures, and from the Faraday cup. In the vicinity of the collision region, the electron beam is estimated to have a diameter of 1 mm.

3.1.2 The CMA Baseplate

The CMA baseplate supports all of the major components of the spectrometer, and alignment of the baseplate to the axis defined by the electron beam is critical. The baseplate is positioned with the aid of a jig that aligns its central hole with that of the spectrometer mounting plate. The baseplate rests on three pillars (see figures 3.1 and 3.2) that may be moved slightly with respect to the mounting plate. With the jig in place, the support pillars are fastened to the mounting plate and define the position of CMA baseplate. As long as the pillars remain fixed, the baseplate may be removed and replaced reproducibly.

3.1.3 The Collision Chamber

The collision chamber consists of a brass tube and an alignment flange that rests in the CMA baseplate. With a molybdenum aperture (1.8-mm) at the bottom end, and the Faraday cup and spray plate (2.0-mm aperture) at the top, the chamber acts as a sample gas cell. Two slots have been cut on opposing sides of the tube, and brass collars have been positioned to define the location and size of the slot opening (1.76-mm). The slot spacing helps to define the collision region, i.e., the volume of the interaction of the electron beam and target sample from which electrons may be scattered into the CMA.

The design of the collision chamber was modified part way through this work, to reduce the distance from the collision chamber entrance to the collision region. The design of the

original collision chamber is shown in figure 3.2, while the cross section of the modified chamber is shown in figure 3.3. The change was found to be necessary after binding energy spectra measurements for the very low intensity final excited ion states of He^+ and H_2^+ (see chapters 5 and 6) revealed weak structure originating from the interaction of the electron beam with the sample gas prior to, as well as within, the collision region (i.e. double scattering). These effects were inconsequential for conventional studies used to test the instrument. To reduce this pre-collision interaction, the bottom of the collision chamber was cut off, and a "top-hat" (TH - fig. 3.3) shaped tube supporting the entrance aperture was press-fit into the alignment flange. In the new design, the aperture is positioned approximately 5 mm below the collision region, and the gas supply is introduced into the collision chamber through a small hole in the side wall of the "top-hat". A wire mesh replaces the tube below the alignment flange to provide a ground plane shield for the electron beam, while allowing improved pumping of gas away from the vicinity of the beam.

3.1.4 The Conical Lenses

The energy resolution of a cylindrical mirror analyzer is approximately a linear function of the electron pass energy [85,86], and to improve the instrumental energy resolution a deceleration stage is often used prior to the entrance to the CMA. In the present instrument, an eight-element conical lens assembly is positioned about the collision chamber (see figures 3.2 and 3.3). This lens assembly was designed by Dr. Tim Reddish, a former postdoctoral fellow in the group of C.E. Brion, to permit deceleration of the electrons exiting the collision

region over the full $\pm 30^\circ$ azimuthal range. Initial test measurements using the lenses exhibited an improved energy resolution (1.6 eV FWHM with 100 eV pass energy); however, extensive focusing/defocusing of electrons in the azimuthal coordinate was also observed, due to “end effects” in the $\pm 30^\circ$ slot apertures. This effect destroys the azimuthal angular scattering information central to the experimental measurement of electron momentum profiles. Future development of the instrument will involve correcting this problem, either by the use of grids on the lens elements or by widening the azimuthal angular range of the lens slits. In the present application of the instrument, all of the lens elements are set to ground potential, and act only to define the range of polar angles of electrons entering the CMA. Figure 3.4 shows the cross section of the conical lenses and collision region. In addition to the size of exit slits (S_1) of the collision chamber, the angular spread of electrons into the CMA and length of the collision region are defined by the slits (S_2) of the fifth lens element.

3.1.5 The Cylindrical Mirror Analyzer

The design of the CMA is based on the characterization of CMA performance by Risley [86]. The cylindrical mirror analyzer consists of two concentric cylinders with a voltage applied between them. The resulting electric field between the cylinders disperses the electrons on the basis of their kinetic energies. Ideally, the CMA would exhibit first and second order focusing characteristics [86] in which $\frac{\partial z}{\partial \theta} = \frac{\partial^2 z}{\partial^2 \theta} = 0$ where z is the central the axis of symmetry of the analyzer (i.e. the vertical axis in the present CMA). However, size

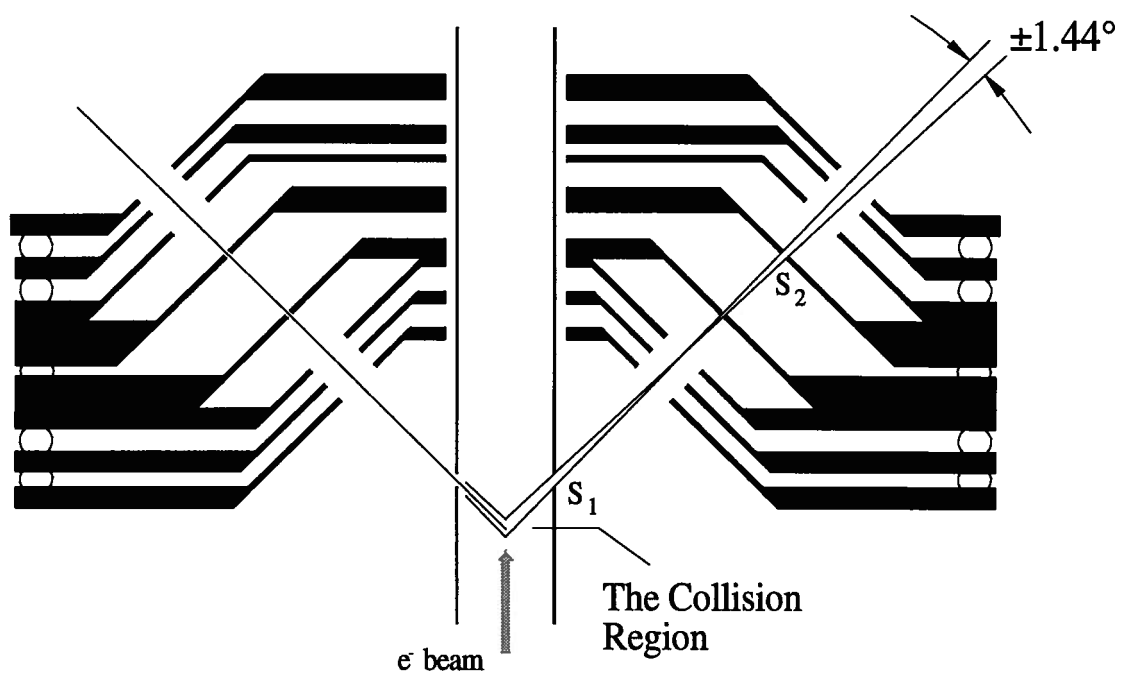


Figure 3.4: A cross sectional schematic of the collision chamber and conical lenses, that, together with the electron beam diameter, define the size of the collision region.

restrictions and the 45° entrance (θ) angle limit the focusing characteristics of the present analyzer. In practice this has not presented a serious impediment to the analyzer resolution.

Considerable attention was given to the alignment of the inner and outer cylinders. A flange on the bottom of the inner cylinder (see figure 3.2) has alignment holes that mate with holes in the CMA base plate. Precision ruby balls (5-mm diameter), placed between the pairs of alignment holes, position the inner cylinder to be coaxial and perpendicular to the CMA base plate. Similarly, holes in the outer cylinder and CMA base plate are aligned using ruby balls (8-mm diameter), allowing the outer cylinder to be reproducibly positioned. The inner and outer cylinders have diameters of 126.4 and 254.0 mm, respectively. Measurements of the gap between the inner cylinder and outer cylinder are consistent around the full 2π circle, having a maximum deviation of less than 0.3 mm (0.011’’).

As the CMA has a finite length (the height of the outer cylinder is 235.2 mm), end corrector rings at the base and the top of the CMA are used to minimize the fringing of electric fields. The voltages are applied to the rings by a resistive divider network between the inner and outer cylinders.

The electron trajectories shown in figure 3.3 were calculated by a PASCAL program that was written to emulate the operation of the analyzer. In the simulation of the motion of an electron within the CMA, the program used the electric field strength of an ideal cylindrical capacitor [87]

$$E = \frac{V}{r \ln(a/b)}, \quad (3.1)$$

where V is the voltage across the cylinders, r is the radial distance of the electron, and a and b are the inner and outer cylinder radii. Commencing with an electron entering the CMA with 600 eV and $\theta = 45^\circ$, the simulation determines the position, velocity, and acceleration of the electron in the CMA in increments of 2 picoseconds. In this fashion, an outer cylinder voltage of -535.3 V was predicted to deflect a 600-eV electron to the exit slit of the analyzer. This is in very good agreement with the experimentally determined value of -538.0 V.

3.1.6 Preliminary Results

As a simple check of the operation of the instrument in a (single channel) coincidence counting mode, two channeltrons were employed, one fixed in position and the other able to be manually rotated through an O-ring-sealed plexiglass plate on the top of the vacuum chamber. Coincident (e,2e) events were determined using a method that was a precursor to the final coincidence detection technique. The CEM signals (after constant fraction discrimination) were added using a power combiner, and discrimination of double height output pulses, indicative of a coincidence event (i.e. pulse-pile-up--see section 3.3.3), was provided by a 2440 Tektronix Digital Oscilloscope with the appropriate trigger threshold. Figure 3.5a presents a binding energy spectrum of argon obtained at a fixed position of the movable analyzer, by manually changing the voltage of the cathode power supply. Figure 3.5b shows the angular distribution of coincidence events obtained with the cathode voltage set to

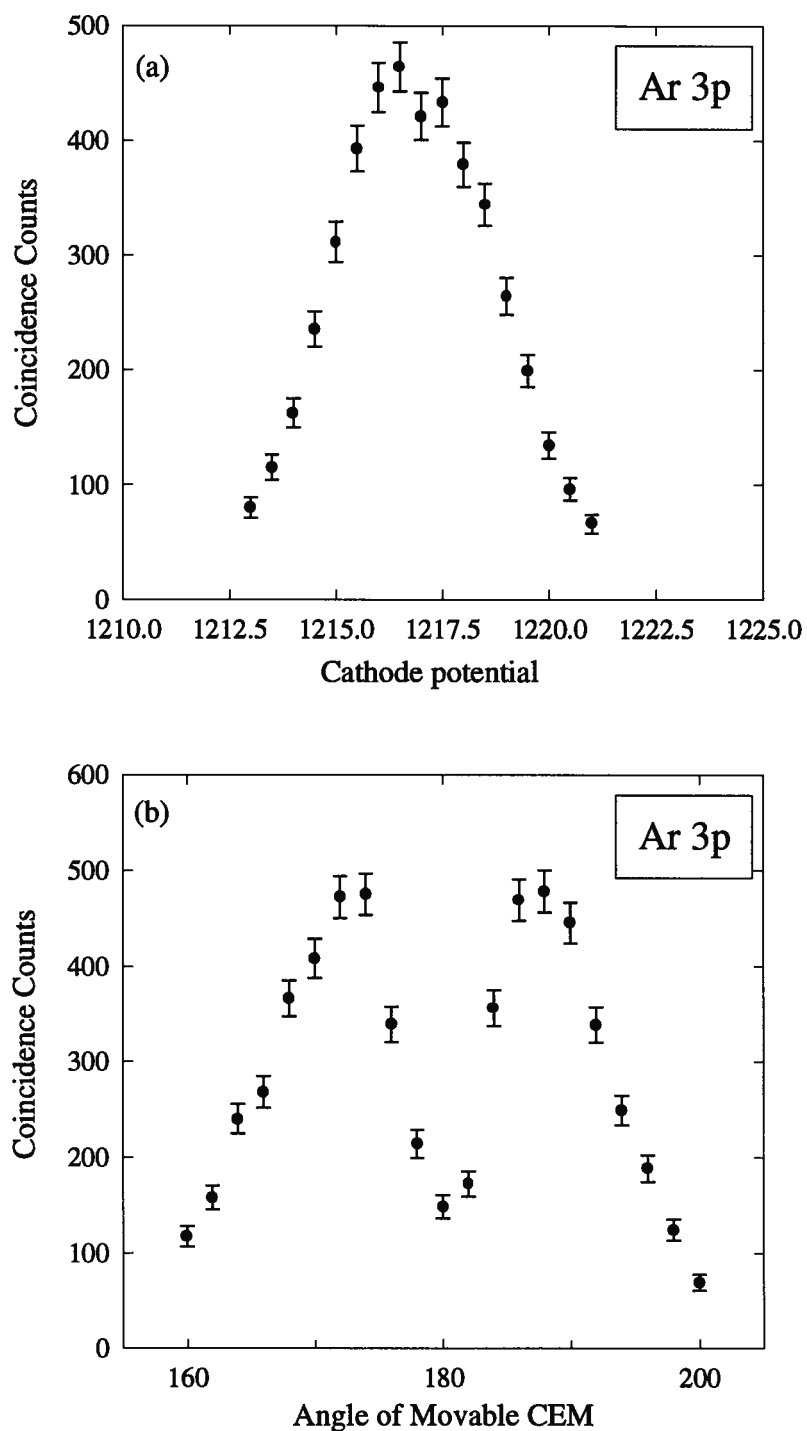


Figure 3.5: Preliminary single channel EMS measurements using two CEM detectors and a rudimentary PPU coincidence detection system. (a) a binding energy (cathode potential) spectrum for the 3p electron of argon at $\phi=8^\circ$. (b) an azimuthal angle distribution with the cathode potential set to the peak of the 3p binding energy.

observe ionization of the $3p$ electron of argon. The symmetric distribution of the data about the position opposing the fixed analyzer (180°) gives a good indication of the alignment of the gun, collision region, lens, and CMA assemblies.

3.2 The Detector Assembly

A momentum dispersive multichannel electron momentum spectrometer requires the means to detect, in parallel, the coincident arrival of pairs of energy analyzed electrons over a range of azimuthal angles. Microchannel plate (MCP) electron multipliers have become popular devices for the detection of single electrons (or ions or photons) over large areas, and are well suited for use in EMS. A myriad of detector designs [88] has been developed to give one or two dimensional position information of the MCP electron cloud. The use of a set of discrete anodes is a conceptually simple method; however, the requirement of an amplifier and discriminator for each channel limits the practicality of such a detection system for EMS at this time. In the present system, a single resistive anode position encoder (RAE) is used to provide positional information over a wide azimuthal range. The detection of coincident (e,2e) events occurring between this detector and a single channel electron multiplier positioned directly across the detection circle, allows the full momentum range of interest to be observed simultaneously.

Both the channeltron and MCP/RAE detectors are mounted on a plate that rests in the inner cylinder, just above the analyzer exit slits. Additionally, the detectors are housed in

grounded metal enclosures (see figure 3.2), which help to eliminate stray electron signals and cross talk between the devices.

3.2.1 The Channel Electron Multiplier

The channeltron is fabricated of glass and coated with a semiconducting layer that, upon impact of an electron of sufficient energy, emits a number of secondary electrons. Accelerated by a positive bias voltage applied to the exit of the channeltron, the secondary electrons collide with the wall of the channeltron to produce additional electrons. If a sufficient bias potential is applied, the avalanche of electrons continues down the length of the CEM until the density of electrons reaches a saturated level. At this point, the charge of the electron cloud in the CEM repels any additional electrons emitted from the CEM surface, causing them to strike the wall before they are sufficiently accelerated to give the further emission of secondary electrons [89,90]. The CEM in this state operates in the saturated, pulse counting mode, having an electron gain on the order of 10^8 [89,91]. The gain variation for each incident electron gives rise to output pulses that have a Gaussian pulse height distribution [55,89,92]. The appropriate setting of the threshold of a discriminator enables the detection of the (amplified) CEM pulses with an efficiency that is relatively invariant to changes in gain that may result from a variation of the incident electron current, or ageing of the CEM [55,56].

The CEM is curved to suppress the effects of ion feedback, in which a positive ion formed at the rear of the detector is accelerated towards the cone where collision with the side

wall may generate a spurious electron cascade [14,89]. The curvature limits the acceleration of the ion before a collision with a wall, such that the ion velocity is insufficient to begin a detectable cascade.

In the present application, a single channeltron (CEM -Phillips B318 AL/01) is configured to detect individual electrons. Two high voltage power supplies (HP 6516) provide front and back bias potentials. The output pulse from the CEM is capacitively decoupled as shown in figure 3.6. Presented in figure 3.7 is a typical CEM pulse¹, having a width of 5.0 ns FWHM and rise time (10-90%) of 3.4 ns. Details of the channeltron operation and performance are given in section 3.4.2.

3.2.2 The Microchannel Plate/Resistive Anode Assembly

A microchannel plate consists of an array of parallel tubes, typically 10 - 40 μm in diameter, capable of providing electron multiplication in a manner similar to the CEM. As microchannel plates are readily available with active areas on the order of 1 - 10 cm in diameter, it is possible to detect single electrons over a large spatial range. To furnish sufficient gain, a number of plates are typically employed in a variety of stacking arrangements. The final configuration used in this instrument was achieved after much trial and error. The original detector was a five-plate (40-mm diameter) device (Surface Science

¹ All of the waveforms presents in this chapter were acquired using a Tektronix 2440 Digital Oscilloscope. The scope has a sampling rate of 5×10^8 samples/sec, and single-shot bandwidth of 250 MHz. Some attenuation and alteration (particularly of the rise and fall times) of the waveforms is likely. The waveform data were transferred to a personal computer using a National Instruments GPIB board.

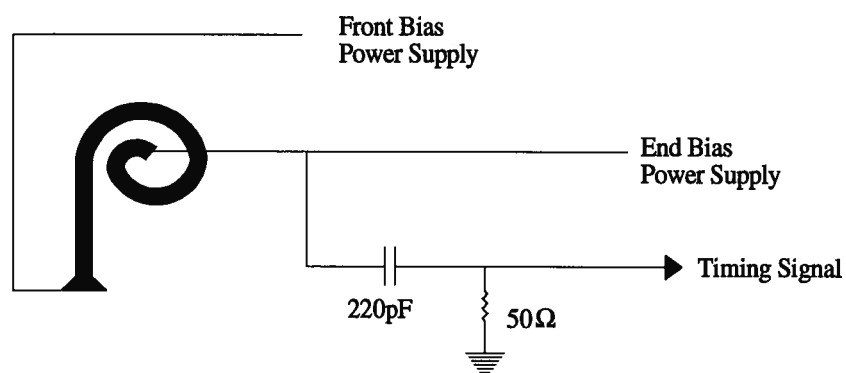


Figure 3.6: The CEM signal coupling circuitry.

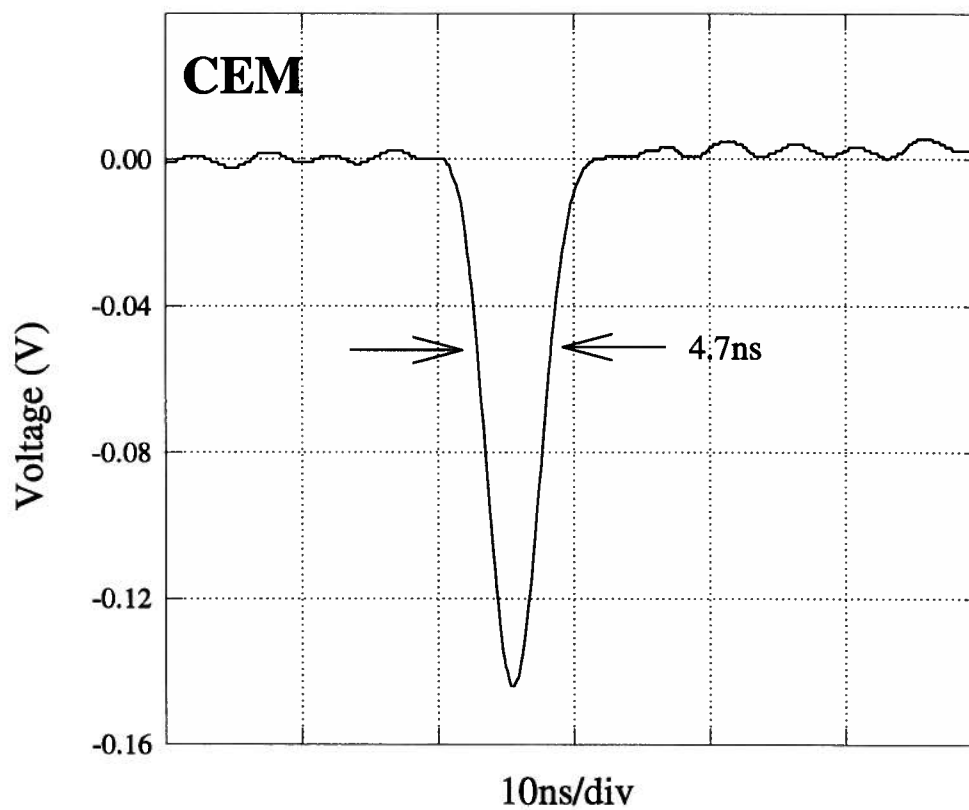


Figure 3.7: A typical CEM timing pulse (after the 50X preamp), with a rise time of 3.0 ns and width of 4.7 ns

Laboratories¹ (SSL) 3390SB), consisting of a two-plate first stage and a three-plate second stage. While the image of the many background (non-coincidence) electrons from the RAE was an intense and uniform arc, the image from the coincidence electrons was less satisfactory. Only the coincidence electrons appearing at the edges of the arc were detected. The poor image of coincidence electrons was reasoned to be a result of the dead time of 10^{-2} seconds [90] for each channel of the MCP involved in a cascade. As each MCP is composed of many channels, the inherent dead time of an individual channel does not generally present a problem [90]. In the five-plate design however, each incident electron would produce many electrons from the first stack which, in turn, would initiate a cascade in a very large number of channels of the second stack. If a sufficient number of channels were stimulated, the channel deadtime would have caused a reduced electron gain, particularly in the region where the concentration of uncorrelated electrons was greatest.

The final arrangement used in the present instrument is the most commonly used chevron configuration of two MCPs [94]. The detector design is essentially that of a SSL-3390SA device, which, according to the manufacturer, should provide lower spatial resolution than the five-plate device. However, the use of the two-plate configuration has not appeared to limit the performance of the spectrometer. The chevron-shaped MCP cross section, shown in figure 3.8, mimics the curvature of the CEM to reduce the effect of ion feedback. A small gap (.1 mm) between plates improves the gain by allowing a number of channels of the second plate to be stimulated (Rogers and Malina [95] estimate 20-30 channels for a gap of .15 -1

¹Surface Science Laboratories is now Quantar Technologies Inc.

mm). However, the gap must be sufficiently small that a large enough number of electrons enter each channel of the second plate to ensure saturation [90]. With a voltage of approximately 1 kV/plate, the electron gain using such a configuration is typically 10^6 - 10^8 [90,95]. The position of the electron cloud from the MCP stack is determined by the resistive anode encoder and associated electronics. The anode is of the Gear design — square with concave sides — which provides approximately distortion-free imaging [96]. On impact of the electron cloud, the anode, which is coated with a series of metalizations and conductive inks, gives a current at the four corners reflective of the position of the incident electrons. A preamplifier unit (SSL 24011) shapes and amplifies the charge pulses from each corner. A position computer (SSL model 2401) subsequently determines the X-Y position of the electron cloud through the analog computation of the relationships:

$$X = \frac{B + C}{A + B + C + D} \quad (3.2)$$

and

$$Y = \frac{A + B}{A + B + C + D} \quad (3.3)$$

where A,B,C,D are the heights of the pulses from the corners. In addition to the (2- μ s wide) bipolar positional pulses from the RAE preamplifier unit, a ‘fast’ E pulse (350-ns wide), representing the sum of the four anode pulses, is also generated. On detection of the E pulse by the position computer, a digital E pulse is generated. This signal initiates a control logic sequence, beginning a position computation, and ultimately yielding X and Y analog output

levels as well as a (TTL) STROBE pulse to inform an external analog-to-digital converter (ADC) of an acceptable event.

The rise time of the resistive anode output pulses precludes the use of these readily available signals for coincidence timing information. Many alternative methods of obtaining narrow timing pulses were investigated. These included the conventional approaches of capacitively [59,97], or inductively [26,98] coupling the signal induced by an electron cascade in the high voltage supply line at the exit of the MCP stack. In the present system the timing pulse is obtained from a molybdenum grid (Buckbee Mears 1-PC) of 0.001-inch-thick wires spaced on 0.025-inch centers, inserted between the MCP stack and the RAE. This method was found to give faster response and less time jitter than the more conventional timing techniques. A similar approach was taken by de Bruijn and Los [98] but was abandoned due to a degradation of the positional information. A poor image was also observed in the present system when a grid of 0.003-inch-thick wires on .020-inch centers (72% transmissive) was employed; however, the presently used mesh, with an open area of 92%, showed no distortion of the RAE image. The grid timing pulse is capacitively decoupled as shown in figure 3.8. The ferrite beads on the supply line are used to dampen the small (~7-10 mV) transients originating from the switching power supply (Wenzel N1130-4). A typical grid timing pulse, having a width of 3.9 ns FWHM and rise time of 2.2 ns, is shown in figure 3.9.

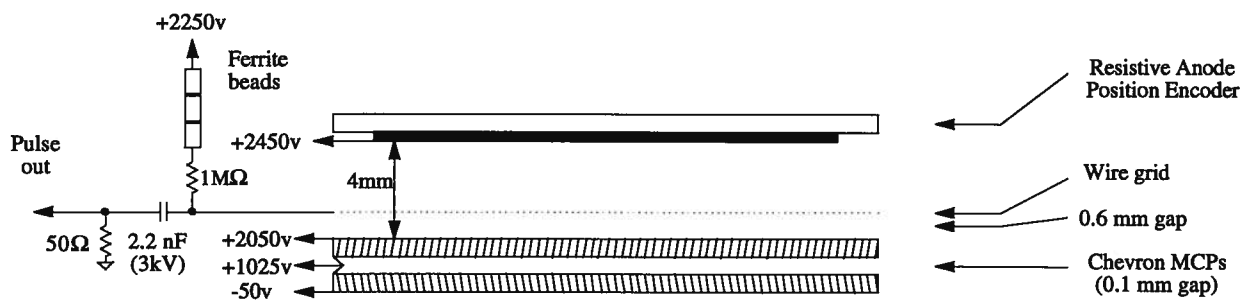


Figure 3.8: The microchannel plate/resistive anode encoder assembly.

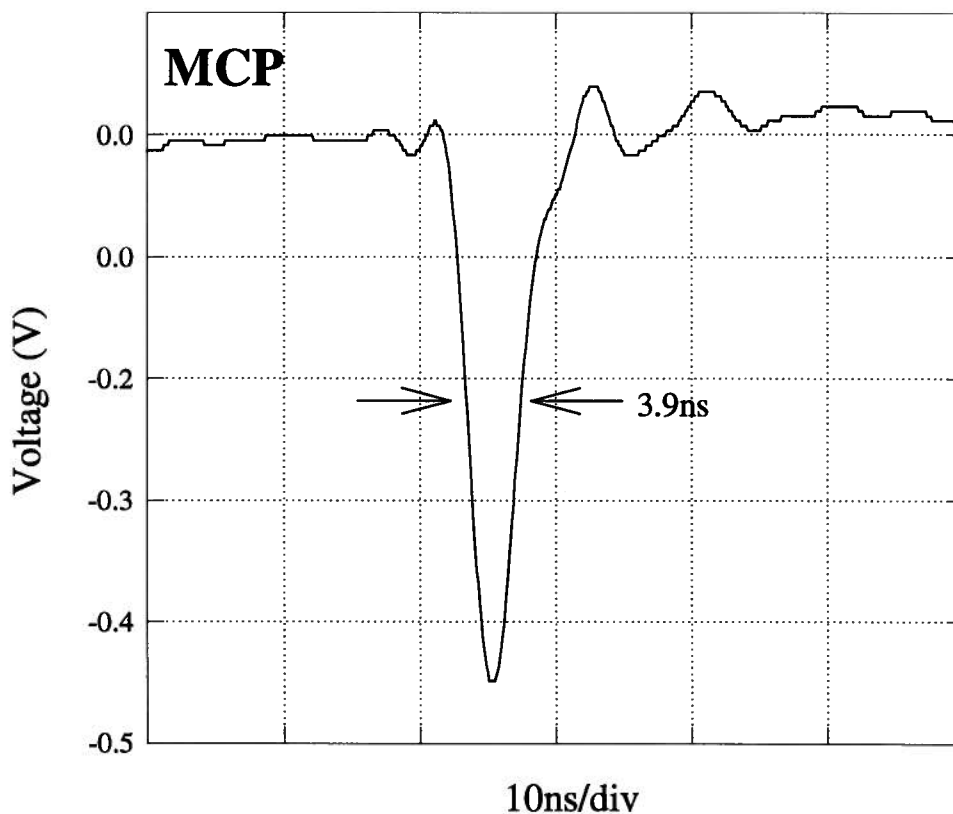


Figure 3.9: A typical MCP timing pulse from the grid (after the 100X preamp) with a rise time of 2.2 ns and FWHM of 3.9 ns .

3.3 Coincidence Timing and Data Acquisition Electronics

3.3.1 Signal Processing

The output pulses of the channeltron are amplified by a preamplifier that was fabricated in-house as a low cost replacement of the ORTEC 9301 preamp. The preamp has a two-stage design originally with a Mini-Circuits MAR-3 input stage (typ. gain 12.5 dB) and a Mini-Circuits MAR-7 output stage (typ. gain 13.5 dB), to give a measured amplification factor of 20 (26 dB). As channeltron efficiency decreases with use [55,56], greater bias voltages across the CEM are required to give pulse heights above the detection threshold. When the maximum bias voltage, limited by the power supply and by ion feedback, was reached in the present system, the preamp was modified in an attempt to delay replacement of the channeltron. A MAR-6 (20 dB) input stage, and MAR-3 (12.5 dB) output stage was found to give a 50X amplification (34 dB), with no apparent change in the pulse characteristics. This modification permitted the continued operation of the channeltron at much lower bias voltages.

The grid timing pulse of the MCP/RAE detector is amplified by a 100X preamplifier (Photochemical Research Associates model 1763). Both the CEM and MCP timing pulses are input into constant fraction discriminators (CFD - ORTEC 934) that provide improved time response over a fixed threshold discriminator in the detection of the signals. A CFD accomplishes this by splitting an input pulse, delaying and inverting one fraction while

attenuating the other, and recombining the two to generate a bipolar signal. As shown in figure 3.10, the detection of the zero crossing of the bipolar signal provides discrimination at a point approximately independent of the amplitude of the input signal. The two CFDs have discrimination thresholds set to (the minimum) -30 mV which is well above the noise levels on the signal lines (< 5 mV). The output of the CFDs are NIM level pulses (0 to -0.8 V) having widths of 50 and 80 ns for the CEM and MCP respectively. The length of the MCP-CFD pulse is more than sufficient to prevent generation of additional CFD pulses on the occasional noisy MCP timing pulse (i.e. after pulses, which are believed to be caused by ion feedback).

3.3.2 The Spectrometer Time Response

To investigate the temporal characteristics of the instrument, a time spectrum was obtained using a time-to-amplitude converter (TAC- Ortec 567). The TAC was configured to generate a signal (0 - 10 V) proportional to the time delay between a CEM-CFD start pulse and a delayed MCP-CFD stop pulse. The time spectrum presented in figure 3.11 was acquired by digitizing and accumulating the TAC output signals, while the spectrometer was set to detect (e,2e) ionization of argon 3*p* electrons. The effectively uniform background¹ of the time spectrum arises from the detection of uncorrelated (random) electrons at the CEM and MCP detectors. The peak in the time spectrum indicates a correlation in the arrival time of the electrons at the MCP and CEM detectors, which originate from an (e,2e) collision event. The

¹As the background pulses from each detector are random in time, the delay times between the arrival of CEM start pulses and MCP stop pulses have an exponential distribution characteristic of Poisson processes [183]. However, over the short 50 ns time window, the probability of observing a particular delay time between pulses is essentially uniform.

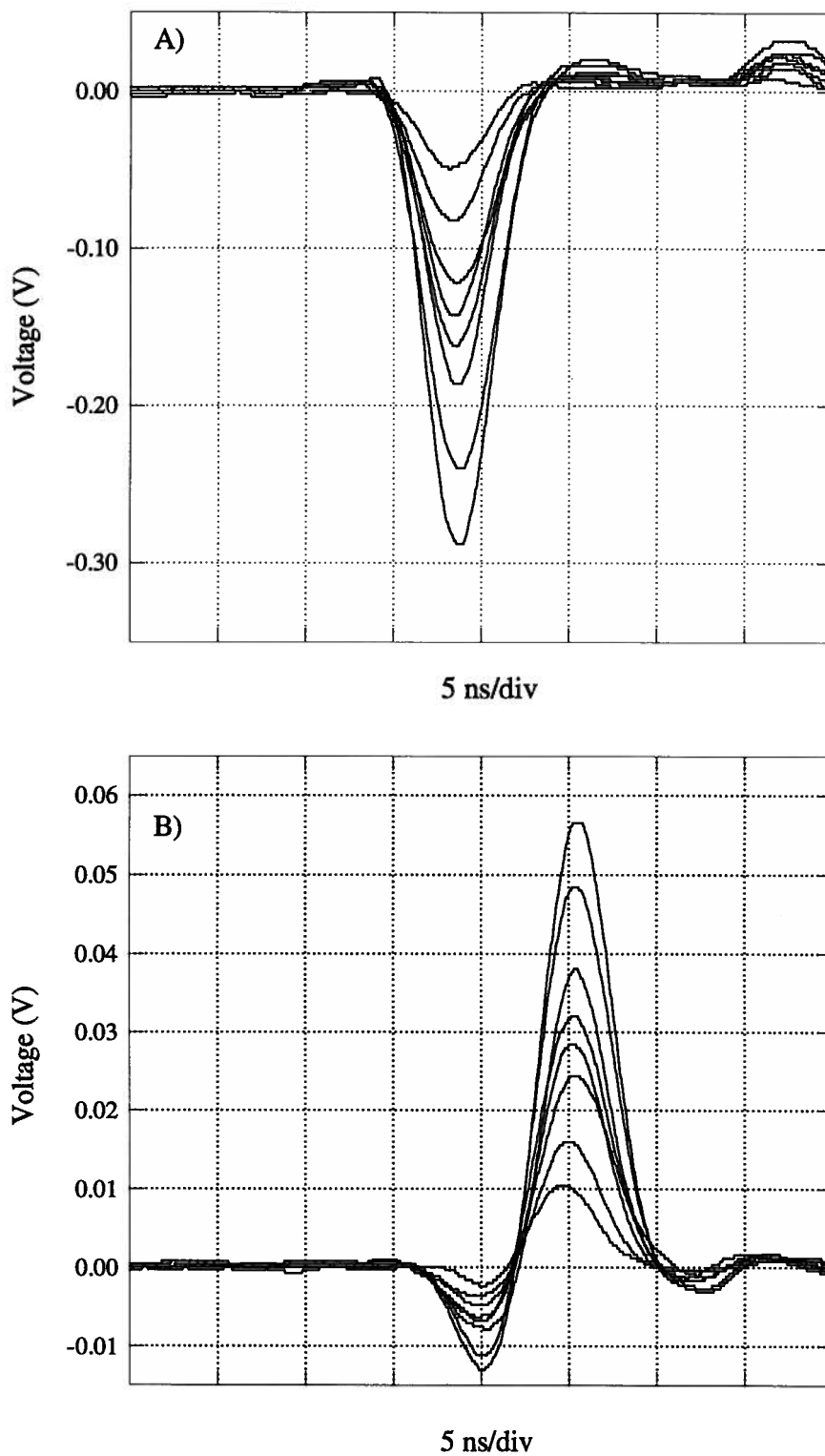


Figure 3.10: a) A distribution of pulse heights from the CEM. b) The corresponding bipolar pulses produced by the CFD to give pulse height invariant timing.

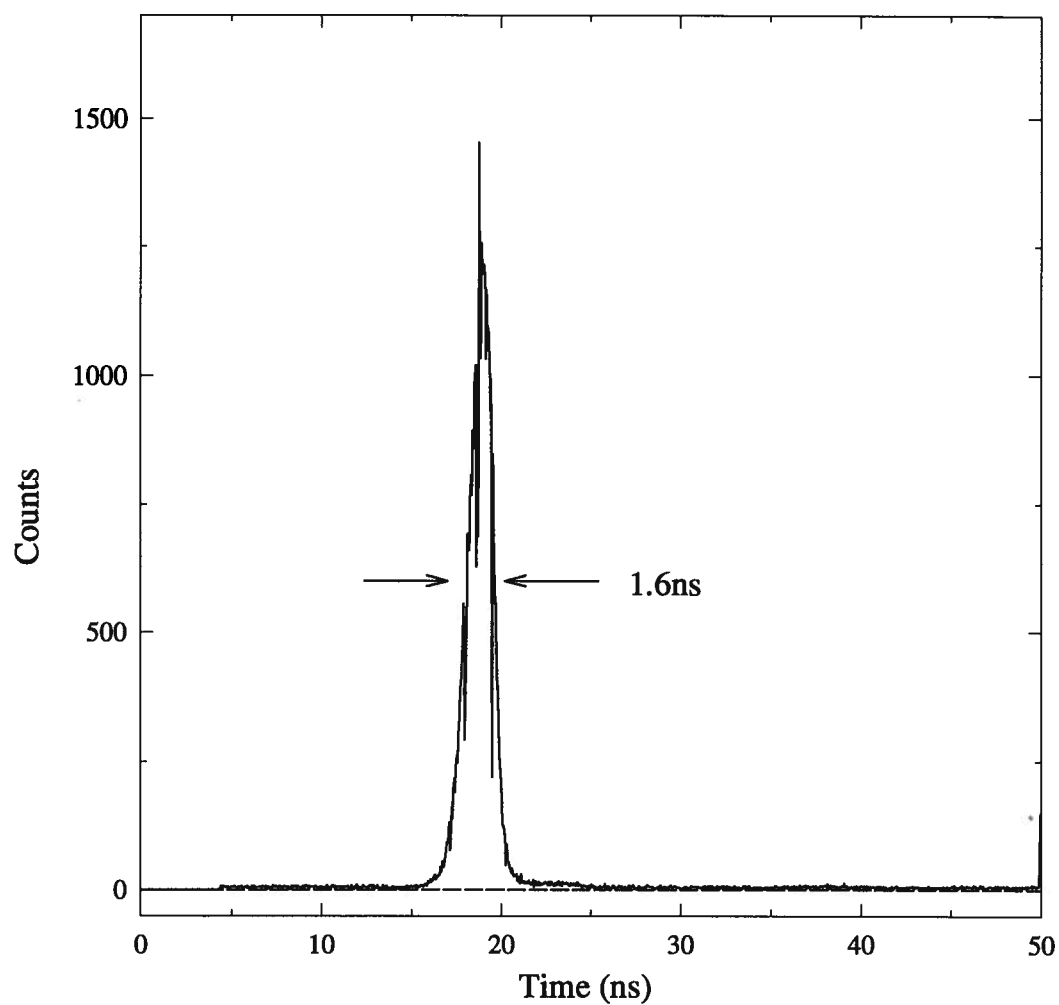


Figure 3.11: A timing spectrum of the multichannel spectrometer acquired using a TAC. The peak in the spectrum corresponds to the coincident arrival of electrons at the MCP/RAE and CEM detectors.

pulse width of 1.6 ns FWHM is considerably more narrow than those typical of EMS instruments, which are generally on the order of 3-10 ns FWHM. A narrow coincidence pulse width is desirable since, as discussed by Lower and Weigold [57], both the signal-to-background ratio and the statistical uncertainty of coincidence measurements are improved with a smaller coincidence timing window.

A number of factors contribute to the width of the coincidence peak in an (e,2e) experiment [99]. These include the time spread from different energies and trajectories of electrons passing through the analyzer, the time spread inherent to each detector, and the time jitter from the electronics components [99]. In the present instrument, the analyzer time spread is considered to be small, due in part to the relatively high energy (~ 600 eV) of the scattered electrons. As well, given the consistency of the timing pulse shapes and the use of constant fraction discrimination, the contribution from timing electronics is likely to be negligible. The principal factor influencing the coincidence width is the transit time variation of the electron charge cloud through the CEM, which may be as high as a 2-3 ns [99]. A microchannel plate detector exhibits considerably less time variation than a CEM [93], and the inevitable future development of an instrument in which the CEM is replaced by a stack of MCPs should realize an improved coincidence time width over the present spectrometer.

3.3.3 The Coincidence Detection System

In all of the EMS instruments developed to date, the detection of (e,2e) coincidence events has been based on systems incorporating a TAC, in a manner similar to that just described. A timing window is set (often with thresholds of a single channel analyzer) about the coincidence peak of the time spectrum to identify both 'true' and 'accidental' coincidence events. Characterization of the level of background 'accidental' events is obtained from another window, positioned away from the coincidence peak. Subtraction of the accidental pedestal yields the true coincidences.

A different approach to coincidence detection was taken in the present system; figure 3.12 illustrates the basis of the technique. The detector timing signals are first shortened and then combined using a 2:1 radio-frequency power combiner. The coincident arrival of electrons at the two detectors is recognized by the pulse-pile-up (PPU) of their timing signals, as double-height pulses at the output of the power combiner are distinguished from the uncorrelated (single pulse height) events by means of a discriminator with an appropriately set threshold level.

TAC-based systems are significantly less demanding to implement than those based on PPU detection [100]. The motivation for the application of the PPU method to the present system lies in its ability to quickly recognize coincidence events. This has permitted the position computer to be gated, such that only the position of electrons that are part of a

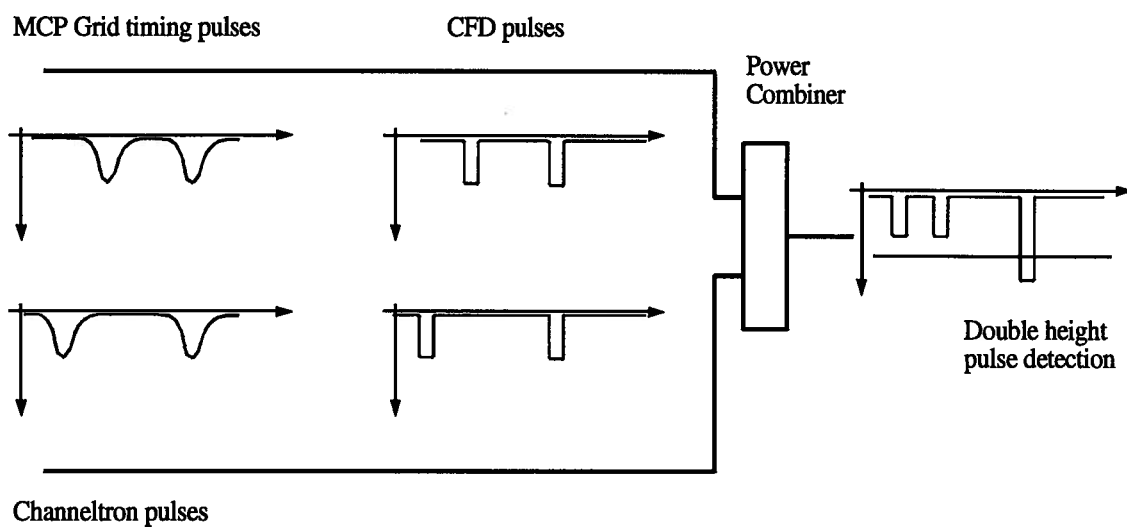


Figure 3.12: The pulse-pile-up (PPU) coincidence detection method. Individual timing pulses are combined using a power combiner. Coincident input pulses yield double height output pulses that can be detected with a discriminator.

coincidence event are calculated. This is important in the present system in which the relatively low coincidence count rate (typically $\sim 2\text{-}20\text{ Hz}$) is somewhat overshadowed by the high count rate of uncorrelated electrons striking the MCP/RAE detector (typically $\sim 20\text{-}80\text{ kHz}$). If the position computer was not gated, the dead time associated with calculating the location of uncorrelated electrons would significantly reduce the efficiency of detecting coincidences.

An xy-position computation is initiated by the detection of the fast E pulse from the RAE preamplifier, which occurs approximately 85 ns after the arrival of an electron at the face of the MCP detector. By comparison, the time response of typical commercially available TACs is on the order of $1\text{-}3\text{ }\mu\text{s}$, and discrimination of the coincidence timing windows further increases the time period between the actual coincident event and recognition of it. Hence, using a TAC-based coincidence system, the computation of the position of an event at the MCP/RAE detector would be well underway by the time the nature (coincidence or non-coincidence) of the event is established. A TAC-based design which incorporates the coincidence gating of the position computer would be difficult to achieve. In contrast to the TAC response, the presently developed PPU circuitry recognizes a coincidence event within 50 ns of the arrival of the electrons at the detectors.

It should be noted that a few commercial coincidence units using pulse-pile-up detection are available (e.g. Canberra Model 2040 and EG&G Ortec 414A). However the minimum resolving time of these systems is greater than 10 ns , and the use of such units for the present

application would offer poor timing resolution relative to the narrow coincidence peak width exhibited in the TAC spectrum in figure 3.11. In the present system, the PPU coincidence circuit was designed to have resolving time of approximately ± 1.5 ns. The PPU coincidence circuit is also an important evolutionary step towards the development of a system able to detect coincidences occurring between any two of a large number of detectors. The use of many discrete detectors is expected to be central to the design of future systems in which coincident pairs are detected around the complete 2π azimuth.

The implementation of the PPU technique in the present instrument is outlined in figure 3.13. The time response of the MCP detector is faster than that of the CEM, due to the greater pulse transit time in the CEM. Hence, the CFD timing signal of the MCP is delayed by 12.5 ns with respect to the CFD signal of the CEM, thereby ensuring that signals arising from electrons that were coincident at the exit of the CMA are coincident upon arrival at the pulse-pile-up circuitry.

The PPU circuitry has a bifurcated design, with one branch configured to identify ‘true + accidental’ coincidence events, and the other to identify only ‘accidental’ events. As the CFD pulses are relatively wide and pulse-pile-up coincidence detection using these signals would give a correspondingly wide coincidence window, the CFD pulses are compressed prior to input to a pair of power combiners. The detection of a pulse-pile-up signal following the lower power combiner (2) indicates the coincident arrival of electrons at each of the detectors.

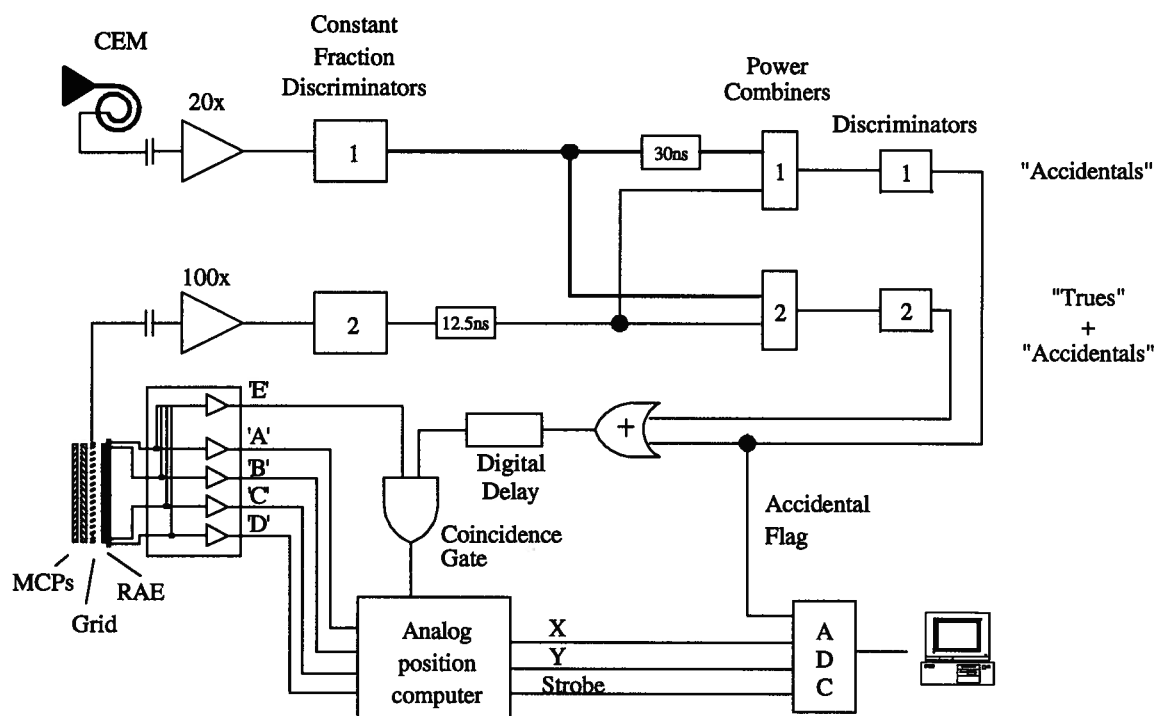


Figure 3.13: A block diagram of the pulse-pile-up (PPU) coincidence detection system.

Prior to input to the upper power combiner (1) the CEM signal is delayed by 30 ns, thereby destroying the overlap of pulses from a true coincidence event. Pulse-pile-up events detected in this channel correspond to the arrival of one electron at the CEM, followed ~30 ns later by a second uncorrelated electron at the MCP. A TTL¹ flag is set to identify the event as an accidental. Observation of the accidental counts using this channel allows the removal of the accidental background from the 'true + accidental' coincidence measurements.

The detection of a coincidence in either branch generates a TTL coincidence signal that is used to gate the position computer. The gating system operates by allowing the digital E pulse to initiate a position computation only when a coincidence signal is observed. Thus only the positions of the electrons at the MCP/RAE detector that give rise to the PPU coincidence ('true + accidental' or 'accidental') signal are calculated.

3.3.4 The Pulse-Pile-Up Coincidence Circuitry

The high speed characteristics of ECL (Emitter Coupled Logic - 10K/10KH) integrated circuits are exploited in the generation and discrimination of narrow pulses for coincidence detection. These components, and additional TTL components, are mounted on a circuit board positioned above the circuit board of the SSL position computer. The operating voltages required for the circuitry are acquired from the position computer. A schematic of the component layout and a circuit diagram of the coincidence detection and position

¹TTL = transistor transistor logic (LO \cong 0V and HI \cong 5V).

computer gating electronics are presented in figure 3.14 and figure 3.15. The letters alongside the circuit correspond to the letters in figures 3.16 and 3.17, which display a series of measurements following a pulse sequence through the coincidence circuitry. The waveforms, acquired with a Tektronix 2440 Digital Oscilloscope, should not be taken as absolute, as the addition of the long oscilloscope probe effects the circuit performance and influences the magnitude, shape and ringing of the pulses. However, the measurements help to illustrate and clarify the operation of the circuitry.

Following the MCP signal (A), the NIM logic (-0.8 to 0 V) pulse from the constant fraction discriminator is input to an ECL 10H115 quad line receiver to generate a corresponding ECL pulse (logic levels : LO \approx -1.8 V, HI \approx -0.8 V) (B). A voltage of \sim 0.4 V — near the mid range of the NIM pulse — is applied to the second input of the line receiver, which acts as differential amplifier. A pair of identical pulse compression circuits is used to generate two short timing pulses, one for the ‘true + accidental’ branch, and the other for the ‘accidental’ branch. In each branch, the long ECL pulse is inverted and delayed by a 10102 NOR gate. A further delay is added by approximately 6" (\sim 1 ns) of RG174 coaxial cable. This delayed and inverted pulse (C) is sent to one input of an OR gate (10103), with the undelayed pulse sent to the other input. A LO output pulse from the OR gate is generated when both inputs are LO, a situation occurring only during the short delay time of the original pulse. In this manner, short ECL pulses (\sim 4 ns FWHM fig 3.16D) are generated on the leading edges of the CFD pulses. These short pulses are routed to the inputs of the radio-

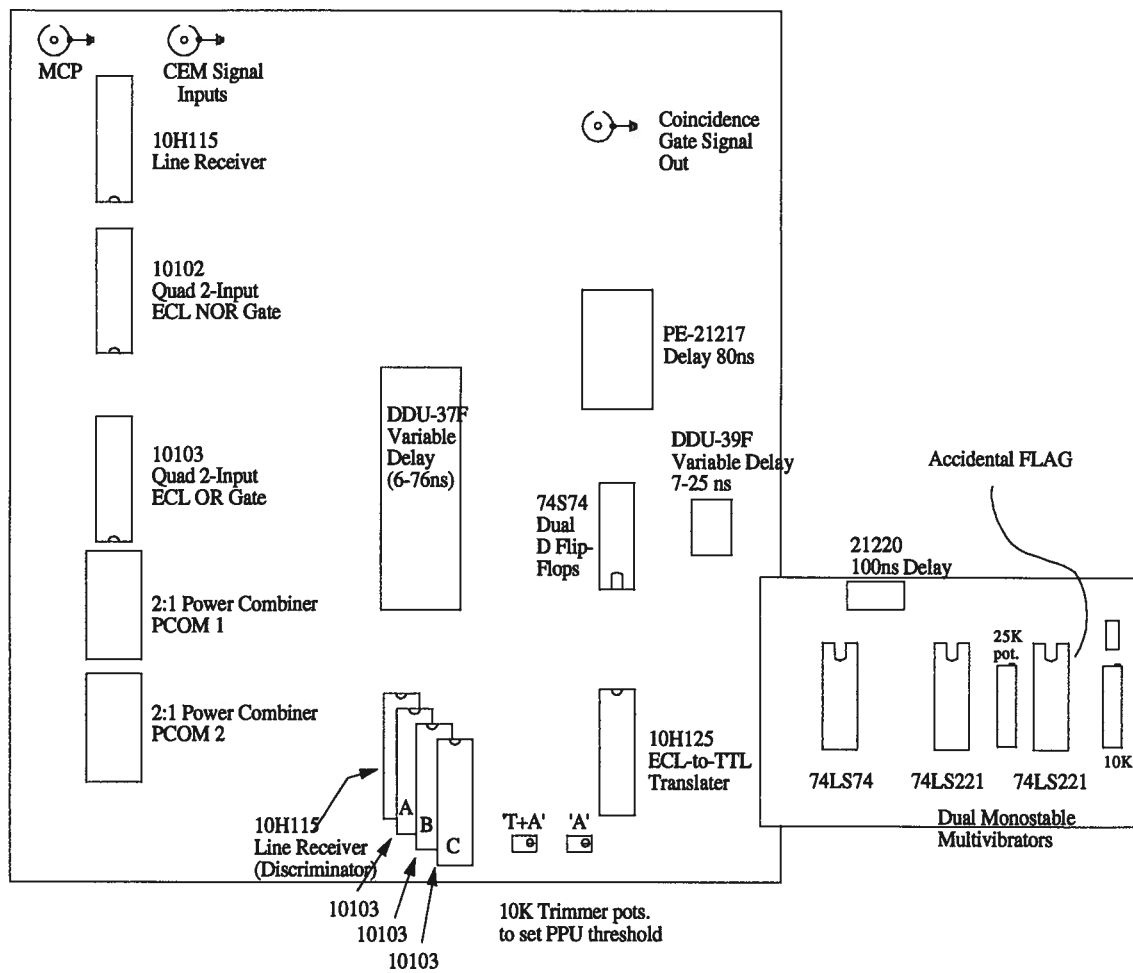


Figure 3.14: A schematic of the coincidence detection circuit board.

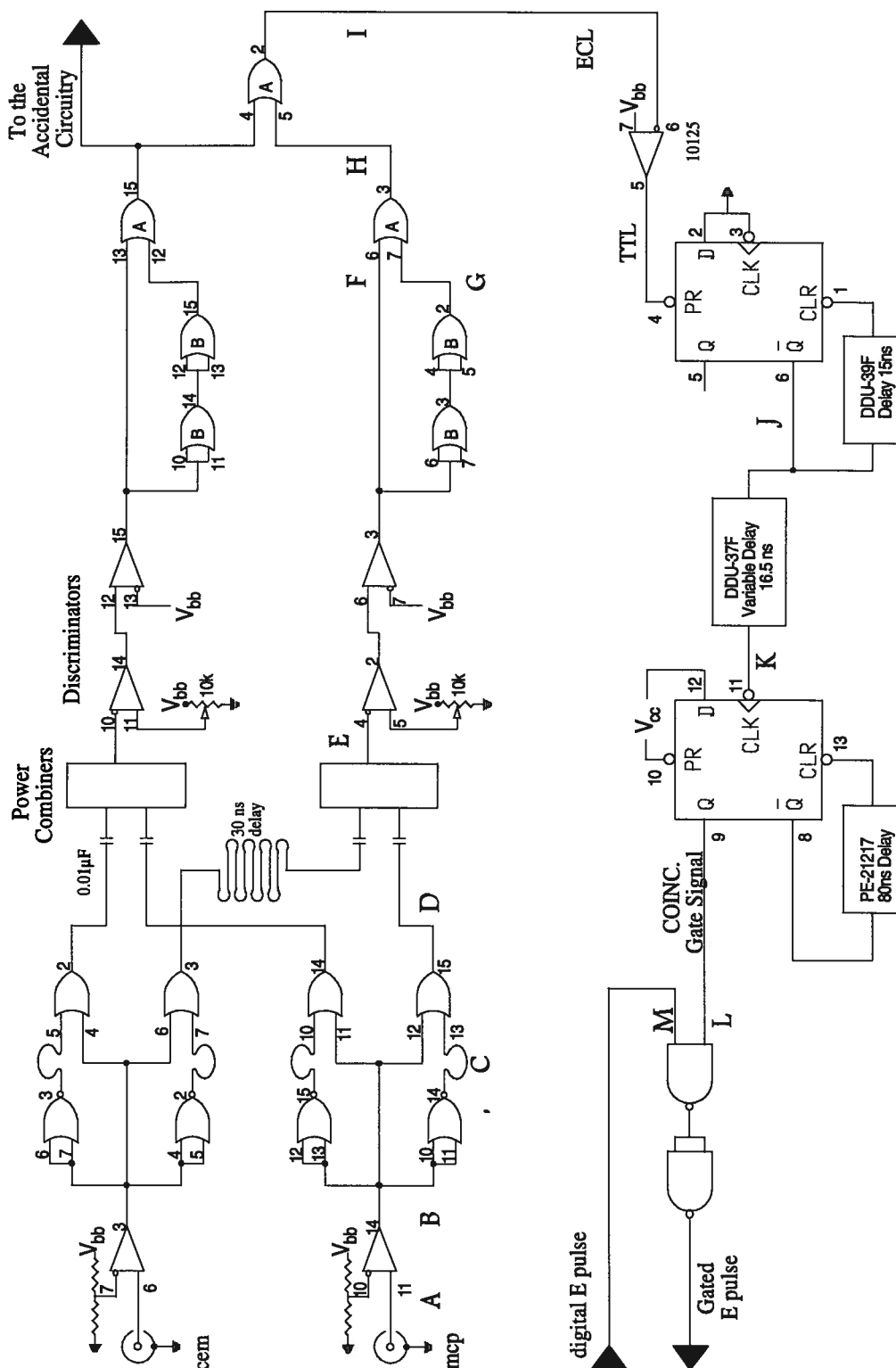


Figure 3.15: The PPU coincidence detection and position computer gating circuit diagram. IC pin connections are numbered, and small letters in the OR gates refer to ICs in figure 3.14. Larger letters correspond to lettering in figures 3.16 and 3.17

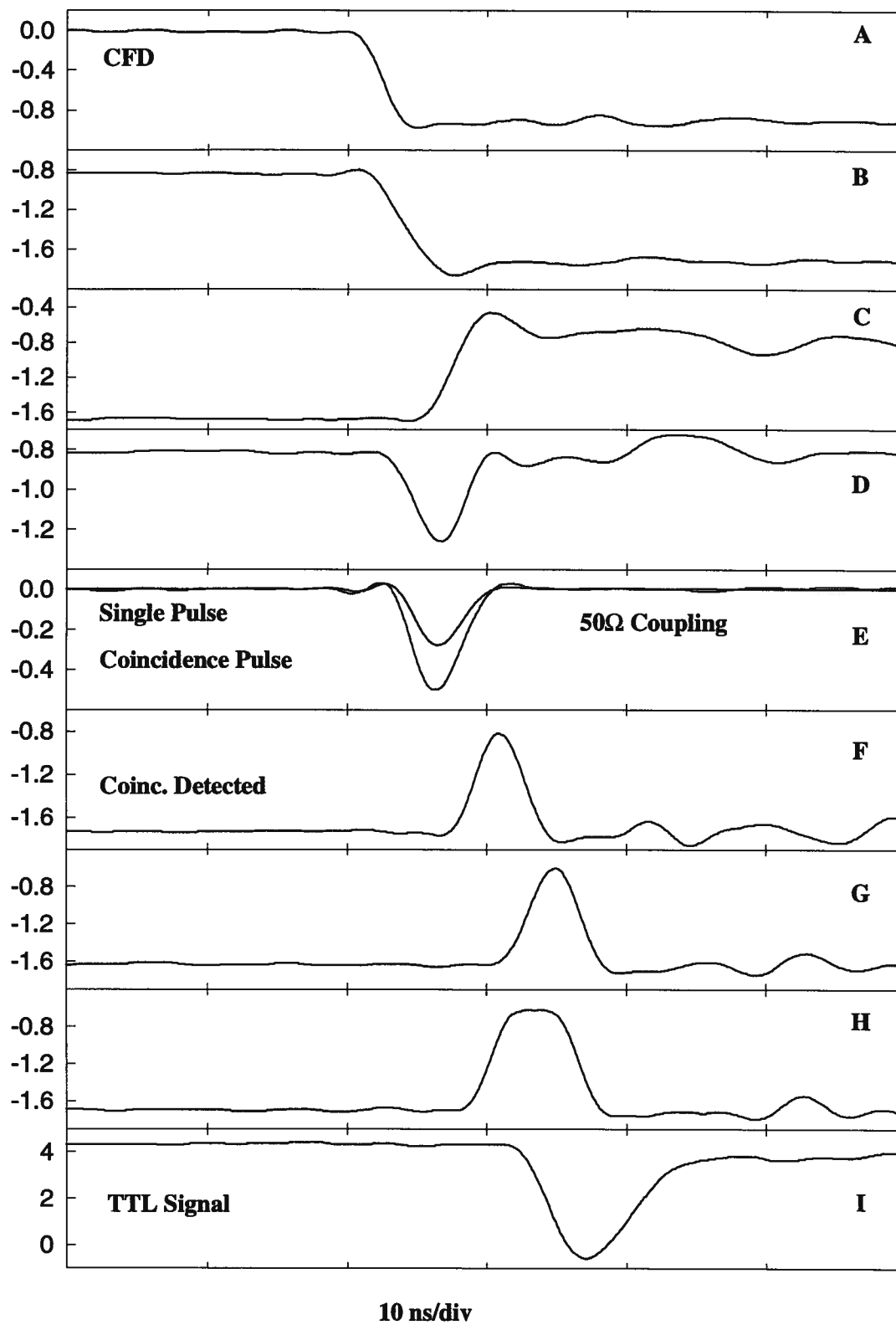


Figure 3.16: A sequence of waveforms following an MCP timing pulse through the coincidence detection circuitry. The pulse shapes should be taken as qualitative. Lettering corresponds to points in figure 3.15. The vertical axes are in volts.

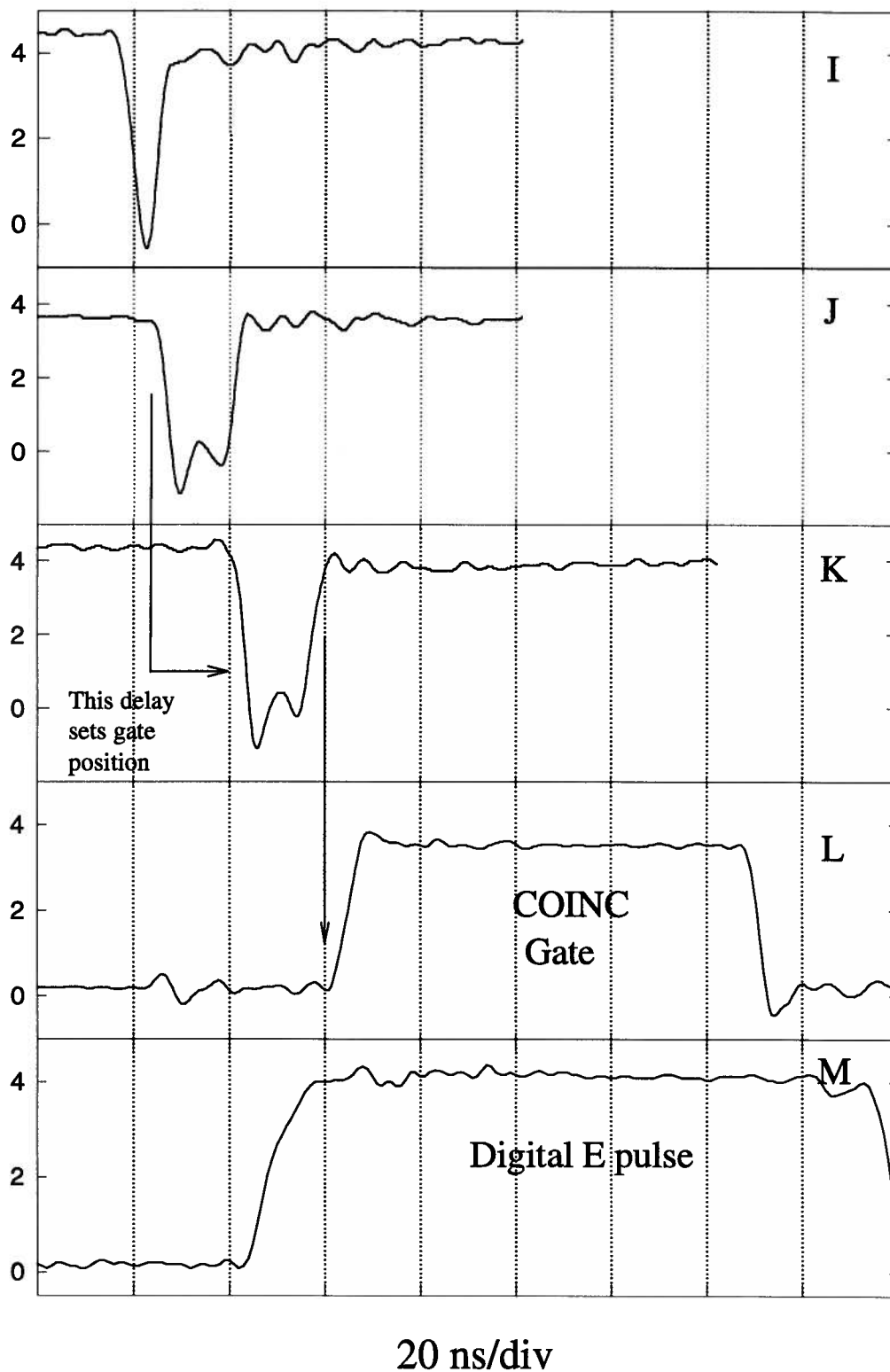


Figure 3.17: Gating the position computer on detection of a PPU event. The TTL coincidence signal is shaped and positioned relative to the digital E pulse. The large letters refer to points in figure 3.15. The vertical axes are in volts.

frequency power combiners (Mini-Circuits PSC-2-W1). Figure 3.16E displays a typical single height pulse and a double height PPU pulse after the power combiners.

The output of each power combiner is detected by another 10H115 line receiver, operating as a discriminator with a threshold voltage at the non-inverting input set by a 10-K variable resistor. The threshold is set above (more negative than) the level of a single height pulse, such that an output signal is given only for large pulses resulting from an overlap of two timing signals at the power combiner. The output of the first 10H115 discriminator is 'cleaned up' by a subsequent 10H115 IC (F). Early designs of the circuitry attempted to discriminate the PPU pulses using a SP93802 sub-nanosecond comparator (Plessey Semiconductors), but the approach was unsuccessful. The comparator was unable to discriminate between the single and double height PPU pulses. While the 10H115 IC is not specifically designed for use as a discriminator, it has proven to be effective in the detection of the double height pulse-pile-up signals.

The next stage in the coincidence circuitry is designed to lengthen the output signal of the discriminator. To accomplish this, a similar process to the pulse compression at the input is used. The output signal is split, with one signal being delayed (fig. 3.16 G) by the propagation time of two ECL 10103 OR gates (typically 1.0 ns per gate [101]). This delayed pulse is then input into another OR gate with the undelayed pulse at the second input, yielding a broadened ECL pulse (H).

As shown in figure 3.15 the 'true + accidental' and the 'accidental' PPU discrimination circuits are identically configured. The broadened outputs of both branches are directed to another ECL OR gate such that an output signal from this gate indicates a coincidence in either of the two timing windows. The ECL signal from this gate is converted to a TTL pulse using a 10125 ECL - TTL translator, and the output TTL coincidence signal (figs. 3.16I and 3.17I) is subsequently used to gate the position computer.

The remaining components of the circuit set the appropriate width and time of the coincidence gate signal (COINC) relative to the digital E pulse from the position computer. A TTL flip-flop (74S74) generates a lengthened¹ pulse that is subsequently delayed by a variable digital delay unit (Data Delay Devices DDU-37F). The delay time determines the position of the COINC signal and has been adjusted appropriately (presently 16.5 ns). The delayed signal (fig. 3.17K) is sent to the clock of a second flip-flop that, on the rising edge of the signal, gives an output HI COINC signal. The output remains in the HI state until a LO level occurs at the clear, the time of which is set by another variable delay (DDU-39F) that determines the width of the COINC signal. The positions of the COINC pulse and digital E pulse are presented in figures 3.17L and 3.17M.

In this manner, the PPU detection of a coincidence event generates a COINC signal, approximately 85-ns wide and positioned to coincide with the arrival of the digital E pulse. The COINC signal and the digital E pulse are input to a TTL NAND gate. An output pulse is

¹The length of the pulse is determined by the delay between \overline{Q} (pin 6) and CLR (pin 1).

given only if both the COINC pulse (HI) and E pulse (HI) are present. If no coincidence is detected, the COINC signal is not generated, and the E pulse is blocked from the circuitry of the position computer. Should a coincidence occur, the overlap of the COINC pulse and digital E pulse yields a gated E pulse that is routed to the position computer circuitry, permitting the calculation the (x, y) position of the event at the anode in its usual fashion.

3.3.5 The Accidental Flag Circuitry

The accidental circuitry is designed to generate a TTL flag to identify PPU coincidence events occurring at the 'accidental' power combiner. The simple generation of an 8-10 μ s TTL pulse, is complicated by a few scenarios in which 'true + accidental' and 'accidental' events would be misinterpreted. These troublesome situations arise from the requirement for resistive anode pulses to satisfy upper and lower thresholds (internal to the position computer) for a position computation to occur. Consequently the detection of a PPU coincidence and subsequent gating of the digital E pulse does not always lead to the output of X,Y and STROBE signals by the position computer. Should an 8.5- μ s accidental flag (ACC) be set without the corresponding STROBE, a 'true + accidental' PPU event occurring shortly afterwards may be interpreted as an 'accidental' event. Similarly, if the ACC flag is set without a STROBE, and an 'accidental' event occurs shortly afterwards, the ACC flag may become LO before digitization, causing the PPU event to be recognized as a 'true + accidental'. Thus, to avoid these problems, the accidental circuitry is designed to generate a TTL ACC flag only if a corresponding STROBE signal has been given.

The accidental circuit diagram is presented in figure 3.18, and a pulse sequence following the generation of the ACC flag is shown in figure 3.19. The accidental ECL coincidence pulse is lengthened by an additional gate delay, and then converted to a TTL pulse using a 10125 ECL-TTL translator. Similar to the gating of the E pulse, the TTL accidental signal must be shaped and delayed to give a signal (GAF — for generate ACC Flag) that coincides with the leading edge of the STROBE pulse. The accidental TTL pulse triggers a monostable (74221), and the falling edge of the output pulse triggers a second monostable that generates the GAF signal. The width of the first monostable pulse determines the position of the GAF pulse, while the variable resistor of the second monostable sets the width. Meanwhile, the leading edge of the (inverted) STROBE signal from the position computer triggers a monostable to generate a 100-ns Short Strobe signal. The GAF pulse is set to arrive at one input of a fourth monostable prior to the expected time of arrival of the Short Strobe signal. If the falling edge of the Short Strobe pulse arrives at the second input of the monostable while the GAF signal is HI (see figure 3.19), an 8.5- μ s TTL HI accidental flag is produced. If the position computer fails to generate a STROBE signal, the flag is not set and the accidental circuitry is ready to process the next event.

3.3.6 Data Acquisition

The end result of a valid coincidence event is the generation of an X,Y pair of analog signals, a STROBE signal, and an ACC flag if the coincidence was an ‘accidental’. In the measurement of a momentum profile or binding energy spectrum, the X,Y and ACC flag

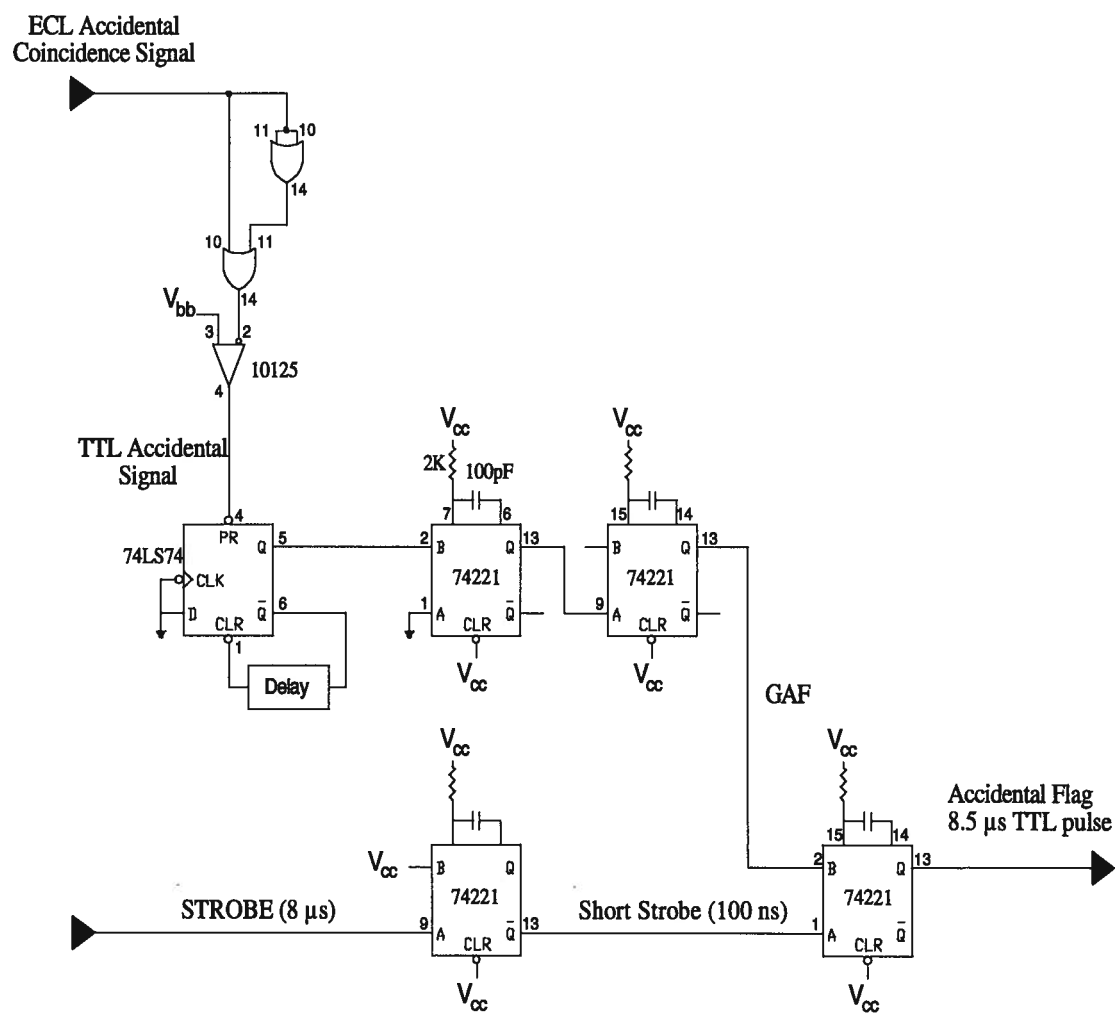


Figure 3.18: The accidental flag (ACC) circuit diagram.

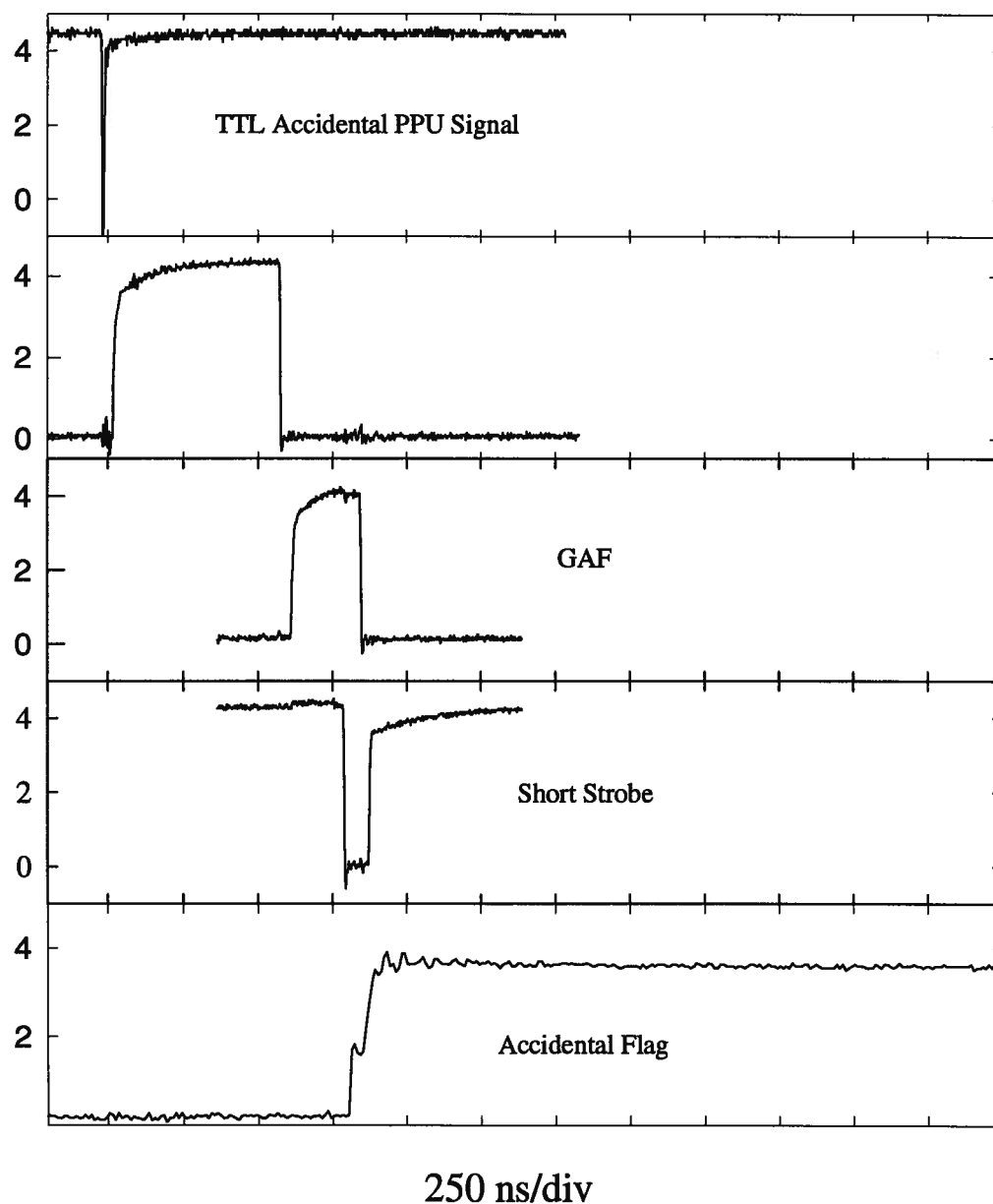


Figure 3.19: A series of waveforms depicting the generation of an ACC flag. The vertical axis are in volts. The TTL accidental GAF signal must be HI upon the arrival of a short strobe signal, to generate the Accidental Flag.

signals are digitized using a slightly modified¹ ISC-16 data acquisition board (R.C. Electronics), which interfaces with a 286 personal computer. With a 12-bit ADC (analog-to-digital converter), the board provides sufficient digital resolution in the acquisition of the position information. The detection of the STROBE pulse at the trigger input prepares the board to acquire data. The STROBE pulse also causes a 74121 TTL monostable to generate a 1- μ s external clock signal that initiates the ADC process. Following a setup time of 2-3 μ s, each channel is digitized on 1- μ s intervals. To ensure that the X,Y and ACC flag information is valid at the time of digitization, the output signals of the position computer and accidental circuitry have been extended to approximately 8 μ s.²

The monostable that generates the external clock pulse is located in a home-built coincidence counting unit. An array of 74390 decade counters, 7447 seven-segment display drivers and 10-mm seven-segment LED displays (MAN8640) were connected using wire wrap techniques in the construction of the counter. This inexpensive counter/clock pulse unit has proven to be convenient in the real-time monitoring of coincidence events.

The ISC-16 acquisition board also has a 12-bit DAC output channel that has been used to provide variable control over the energy of the incident electron beam. The voltage level of this DAC is set by the acquisition computer and modifies the output of the Fluke 415B

¹Each input channel of the board was designed with a low pass filter, which seriously affected the rise times of the input pulses. Input capacitors (to ground) were removed to remedy the problem.

² A pair of sample-and-hold amplifiers internal to the position computer were modified to enable adjustment of the X and Y analog output durations.

cathode high voltage power supply. Calibration of the power supply has shown the cathode potential to be very linear as a function of the DAC output over the available 133-V range (1189-1322 V). Within this range, any potential in increments of 33 mV can be established.

A PASCAL program has been written to control the acquisition board in the measurement of ϕ -angle distributions and momentum profiles. This program requests user input of the cathode potentials to be investigated and the accumulation time at each potential. The cathode potential is set by the DAC, and the board is signaled to acquire data, upon which a BIOS Delay Interrupt (Int 15, Function 80) is called. This pauses the program for period of time, typically 30-60 seconds, specified in microseconds. During a time delay, X, Y and ACC flag data for each coincidence event are stored in the buffer memory of the ISC-16 acquisition board. On detection of each coincidence event, the ISC-16 board also generates an IRQ3 interrupt that advances an accumulator variable in a software interrupt handler routine. At the end of each time period, the program queries the ISC-16 buffer memory and reads in the stored X, Y, FLAG data for each coincidence. If a range of binding energies is to be scanned, the program sets a new cathode potential, resets the buffer memory, and initiates a new acquisition period. At the end of each measurement period, an updated binding energy spectrum and momentum distribution are displayed on the computer monitor.

3.4 Characterization of the Instrument

As a chain is only as strong as its weakest link, so too is a spectrometer only as efficient as its 'weakest' component. To obtain the optimal (or close to optimal) performance of any

spectrometer, each of its individual components must be properly configured and operated. The sections presented below explore some of the measurements conducted to test and characterize each of the individual devices that together comprise the momentum dispersive multichannel spectrometer.

3.4.1 The CMA

For a particular setting of the CMA voltages, electrons within a range of energies and polar angles will pass through the CMA to the detectors. To characterize the energy resolution provided by the spectrometer, the transmission of elastically scattered electrons to the MCP and CEM detectors was measured. The variation of the count rates of the detectors with the energy of the incident electron beam is shown in figures 3.20a and 3.20b. The shapes and widths of the transmission peaks are slightly different, due to the different effective entrance apertures to the detectors. In addition to the intrinsic resolution of the analyzer, the widths of the peaks include a contribution from the energy distribution of electrons in the incident beam [102]. Assuming Gaussian peak shapes with widths (FWHM) of 2.8 and 3.4 eV for the CEM and the MCP/RAE respectively, a coincidence mode binding energy resolution of 4.4 eV is anticipated. This is consistent with the measured value of 4.3 eV, exhibited in the BES of the argon 3*p* electron shown in figure 3.20c.

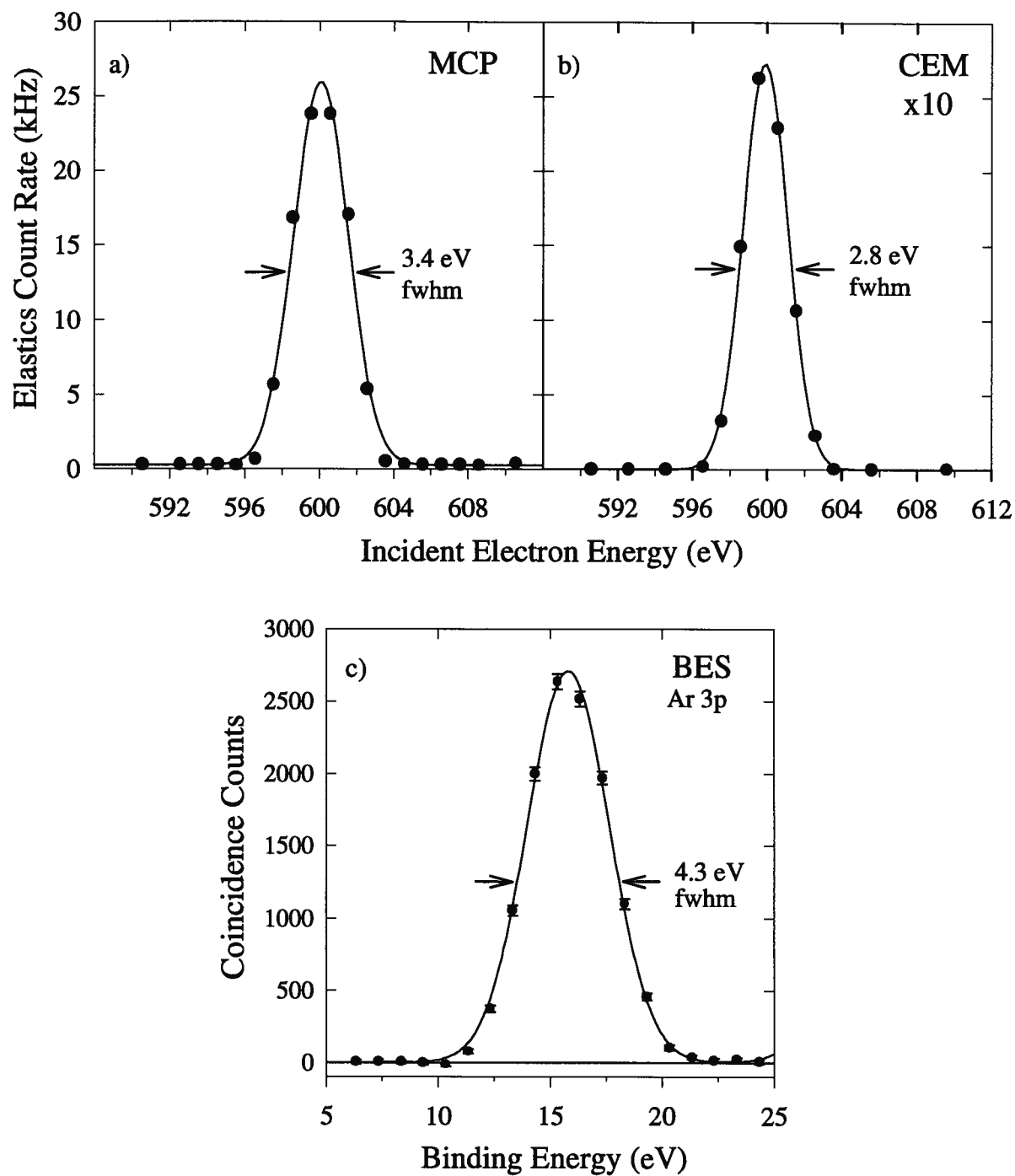


Figure 3.20: Characterization of the CMA energy resolution: (a) Transmission of elastically scattered electrons to the MCP/RAE detector (b) to the CEM. (c) The (e,2e) coincidence energy resolution.

3.4.2 The Channel Electron Multiplier

Following techniques typically employed in this laboratory, the CEM was positioned such that the electrons passing through the analyzer would strike the horn of the CEM. As well, a retarding bias voltage of -500 V with respect to the (grounded) inner cylinder was originally applied to the horn to help reduce the detection of stray electrons. Subsequent testing of the operation of the CEM has revealed an interesting dependence of the count rate on the front bias potential. Figure 3.21 presents saturation curves, depicting the count rate from the CEM as a function of the rear bias potential, for a number of different front bias values. The explicit dependence on the front bias is more clearly displayed in figure 3.22 in which the total electron count rate from the CEM and the (e,2e) coincidence event rate are plotted as a function of the front bias voltage, with the total bias across the CEM held constant. It is apparent from these figures that the detection efficiency of both background and coincidence electrons at the CEM is greatest for a front bias of ≈ -570 V. This appeared to be counter to the intuitive belief that the faster impact energy electrons would give a greater emission of secondary electrons and hence more efficient detection. Indeed, Seah [15] has indicated that the maximum detection efficiency of the CEM occurs for electrons striking the horn with an energy of 100-1000 eV.

However, in addition to the incident electron energy, the efficiency of a channeltron has been shown to be dependent on both the location and angle of impact [91,103]. In particular, Seah and Smith [91] have demonstrated that the efficiency of a channeltron is greater for an electron striking the edge of the channel or entering directly into the channel, than for an

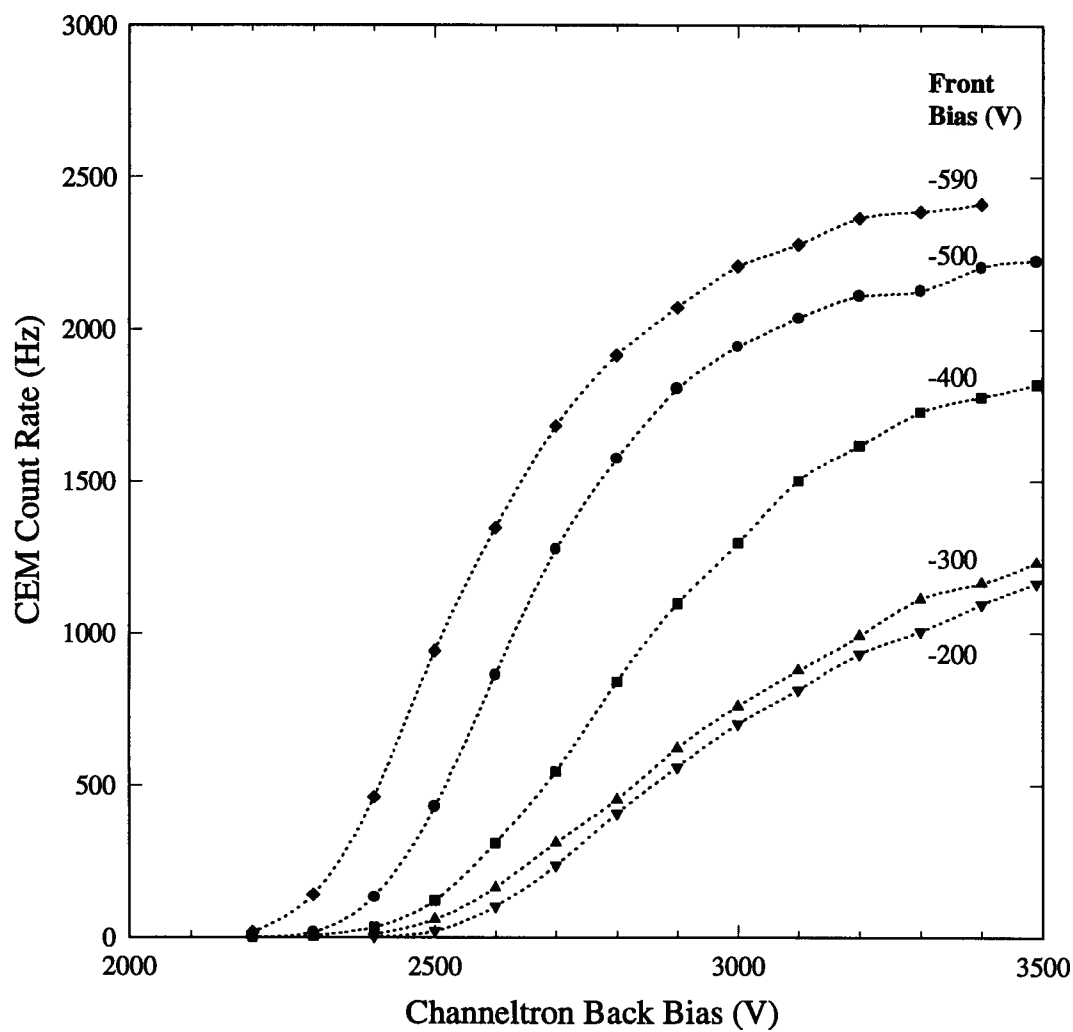


Figure 3.21: CEM saturation curves, depicting the count rate as a function of the back bias potential, for a number of retarding front bias potentials. Spline curves are shown between the data points, to aid the eye.

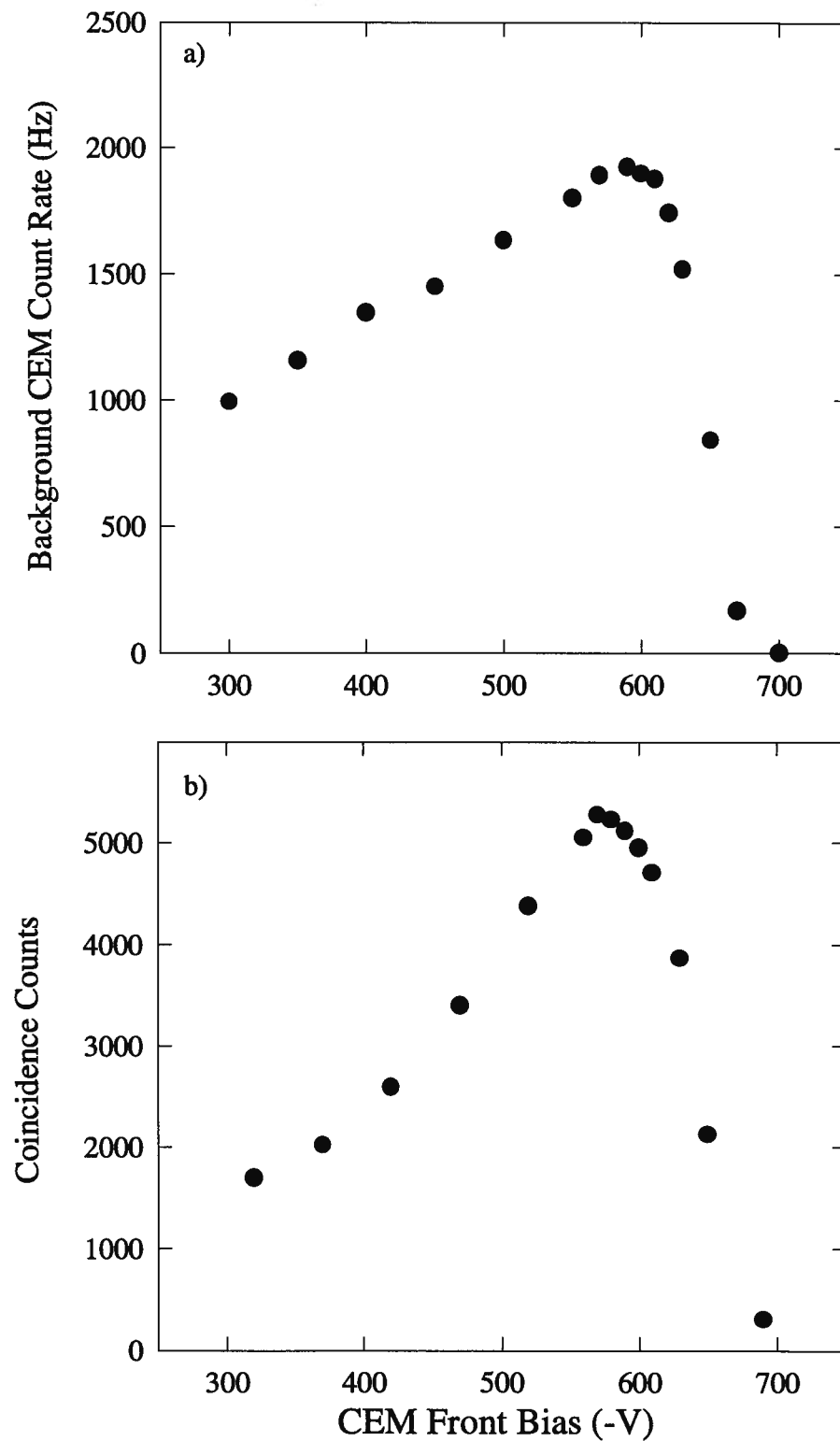


Figure 3.22: The variation with the retarding front CEM bias potential of (a) the total electron count rate from the CEM, (b) the (e,2e) coincidence counts rate (5 minute collection time).

electron striking the horn. Since an electron that directly enters the channel will initiate a cascade closer to the end of the CEM than one striking the horn, fewer multiplication stages will occur, giving a reduced output gain [91]. However, the overall detection efficiency may be higher in this case, as the electron directly entering the channel is more likely to *initiate* a cascade down the length of the channel than an electron striking on the horn, where scattering of electrons or quenching of the cascade before entering the channel may occur. The most efficient location of impact seems to be the intersection of the channel and horn, where the probability of a cascade is high and the gain from the full cascade through the CEM is achieved [91].

In the present system, the increase in detection efficiency with the retarding potential is believed to be caused by the deflection of electrons towards the channel opening, or into the channel itself. To illustrate this effect, two simulations of the trajectory of a 600-eV electron entering a CEM are presented in figures 3.23a) and 3.23b). The simulations were performed using SIMION (EG&G Idaho Inc.), a computer program for the modeling of motion of charged particles. The front biases on the CEMs of figures 3.23a and 3.23b are -500 V and -570 V respectively. As well, the potential from the horn edge towards the channel was increased slightly (~ 2% of total bias at the channel edge) to account for the effect of the positive back bias [91]. In both simulations, the electron is deflected towards the center of the CEM, although with a front bias of -500 V the deflection is small. The influence of the greater retarding potential on the electron trajectory is quite dramatic, as the electron is deflected into

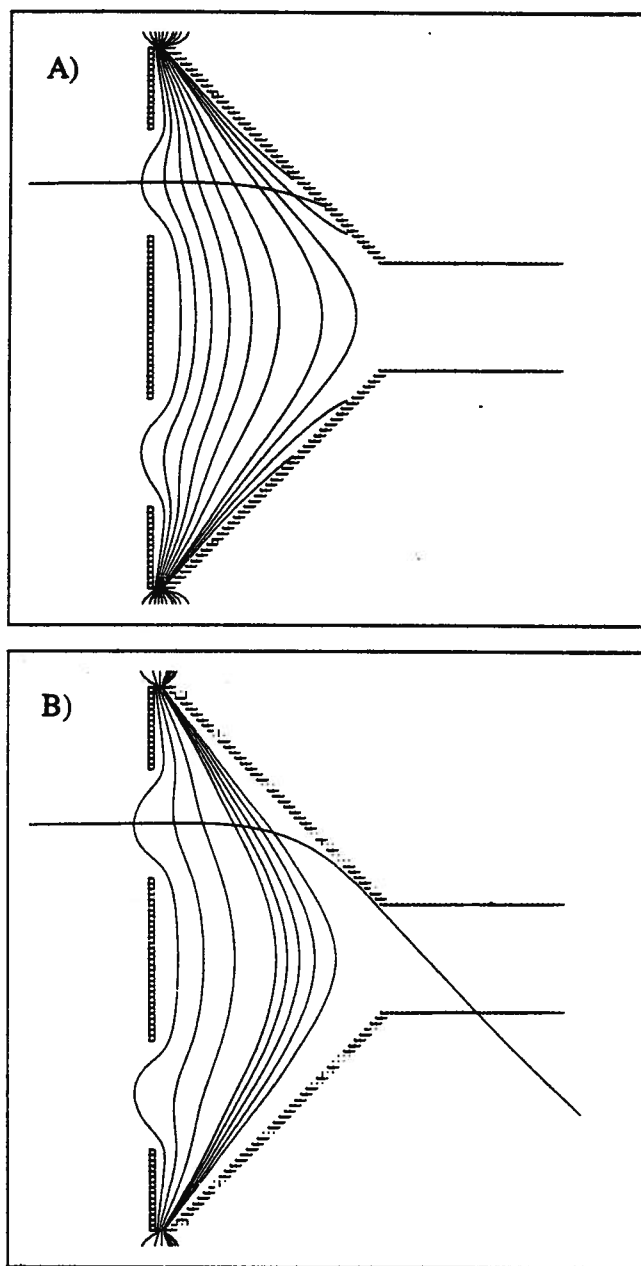


Figure 3.23: A simulation of the trajectories of 600 eV electrons at the entrance of the CEM, with a retarding potential of a) -500V and b) -570V applied to the CEM horn. The horizontal line to the left of each figure represents the electron trajectory. The curved, more vertical lines are equipotentials. The lower aperture in each figure is an artifact of the simulations.

the channel of the CEM. As this region gives more efficient detection, it follows that the count rate of electrons with the higher front bias potential should be greater than lower bias, in accord with the measurements of figure 3.22. A related effect has been discussed by Seah and Holbourn [104], who noted that the CEM efficiency was found to decrease with the application of an increased (positive) cone bias. In their study, a grid was applied to the front of the CEM to remove the distortion of the electric field in the horn, and a much more uniform CEM efficiency with applied front bias was obtained [104].

As a result of the investigation of the influence of the front bias on CEM efficiency, the CEM is operated with a retarding front bias potential of -570 V. The positive bias at the back of the CEM is set to ensure CEM operation in the saturated pulse counting region (typically 3100-3900 V across the CEM), exhibited by the plateau in the higher curves of figure 3.21.

3.4.3 The Microchannel Plate / Resistive Anode Operating Voltages

The operation of the MCP/RAE detector is inherently more complex than the operation of the CEM. For efficient performance, the pulse height distribution of the timing signals must be above the threshold of the constant fraction discriminator. As well, the distribution of RAE pulses must lie within an upper and lower threshold window determined by the position computer electronics. Furthermore, the pulse height distributions of the anode pulses and the timing pulses are both influenced by the bias potential across the MCP chevron. An acceleration bias of 200 V from the back of the MCP chevron to the timing grid, and a

subsequent 200-V accelerating bias to the RAE (as shown in figure 3.8) have been found to give both a sharp and narrow timing pulse and a high-contrast uniform image from the RAE. Presented in figure 3.24a are measurements of the count rates of the timing signals and position computer STROBE signals as a function of the MCP bias potential, obtained while maintaining the 200-V grid and anode acceleration potentials. As the MCP bias potential is increased, the count rate of the MCP timing signals (solid circles) rapidly increases and begins to plateau. At higher potentials, the onset of ion feedback lead to a sharp rise in the timing signal rate and a degradation of the anode image. The count rate of STROBE signals from the position computer (open circles) also rises with increased bias, but only up to a maximum. At bias potentials beyond this point, the larger anode pulses are rejected by the upper threshold of the position computer, and the STROBE count rate drops off. The lower count rate of the STROBE signals relative to the timing signals is primarily due to the position computer dead time. Presented in figure 3.24b is the number of coincidence events detected over a range of MCP bias potentials. The coincidence count rate should be dependent on both the STROBE and CFD count rates, and indeed the coincidence count rate exhibits a similar rise and fall with MCP potential as observed for the STROBE count rate.

Presently, the bias potential of the MCP stack is set to maximize the number of coincidence events. At this point, the grid timing pulses are on the leading edge of the saturation plateau. Future developments may add an additional amplification stage for the MCP timing pulses, which should provide more flexibility to meet the threshold requirements

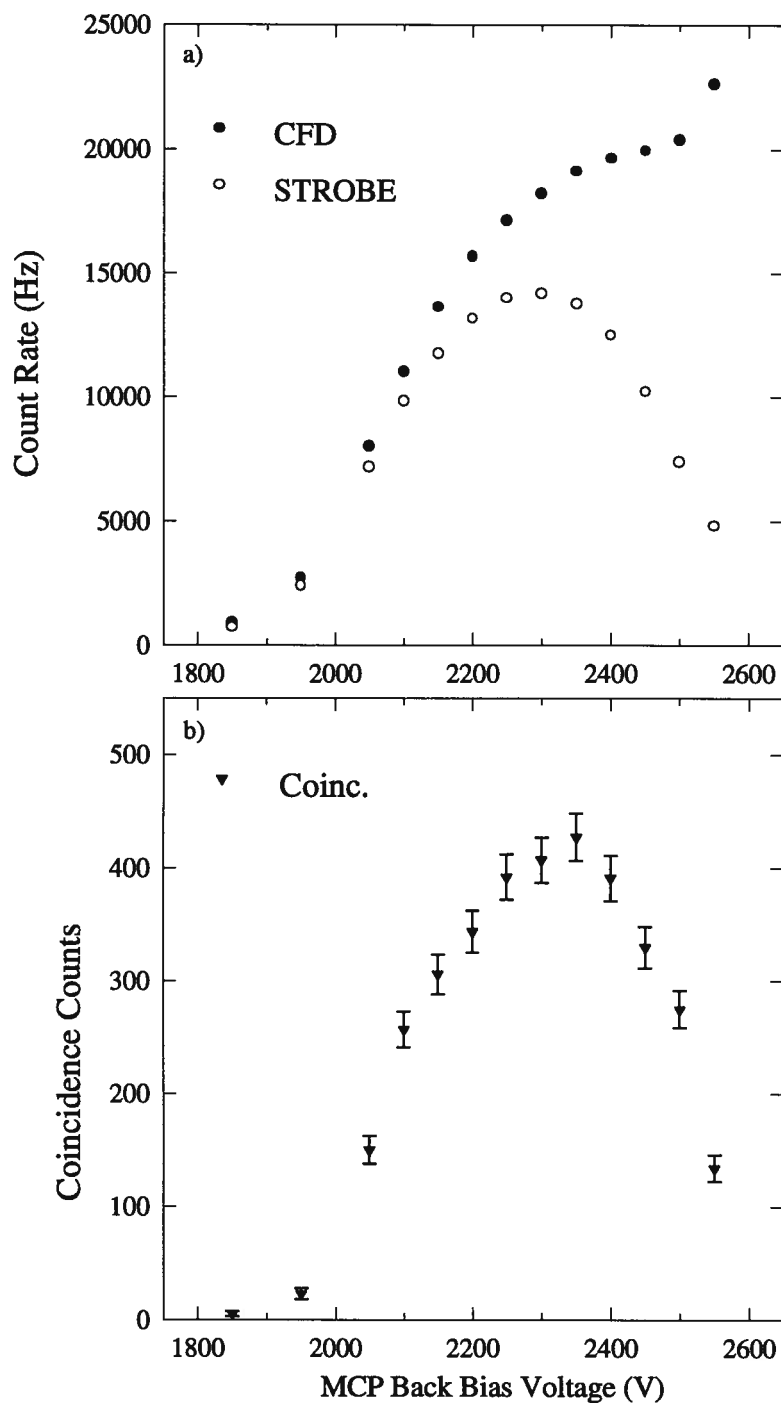


Figure 3.24: The influence of the MCP bias potential on the count rates of the a) grid timing pulse at the CFD and the STROBE signal after the position computer b) coincidence events.

and may allow for some improvement in sensitivity. As well, some enhancement in performance may be possible through the optimization of the thresholds for the anode pulses at the position computer.

3.4.4 The MCP/RAE Position Calibration and Uniformity

The nature of an $(e,2e)$ scattering reaction identified by the pulse-pile-up circuitry is characterized by the (x,y) coordinate of the electron impinging on the MCP. As the information of interest in EMS is the relative azimuthal angle between this electron and its coincident partner at the channeltron, a method of transforming the (x,y) coordinate to ϕ -angle must be employed. In principle the conversion could be based on the knowledge of the geometric positions of the MCP/RAE and CEM detectors. However, any non-linearities in the response of the RAE or different gains in the X and Y output channels of the position computer would destroy the necessary one-to-one correspondence between the anode image and the positions of electrons striking the incident face of the MCP. To calibrate the image of the RAE, an angular mask, with 1° slots spaced every other degree, was fabricated from 0.002-inch thick beryllium copper shim stock. A photoreduced CAD (computer aided design) drawing of the mask was used in the photolithographic etching of the shim stock. Calibration was performed with the mask positioned in front of the incident face of the MCP stack and aligned relative to the CEM. An angular definition obtained in this manner negates the effects of any distortion of the RAE image, since the image of the mask would be equally distorted.

Presented in figure 3.25a is an image of the mask obtained by accumulating (x,y) position coordinates of electrons elastically scattered from argon at 600 eV and striking the MCP/RAE detector. The slots in the mask are well defined in the image, although scattering of electrons from the edges of the slots is suspected of slightly broadening the image of the 1° slots relative to the 1° filled area of the mask. Figure 3.25b displays a similar mask image representing the accumulated positional information of coincidence events, resulting from the (e,2e) ionization of argon 3p electrons. The variation of intensity of the image with phi angle is quite evident. As the different collision volumes for elastic scattering and (e,2e) scattering have an effect on the MCP/RAE image, the coincidence image is used to specify the angular definition.

In formulating an angular definition of the image, a balance between individually defining each bin and fitting the entire image with a single arc was required. A good compromise was obtained by using two arcs, having independent focal points and angular positions. One arc is used to describe the slot spacing on the inside of the mask image, while the other describes the slots at the outer region of the arc. An interactive computer program has been written to facilitate the definition of the angular bins. The program permits a region of the mask image to be magnified (on a computer monitor) and the parameters of the two arcs to be modified to give a description of the image. Joining the corresponding angles of the two arcs gives rise to the angular definition presented in figure 3.25c. The mask is removed in the normal operation of the spectrometer, and the angular definition is used to assign an azimuthal coordinate to

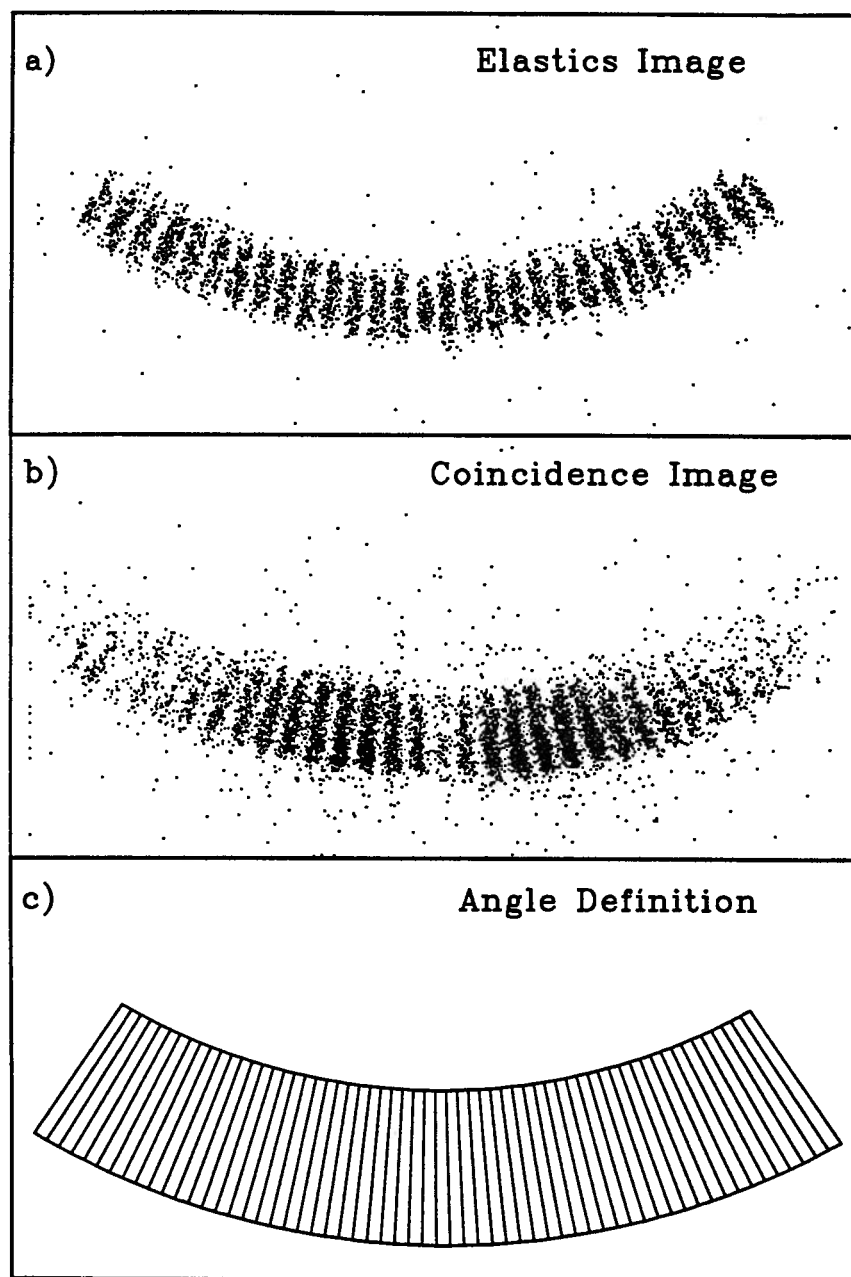


Figure 3.25: Calibration of the MCP/RAE ϕ -angle information: (a) image of electrons elastically scattered from argon, (b) image of coincident electrons from the ionization of the $3p$ electron of argon, (c) the definition of azimuthal angle bins.

each (x,y) position of an (e,2e) coincidence event. At present, the positions are allocated into 1° bins, which sets the azimuthal angular resolution of the MCP/RAE detector to $\Delta\phi = \pm 0.5^\circ$.

An important requirement in the momentum dispersive design of the spectrometer is the uniform transmission and detection of electrons about the observed azimuthal range. As discussed in chapter 1, an EMS instrument developed by Moore and colleagues [53,54] using an array of CEM detectors, requires frequent calibration to account for the variation of the efficiency of each CEM. Significantly more uniform response should be provided by the use of an MCP/RAE detector. A recent study by Brigham *et al.* [105] tested the characteristics of an MCP/RAE detector similar to the device used here, and found the detector to have less than 1% deviation in the count rate at various positions over its surface. An indication of the response of the MCP/RAE detector employed in the present application is given in figure 3.26, in which a typical distribution of the background (i.e. non-coincidence) electrons impinging on the MCP/RAE detector is presented. The distribution is very consistent over a ϕ -range of $\pm 26^\circ$, although outside of this angular window the intensity decreases. The drop in intensity at the larger angles is believed to be a result of a restriction in the transmission of the electrons near the ends of the slits in the conical lenses. Presently these slits extend over a ϕ -range of $\pm 30^\circ$, and the widening of the slits to permit the deceleration of electrons without “end effects” is also expected to improve the observed distribution at the larger angles. As a result of the distortion at the larger ϕ , the momentum profiles presented in this thesis are only shown

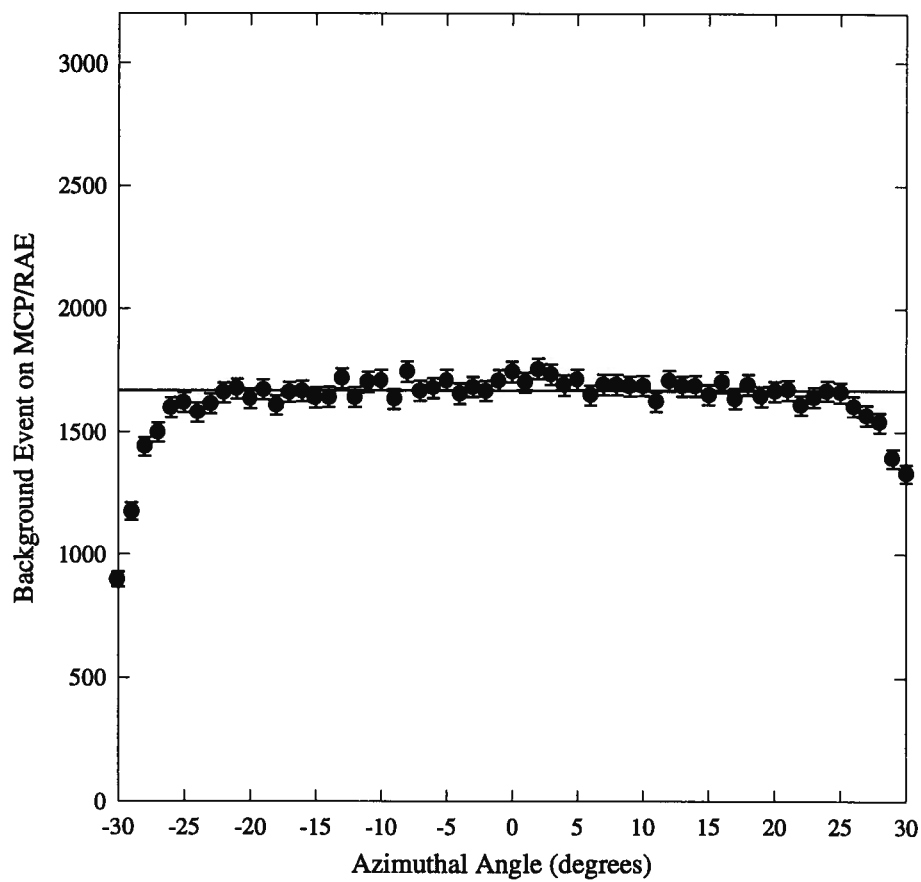


Figure 3.26: The angular distribution of background (non-coincidence) electrons at the MCP/RAE detector.

to $\pm 26^\circ$. However, the uniformity shown over this range is encouraging for the application of the detector to the measurement of the angular distribution of (e,2e) coincidence events.

3.4.5 Linearity of the Detectors

The saturated operation of the MCP and CEM detectors is important to ensure their uniform response over a range of experimental conditions. The gain of each detector decreases at higher rates of incident electrons [56]. If an increased incident flux causes the output pulse height distribution of a detector to pass below the discrimination threshold, the measured count rate may decrease or register a smaller increase than expected. As a thorough test of the operation of the CEM and MCP detectors, a series of investigations (using helium as the target gas) was performed in which the rates of electrons striking the detectors were dramatically varied. Figure 3.27 presents the CEM, the MCP (timing grid), and the coincidence event count rates as a function of the electron beam current measured at the Faraday cup. The linear response of the CEM and MCP detectors is clearly displayed. The observed linearity of the coincidence count rate is also a reflection of the low dead time of the coincidence and gated position computation circuitry. The count rates were also monitored as a function of the gas pressure and a similar linear response was obtained. It should be noted that the variation of electron flux in these measurements represents extreme conditions. In the typical measurement of a binding energy spectrum, the rate of electrons incident on the detectors changes very slightly ($< 3\%$ for a change in cathode potential from 1224 eV to

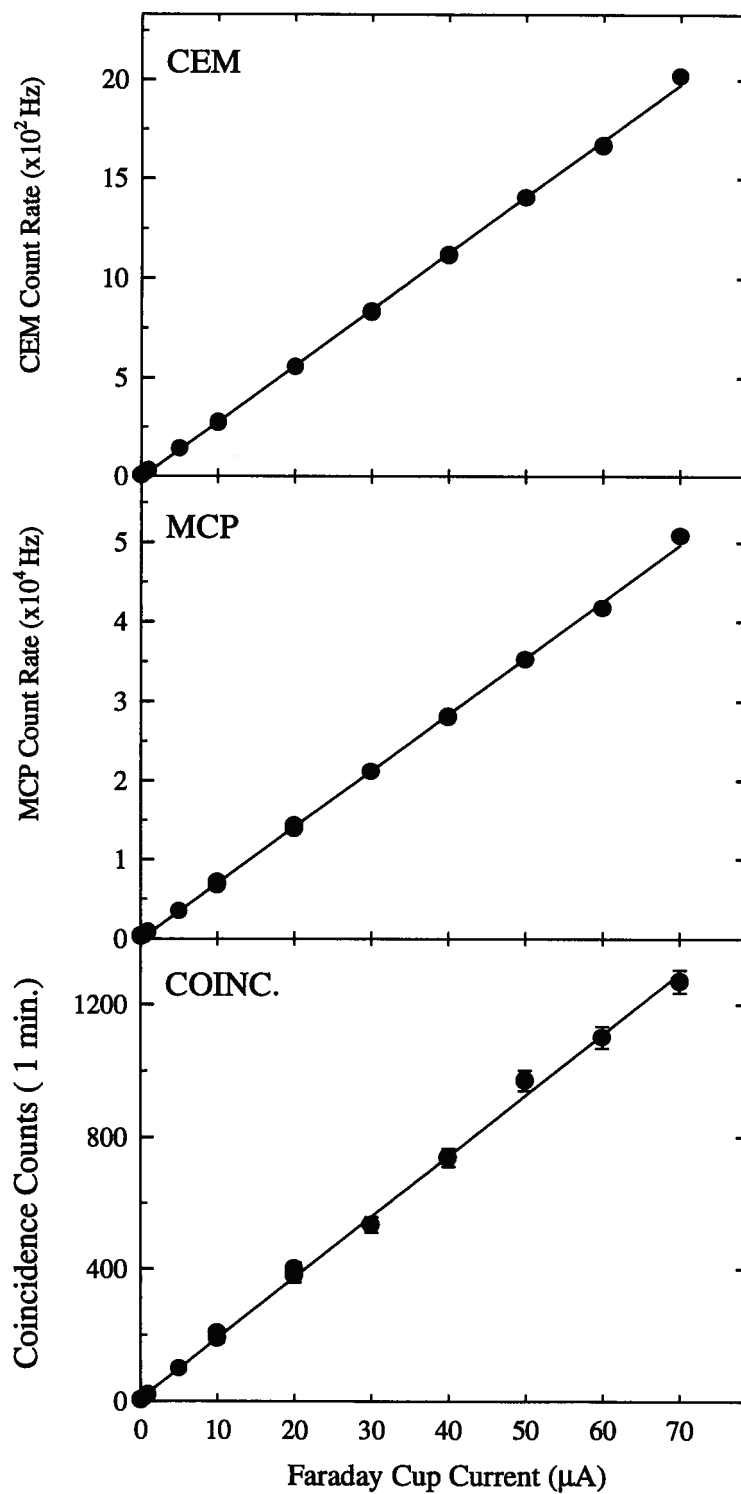


Figure 3.27: The response (count rate) of the detectors and coincidence detection circuitry over a range of electron beam currents.

1265 eV), while during the determination of a momentum distribution at a given binding energy, the electron flux is essentially constant.

3.4.6 The Coincidence Timing Windows

The size of the coincidence timing windows of the pulse-pile-up circuitry is primarily a function of the width of the pulses input into the power combiners and of the discriminator levels of the power combiner outputs. The widths of both the 'true + accidental' and the 'accidental' windows were measured by splitting the signal from a pulse generator (HP8082A) and inputting the two pulses to the CFDs to simulate coincidence events. A fixed delay was introduced after one CFD, and a digital delay generator (Stanford Research Systems DG535), interfaced with the 286 PC using a GPIB board, was used to introduce a variable delay after the other CFD. The time delay between pulses was varied in short (typically 0.05 ns) steps through the two timing windows, identifying the degree of overlap of timing pulses required to give a PPU coincidence detection. With this measurement procedure, the thresholds of both channels were adjusted to record coincidences on the condition of two pulses arriving at the inputs of the power combiner within ± 1.5 ns of each other. Displayed in figure 3.28 is the simulated coincidence count rate measured as the digital delay was swept through the 'true + accidental' window.

In a TAC-based system, the 'true + accidental' coincidence timing window is adjusted about the peak in the TAC spectrum. In contrast, the present system requires the coincidence

peak to be adjusted to fit within the coincidence timing window. The appropriate delay required to align the coincidence peak and timing window has been determined by adding short lengths of RG-174 coaxial cable to the output of the CFDs. Figure 3.29 displays the variation of the coincidence count rate for the different lengths of delay line. The shape of the distribution is effectively the convolution of the 3.02-ns coincidence timing window (figure 3.28) by the coincidence peak shape (1.6 ns FWHM, see TAC spectrum figure 3.11). In normal operation the delay is set to the middle of the distribution, ensuring that the coincidence peak is centered in the timing window.

The relative PPU detection efficiencies of the ‘true + accidental’ and ‘accidental’ channels are periodically tested using a pulse generator (HP8082A) in place of the CEM signal to provide pulses of greater frequency (typically 20-40 kHz). As the simulated CEM and the MCP pulses are uncorrelated in this situation, both channels are subjected to the same accidental count rate, and the PPU coincidence count rate of each channel is indicative of its coincidence detection efficiency. Additionally, during the course of an EMS measurement, the detection efficiency of the channels is monitored by the relative counts of the channels when the cathode potential is set below the energy required for (e,2e) ionization of the sample. The relative efficiencies are taken into account in removing the accidental background from the binding energy and momentum profile measurements.

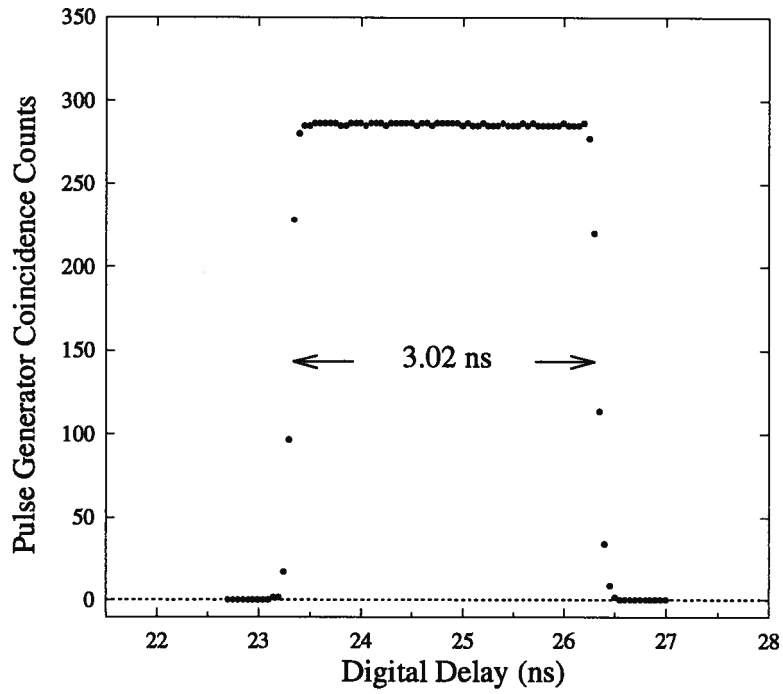


Figure 3.28: The 'true + accidental' PPU coincidence timing window.

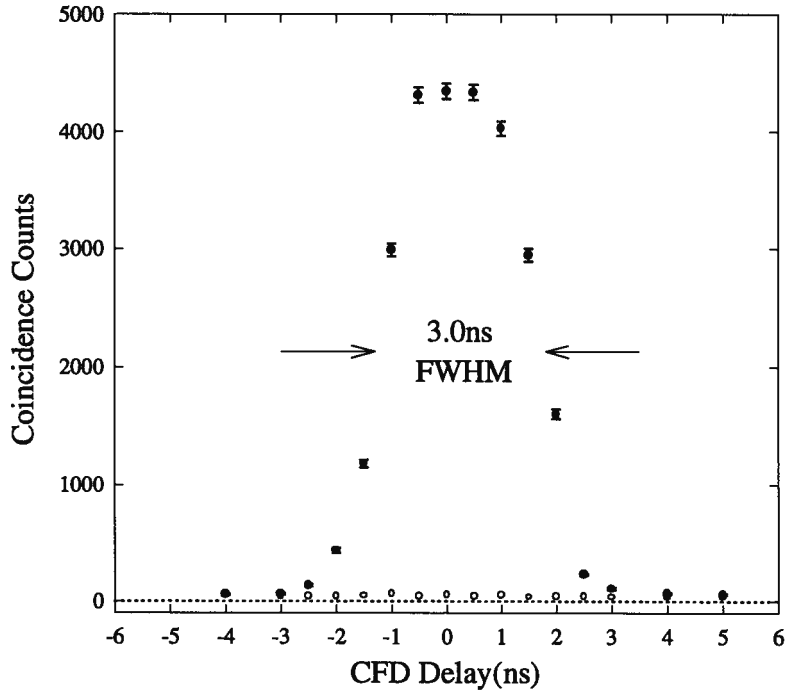


Figure 3.29: The variation of coincidence counts with the addition of delay line after the CEM or MCP CFD. The solid points are 'true + accidental' coincidence events and the open circles are 'accidental' events.

3.5 Experimental Results

The stage is now set for the presentation of some proof-of-concept measurements illustrating the capabilities of the momentum dispersive, multichannel spectrometer. Only the ‘opening act’ is given in this section, as a more full presentation of the multichannel EMS investigation of a number of atomic and molecular systems is given in the following chapter. During the measurements presented in the figures below, argon was introduced to the collision chamber through a Granville-Phillips leak valve to a pressure of 1.0×10^{-5} torr (measured with an ion gauge at the top of the vacuum chamber). Additionally, the electron beam current was set to 60 μA .

The improved coincidence collection efficiency of the new instrument permits a large reduction in the acquisition time required for EMS measurements of a given statistical precision. This is clearly illustrated in figures 3.30 and 3.31, which respectively show a binding energy spectrum and momentum distribution of the argon $3p$ electron. Each point in the binding energy spectrum was acquired for a period of 53 seconds, and represents the total of coincidence counts collected over the $\pm 26^\circ$ angular range of the MCP/RAE detector. The total acquisition time of the spectrum was 15 minutes. The angular (ϕ) distribution of argon $3p$ presented in figure 3.31 was acquired at 53 angles simultaneously, over a period of 15 minutes. Both spectra exhibit a high signal-to-noise ratio and a statistical quality comparable to many single channel results in the literature that required at least several days or weeks of

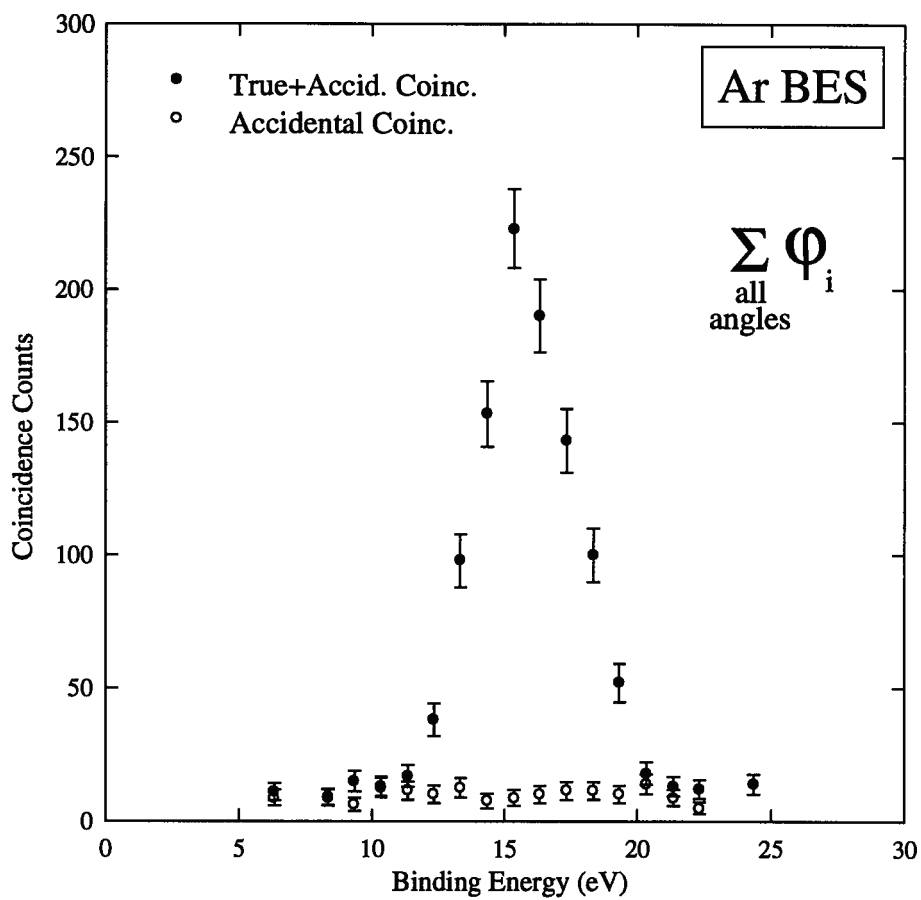


Figure 3.30: A binding energy spectrum of the argon 3*p* electron acquired in a total of 15 minutes (~ 53 seconds per point).

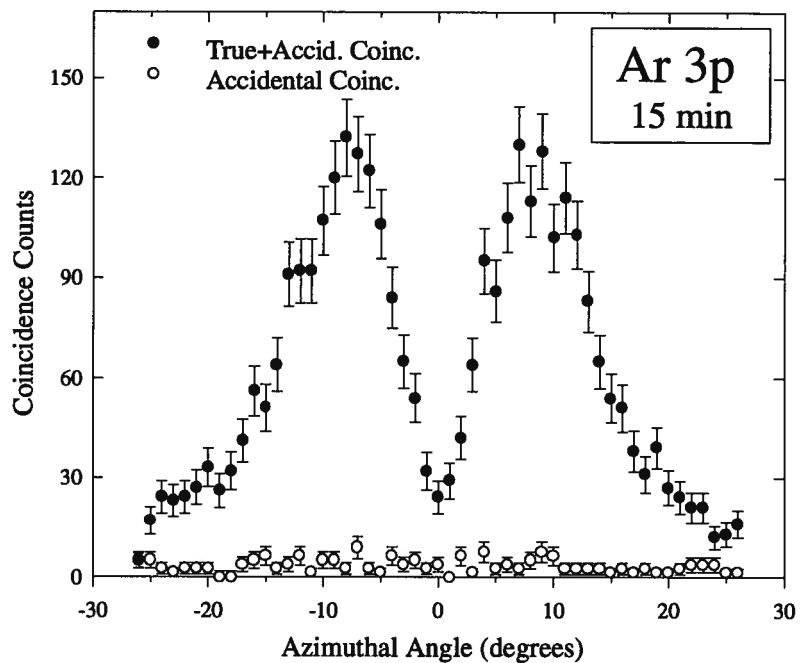


Figure 3.31: A momentum dispersive multichannel ϕ distribution of the 3p electron of argon acquired in 15 minutes.

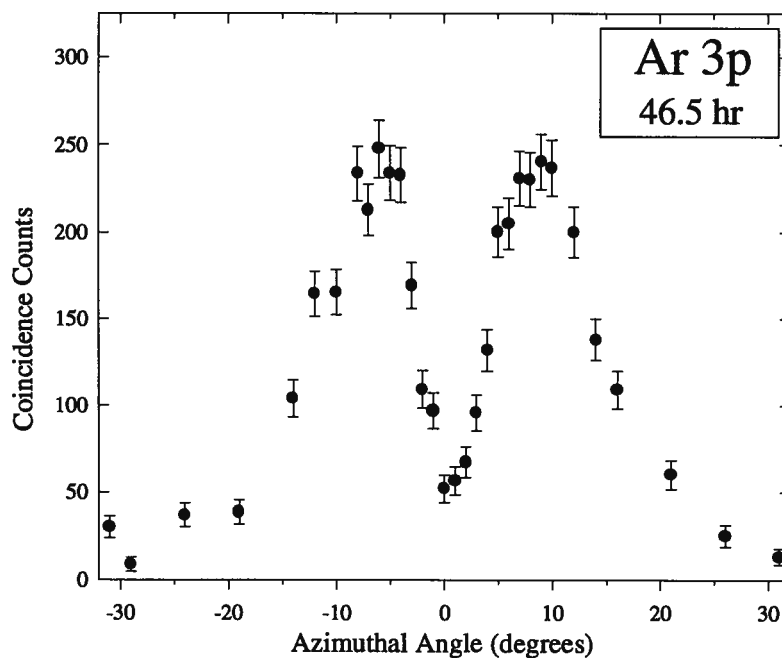


Figure 3.32: A momentum distribution acquired in 46.5 hours using a single channel, ϕ -angle scanning instrument [188].

measuring time. The ability to measure binding energy spectra and momentum profiles is relatively short periods of time has been described as “rapid orbital imaging”.

To provide some perspective on the enhancement of sensitivity of the new instrument, a momentum profile of the Ar 3*p* electron obtained with a single channel instrument [188] (a recently retired predecessor of the present spectrometer) is shown in figure 3.32. The total acquisition time of the 31 points in this spectrum was 46.5 hours. It is clear from a comparison with figure 3.31 that a very significant improvement in sensitivity has been realized in the new multichannel instrument. A more detailed assessment of the degree of improvement would require consideration of many factors, including the operating conditions, detector performance, and energy resolution of both instruments.

Measurements acquired over longer periods are presented below and permit a more quantitative evaluation of the instrumental performance. Figure 3.33 is a binding energy spectrum of the valence region of argon, acquired in 13.5 hours (15 min/point). The spectrum exhibits peaks arising from ionization to the $(3p)^{-1}$ and $(3s)^{-1}$ states as well as a broad peak from ionization to $(3s)^{-1}$ satellite states that occur through electron correlation effects [76]. The energy resolution exhibited in this spectrum is 4.3 eV.

A typical high precision measurement of the phi-angle distribution of (e,2e) events from the argon 3*p* orbital, measured over a period of 6.2 hours, is displayed in figure 3.34a. The

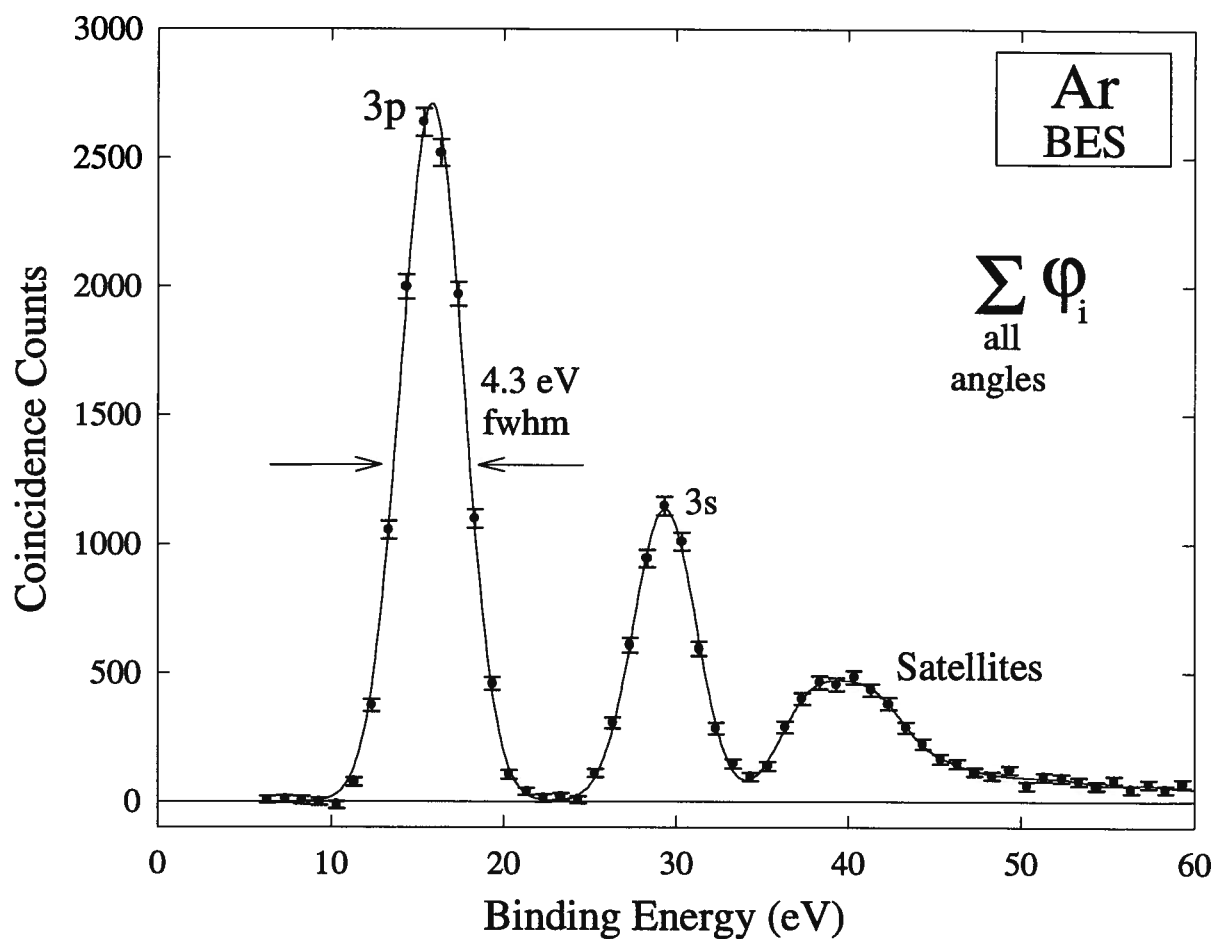


Figure 3.33: A high precision, φ -angle integrated, binding energy spectrum of argon acquired in 13.5 hours (15 min. per point).

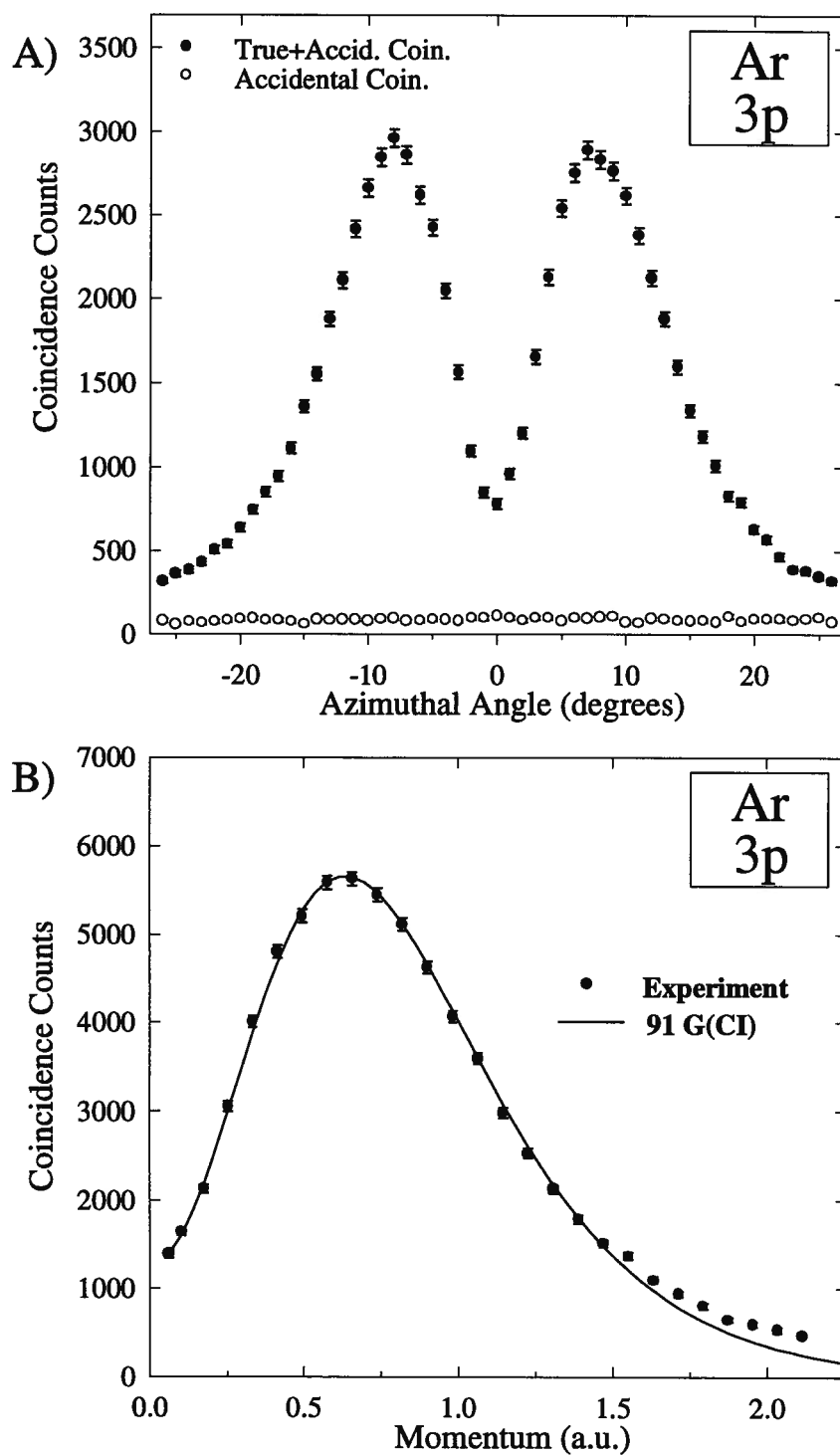


Figure 3.34: (a) A high precision momentum dispersive multichannel ϕ -distribution of the 3p electron of argon, acquired in 6.2 hours. (b) A high precision momentum profile of the 3p electron of argon, derived from the ϕ -distribution in (a).

accidental background (open circles) has been scaled by the relative sensitivities of the two PPU channels (measured to be 1.37 ± 0.03), and exhibits an isotropic intensity distribution similar to that shown in figure 3.24. Subtraction of the background intensity, summation of the points at corresponding angles about $\phi = 0^\circ$, and conversion from an angular to a momentum scale using equation (1.5), furnished the experimental momentum profile (XMP) displayed in figure 3.34b. Included in this figure is a theoretical momentum profile obtained using the ion-neutral overlap expression of the EMS cross section given in equation (2.6). The theoretical momentum profile was evaluated by E.R. Davidson using high level ion and neutral wavefunctions from an MRSD-CI calculation involving a basis set of 91 Gaussian-type functions [49,113]. For comparison to the XMP, the theoretical profile has been height normalized to the experimental data, and has been folded with the estimated instrumental response function using the Gaussian-weighted planar grid method of Duffy *et al.* [49]. With error bars (one standard deviation) comparable to, or smaller than, the symbols representing the data points, the profile exhibits significantly greater statistical precision than any previously published work in the field of EMS. As well, the accuracy of the data is supported by the agreement with the high quality theoretical calculation in the momentum region below ~ 1.5 a.u.. As discussed in chapter 2, the effects of distorted waves on the (e,2e) cross section become more pronounced at higher momenta. The degree of distortion observed in figure 3.34b is of the same order as measurements and DWIA calculations reported by McCarthy *et al.* [76].

It is clear from these measurements and a consideration of existing published work that the multichannel momentum dispersive spectrometer described in this chapter provides a significant improvement in detection efficiency for EMS measurements. The application of a multichannel detector in a momentum dispersive architecture, and the development of a novel PPU coincidence detection system described herein, represents an important development as the field of EMS strives to investigate increasingly complex systems and lower target densities. To conclude this chapter, a two-dimensional EMS measurement (2D-EMS) — the first of its kind — is presented in figure 3.35, giving a further illustration of the enhanced capabilities of the new instrument. The binding energy/ ϕ angle surface of argon for impact energies from 1200 to 1260 eV, in 1eV increments, was obtained in 93.4 hours. Such a 2D-EMS surface represents an alternative method of displaying EMS results and contains a wealth of information regarding the intensities and symmetries of the various ionization transitions.

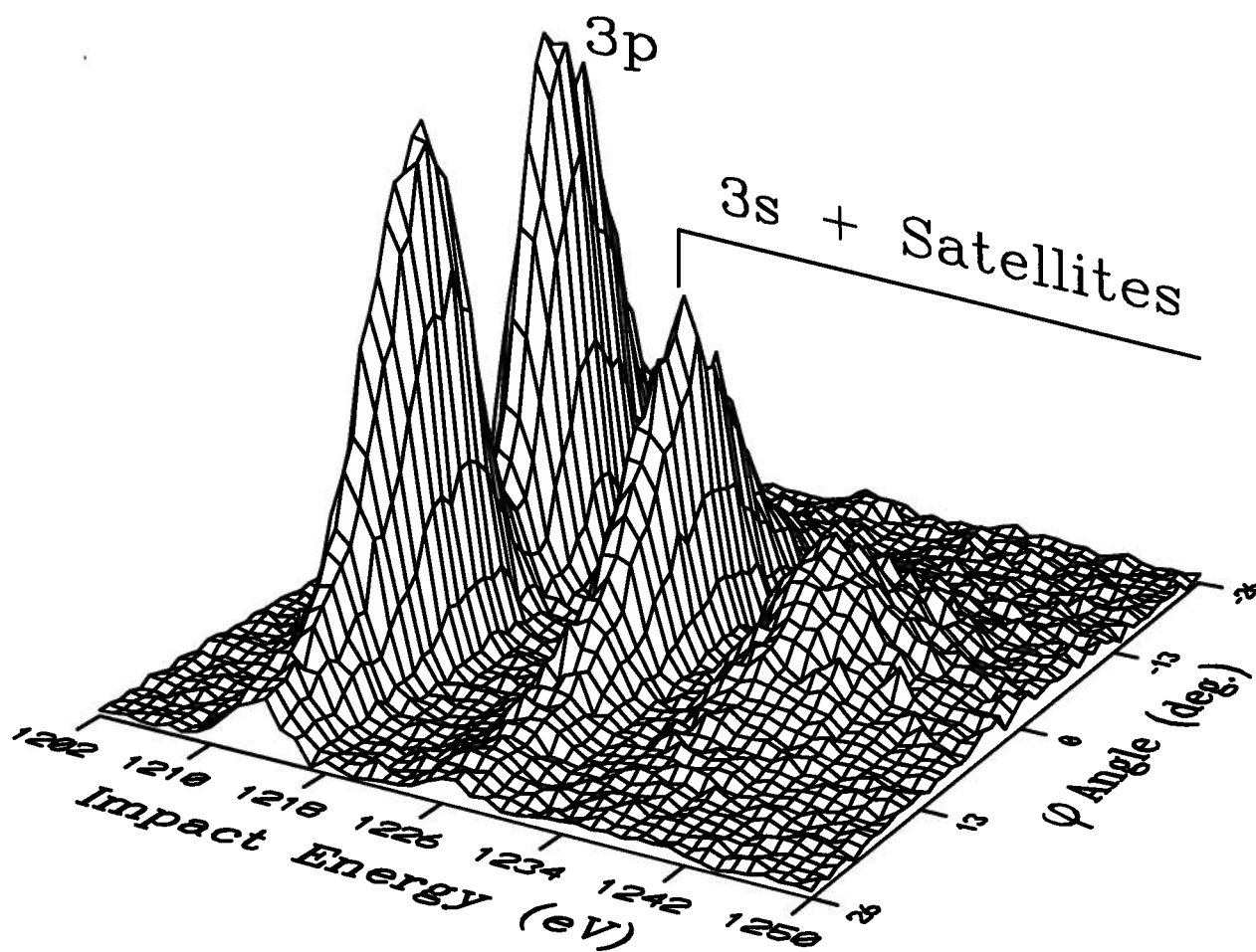


Figure 3.35: Two dimensional electron momentum spectroscopy (2D-EMS): an impact energy / ϕ angle distribution surface of argon, acquired in 93.4 hours.

Chapter Four

Momentum Dispersive Multichannel EMS Measurements

The binding energy spectra, the angular distributions, and the experimental momentum profiles of the valence regions of the noble gases Ne, Kr and Xe, and of CH₄ and SiH₄ are presented in this chapter. Argon results have already been presented in chapter 3. The principal motivation for these studies was to establish the quantitative response of the momentum dispersive multichannel spectrometer over the full valence region of a number of systems. The detailed characterization using relatively simple atomic and molecular systems is important for the application of the multichannel spectrometer to more demanding (in terms of instrumental performance) studies such as those presented in chapters 5 and 6. A second motivation was to obtain the most precise measurements to date, albeit at low energy resolution, of the experimental momentum profiles of these systems.

As the noble gases have been thoroughly investigated in previous EMS studies, they present an excellent series of target systems for the quantitative evaluation of the multichannel instrument. Earlier studies have investigated three general facets of the EMS scattering cross section. The XMPs have been compared to the theoretical profiles calculated with a variety of wavefunctions using a PWIA description of the collision process (see for example, Leung and

Brion [25]). As well, the influence of distorted waves on the (e,2e) cross section has been investigated [27,76,106,107]. Recently, much attention has focused on the EMS investigation of the satellite structure of the inner valence region of the binding energy spectra of noble gases [76,108,109,110,111]. This satellite structure arises from many-body (i.e. electron correlation) effects in the final-state (see for example, ref. [25]). The EMS investigations have found the shapes of the XMPs of the valence orbitals of the noble gases, obtained at impact energies in the region of 1200 eV, to be well described at low momentum ($< \sim 1$ to 1.5 a.u.) by theoretical profiles using the PWIA and near-Hartree-Fock limit wavefunctions. However, the relative intensity of the inner valence (ns - where n is the principle quantum number) XMP to the outermost (np) orbital XMP is generally overestimated by the PWIA cross section, while improved agreement is given by a distorted wave description [76,106,107]. This intensity variation must be considered in the comparison of the momentum dispersive multichannel XMPs to PWIA theoretical profiles presented below.

All of the PWIA theoretical momentum profiles presented in this chapter have been folded by the GW-PG method [49] using empirically determined angular resolution widths of $\Delta\theta = \pm 0.7^\circ$ and $\Delta\phi = \pm 1.2^\circ$. A direct evaluation of the range of azimuthal and polar angles associated with the (e,2e) scattering events detected by the multichannel instrument is difficult. However, the value of $\Delta\phi$ is very consistent with the azimuthal resolution assigned to the RAE image, and the range of angles determined by the entrance aperture to the CEM. The value of $\Delta\theta$ is considerably smaller than the expected range of polar angles of electrons entering the cylindrical mirror analyzer, defined by the conical lens elements and collision

chamber slits (fig. 3.4). As the CMA is not expected to exhibit first or second order focusing of electrons to the exit slit, the range of polar angles of electrons detected by the MCP/RAE and CEM detectors should be smaller than the range entering the CMA. The polar angle resolution used in the folding procedure is not inconsistent with these instrumental considerations.

Finally, it should be noted that in each of the experimental measurements presented below, the ambient gas pressure was $\sim 1.0 \times 10^{-5}$ torr, and the incident electron beam current, measured at the Faraday cup, was maintained at $\sim 60 \mu\text{A}$.

4.1 Neon

The angle integrated ($0 - \pm 26^\circ$) binding energy spectrum of neon, obtained with the momentum dispersive multichannel EMS instrument, is presented in figure 4.1. To calibrate the energy scale, the lower energy peak, corresponding to the ionization of neon $2p$ electrons, has been positioned to the ionization potential of 21.57 eV, determined by PES measurements [112]. The second peak, corresponding to ionization of $2s$ electrons, is centered at 48.47 eV which is in good agreement with the IP of 48.46 eV measured by photoelectron spectroscopy [112], giving a good indication of the linear operation of the programmable high voltage power supply used to scan the impact energy in the present instrument. Above the main $2s$ peak, some low intensity satellite structure is apparent, in agreement with the more detailed EMS investigation of this region of Samardzic *et al.* [110]. The solid line in the satellite

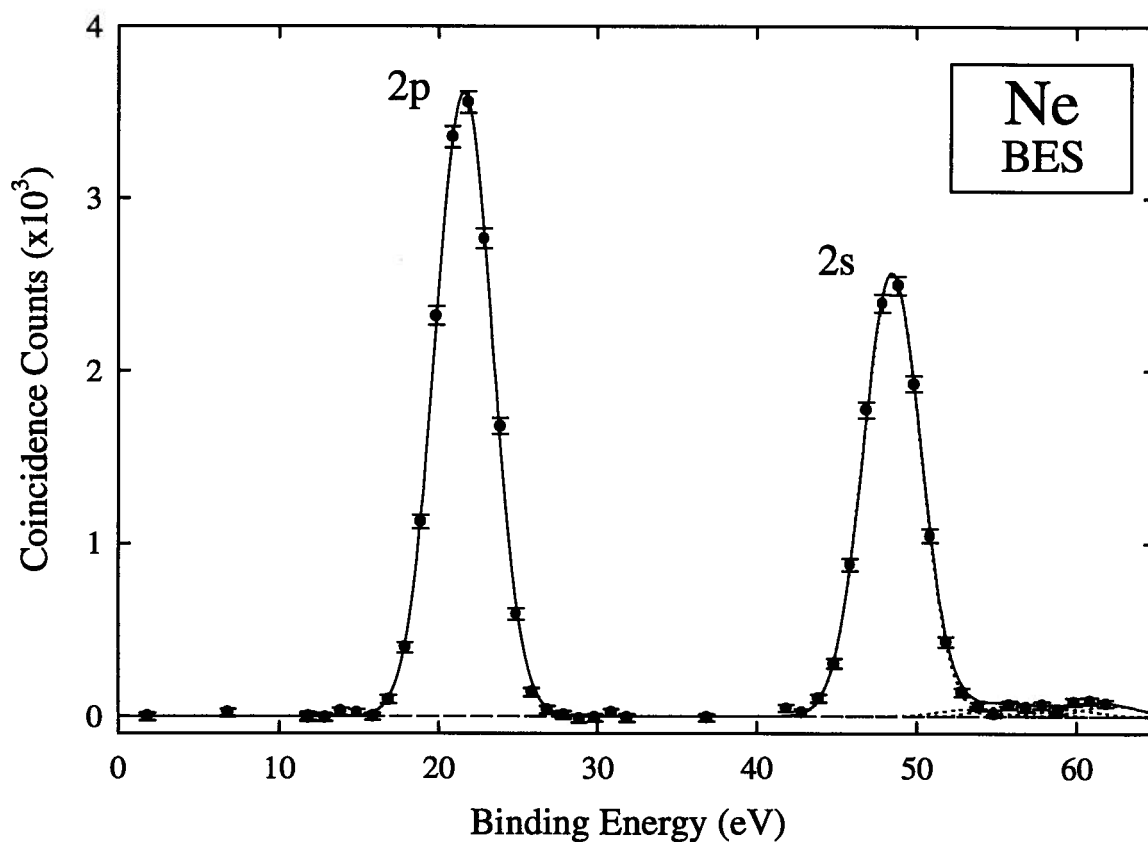


Figure 4.1: A multichannel ($0 - \pm 26^\circ$) binding energy spectrum of the valence region of neon. The solid line represents the sum of Gaussian functions, fit to the $2p$ and $2s$ peaks. Additional Gaussians, with intensities determined from the EMS measurement of Samardzic *et al.* [110], are shown as dotted lines. The energy scale has been determined by setting energy of the $2p$ peak to the ionization potential identified by PES measurements [112].

region of figure 4.1 (above the $2s$ main peak) represents the sum of Gaussian functions determined from the energies and spectroscopic factors given by Samardzic *et al.* [110].

The experimental momentum profile of the $2p$ electron is presented in figure 4.2. The experimental data are represented as solid circles, and the (one standard deviation) statistical error bars are similar to the point size. The single channel XMP (open circles) reported by Leung and Brion [25] is also shown in figure 4.2, and is in good agreement with the multichannel experimental profile. The improved statistical precision of the present multichannel measurements is readily apparent. Additionally, two theoretical momentum profiles are also displayed: one based on a near-Hartree-Fock limit wavefunction [81] and the other an OVD determined from a MRSD-CI calculation using a 106-Gaussian basis set. The two theoretical profiles have been individually normalized to the height of the multichannel XMP. While the single channel data have previously been reported to give good agreement with the near-Hartree-Fock limit TMP [25], the present multichannel measurement indicates that both of the TMPs displayed in figure 4.2 overestimate the relative intensity momentum (>1 a.u.). This presented some confusion, since any discrepancy between theoretical profiles (using high-quality wavefunctions and the PWIA) and experimental profiles at high momentum values is typically in the opposite direction; the effects of distorted waves in the scattering process generally cause the PWIA cross section to underestimate the EMS cross section in this region. However, reported theoretical profiles of neon $2p$, calculated using the DWIA

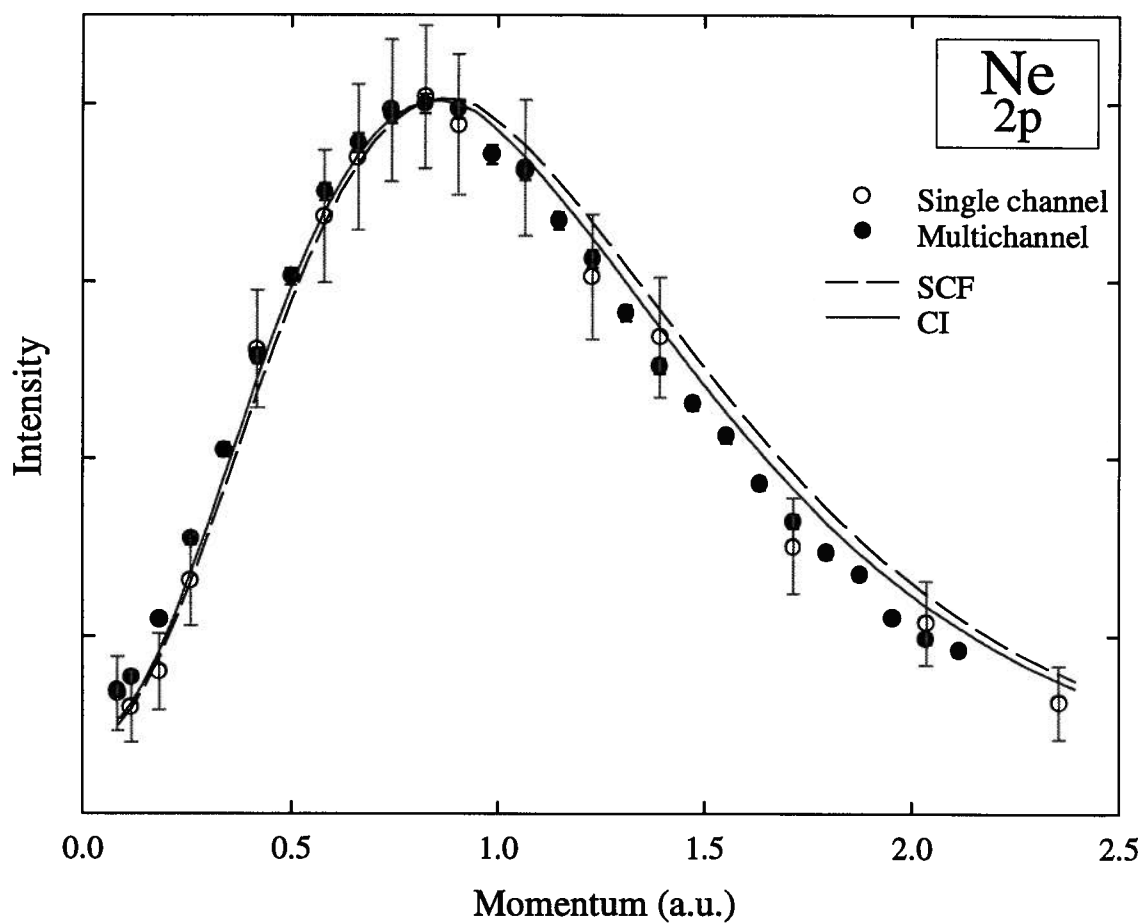


Figure 4.2: The multichannel experimental momentum profile for the 2p electrons of neon (filled circles), compared to PWIA theoretical profiles calculated with an SCF wavefunction (dashed line) and with a CI wavefunction (solid line). The single channel XMP reported by Leung and Brion [25] is shown as open circles.

[27] and the distorted wave Born approximation (DWBA) [106]¹, exhibit a reduced intensity relative to the PWIA profiles in the region above 1 a.u., consistent with the present observations. The variation of the profiles calculated in the plane wave and distorted wave approximations is reasonably small, and an earlier experimental measurement of the neon 2*p* XMP by Braidwood *et al.* [106] (obtained at an impact energy of 1500 eV) was unable to distinguish between the PWBA and DWBA theoretical profiles. The present XMP of the neon 2*p* electron is displayed in figure 4.3a with the digitized DWBA and PWBA theoretical profiles reported by Braidwood *et al.* [106], and is clearly in better agreement with the TMP using the distorted wave analysis. It should be noted that the PWBA profile has been scaled by 0.9 to match the peak intensity of the lower DWBA profile [106].

The multichannel experimental profile for the 2*s* electron, normalized to the 2*p* XMP using the relative areas of the 2*p* and main 2*s* binding energy peaks, is shown in figure 4.3b. The DWBA cross section from Braidwood *et al.* [106] is also shown, and has been scaled by the spectroscopic factor of 0.85, as in the original work [106]. Reasonable agreement of this theoretical profile with the present experimental data is obtained.

¹ The DWBA calculation uses an alternative description of the (e,2e) scattering process, and includes the influence of distorted wave effects in the calculation of EMS cross sections, as in the DWIA. For a description, see Braidwood *et al* [106].

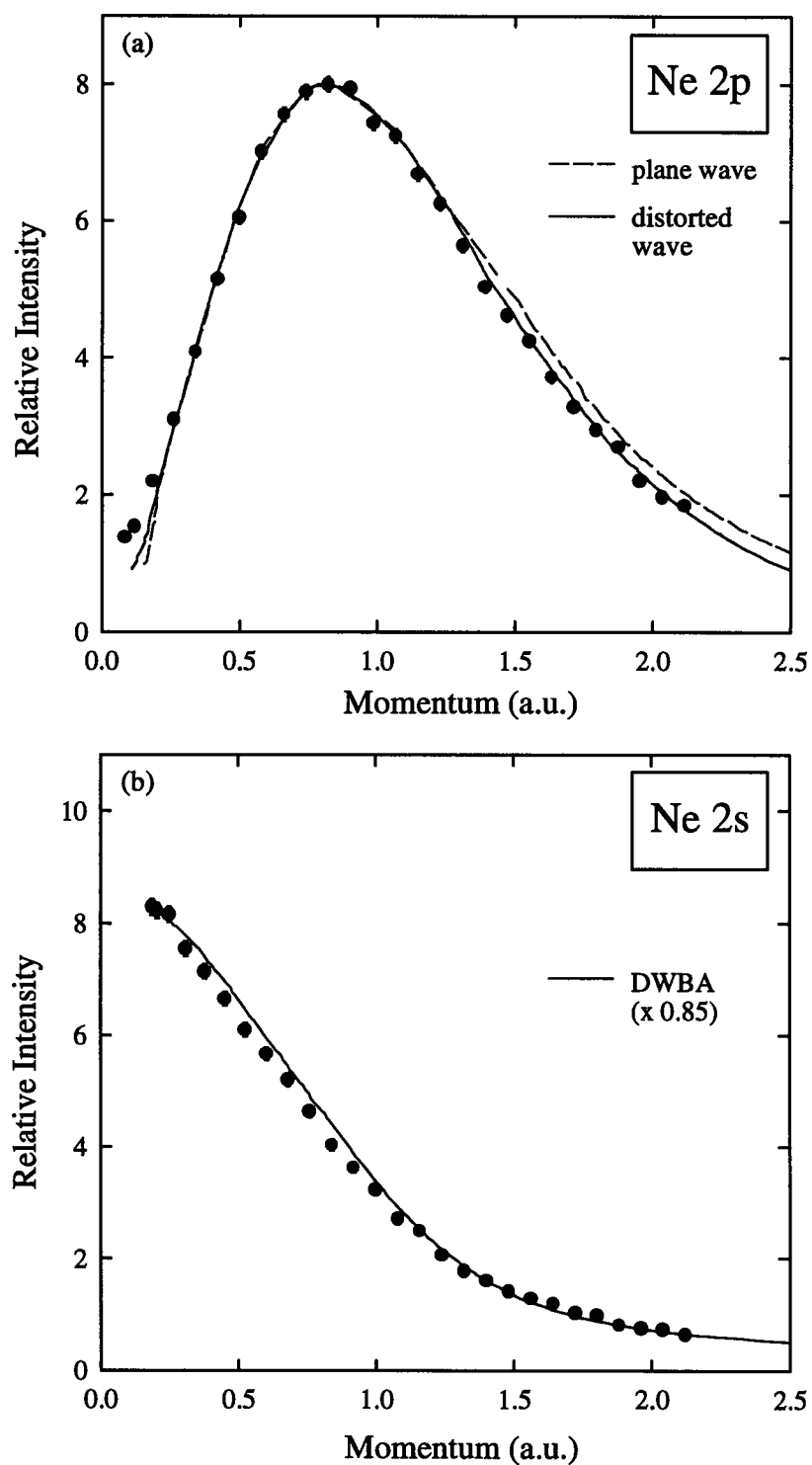


Figure 4.3: Experimental momentum profiles of the 2p and 2s electrons of neon. The solid and dashed lines are digitized theoretical profiles from Braidwood *et al.* [106]

The PWBA and DWBA cross sections presented in figure 4.3 were folded in the original study [105] using the angular resolution of the energy dispersive EMS spectrometer at the Flinders University of South Australia. The resolution is likely slightly different in the two instruments, and different folding parameters would influence the shapes of the theoretical profiles. However, because of their large breadth, the TMPs and XMPs of the Ne $2p$ and $2s$ electrons should be less sensitive to instrumental resolution effects than the narrower profiles of larger systems such as Kr and Xe, presented below.

4.2 Krypton

The angle integrated ($0 - \pm 26^\circ$) momentum dispersive EMS binding energy spectrum of krypton is presented in figure 4.4. The dashed curves shown in this figure are Gaussian functions centered on the more intense lines of the Kr PES spectrum reported by Svensson *et al.* [112]. The energy scale of the present BES was set relative to the Gaussian curve positioned on the $4s$ ionization potential. Experimental momentum profiles were obtained at the energies of the $4p$ and $4s$ binding energy peaks, and are presented in figure 4.5. The relative areas of the $4p$ and $4s$ XMPs have been normalized to the areas observed in the binding energy spectrum, in which all of the satellite intensity was assigned to the $4s$ manifold. Excellent agreement between the $4p$ XMP and the $4p$ TMP calculated using a near-Hartree-Fock limit wavefunction [81] is obtained below ~ 1.3 a.u.. The theoretical profile for the $4s$ electron, shown in figure 4.5b, has been scaled by 0.74 and is in good agreement with the shape of the XMP below ~ 0.8 a.u.. The requirement of a scale factor is not unexpected, as

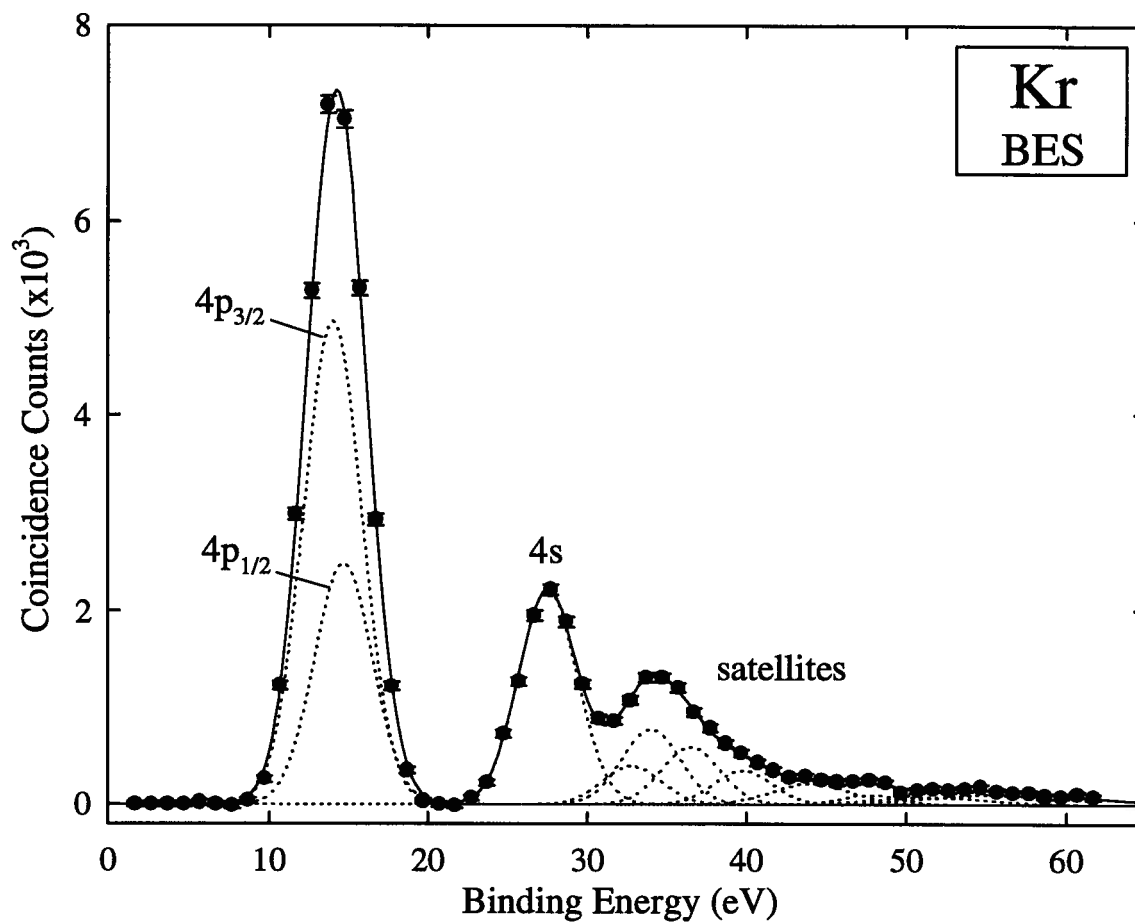


Figure 4.4: A binding energy spectrum of the valence region of krypton. Dashed lines are Gaussian functions centered on the energies of the (more intense) PES transitions reported by Svensson *et al.* [112].

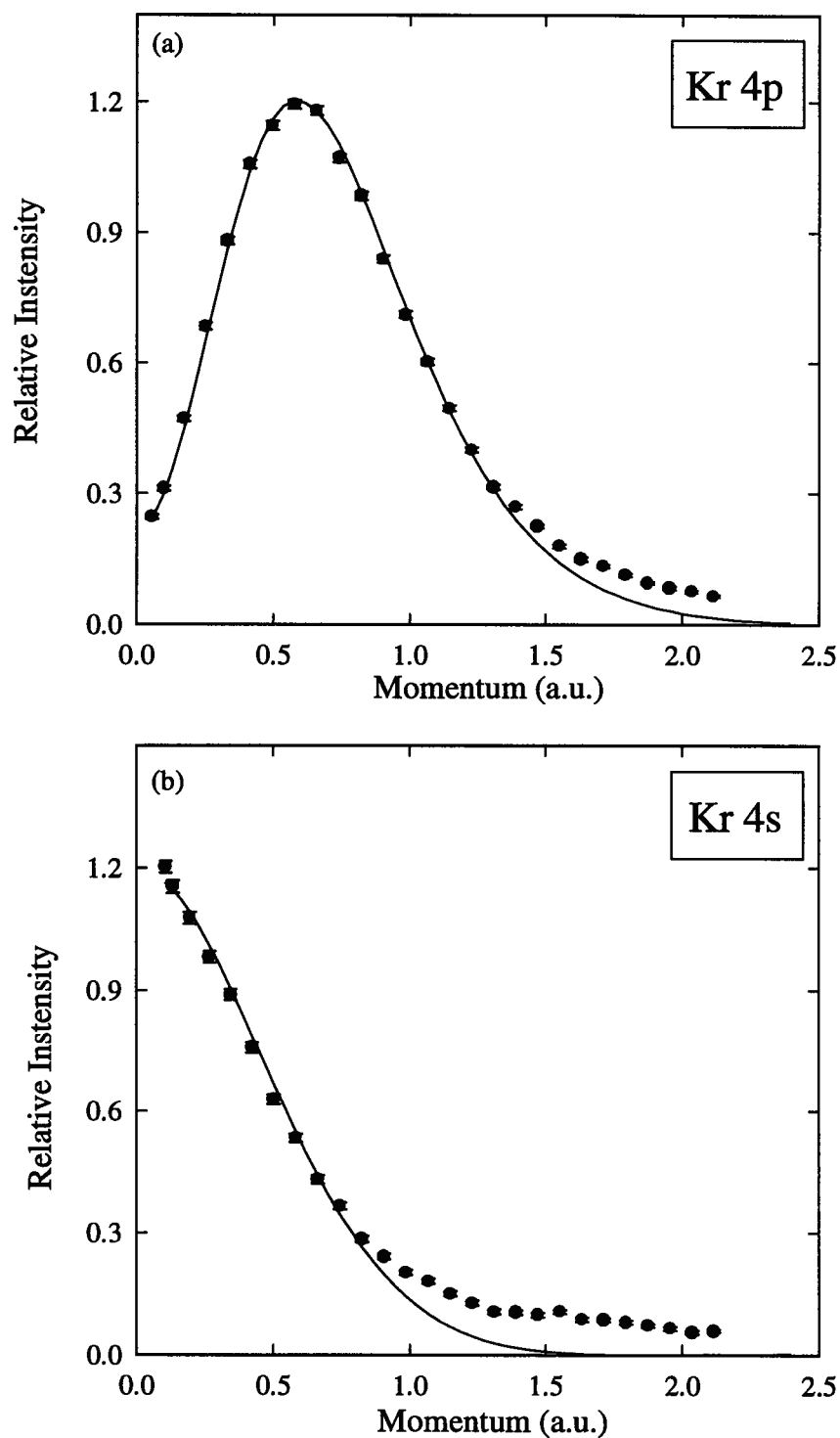


Figure 4.5: Experimental momentum profiles of the $4p$ and $4s$ electrons of krypton. Solid lines are theoretical profiles calculated using the near-Hartree-Fock limit SCF calculation of Clementi and Roetti [81]. The $4s$ TMP has been scaled by 0.74.

similar attenuation of the theoretical profiles obtained using the PWIA (or PWBA) were needed to fit the XMPs of the inner valence electrons of neon [106], argon [76], and xenon [106] measured at similar electron impact energies to that used in the present study. Distorted wave cross section calculations for the inner valence electrons of these systems exhibit reduced intensities relative to the PWIA calculation at low momentum, and are in much better agreement with the XMPs [76,106,107].

4.3 Xenon

The angle integrated ($0 - \pm 26^\circ$) binding energy spectrum of the valence region of xenon is presented in figure 4.6. The increase in the intensity of the satellite structure relative to Ne, Ar (fig. 3.31) and Kr is quite apparent, although the number of individual states in the Xe $5s$ manifold is impossible to determine, due to the relatively low energy resolution of the present measurements. A higher energy resolution EMS investigation of xenon has recently been reported by Braidwood *et al.* [111], and the transitions identified in this study were used in the analysis of the present binding energy spectrum. To calibrate the energy scale, the $5p$ peak was positioned to the summed intensity of two Gaussian functions, representing the $5p_{3/2}^{-1}$ and $5p_{1/2}^{-1}$ transitions, with positions and relative areas obtained from Braidwood *et al.* [111]. The Gaussian functions (dotted lines) at higher energies have fixed positions and relative areas as given by the earlier study [111]. The summed intensity of the Gaussians is represented by the solid line, and is in very good agreement with the present binding energy spectrum.

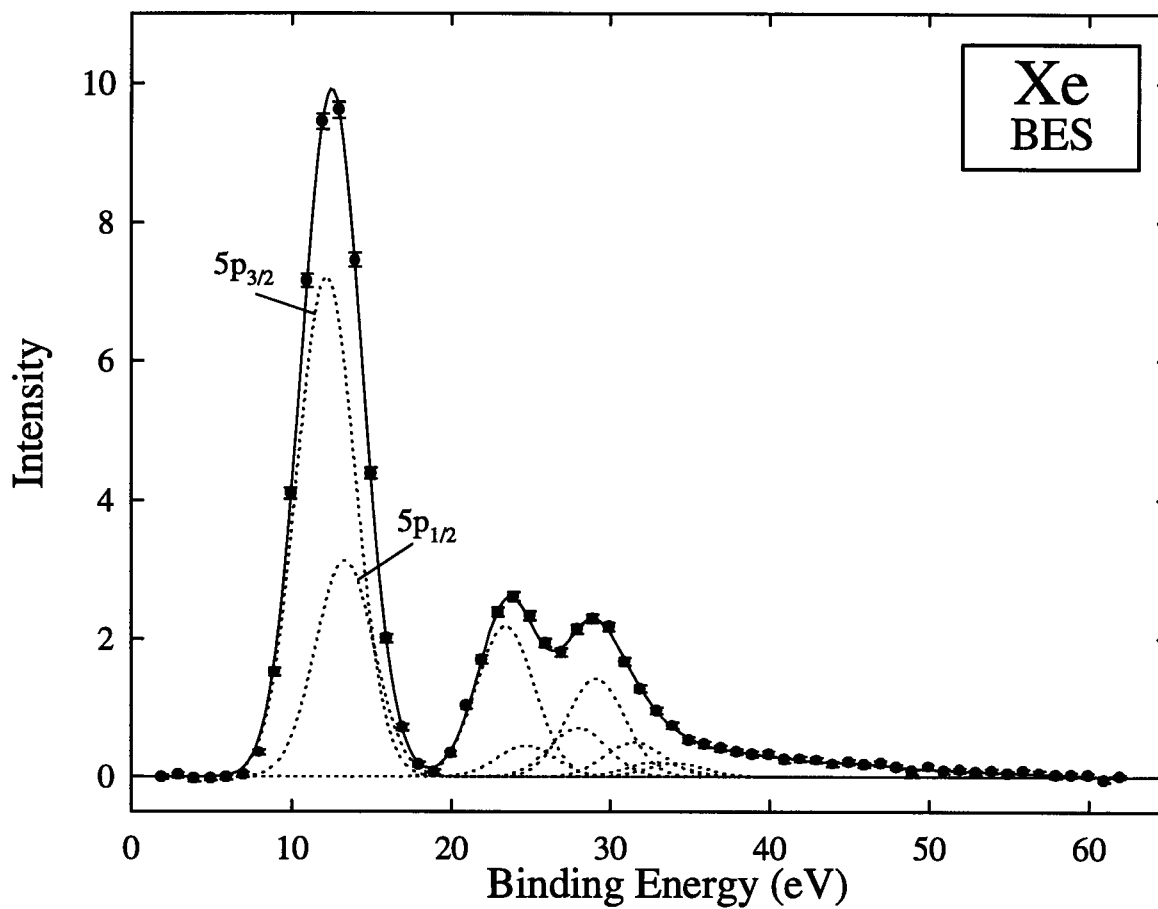


Figure 4.6: A momentum dispersive multichannel ($0 - \pm 26^\circ$) binding energy spectrum of the valence region of xenon. The dotted lines are Gaussian functions with energies and relative intensities determined from the EMS measurement reported by Braidwood *et al.* [111].

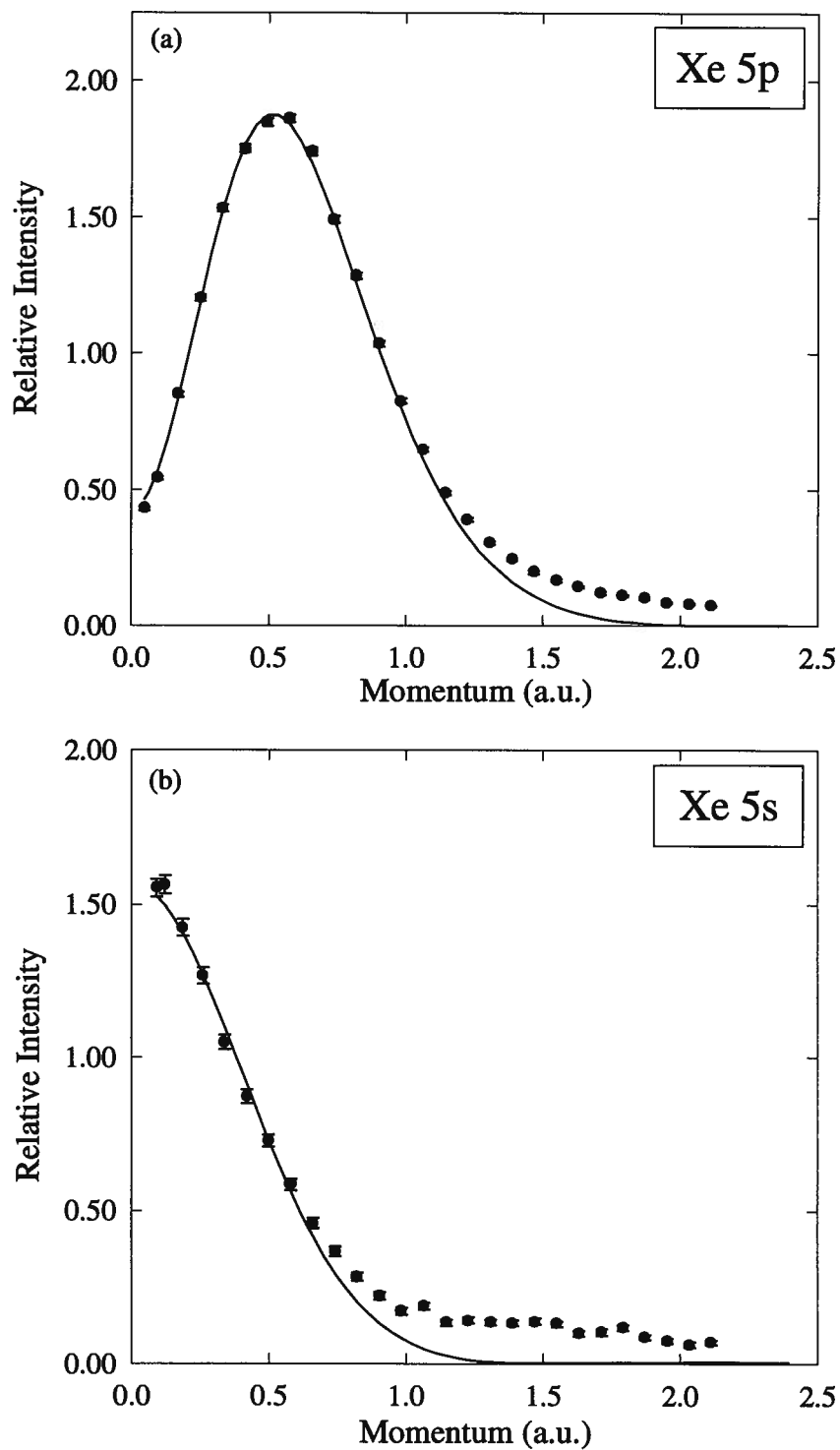


Figure 4.7: Experimental momentum profiles of the 5p and 5s electrons of xenon. The PWIA theoretical profiles were obtained using the near-Hartree-Fock limit SCF calculation of Clementi and Roetti [81]. The 5s TMP has been scaled by 0.62.

The area of the $5p$ BES peak and the summed area of the $5s$ main peak and satellite intensity are used in the relative normalization of the experimental momentum profiles shown in figure 4.7. The shape of the $5p$ XMP is very well described by the theoretical profile calculated in the PWIA, using the near-Hartree-Fock limit wavefunction of Clementi and Roetti [81]. The $5s$ TMP in figure 4.7b has been scaled by 0.62 and gives reasonable agreement to the low momentum region of the XMP. The $5s$ experimental profile exhibits a relatively large intensity at high momentum, indicating a considerable contribution from distorted wave effects. The EMS measurements of xenon by Cook *et al.* [107] and Braidwood *et al.* [111] display a similarly large plateau in the $5s$ XMP at higher momentum, which is in agreement with distorted wave calculations presented in these studies.

4.4 A Summary of the Noble Gas Measurements

Figure 4.8 presents a collection of the momentum dispersive multichannel measurements of the outer valence (np) momentum profiles of the noble gases. The azimuthal angular distributions ($0 - \pm 26^\circ$) are displayed in the left-hand column. The distributions are very symmetric about the central angle, providing further evidence of the uniform detection efficiency of the MCP/RAE detector, as well as the uniform transmission of electrons through the analyzer, over the measured range of azimuth. The experimental momentum profiles obtained from these angular distributions are shown in the right-hand column of figure 4.8. The XMP for the $3p$ electron of argon is compared to the TMP calculated from a MRSD-CI wavefunction having a basis set of 190 GTOs, recently provided by E.R. Davidson [113].

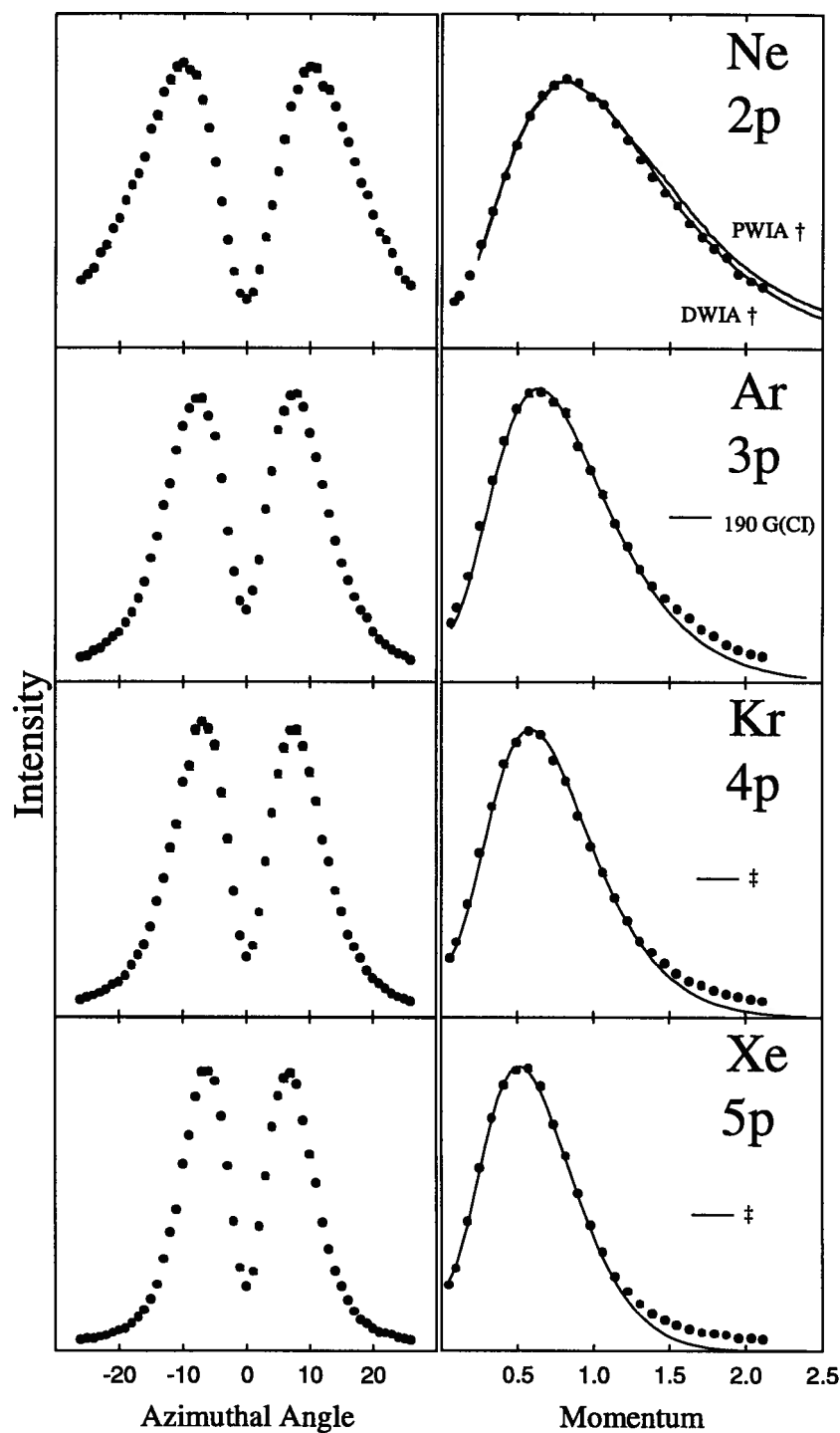


Figure 4.8: The angular distributions and experimental momentum profiles for the noble gases Ne-Xe. The Ne theoretical profiles (\dagger) are from Cook *et al.* [107]. The Ar 190-G(Cl) OVD calculation was provided by E.R. Davidson [113]. The Kr and Xe TMPs (\ddagger) were calculated using a Clementi and Roetti SCF wavefunction [81].

With the exception of neon (see above discussion), all of the TMPs shown in this figure have been folded using the GW-PG method [49] with angular resolution values of $\Delta\theta = \pm 0.7^\circ$ and $\Delta\phi = \pm 1.2^\circ$. Very good agreement between the theoretical and experimental profiles is shown, below 1 to 1.5 a.u.. Finally, it is interesting to note that the column of XMPs in figure 4.8 clearly exhibits the contraction in momentum space of the outermost orbital as the spatial extent of the orbital increases (i.e. with increasing principal quantum number). The reciprocal nature of the momentum and position space distributions is explored in detail by Leung and Brion [25].

4.5 Multichannel EMS of Methane and Silane

The noble gas measurements give a clear display of the ability of the new instrument to accurately measure XMPs for a range of target systems. However, the influence of distorted waves prevents the quantitative comparison of the inner valence experimental profiles to theoretical profiles calculated in the plane wave impulse approximation. A further investigation of the response of the new spectrometer to the measurement of XMPs, over the full valence binding energy region of a target system, was performed by the study of the molecular target systems methane and silane. Previous EMS investigations of these systems have shown the experimental momentum profiles for the outer and inner valence electrons to be well described by TMPs obtained from near-Hartree-Fock or CI wavefunctions, in the PWIA representation of the scattering cross section [32,38]. The multichannel ($0 - \pm 26^\circ$) binding energy spectrum of methane is presented in figure 4.9. Gaussian functions, having

widths estimated from the EMS measurements of Clark *et al.* [32] and a consideration of the different instrumental energy resolution of the earlier [32] and present studies, were fitted to the BES and are shown in figure 4.9. Calibration of the energy scale was performed by centering the $2a_1$ peak to the vertical ionization potential of 23.05 eV given by photoelectron spectroscopy [114,115]. In accord with previous work [32], the satellite intensity above the main $2a_1$ peak has been assigned to the $2a_1^{-1}$ process.

This assignment is reflected in the relative normalization of the $1t_2$ and $2a_1$ experimental momentum profiles, presented in figure 4.10. The (angular resolution folded) theoretical momentum profiles of both orbitals, calculated using 146-Gaussian basis function MRSD-CI (146-G(CI)) wavefunctions of the molecule and final ion [32], are also shown in this figure. The $1t_2$ XMP has been normalized to the height of the theoretical profile, and exhibits very good agreement with the shape this profile. In terms of both shape, as well as intensity, the theoretical profile of the $2a_1$ orbital corresponds very well with the $2a_1$ XMP. The excellent agreement between both the present and previous measurements with the 146-G(CI) theoretical profiles, confirms the quantitative accuracy of the new instrument.

The only previous EMS investigation of the valence region of silane has been reported by Clark *et al.* [38]. While a small, but significant, discrepancy was reported [38] between the XMP of the $2t_2$ orbital and the TMPs calculated from a 126-GTO SCF wavefunction and from 126-G(CI) neutral and ion wavefunctions, this has since been shown to be due to inadequate accounting for angular resolution effects in the original study [20]. The theoretical profiles of

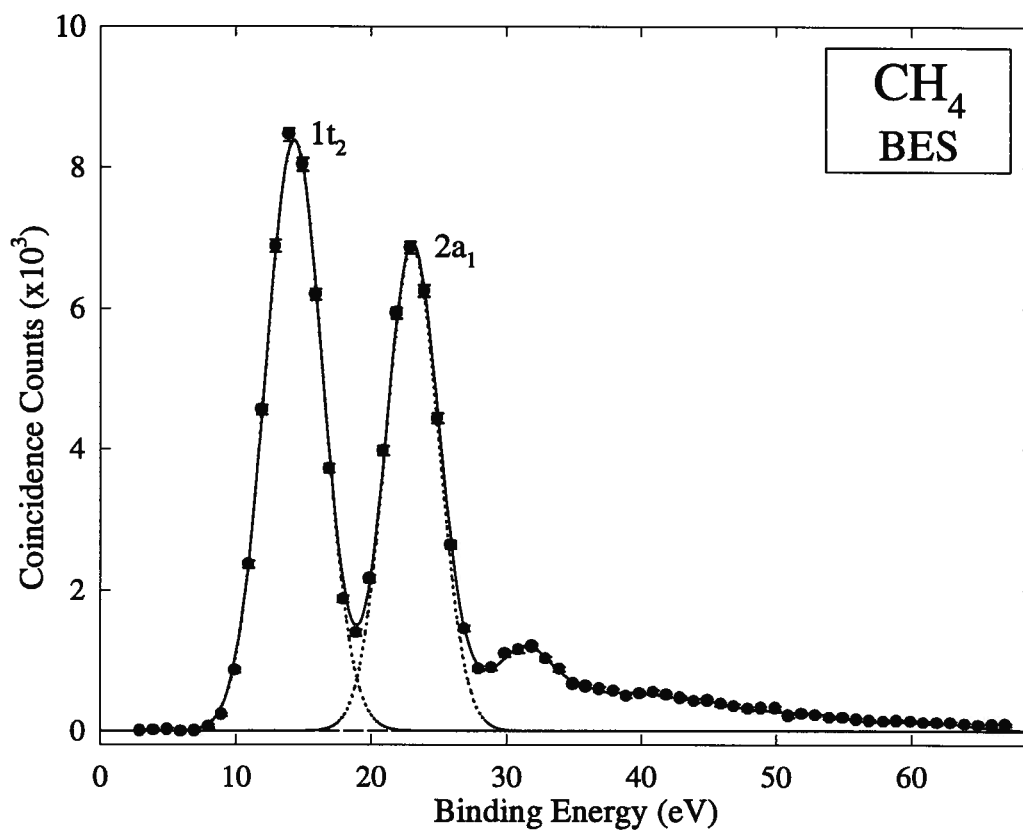


Figure 4.9: A multichannel ($0 - \pm 26^\circ$) binding energy spectrum over the valence region of methane. The peak of the $2a_1^{-1}$ transition has been set to the ionization potential of 23.05 eV [114,115] to calibrate the energy scale.

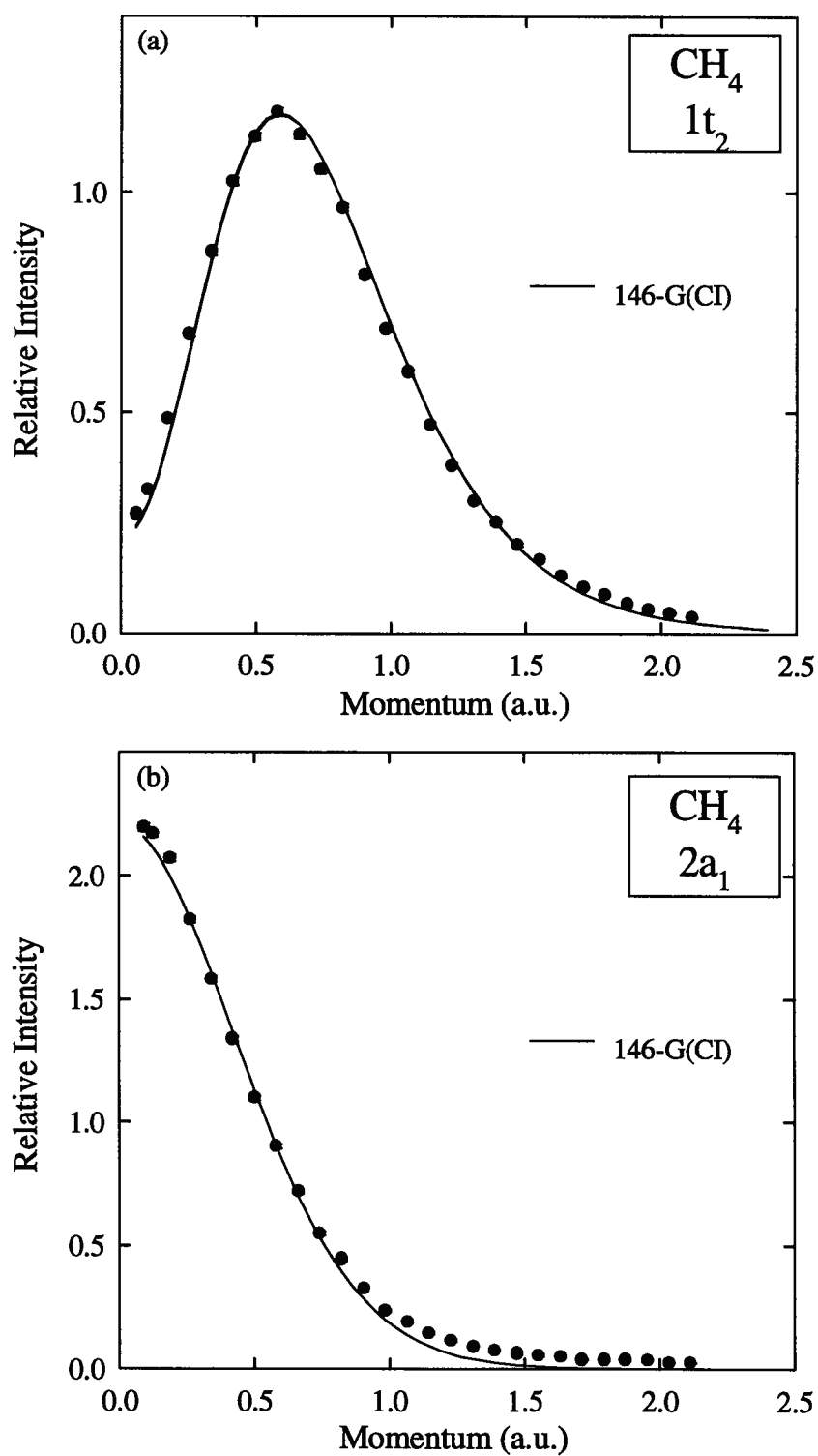


Figure 4.10: The multichannel momentum dispersive XMPs for the $1t_2$ and $2a_1$ electrons of methane. The solid lines are the TMPs calculated using a 146-G(CI) wavefunction [32].

the $3a_1$ orbital exhibited a very similar shape to the XMP, although the TMPs were generally $\sim 10\%$ greater in intensity[38]. The present measurement of the momentum dispersive multichannel binding energy spectrum of silane is displayed in figure 4.11. Using peak widths estimated from the BES measurements of Clark *et al.* [38], the main $2t_2$ and $3a_1$ peaks were fitted by appropriate Gaussian functions. In accord with the earlier study [38], all of the intensity in the inner valence region has been attributed to the $3a_1^{-1}$ transition, in the relative normalization of the XMPs.

The multichannel experimental momentum profiles for $2t_2$ and $3a_1$ electrons of silane are presented in figure 4.12. The $2t_2$ XMP has been height normalized to the 126-G(CI) TMP, and the agreement observed with the shape of the theoretical profile is reasonable. The XMP of the $3a_1$ electron also agrees well with the shape of the $3a_1$ TMP, although the experimental cross section has slightly greater intensity. The XMP intensity at higher momentum values suggests the existence of distorted wave effects. Some of the intensity variation, particularly at lower momentum, may be a result of the assignment of the BES satellite intensity to the $3a_1^{-1}$ transition. A Green's function (ADC(4)) calculation of the pole strengths (spectroscopic factors) in the silane BES reported by Clark *et al.*[38] suggests that some of the satellite intensity arises from the $2t_2^{-1}$ ionization process, with at least 2.4% of the intensity of the main $2t_2$ peak appearing at transition energies above 20 eV. This would influence the height of the $3a_1$ XMP, as the satellite intensity has been included in the relative normalization of the profile to the $2t_2$ XMP. Correcting the normalization for $2t_2$ satellites, using 2.4% of the main peak

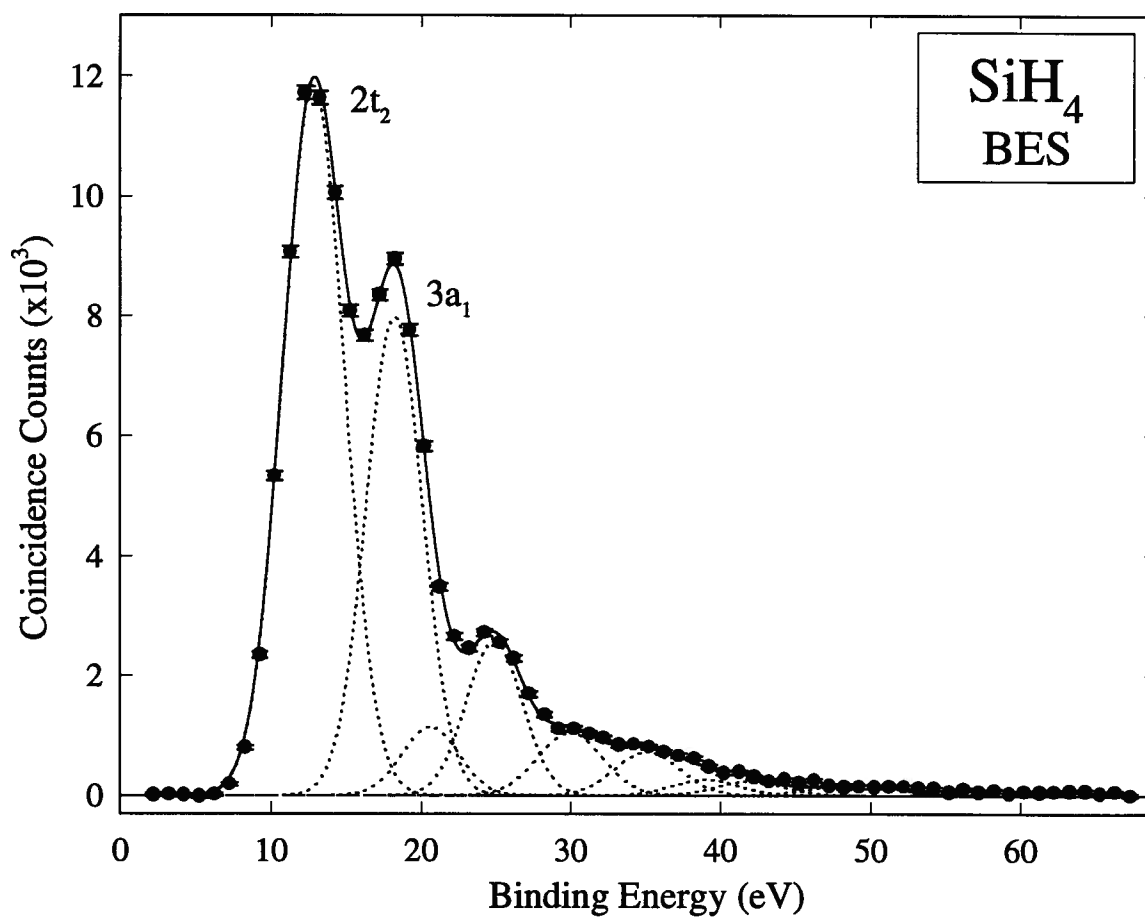


Figure 4.11: A binding energy spectrum of the valence region of silane. The widths of the Gaussian functions fit to the $2t_2$ and $3a_1$ peaks have been estimated from the higher energy resolution measurements of Clark *et al.* [38], and the energy scale of the present BES has been determined relative to the two Gaussian functions. Additional Gaussians are included to fit the satellite intensity.

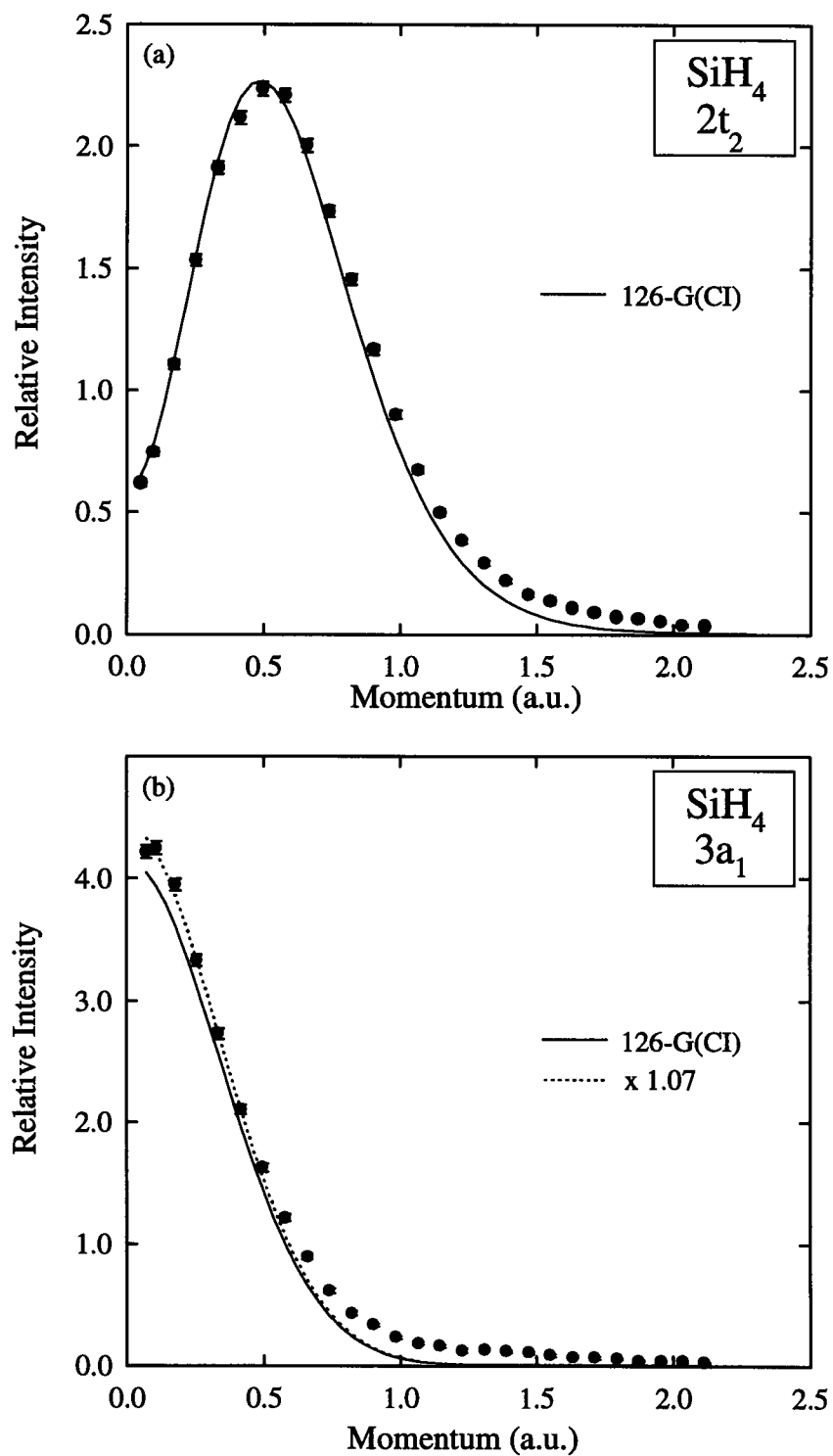


Figure 4.12: The experimental and theoretical momentum profiles for the $2t_2$ and $3a_1$ electron of silane. The solid lines are the theoretical momentum profiles obtained from a 126-G(CI) wavefunction [38]. The dashed line is the $3a_1$ TMP scaled by 1.07.

intensity, requires the $3a_1$ XMP to be scaled down by approximately 95.6%. Alternatively, the $3a_1$ theoretical profile may be scaled up by an additional 4.6%. The dashed line in figure 4.12b represents TMP of the $3a_1$ electron scaled by a slightly larger value of 7% and is in good agreement with the experimental cross section in the low momentum region. Hence, the present measurements offer support for the theoretical ADC(4) calculation, indicating a small but significant degree of splitting of the $2t_2$ main peak intensity.

4.6 Conclusions

The generally good agreement between the theoretical and experimental momentum profiles for Ne, Ar, Kr, Xe, as well as for CH_4 and SiH_4 , together with the good overall consistency with previous EMS measurements [32,38,76,105,105] lends confidence to the quantitative accuracy of the presently reported momentum dispersive multichannel EMS instrument. The agreement over the range of systems investigated also gives an indication of the reasonable characterization of the instrumental angular resolution effects.

Chapter Five

EMS of Two Electron Systems: Helium

5.1 Background

As the simplest many-electron atom, helium is a particularly favorable system for the experimental and theoretical investigation of electron correlation, or many-body, interactions. As early as 1929, Hylleraas [116] applied a formalism that explicitly included the interelectron coordinate r_{12} to obtain a very accurate correlated wavefunction for the ground state of helium. This formalism is not easily extended to larger systems however, and since this pioneering work much attention has focused on alternative methods of accounting for electron correlation to permit an accurate description of the system (see chapter two). Early in the development of the EMS technique, it was shown [5,24] that the (e,2e) scattering cross section for the ionization of helium from the ground state atom to the ground state ion was already well described by a theoretical profile calculated using a near-Hartree-Fock limit wavefunction, and subsequent studies [26,70] indicated that the inclusion of electron correlation in the description of the helium wavefunction had little effect on the theoretical EMS profile. In contrast, the theoretical estimate of the cross section for the (e,2e) transition to the $n=2$ excited final ion state of helium was shown to be much more sensitive to the effects of electron correlation in the target wavefunction [117,118], indicating the possibility for

experimental measurement of these transitions to provide insight into the wavefunction of the neutral helium atom and the influence of initial state electron correlation.

In the plane wave impulse approximation (PWIA), the EMS cross section is proportional to the momentum-space overlap of the neutral target and final ion wavefunctions (eqn. 2.6). As the wavefunction for the helium ion may be obtained exactly, the EMS cross section provides a direct probe of the ground state atomic wavefunction. In the configuration interaction formalism, the ground state wavefunction for helium is dominated by the Hartree-Fock configuration consisting of two electrons in a $1s$ orbital, with smaller contributions to the wavefunction given by singly and doubly excited configurations (see for example refs. [119,120]). Since the theoretical momentum profile corresponding to the $(e,2e)$ ionizing transition to the ground state ion is dominated by the overlap of the $1s$ ion wavefunction with the primary Hartree-Fock configuration of the neutral atomic wavefunction, it is not very sensitive to initial state correlation. However, if the $(e,2e)$ collision leaves the final ion in an $n=2$ or higher excited state, the overlap of the final ion wavefunction with the excited configurations of the target atom wavefunction contribute significantly to the EMS cross section. For such transitions to excited ion states, both the shape and magnitude of the EMS cross sections are sensitive to the effects of initial state correlation.

The accurate measurement of the experimental momentum profiles for the transitions to the excited ion states is hampered by their relatively low cross sections. The investigation of the $(e,2e)$ ionization to the ground and degenerate $2s$ and $2p$ excited ion states were

investigated first in the symmetric coplanar geometry by McCarthy *et al.* [117], and subsequently in the symmetric non-coplanar geometry by Dixon *et al.* [118]. As these experimental studies predated the development of multichannel EMS techniques, single channel instruments were employed and the (e,2e) cross sections were measured at a few (polar [117], and azimuthal [118]) angles with poor statistical precision. Nevertheless, these studies clearly indicated that the EMS cross section for the transition to the $n=2$ excited ion state calculated using an SCF description of the helium atom gave an extremely poor description of the experimental results, while significantly improved agreement was given by a TMP calculated with the correlated wavefunction of Joachain and Vanderpoorten (JV) [121].

Using an energy dispersive multichannel instrument, improved measurements were obtained by Cook *et al.* [26], and their results are reproduced along with the reported theoretical profiles in figure 5.1. The XMP for the transition to the $n=1$ ion state (fig 5.1a) is in very good agreement with the (digitized) theoretical profile calculated using the JV correlated wavefunction, which, as expected, is very similar to the TMP obtained using a near-Hartree-Fock limit wavefunction [26]. The wavefunction sensitivity of the cross section for the (e,2e) transition to the $n=2$ ion state is evident in figure 5.1b. The $n=2$ theoretical profile obtained using a near Hartree-Fock limit wavefunction has the same shape as the TMP for the transition to the $n=1$ final ion state, while the profile obtained with the correlated JV wavefunction, exhibits a much different cross section in both magnitude and shape. The experimental measurement of the $n=2$ cross section is clearly in much better agreement with

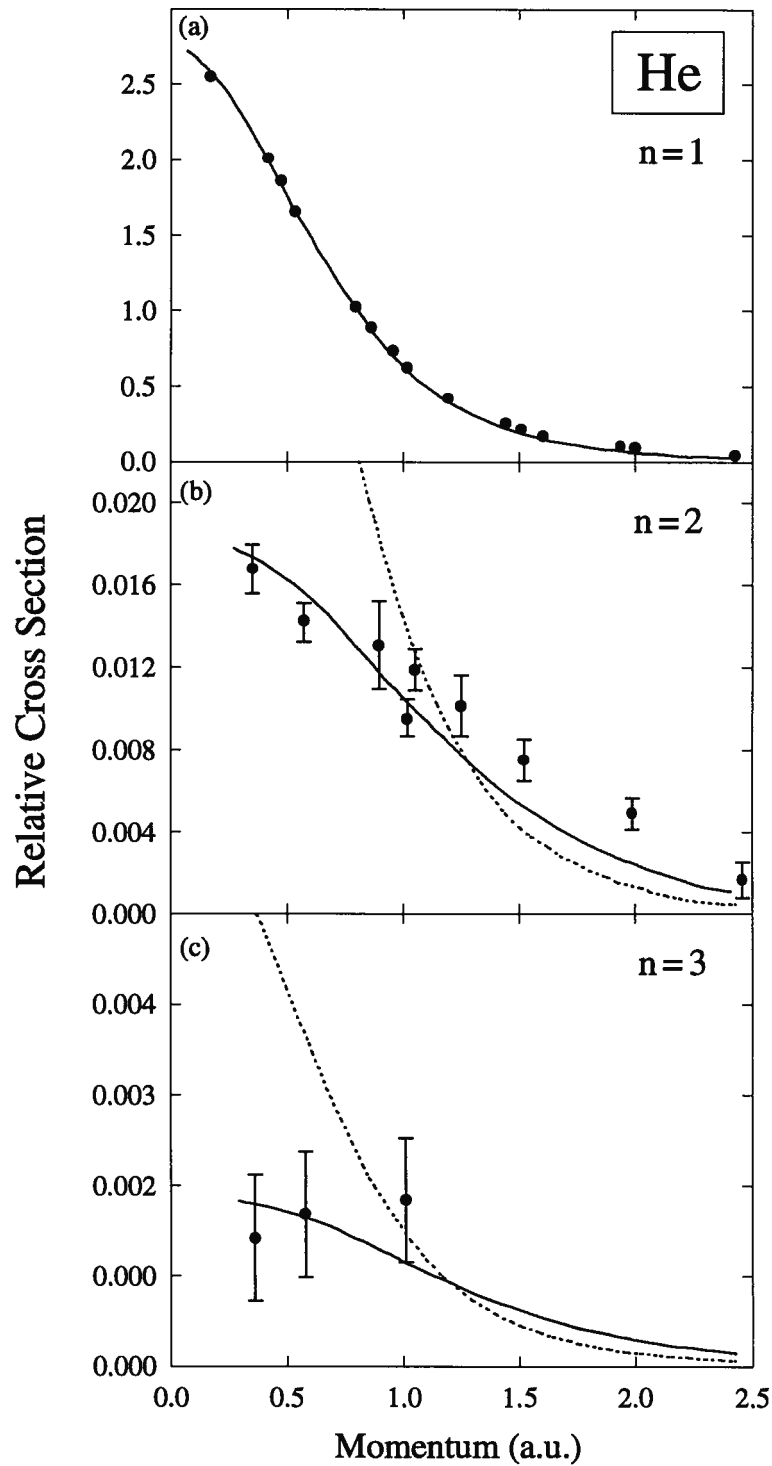


Figure 5.1: The EMS cross section for the ionization of helium to the $n=1$, $n=2$, $n=3$ final ion states. The experimental data (solid points) and theoretical profiles have been digitized from Cook *et al.* [26]. The dashed profile was calculated using an SCF wavefunction while the solid profile used the correlated wavefunction of Joachain and Vanderpoorten [121].

the JV profile than with the profile calculated from the SCF wavefunction. However, the agreement between the JV profile and the XMP is reasonable, particularly in the region below 1 a.u.. In figure 5.1c the TMPs for the transition to the $n=3$ final ion state, calculated with a correlated wavefunction [121] and a near Hartree-Fock limit wavefunction, are presented. Also shown on figure 5.1c are three experimental points, representing the EMS cross section measured by Cook *et al.* [26] at three relative azimuthal angles. These are the only experimental values for the EMS transition to the $n=3$ ion state reported prior to the present work, and the size of the error bars gives an indication of the difficulty of measurement. Nevertheless, the data points strongly suggest the importance of electron correlation effects in the transition to the $n=3$ state of He^+ .

Two additional experimental measurements of the EMS cross section for the ground and excited final ion transitions of helium have been reported since the earlier work. Using a momentum dispersive multichannel spectrometer (see chapter one or ref. [53]), Smith *et al.* [30] investigated the $n=1$ and $n=2$ helium cross sections¹. Unfortunately, both the $n=1$ and $n=2$ experimental cross sections reported by Smith *et al.* [30] were independently normalized to theoretical profiles, preventing direct comparison of the magnitude of the $n=2$ XMP to theory or to other experimental measurements. A much more stringent investigation of the $n=2$ theoretical cross section is permitted if the relative normalization of the $n=1$ and $n=2$ experimental profiles is maintained. One point emphasized by Smith *et al.* [30] is the

¹ For convenience, the cross section for the $(e,2e)$ transition of helium to the $n=1$ (2,3) final ion state is referred to throughout this chapter as the $n=1(2,3)$ cross section.

difference in distortion potentials for the $n=1$ and $n=2$ helium ion states, which influences the outgoing electrons and gives rise to an increase in distorted wave effects in the $n=2$ experimental cross section relative to the $n=1$ cross section. Distorted wave effects were shown to influence the shapes of the $n=1$ and $n=2$ cross sections, particularly in the momentum region above ~ 1.5 a.u. and ~ 1.0 a.u. respectively [30]. However, an additional study of distorted waves effects in the EMS investigation of helium reported by McCarthy and Mitroy [122] indicated only a small influence on the cross sections of both the $n=1$ and $n=2$ transitions at higher momentum.

More recently, an asymmetric scattering geometry was employed by Lahmam-Bennani *et al.* in an (e,2e) study of helium [31]. Asymmetric (e,2e) measurements offer some increase in (e,2e) cross section, and involve coincidence detection of a fast (~ 5 -10 keV) electron scattered into a small polar angle with respect to the incident beam direction, and a slower electron detected over a range of polar angles. For sufficiently high energy of the 'slow' outgoing electron it was earlier shown [74] that (e,2e) Bethe-ridge measurements in this geometry permit a PWIA evaluation of the experimental momentum profile, as in the more conventional measurements using the symmetric non-coplanar geometry. Additionally, using 'slow' outgoing energies of 405 and 598 eV, experimental measurements in the asymmetric geometry have been shown by Lahmam-Bennani *et al.* [74] to be less influenced by distorted wave effects than XMPs measured with typical symmetric non-coplanar scattering kinematics. In the 1992 asymmetric (e,2e) study of helium [31], coincidence events were detected between fast electrons having energies of ~ 5500 eV, scattered into a polar angle of $\sim 6.61^\circ$, and 'slow'

electrons having (reasonably low) energies of ~ 75 eV. Following a format used by Dixon *et al.* [118], and Cook *et al.* [26], these asymmetric scattering measurements [31] were presented as the ratio of the cross sections for the $n=2$ and $n=1$ transitions. This experimental ratio, along with that given by the data of Cook *et al.* (figure 5.1a and 5.1b) is reproduced in figure 5.2. Also shown in this figure are the cross section ratios presented by Lahmam-Bennani *et al.* [31], obtained from theoretical profiles calculated using an SCF wavefunction, and the four different CI wavefunctions of Tweed and Langlois (TL) [123], Taylor and Parr (TP) [119], Joachain and Vanderpoorten (JV) [121], and Nesbet and Watson (NW) [119]. The percentage of the total correlation energy accounted for in each calculation, are shown in brackets in figure 5.2. Although all of the wavefunctions recover a large fraction of the correlation energy, a significant variation in the theoretical $n=2/n=1$ cross section ratios is present. With the exception of a single point at ~ 1.5 a.u., the data points of Lahmam-Bennani *et al.* [31] (solid circles in figure 5.2) are consistently lower than those of Cook *et al.* [26] (open circles), and are in better agreement with the theoretical ratios calculated using the lower energy JV and NW wavefunctions. Lahmam-Bennani *et al.* [31] have suggested that their asymmetric measurements are less influenced by distorted wave effects than the measurements of Cook *et al.* [26], giving rise to the lower experimental cross section ratio, particularly in the higher momentum region. Lahmam-Bennani *et al.* [31] also noted that while the TL theoretical cross section ratio is significantly higher than their data points at larger momenta, the TL ratio gives an improved agreement over the JV and NW ratios to the experimental data in the low momentum region (although the JV ratio appears to give quite

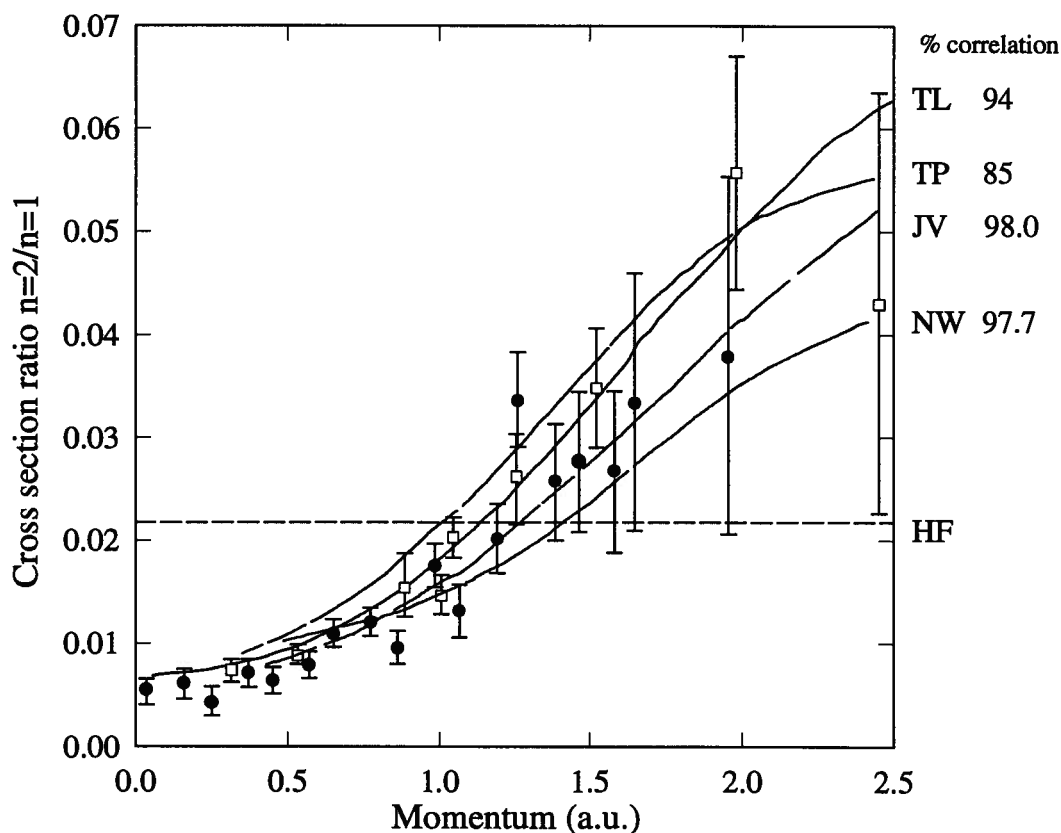


Figure 5.2: The theoretical and experimental helium $n=2$ to $n=1$ cross section ratios, digitized from ref. [31]. The solid points are the experimental measurements of Lahmam-Bennani *et al.* [74], and the open points represent the measurement of Cook *et al.* [26]. The helium wavefunctions used in the evaluation of the theoretical profiles are identified on the right axis with the percentage of the correlation energy recovered by each wavefunction calculation. The wavefunctions are: TL [123], TP [119], JV [121], NW [120].

good agreement to 0.5 a.u.). A more detailed evaluation of the theoretical cross section ratios is limited by the statistical precision of the experimental measurements of both Cook *et al.* [26] and Lahmam-Bennani *et al.* [31].

5.2 A Momentum Dispersive Multichannel EMS Investigation of Helium

It is evident that the unambiguous assessment of the theoretical profiles calculated with the various correlated wavefunctions requires a marked improvement in the measurement of the experimental profiles for the transitions to the $n=2$ and $n=3$ ion states. Data of higher statistical precision and accuracy are clearly needed. In this regard, it was noted by McCarthy and Mitroy [122] that “further refinements to the (DWIA) calculation would be justified only if more-accurate experimental data are available”. The enhanced collection efficiency of the presently reported multichannel EMS spectrometer should provide an opportunity to measure the helium $n=1$, 2, and 3 cross sections with significantly improved statistical precision and accuracy, as well as with more data points, since all 53 azimuthal angles are sampled simultaneously. At the outset of the study of helium, it was anticipated that the previous experimental investigations, particularly that of Cook *et al.* [26], would provide a solid foundation to aid in the interpretation of the present measurements. However, as will be discussed below, the present measurements exhibit some significant differences from the previously reported experimental cross sections and also from the theoretical predictions.

5.2.1 Theoretical Momentum Profiles

Despite the high quality of the correlated wavefunctions used in the calculation of the previously reported theoretical cross sections for the (e,2e) transition to the $n=2$ state of the helium ion [26,28,29,31], the various theoretical profiles have shown a significant variation in both shape and intensity. In an effort to identify a degree of convergence in the theoretical profiles, the $n=1$ and $n=2$ TMPs calculated with more accurate correlated wavefunctions have been obtained in the present work (see below). The theoretical momentum profiles for the (e,2e) ionization to the $n=1$ and $n=2$ final ion states were first recalculated using the helium wavefunction of Nesbet and Watson (NW) [120] to provide a quantitative reference to earlier studies [29,31]. The CI wavefunction consists of 20 Slater determinants and yields an energy of -2.90276 a.u., corresponding to 97.7 % of the correlation energy. As the $2s$ and $2p$ helium ion wavefunctions are (essentially) degenerate, the calculation of the $n=2$ TMP includes the overlap of the NW wavefunction with both the $2s$ and the $2p$ helium ion wavefunctions. Theoretical momentum profiles were also calculated in the present work using the CI wavefunction of Weiss (W) [124]. This wavefunction consists of 35 Slater determinants and gives an energy of -2.90320 a.u., corresponding to 98.75% of the correlation energy.

All of the theoretical momentum profiles for the helium transitions reported to date have been based on SCF or CI wavefunctions. It is well known, however, that even more accurate wavefunctions for the ground state of helium can and have been determined by alternative approaches. Therefore, in the present work, two profiles based on very high quality correlated

wavefunctions have been obtained. First, the theoretical profile based on the explicitly correlated wavefunction of Cann and Thakkar (CT) [125] was calculated by N.M. Cann, a post-doctoral fellow in the research group of C.E. Brion. The 200-term wavefunction gives an energy of -2.903724376 a.u., which is less than 10 nHartree from the estimated limit for the exact nonrelativistic energy of the helium atom [126], and hence accounts for greater than 99.9999% of the correlation energy. Additionally, a theoretical profile obtained from an atomic natural orbital expansion of a 141-term Kinoshita-type wavefunction [127,128], was provided by S. Chakravorty and E.R. Davidson (CD) of the University of Indiana [129]. The original Kinoshita type wavefunction yielded an energy of -2.9037243667 a.u., similar to the CT wavefunction, and also accounting for greater than 99.9999% of the correlation energy.

The four theoretical momentum profiles (NW, W, CT, CD) calculated in the present work for the transition to the $n=1$, and $n=2$ ion states, and convoluted with the instrumental resolution (see chapter 4), are shown in figure 5.3. Additionally, the (resolution folded) theoretical profiles for the transition to the $n=3$ final ion state, calculated with the CT and CD wavefunctions, are shown in figure 5.3c. As expected, the $n=1$ profiles are very similar to one another, with the CT and CD profiles slightly more intense than the profiles labeled W and NW. The momentum profiles for the transition to the first excited ion state are shown in figure 5.3b. It should be noted that each of the profiles includes a factor of 0.92 to account for the variation of the kinematic terms of the EMS cross section [28] at the different impact energies of the $n=1$ (1224.6 eV) and $n=2$ (1265.4 eV) transitions. This factor primarily reflects

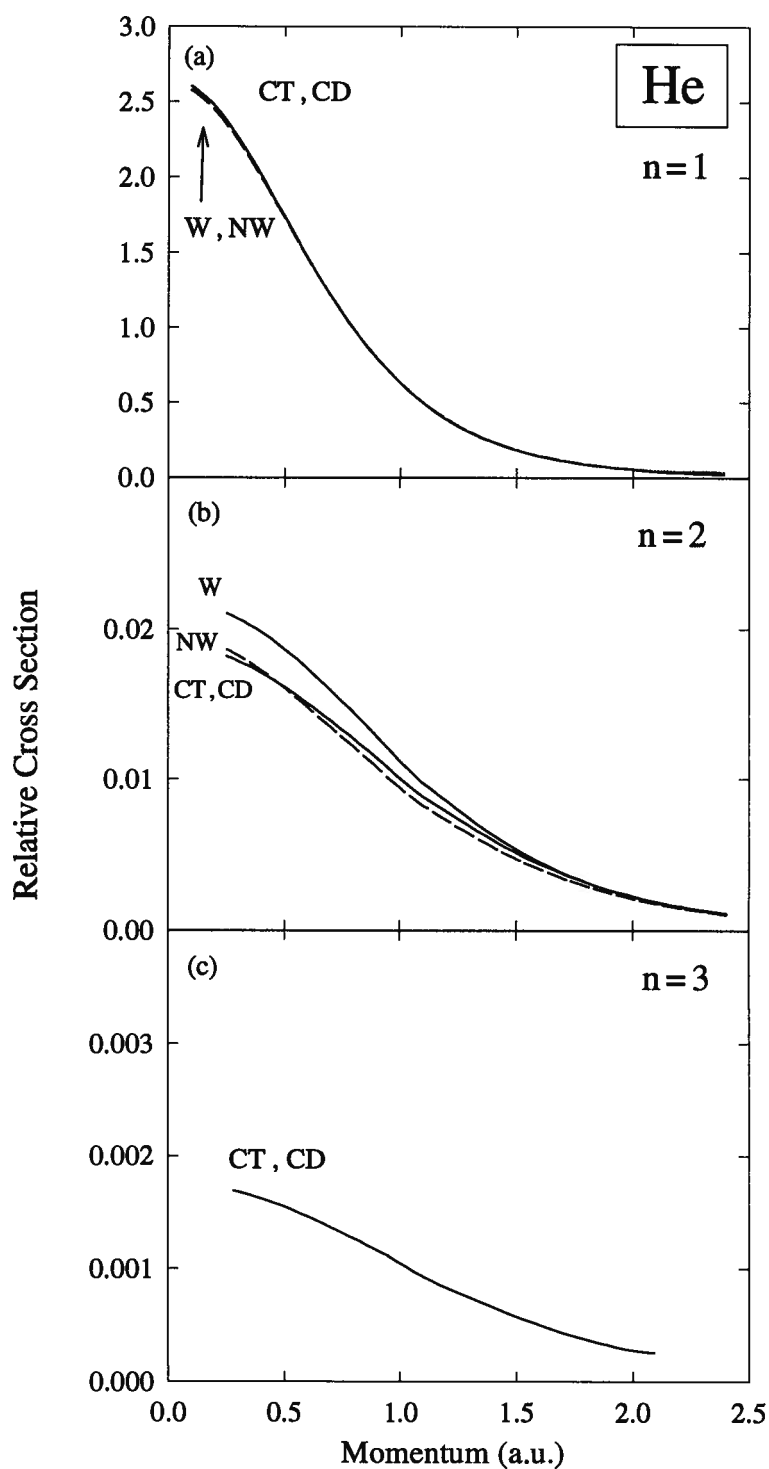


Figure 5.3: Theoretical momentum profiles for the ionization of helium to the $n=1$, $n=2$, and $n=3$ final ion states. The cross sections have been obtained from the correlated wavefunctions of Weiss (W) [124], Nesbet and Watson (NW) [120], Cann and Thakkar (CT) [125], and Chakravorty and Davidson (CD) [129].

the change in the Mott scattering cross section at the higher impact energies (see figure 2.1). While the W and NW theoretical profiles, based on CI wavefunctions, continue to exhibit some variation, the CT and CD profiles, each based on extremely accurate helium wavefunctions, are essentially in exact agreement with each other, indicating that the variation in profiles has converged at this level of theory. These two profiles (CT,CD) therefore provide an excellent reference to assess the experimental measurements. The CT and CD profiles for the transitions to the $n=3$ state, shown in figure 5.3c, are also in excellent agreement. Due to the change in the kinematic factors in the cross section for the $n=1$ (1224.6 eV) and $n=3$ (1273.0 eV) transitions, the $n=3$ profiles have been scaled by a factor of 0.91.

5.2.2 Multichannel Binding Energy Spectra and Momentum Distributions

An angle integrated ($0 - \pm 26^\circ$) binding energy spectrum of helium, exhibiting a large peak corresponding to (e,2e) ionization to the $n=1$ final state, and a very small peak for ionization to the $n=2$ final state, is shown in figure 5.4a. The $n=2$ region is expanded in figure 5.4b. An initially unanticipated feature exhibited in the spectrum is the additional intensity between the helium $n=1$ and $n=2$ peaks. Careful investigation has shown that the extra intensity originates from multiple scattering effects. These effects, which involve the interaction of an incident electron with two helium atoms in separate, sequential scattering

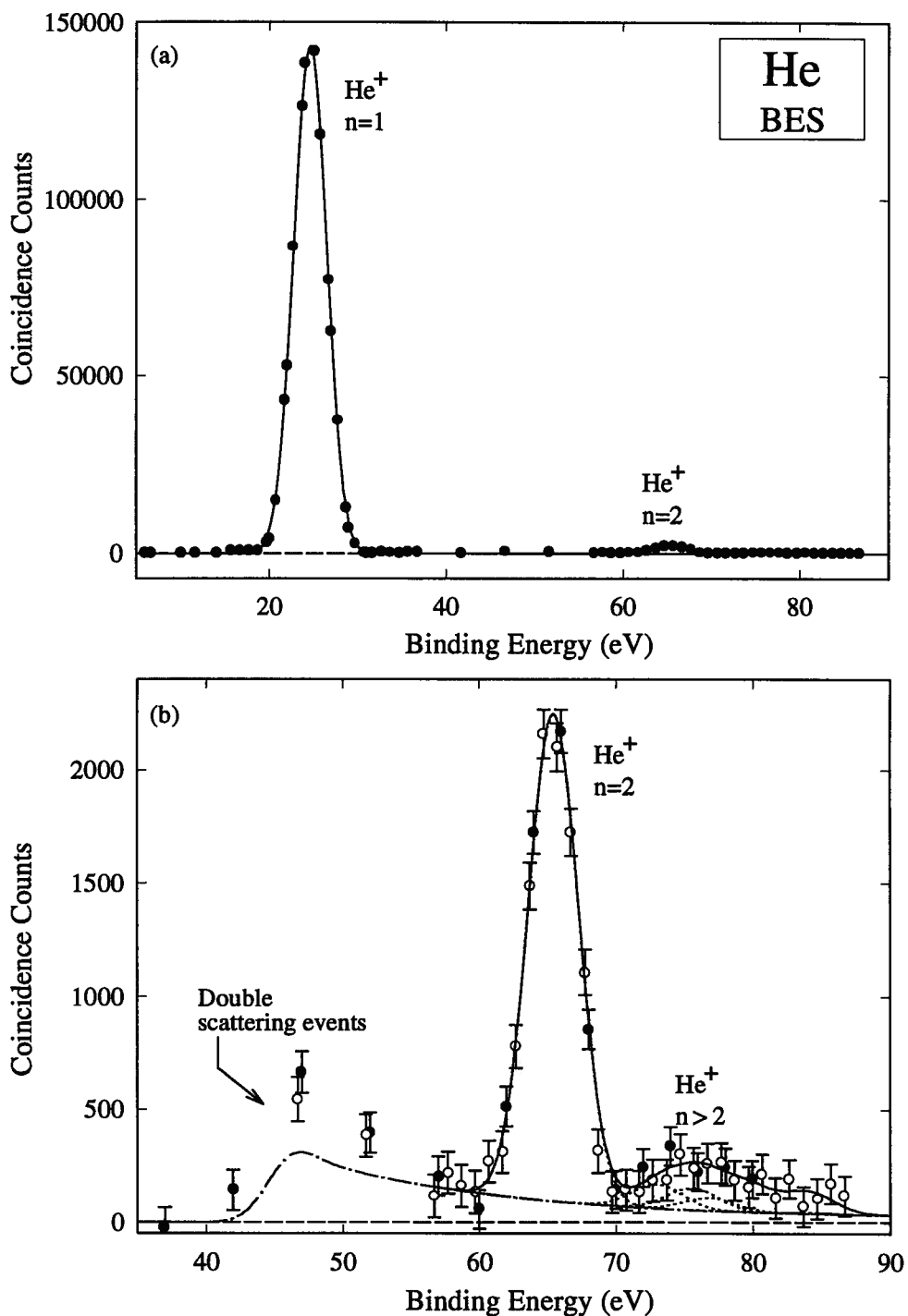
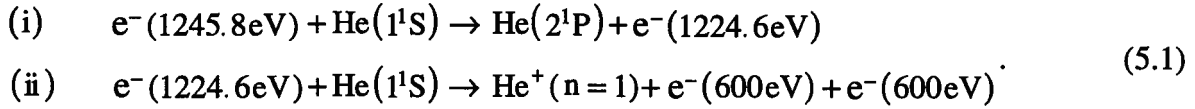


Figure 5.4: (a) An angle integrated ($0 \pm 26^\circ$) binding energy spectrum of helium. (b) An expanded view of about the $n=2$ helium ion peak, exhibiting extra intensity from double scattering effects. The solid and open circles represent two separate measurements performed under similar conditions. The two data sets are normalized on the $n=1$ peak.

events along the incident electron beam direction, can be summarized as follows for the most likely double collision process:



The first interaction (eqn. 5.1i) is essentially a dipole (e,e) scattering event [130,131] which is characterized by a low momentum transfer, forward scattering, collision along the incident beam path prior to the coincidence interaction region. The excitation of helium from the ground state to the 2^1P state is commensurate with an energy loss of an incident electron of 21.2 eV (see for example refs.[125,132]). With the cathode potential set to yield an incident electron beam with a mean energy of 1245.8 eV, this energy loss process would give rise to electrons with an energy of ~1224.6 eV in the ongoing incident electron beam. At this reduced kinetic energy, the incident electrons may undergo an (e,2e) collision, ionizing a helium atom (to the $n=1$ final ion state) in the coincidence interaction region (eqn. 5.1ii), to give a detected ‘true’ coincidence event. In this manner, intensity corresponding to the (e,2e) ionization of helium ($n=1$) may be observed at (and at all energies above) an apparent binding energy of 45.8 eV (with a spread due to the ~4.5 eV FWHM energy resolution). Of course, the (e,e) excitation of helium represented in 5.1i, may also occur from the ground state to any of the higher helium $n^1\text{P}$ states, as well as to the ionization continuum [132]. Intensity from such double scattering processes may therefore be observed at any setting of the cathode potential above approximately 1245 eV, corresponding to a binding energy of 45 eV (in

actuality above $\sim 40\text{eV}$ due to the energy resolution of $\sim 4.5\text{ eV FWHM}$). Since the (e,e) cross section producing $\text{He}(n^1\text{P})$ is much larger than the $(e,2e)$ cross section producing $\text{He}^+ (n=1)$, the $(e,2e)$ signal resulting from electrons formed in such double collision processes can become significant compared with that for the, even lower cross section, $(e,2e)$ production of the $\text{He}^+ n=2$, and 3 excited ion states, as can be seen in figure 5.4b.

The nature of the additional, unexpected intensity in the BES of figure 5.4b , and the above hypothesis, were investigated by measuring the helium BES at a reduced sample gas pressure. The EMS scattering count rate (eqn. 2.10) is directly proportional to the number density of target atoms, while the double scattering count rate should to be proportional to the square of the target density. Hence, intensity from the double scattering processes would be expected to decrease relative to the intensity of the $n=1$ and $n=2$ peaks, at the reduced pressure. Indeed, such a reduced intensity was observed (see for example, figure 5.5b) at the lower gas pressure, providing strong support for the proposed double scattering mechanism.

Of particular concern for the present investigation of the helium XMPs, is the possibility of a significant contribution from the double collision processes underlying the intensity of the $\text{He}^+ n=2$ transition at 65.4 eV . To evaluate this contribution, the variation of the intensity from the double collision processes with electron impact energy (E_0) was estimated from the highly accurate helium optical oscillator strength measurements obtained from low-momentum transfer, electron impact (dipole (e,e)) spectroscopy by Chan *et al* [132]. The optical

oscillator strength is proportional to the differential (forward) electron scattering cross section by a factor which varies as $\sim E_0^{-3}$ [133]. The dash-dot curve presented in figure 5.4b is the complete excitation and ionization optical oscillator strength spectrum of Chan *et al.* (see figure 7 of ref. [132]), scaled by E_0^{-3} , convoluted with the present energy resolution, and shifted to the appropriate energy scale by adding the ionization potential of helium (24.59 eV) to give a threshold of ~ 41 eV. Normalized to the BES intensity at the left of the $n=2$ peak, the curve reproduces the general trend of the double collision peak; however, the intensity at ~ 47 eV is underestimated. This may reflect a breakdown in the assumption that the first scattering event does not significantly alter the direction of the incident electron. Small momentum transfer collisions involving (e,e) dipole forbidden energy loss transitions, may have contributed to intensity arising from the double scattering processes.

The contribution of the double collision processes is estimated from the optical oscillator strength (dash-dot) curve to be 4% of the maximum peak height of the $n=2$ transition. Experimental momentum profiles for the $n=1$ and $n=2$ transitions were measured by accumulating (e,2e) events at the maxima of the peaks in the BES. To correct for the small contribution of the double collision processes, a fraction of the $n=1$ XMP, totaling 4% of the summed intensity (0 to $\pm 26^\circ$) of the $n=2$ XMP, was removed from the $n=2$ experimental profile. The correction had a very small influence on the shape and intensity of the $n=2$ XMP.

To permit the relative intensities of the $n=1$, $n=2$ and $n=3$ EMS cross sections to be determined in the absence of, or at least with a reduced contribution from the double

scattering processes, the multichannel EMS spectrometer was slightly modified. As discussed in section 3.1.3, the collision chamber was altered to reduce the length of the gas cell in front of the (e,2e) collision region. In addition, a differential pumping enclosure, separating the CMA entrance and collision region from the rest of the analyzer and detector system, was removed to reduce the concentration of helium in the vicinity of the incident electron beam prior to the coincidence collision region. The binding energy spectrum of helium obtained following the modifications is shown in figures 5.5a and 5.5b. The solid circles in figure 5.5, represent the angle integrated ($0 - \pm 26^\circ$) intensity obtained at a sample gas pressure of 5.0×10^{-6} torr (measured with an ion gauge at the top of the vacuum chamber). Relative to the BES measurements obtained prior to the modifications (fig 5.4), the intensity arising from the double collision processes is significantly reduced. The triangular symbols in figure 5.5 represent measurements at a gas pressure of $\sim 2.1 \times 10^{-6}$ torr, with the areas of the $n=1$ peak normalized to the higher pressure data (fig. 5.5a). These low pressure measurements exhibit a further significant reduction in the contribution from the double scattering processes. Importantly, the shape and area of the peak of the $n=2$ transition does not exhibit any detectable pressure dependence, indicating that any contribution of the double collision processes is negligible.

The energy scale of the BES was determined by setting the peak of the $n=1$ transition to the ionization potential of 24.59 eV [134]. The $n=2$ and $n=3$ peaks were fit by Gaussian functions centered at transitions energies of 65.41 eV and 72.97 eV, determined from the

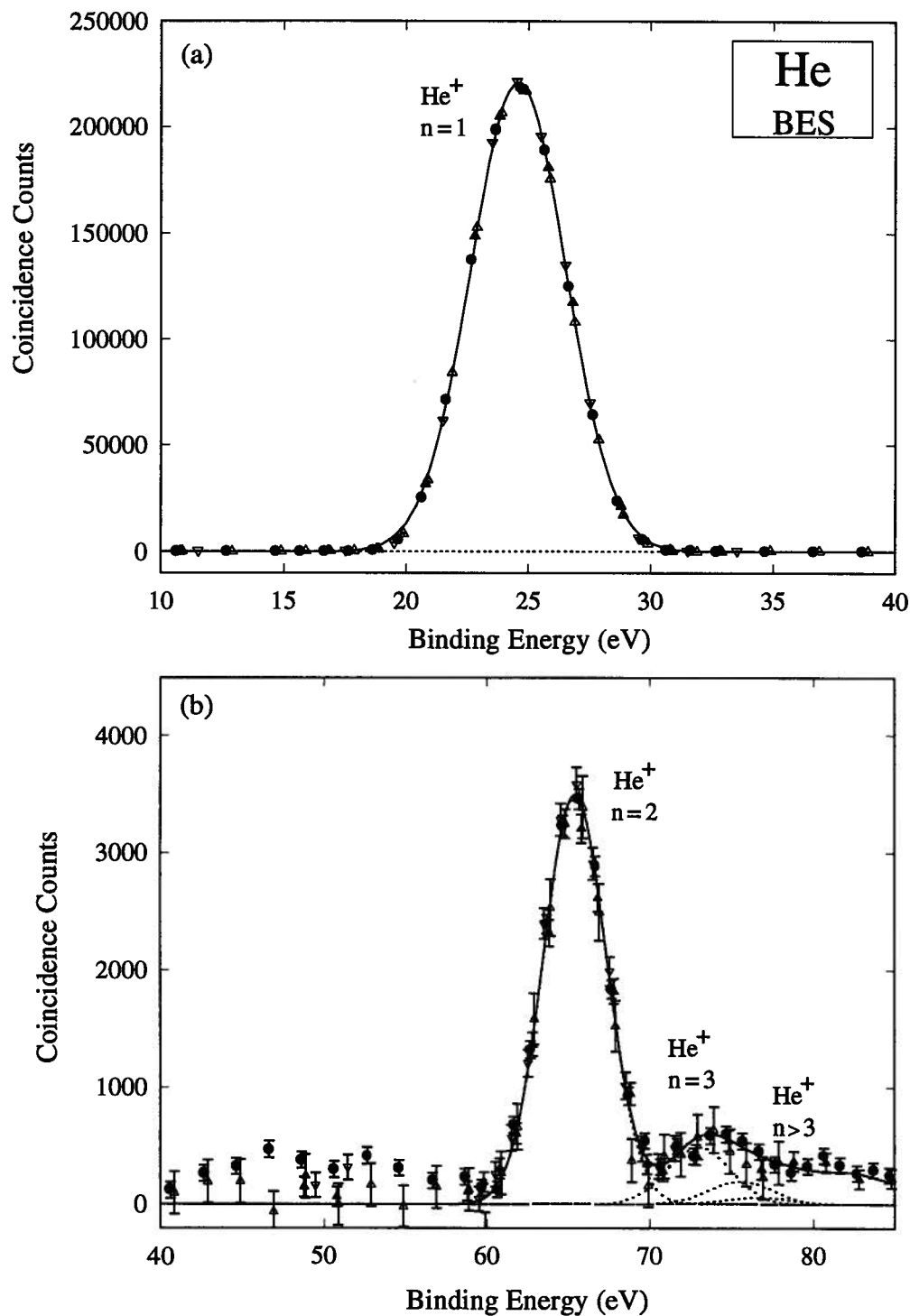


Figure 5.5: An angle integrated ($\pm 26^\circ$) binding energy spectrum of helium obtained measured following the modifications to the collision chamber, showing peaks for a) the $n=1$ transition, and b) the $n=2$ and $n>2$ transitions. Triangular points are (scaled) BES measurements obtained at approximately half the gas pressure used in the measurements represented by the solid circles.

calculated energy levels of the helium ion [135]. These values are in excellent agreement with the PES studies of Svensson *et al.* [112], and Heimann *et al.*[135]. Additional Gaussians, centered on the transition energies for ionization to the $n>3$ ion states were added to account for the intensity at the higher binding energies. It is important to note that in the fitting procedure to obtain the areas (i.e. relative intensities) of the $n=2$ and $n=3$ peaks, the energies and widths of the Gaussian functions were fixed.

The experimental momentum profile for the $n=1$ transition is shown in figure 5.6a and is in very good agreement with the theoretical profiles (solid lines) obtained using the correlated wavefunctions of Cann and Thakkar (CT) and of Chakravorty and Davidson (CD). The small discrepancy at higher momenta is due to distorted wave effects. The experimental momentum profile for the transition to the $n=2$ ion state is presented in figure 5.6b together with the theoretical profiles (NW), (W), (CT),and (CD). The $n=2$ XMP obtained prior to the modification of the instrument and corrected for double scattering, was found to be in good agreement with the profile taken following the (collision chamber) modification. The XMP shown in figure 5.6b includes the experimental data from both measurements.

It is immediately apparent from this figure that the experimental profile for the $n=2$ transition is significantly more intense than all of the theoretical profiles. At low momentum values, the experimental measurements are estimated to be higher than the CT, CD profiles by a factor of 1.35 ± 0.05 . These TMPs, scaled by 1.35 are also shown in figure 5.6b. While the

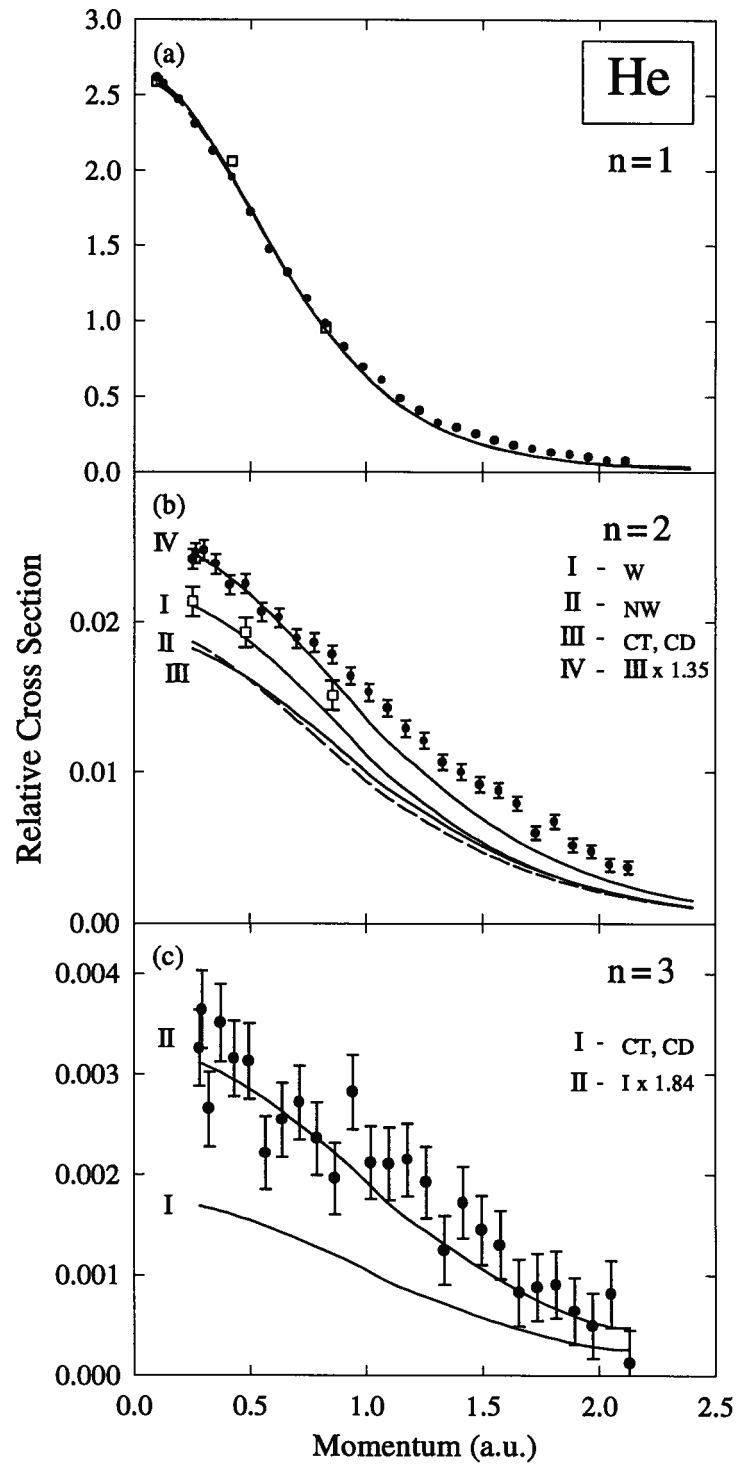


Figure 5.6: The XMPs for the transitions from the helium ground state to the $n=1$, $n=2$ and $n=3$ ion states, measured with the momentum dispersive multichannel spectrometer (solid points). The open squares represent energy dispersive multichannel measurements of Zheng and Neville [136].

shape of the XMP is similar to the scaled TMP, the XMP exhibits increasing intensity at higher values of momentum. This may indicate the effects of distorted waves, however the difference between the XMP and the scaled TMP is larger than predicted by the distorted wave calculations of McCarthy and Mitroy [122].

The XMP for the transition to the $n=3$ final ion state is shown in figure 5.6c, together with the CT and CD theoretical profiles. It should be noted that the XMP was obtained at an energy corresponding to the expected position of the $n=3$ peak in the BES. At this energy, a small contribution from the $n=4$ transition (see figure 5.5) is anticipated; however, the influence on the shape of the XMP is expected to be small. Accordingly, the XMP is normalized to the relative area of the $n=3$ Gaussian function in the BES spectrum (figure 5.5). As in the case of the $n=2$ results, the experimental momentum profile for the $n=3$ transition is significantly higher (1.85 ± 0.30) than the $n=3$ theoretical profiles. The CT and CD profiles, scaled by 1.85 to give reasonable agreement to the experimental data below ~ 0.9 a.u., are also shown in figure 5.6c. At higher momentum values, the $n=3$ experimental data points are consistently higher than the scaled TMPs, as found in the $n=2$ results, although the limited statistics of the $n=3$ measurement prevents an accurate assessment of the divergence from (scaled) theory in this region.

5.3 Discussion

The disparity between the intensities of the XMPs for the $n=2$ and $n=3$ transitions and the theoretical profiles is significant, and indicates a problem with either the experimental measurement, or the calculation of the theoretical cross sections, or both. It should be noted that the experimental cross section measurements for helium are normalized to theory by scaling the $n=1$ XMP to the $n=1$ TMPs. Therefore, if the coincidence detection efficiency over the $n=1$ peak was somehow reduced, or the efficiency about the $n=2$ and $n=3$ peaks was increased, the $n=2$ and $n=3$ XMPs would appear to be elevated. However, the thorough characterization of the new multichannel instrument, outlined in chapters 3, was performed to ensure the uniform detection efficiency of $(e,2e)$ coincidence events over a much larger range of experimental conditions than typically experienced in normal operation. During the course of the measurement of a binding energy spectrum or momentum distribution, the experimental conditions change very little.

The incident electron beam current collected by the Faraday cup exhibited a very small dependence on the cathode potential. For a typical mean setting of $\sim 60 \mu\text{A}$, the electron beam current entering the Faraday cup increased by less than three percent over the range of cathode potential from 1220 eV to 1265 eV. The actual change in the electron flux through the collision region was likely even smaller.

The coincidence count rate obviously changed considerably during the measurement over the peaks of the transitions to the $n=1$, $n=2$ and $n=3$ final ion states, and the instrumental dead time for coincidence detection should be considered. In the present system, the instrumental dead time is essentially that required to process and store the positional information from the MCP/RAE detector; approximately 8 microseconds per event. As the position computer is gated on the PPU detection of a coincidence event, only the positions of electrons which are one-half of an $(e,2e)$ coincidence pair are calculated. Even for the maximum coincidence count rate of 20 Hz obtained at the peak of the $n=1$ transitions, the instrumental dead time is negligible.

The uniform $(e,2e)$ coincidence detection efficiency of the present spectrometer over a large variation in experimental conditions is most clearly and convincingly demonstrated by the test measurements presented in figure 3.27 of chapter three. The non-coincidence (singles) electron count rates of the MCP/RAE and CEM detectors, as well as the $(e,2e)$ coincidence count rate were shown to vary linearly with the incident electron beam current over a range from 0.1 to 70 μA . This effectively rules out the possibility of any non-linearity in the instrumental response over the range of electron impact energies and experimental conditions in the measurement of the $(e,2e)$ transitions of helium to the ground and excited ion states. As well, the study of the noble gases and of methane and silane presented in chapter 4 have clearly demonstrated the quantitative response of the momentum dispersive spectrometer in the measurement of the binding energy spectra and the outer and inner valence XMPs.

As an independent test of the present momentum dispersive experimental results, the EMS cross sections for ionization of helium to the $n=1$ and $n=2$ final ion states have been measured in this laboratory by Y. Zheng and J. Neville [136] at three azimuthal angle (momentum) values using a recently constructed energy dispersive multichannel spectrometer at the University of British Columbia. This instrument is very similar to that used in the earlier helium study of Cook *et al.* [26]. The energy dispersive data are represented in figure 5.6a and 5.6b as open squares. Normalized to the $n=1$ TMPs, the $n=2$ cross section measurements exhibit an increased intensity by a factor of 1.20 ± 0.05 compared to the CD and CT theoretical profiles. While this measurement is somewhat lower than the present momentum dispersive multichannel results, both of the $n=2$ XMP measurements are significantly above the $n=2$ theoretical profiles. This is in conflict with the XMP measurements of Cook *et al.* [26] and suggest that the $n=2$ (and $n=3$) profiles of the earlier reported energy dispersive studies may be too low. In connection with the energy dispersive multichannel EMS measurements, it should be noted that Zheng and Neville used the much more accurate binning mode [137], rather than the less accurate non-binning mode employed by Cook *et al.* [26]. While the $n=2$ experimental cross section measurement of Lahmam-Bennani *et al.* [31] (presented as a ratio to the $n=1$ cross section) is also lower than the present studies, this may be due to kinematic effects resulting from the different geometry and outgoing energies employed in the study (see below). In addition, Lahmam-Bennani *et al.* [31] found it necessary to correct their $n=2$ intensity for a long range binding energy 'tail' from the much larger $n=1$ signal [138]. The magnitude of the correction was reported to be 10-20% of the $n=2$ intensity [31].

While the presently reported EMS momentum profiles for the transition to the ground ion state is in very good agreement with the shape of the theoretical profiles, the $n=2$ and $n=3$ XMPs obtained using both the multichannel momentum dispersive and the multichannel energy dispersive EMS instruments are significantly higher than the theoretical profiles based on even the most highly correlated wavefunctions. As the profile labeled CT was calculated using a wavefunction which gives an energy within 10 nHartree [125] of the exact (non-relativistic) energy for the ground state of helium [126], and is in agreement with the profile CD, which is based on a similarly high quality wavefunction, the discrepancy between theory and experiment is not believed to arise from a deficiency in the helium wavefunctions. More suspect is the viability of the plane wave impulse approximation used to evaluate the theoretical momentum profiles. In the theoretical description of the scattering cross sections for the ionizing transitions to excited final ion states (ionization + excitation) it has been assumed that the scattering process is identical to that for the transition to the ground ion state (ionization). With the exception of studies of distorted wave effects [30,122], the possible breakdown of this assumption has not been addressed in earlier EMS studies. This is likely because the scattering kinematics for EMS is specifically chosen to permit a plane wave description of the incoming and outgoing electrons as well as an impulsive binary encounter description of the scattering events.

In the PWIA (or a first Born) treatment of the scattering, the excitation of the final ion is essentially a 'shake-up' process [139], in which the removal of one target electron modifies

the potential of the second target electron which may relax into excited or a continuum (double ionization - 'shake-off') state [139]. As discussed above, electron correlation in the initial state has a considerable influence on the probability of an excited final ion state transition. Recently, the role of other mechanisms which may contribute to the cross section of scattering processes involving two-electron transitions in the target (for example, excitation - ionization, double ionization, double excitation) has been of much interest. An excellent review of the mechanisms contributing to two-electron processes has been presented by Tweed [139] using the framework of the first and second Born approximations to describe the projectile scattering. Essentially, the first Born terms account for a single interaction of the projectile with the target electron, while the second Born terms account for two interactions with the target, including double collision mechanisms involving two target electrons¹ [139]. The second Born, double collision terms identified by Tweed are often referred to as two-step (TS) processes, using nomenclature introduced by McGuire [140] and by Andersen *et al.* [141]. In the TS-1 process [141], the projectile undergoes a collision with one of the target electrons, which subsequently interacts with a second target electron. A second process, often labeled TS-2, involves the collision of the projectile with one target electron followed by a second collision of the projectile with another target electron. [141,142]. The neglect of these two processes in the calculations of the EMS cross sections for the ionization of helium to excited ion states, is a possible cause of the discrepancy

¹ It should be noted that, to avoid (or at least to minimize) confusion, the double processes referred to here and in the remainder of the chapter are termed double *collision* processes, while processes described earlier, in reference to the additional intensity in the helium BES at ~45 eV, are termed double *scattering* processes. While the names are similar, the events they describe are significantly different.

observed between the (correlated wavefunction) TMPs calculated in the PWIA, and the present experimental cross sections.

A diverse array of experimental measurements of two-electron processes has been performed, and has indicated the importance of including two-step mechanisms in the description of the scattering cross sections. Almost thirty years ago, Carlson and Krause [143] suggested that the interaction (TS-1) of a photoelectron with the remaining electrons of a target neon atom may influence the yield of multiply charged neon ions produced by X-ray photoionization. More recently, Andersson and Burgdörfer [144] incorporated the contribution of the TS-1 process in a calculation of the ratio of double to single photoionization cross sections of helium, and demonstrated a significant influence of the TS-1 process on the ratio, particularly for photon energies below 5 keV. The investigation of the double ionization of helium by charged particle impact was particularly important in the elucidation of the contribution of these two-step processes [140,141]. Specifically, the (total) single ionization cross section for impact of electrons and protons were shown to give identical results and were in agreement with theory using the first Born approximation [140,145]. In contrast, the electron impact cross section for double ionization of helium was found to be significantly greater than the proton impact cross section at equivalent velocities [140,145]. The charge dependence of the double ionization process was confirmed by measurement of the cross section using antiproton projectiles [141,146] which was shown to be in good agreement with the cross section using electron projectiles. In the

first Born approximation, the double ionization cross section is identical for positively or negatively charged projectiles, and hence the first Born treatment cannot account for the experimental results. The theoretical description of the enhanced double ionization cross section for impact of negatively charged particles has received much attention [140,147,148, 149,150]. While the details of the process are still the subject of some debate [151], the theoretical cross section has been shown to require the inclusion of the double collision (second Born) terms TS-1 and TS-2 to explain the experimental double ionization results [142,151]. The influence of two-step terms was also shown to be required to explain experimental measurements of the cross section of ionization-excitation processes. The total cross section for ionization of helium to excited final ion states, has been studied for electron and proton impact [152,153,154] by measuring the emission of Lyman radiation from the excited helium ions ($np \rightarrow 1s$). Similar to the double ionization process, the cross section for ionization of helium to an excited (np) helium ion final state has been shown to be considerably higher (approximately a factor of 2 - 3 for projectile velocities of 3.5 - 8 a.u.) [152,153,154] for electron impact than for proton impact. These results cannot be explained using a first order (first Born) description of the scattering process.

In the light of the above discussion, the two-step, TS-1 and TS-2, scattering mechanisms are proposed to be the source of the discrepancy between the present measurements of the EMS cross sections for transitions from the ground state helium atom to the excited ($n=2$ and $n=3$) helium ion states, and the PWIA theoretical profiles (NC and CD) using highly accurate

correlated wavefunctions. In the present EMS kinematics, the two-step processes would entail a large momentum transfer, binary collision of an incident electron and target electron, with the subsequent interaction of either of the outgoing electrons with the second target electron. This second interaction is not considered in the PWIA formalism, and the additional contribution from the two-step processes to the EMS scattering cross section may account for observed discrepancies. In parallel with the electron (and photon) impact studies discussed above, the two-step processes may be expected to give an increased intensity of XMP for the transitions to the excited $n=2$ and $n=3$ final ion states. As well, since the second collision event may influence the direction of one of the outgoing electrons, the angular relationship of the coincident $(e,2e)$, and hence the experimental momentum profile, may be modified. In the extreme case of large deflections in the direction of the outgoing electron, the contribution from the double collision events may be expected to be homogeneous over the $\pm 26^\circ$ azimuthal angle, leading to a 'flatter' shape of the XMP. Both the increased intensity and modified shape of the profile expected from the double collision events, are in qualitative agreement with the differences in the experimental and (PWIA) theoretical profiles presented in figure 5.6.

A significant difference between the EMS scattering process and the high energy electron/proton impact studies (leading to double ionization) discussed above, exists in the energies of the electrons ejected from the target. The ejected electrons in the electron/proton impact, total cross section measurements may be expected to have relatively low energies

[151], while the outgoing electron energies in EMS are relatively high ($\sim 600\text{eV}$). However, in the recent study of Andersson and Burgdörfer [144] described above, the theoretical description of the double photoionization cross section indicated a significant contribution from the TS-1 process, even at high photon energies corresponding to high outgoing photoelectron velocities. As a result of the TS-1 process, the calculated ratio of double to single ionization cross sections rises from the high energy limit (1.66%) by $\sim 10\%$ at a photon energy of 5 keV, and by $\sim 35\%$ at a photon energy of 2.5 keV. The calculated ratio continues to rise at lower photon energies [144]. This result offers additional support for the proposed contribution of the two-step processes to the $(e,2e)$ cross section, at the outgoing electron energies detected in the present EMS measurements.

The studies of double ionization and ionization with excitation, have primarily focused on total cross section measurements. Differential measurements permit a much more detailed examination of the collision dynamics, and would be of great value for the investigation of two electron transitions. In this respect, the nascent experimental technique of $(e,3e)$ scattering [155], in which the energies and angles of three outgoing electrons are determined, may provide further insight into the double ionization scattering process. Unfortunately, the difficulty associated with the experimental measurement of the $(e,3e)$ cross sections has thus far limited the effectiveness of the technique [155]. In the case of ionization+excitation of a target system, the present measurement of the triple differential EMS cross sections for helium should provide a basis for the theoretical examination of the two-step scattering

process. The kinematics used in the present EMS study should permit a relatively simple description of the incident and outgoing electrons, as well as of the single and two-step collision mechanisms. It is hoped that the present measurements will provide the impetus for new investigations of the EMS scattering cross sections for transitions to the excited ion states, at a level of theory which accounts for two-step processes.

5.4 Conclusions

The experimental momentum profiles for the ionization of helium to the $n=1$, $n=2$ and $n=3$ final ion states have been measured with the high sensitivity of the recently developed momentum dispersive multichannel spectrometer, to a greater statistical precision, and for an increased number of data points, than previously reported. In addition, theoretical profiles based on highly correlated wavefunctions have been obtained. Two of these profiles (NC, CD), calculated using extremely accurate helium wavefunctions, represent an effectively converged limit to the cross section calculations using the PWIA. The XMP for the ionization to the ground state ion is in good agreement with these theoretical profiles. In contrast, the XMPs for the transitions to the $n=2$ and $n=3$ final ion states are significantly larger than all of the theoretical profiles. It is proposed that the enhancement of the intensity of the experimental cross sections relative to theory is due to the need to include second order scattering effects in the evaluation of the theoretical cross sections. In particular, the two-step processes (TS-1 and TS-2) describing the interaction of the two outgoing electrons with the third (helium ion) electron, have been identified as possible sources for the additional intensity

of the experimental measurements. These processes have recently received much attention in experimental and theoretical studies of the total cross sections for the ionization-excitation , and double ionization, of helium [139,151], but have not been previously discussed specifically with respect to EMS studies. The present measurements may provide important insight into the two-step scattering mechanism, and a theoretical evaluation of the EMS cross section at a level of theory sufficient to account for the TS-1 and TS-2 processes is eagerly anticipated.

Chapter Six

EMS of Two Electron Systems: Molecular Hydrogen and Deuterium

6.1 Background

The investigation of the electron impact ionization of two electron systems to excited final ion states is extended in this chapter, with the study of molecular hydrogen and deuterium. In parallel with the theoretical cross sections of helium, discussed in the previous chapter, the EMS PWIA cross sections for the transitions to the excited H_2^+ ion states may be expected to be particularly sensitive to the description of electron correlation in the ground state molecular wavefunction. Accordingly, the experimental measurement of the momentum profiles for these transitions may provide insight into the role of electron correlation, as well as the accuracy of theoretical wavefunctions for the ground state molecular species. As the simplest two-electron neutral molecular system, the theoretical description of the H_2 ground state, and the influence of electron correlation, have received much attention. An early example of this is given in the “long and illustrious list of calculations...” [156] performed prior to 1960, summarized by McLean *et al.* [156].

The experimental measurement of the transitions to the excited ion states is complicated by the relatively low (e,2e) cross sections associated with the transitions. In the study of

hydrogen, further difficulties arise from the broad, overlapping binding energy line profiles, which result from the vibrational motion of the ground state molecule and the dissociative nature of the (unbound) excited ion states (see figure 6.2). In spite of these difficulties, Weigold *et al.* [157] have reported single channel measurements of binding energy spectra of H₂ (up to ~45.5 eV) at two relative azimuthal angles, and experimental momentum profiles obtained at a few binding energies. The experimental profiles were compared to the theoretical profiles based on the ground state molecular wavefunction of McLean *et al.* [156]. Significant discrepancies between theory and experiment were exhibited, particularly in the intensities of the $2s\sigma_g$ profiles at low momentum. Similar discrepancies between the single channel measurements [157] and theoretical momentum profiles calculated using more accurate correlated ground state wavefunctions, were subsequently reported by Liu and Smith [66]. However, the low cross sections of the excited ion transitions, coupled with the limitations of the single channel EMS architecture, resulted in relatively large uncertainties in the experimental profiles reported by Weigold *et al.* [157]. This prompted Liu and Smith to state, somewhat emphatically, that “experimental data for the transitions to all the $n=2$ and $n=3$ excited states are urgently needed” [66]. The single channel results of Weigold *et al.* [157] represent the only published measurement of the H₂ EMS cross sections for the transitions to excited ion states that is published in the literature, although unpublished measurements using an energy dispersive multichannel spectrometer have been obtained by Bharathi *et al.* [158]. The original aim of the present study of molecular hydrogen, was to exploit the greatly enhanced collection efficiency of the momentum dispersive multichannel

spectrometer to obtain improved measurements of the momentum profiles for the (e,2e) transitions to excited ion states and thus a more precise test of theory. However, in light of the multichannel measurements of helium presented in chapter 5, the present study also provides an additional opportunity to investigate the possible influence of second order (i.e. two-step) collision processes in the transitions to excited ion states.

6.2 Theoretical Momentum Profiles of Molecular Hydrogen

Theoretical momentum profiles for the EMS transitions from the ground state of H_2 to the $1s\sigma_g$ ion state, and $n=2$ ($2p\sigma_u$, $2p\pi_u$, and $2s\sigma_g$) excited ion states have been tabulated by Liu and Smith [66], and are presented in figure 6.1. The TMPs using the SCF and correlated wavefunctions of Davidson and Jones (DJ) [159], and the correlated wavefunction of Hagstrom and Shull (HS) [160] are shown. The DJ and HS wavefunctions are of similar accuracy, accounting for 96.5% and 96.7% of the total correlation energy respectively. The calculation of the EMS cross sections involved the overlap of these wavefunctions with the final ion wavefunctions, which, within the Born-Oppenheimer approximation, are expressed exactly [66]. All of the TMPs in figure 6.1 have been folded with the present instrumental resolution (see chapter 4) using the GWPG method [49]. Additionally, the excited ion profiles include a term representing the small change in kinematic factors at the various impact energies of the transitions [28].

The variation amongst the profiles for the transition to the ground state ion is small; on the order of a few percent at low momentum. The shapes of the TMPs for the $2s\sigma_g$ ion state

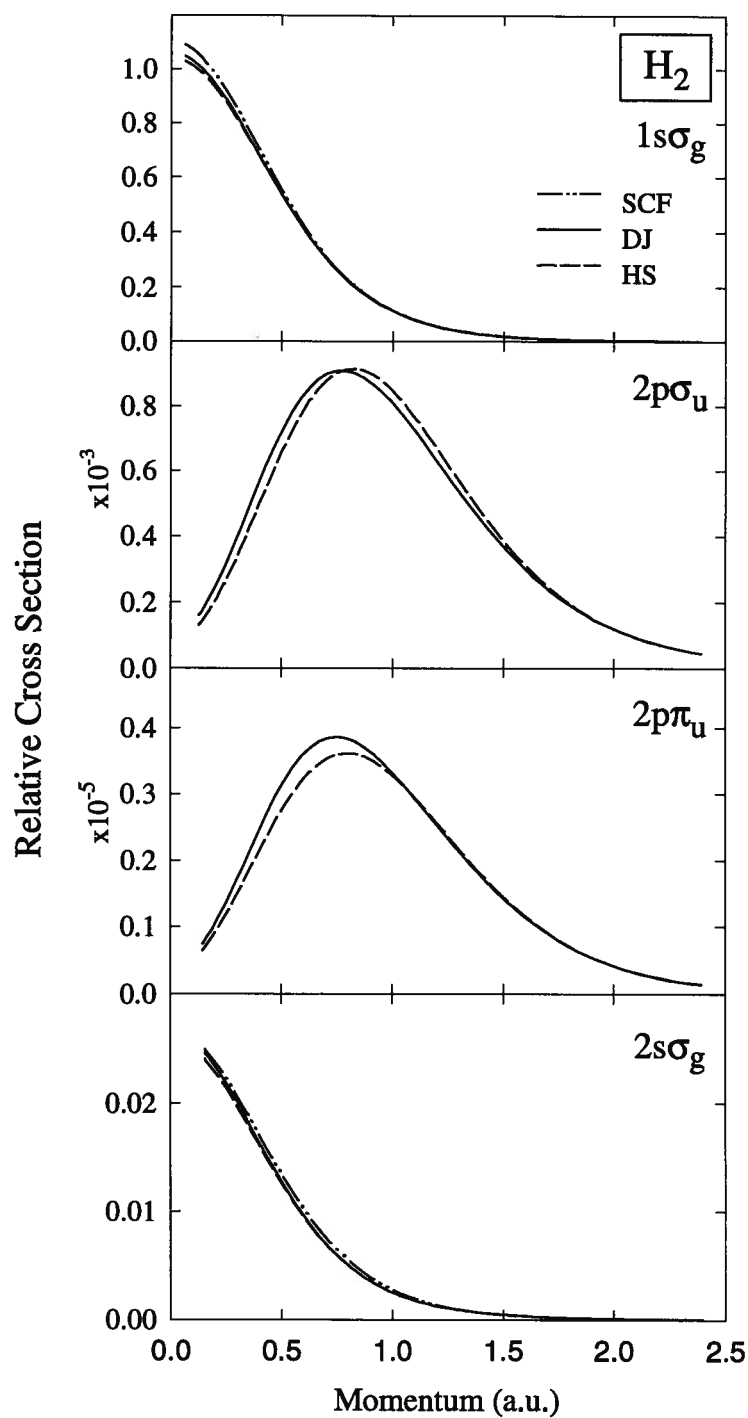


Figure 6.1: The TMPs for the transition from the ground state of H_2 to the ground and excited final ion states, obtained from Liu and Smith [66]. The profiles have been folded by the present instrumental resolution, and include the variation in the kinematic (i.e. Mott) scattering factors with impact energy. Note the scale of the $2p\sigma_u$ and $2p\pi_u$ profiles.

are very similar to those for the $1s\sigma_g$ transition, in contrast with the large change of shape between the helium $n=2$ and $n=1$ TMPs. Only a small difference is observed between the $2s\sigma_g$ profile using the uncorrelated SCF wavefunction and the profiles using highly correlated wavefunctions. Initial state electron correlation has a greater influence on the theoretical cross sections for the transition to the $2p\sigma_u$ ion state. While no theoretical cross section is predicted if an (uncorrelated) SCF wavefunction is used, relatively low cross section TMPs for this ionization process are given using the correlated wavefunctions. Additionally, the TMPs using the two correlated wavefunctions, DJ and HS, are in fair agreement with each other, and further improvements to the H₂ wavefunction may be expected to exhibit little change from these TMPs. Finally, the cross sections of the theoretical profiles for the transition to the $2p\pi_u$ state, based on the correlated wavefunctions, are extremely small. In the analysis of the experimental BES measurement presented below, the intensity for the transition to the $2p\pi_u$ state is assumed to be negligible (i.e. $<0.5\%$ $2p\sigma_u$).

6.3 Multichannel BES Spectra and Momentum Profiles of H₂

As PES measurements of the ionization of H₂ to the excited final ion states have not been reported, except for a relatively crude retarding potential measurement by Samson [161], theoretical estimates of the BES lineshapes were required. The potential energy curves of the H₂ ground state and H₂⁺ ion states were obtained from the tabulated data of Bates *et al.* [162], and of Sharp [163], and are presented in figure 6.2.

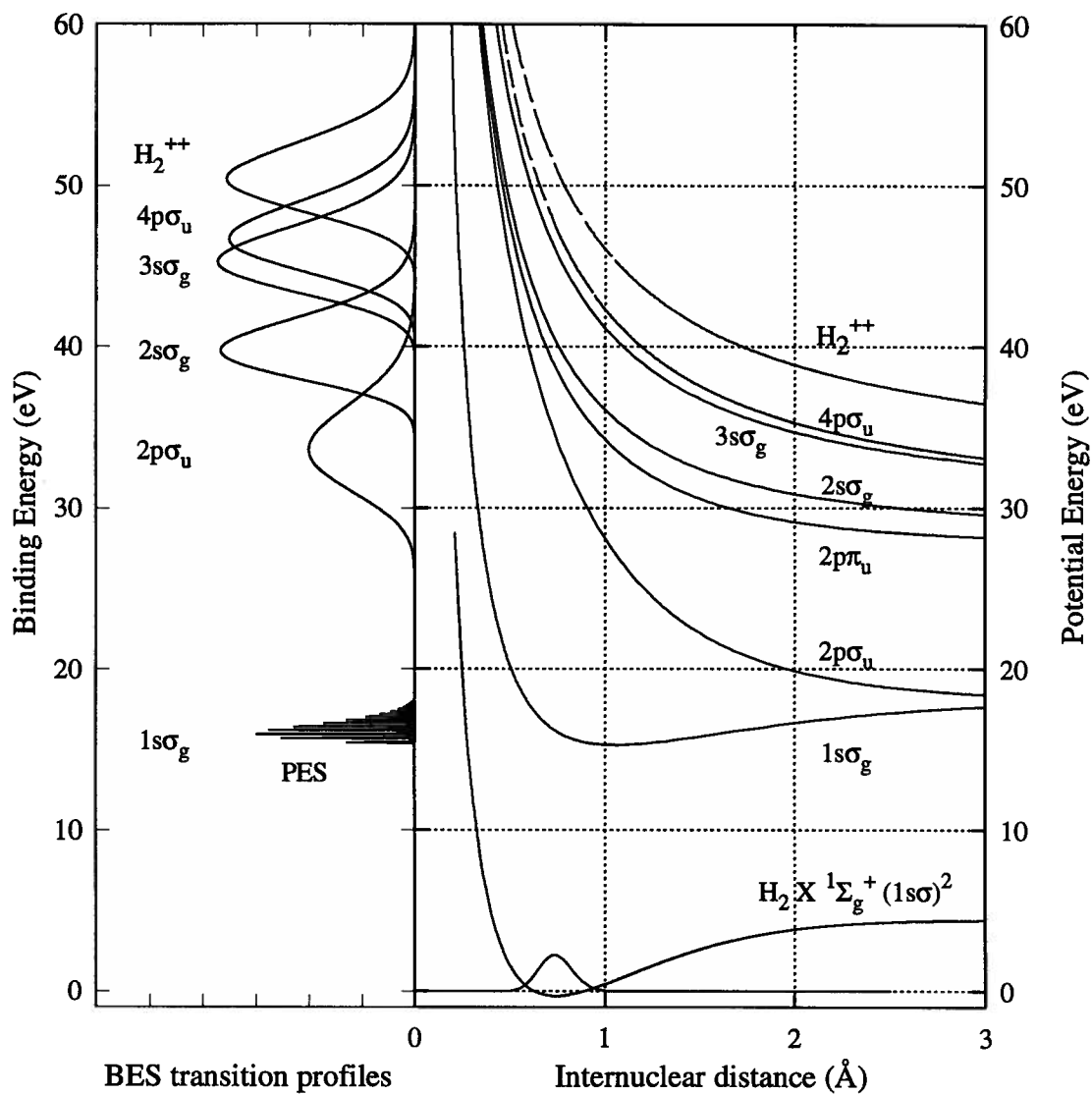


Figure 6.2: The potential energy curves of the H_2 ground state and the H_2^+ ion states, obtained from Bates *et al.* [162] and Sharp [163]. To the left are calculated binding energy line profiles for the transitions to the excited ion states, and the PES spectrum [164] for the transitions to the ground state ion. For clarity, many ion states have been ignored. This figure is similar to figure 3 of Gardner and Samson [161].

The probability distribution of the internuclear separation in the hydrogen molecule (shown in figure 6.2) was obtained from the ground state H₂ vibrational wavefunction, calculated using a Morse potential [166]. Applying the probability for a given internuclear separation to the appropriate transitions energy given by the energy of the excited ion potential curves, produced an estimate of the (asymmetric) binding energy spectrum line profiles. However, these line profiles were found to be in very poor agreement with experimental measurements, and additionally, were ~ 1 eV higher in energy than the BES line profiles reported by Gardner and Samson [165]. The high values of the transition energies, calculated in this manner, result from the neglect of the continuum wavefunctions of the excited ion states. A more realistic estimate of the line profiles was obtained by evaluating the Frank-Condon overlap of the ground state vibrational wavefunction, with the radial continuum wavefunction of an excited state at a specific energy. These overlaps were calculated using a computer program [167] written and provided by R. Le Roy of the University of Waterloo [168]. The resultant BES transition lineshapes are shown on the left hand side of figure 6.2, and are in good agreement with the curves of Gardner and Samson, evaluated in a similar manner [165].

The angle integrated (0 - ±26°) binding energy spectrum of H₂ over the range from 10-65 eV is shown in figure 6.3. The spectrum is clearly dominated by the transition to the 1sσ_g ion state. The energy scale of the spectrum was determined by positioning the 1sσ_g peak with respect to the vibrationally resolved photoelectron spectrum of H₂, reported by Samson [164].

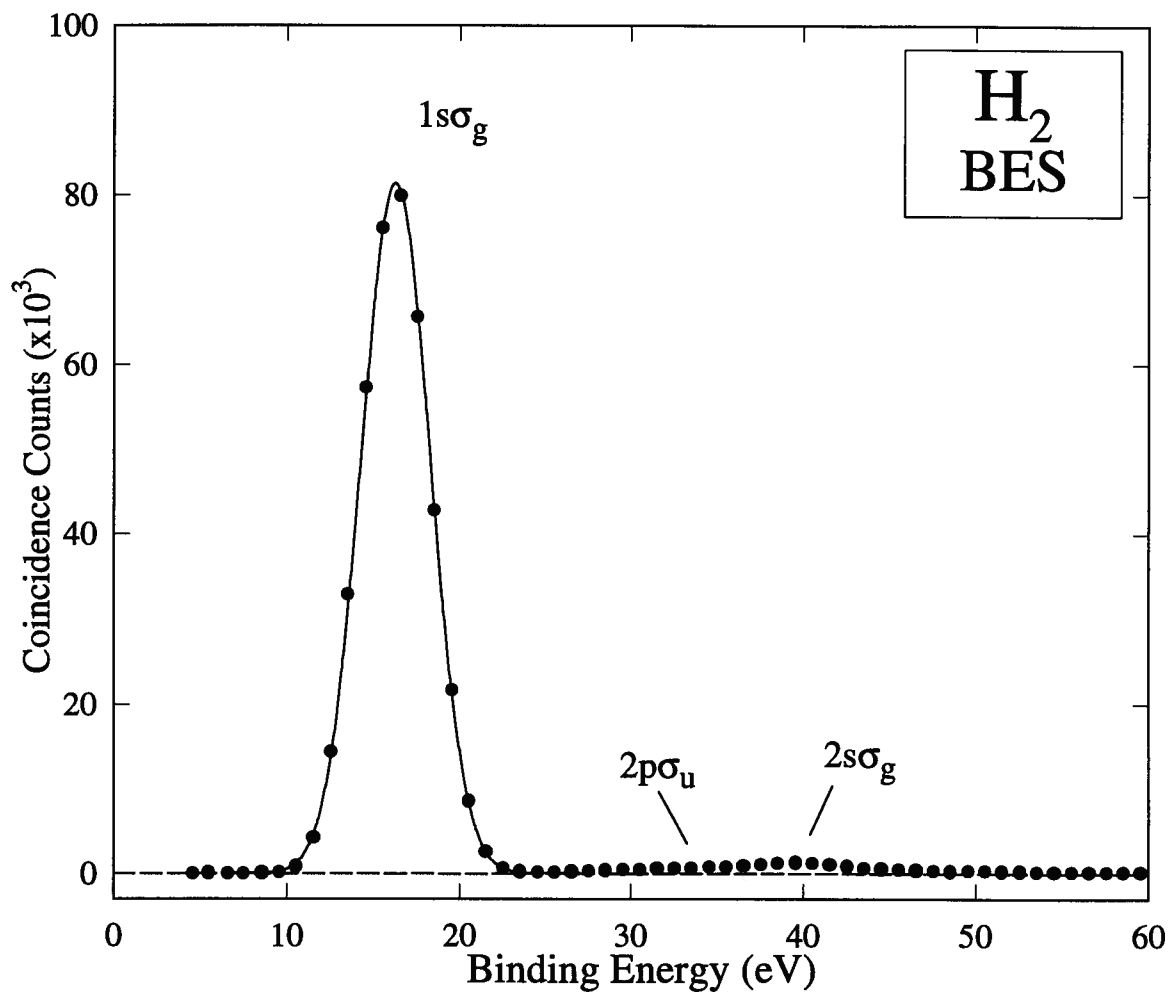


Figure 6.3: The angle integrated ($0 - \pm 26^\circ$) binding energy spectrum of molecular hydrogen. The solid line through the $1s\sigma_g$ peak represents the PES spectrum of Samson [164], convoluted by the present instrumental energy resolution.

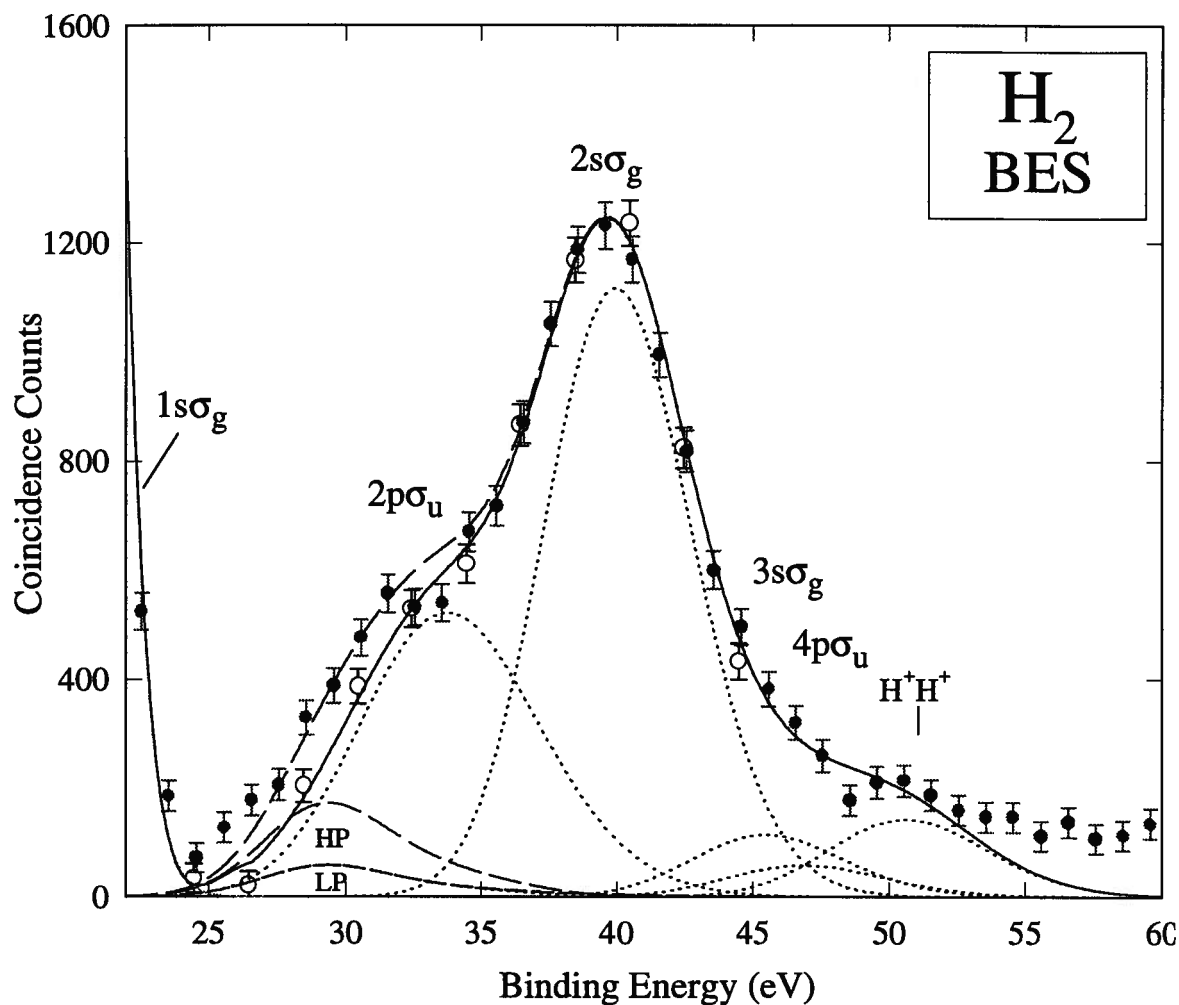


Figure 6.4: An expanded view of the H_2 binding energy spectrum about the region of the transitions to excited ion states. The solid points represent higher pressure (8.8×10^{-6} torr) measurements, while the open circles represent low pressure (3.0×10^{-6} torr). The dotted lines are the line profiles obtained from the overlap of the ground state H_2 and continuum H_2^+ vibrational wavefunctions. The long dash lines labeled HP and LP represent the modified (see text) optical oscillator strength measurements of Chan *et al.* [169], added to estimate double scattering events at higher pressure (HP) and lower pressure (LP). The higher dashed curve is the sum of the BES components including HP, while the solid line is the sum including LP.

The PES measurement, presented on the lower left hand side of figure 6.2, was corrected for a small background intensity and was convoluted by the present experimental energy resolution. The resultant slightly asymmetric peak is presented in figure 6.3 (solid line), and is in very good agreement with the experimental data.

The region of the binding energy spectrum about the excited state transitions has been expanded in figure 6.4. Prior to the modification of the collision chamber outlined in section 3.1.3, BES measurements exhibited a considerable intensity in the region just below the position of the $2p\sigma_u$ transition. The additional intensity in this region was found to originate from multiple (two molecule) scattering effects, also seen in the BES measurements of helium, and discussed in section 5.2.2. In the present measurements of hydrogen, the multiple scattering process involves a forward scattering energy loss interaction of an incident electron with one hydrogen molecule, followed by an (e,2e) ionization collision with a second hydrogen molecule in the collision region. Shortening the length of the gas cell prior to the collision region and improving pumping efficiency in the vicinity of the incident electron beam, significantly reduced the intensity from the double scattering process, although some small intensity from this source remains.

The solid circles in figure 6.4 represent measurements obtained following the collision chamber modification at a sample gas pressure of approximately 8.8×10^{-6} torr. The open circles represent measurements obtained at a reduced gas pressure of 3.0×10^{-6} torr. The

pressure dependence of the BES spectra, in the region between 25-35 eV, is a good indication of the influence of the multiple scattering process. The lineshape of the contribution from this multiple scattering process was estimated from the optical oscillator strength measurement of Chan *et al.* [169]. The optical oscillator strength cross section was scaled by E_0^{-3} , where E_0 is the electron impact energy, to yield the differential (forward) electron scattering cross section. Convolution by the experimental width of the $1s\sigma_g$ transition produced the lower dashed curve in figure 6.4, representing the influence of double scattering in the lower pressure (LP) measurement. The summed intensity of this curve and the BES line profiles is shown by the solid line, and is in good agreement with the low pressure measurement in the 25-35 eV region. Scaling the intensity of the double scattering process to account for the change in gas pressure produces the higher dashed curve (HP) shown in figure 6.4. The summed intensity using the higher double collision estimate is also represented by a dashed curve, and is in reasonable agreement with the higher pressure BES measurements.

The binding energy spectrum shown in figure 6.4 has been fit with the calculated line profiles and positions for the transition to the $2p\sigma_u$, $2s\sigma_g$, $3s\sigma_g$, $4p\sigma_u$, and doubly ionized states (see figure 6.2), in addition to the double collision estimates. The $2p\pi_u$ state is not included as the theoretical cross section calculation of Liu and Smith [66] indicates that the (e,2e) transition probability to this state is very low (see figure 6.1). Other $n=3,4$ and higher excited ion states have also been neglected as the intensities for these transitions should be small [66], and would overlap considerably with the transitions to the $3s\sigma_g$ and $4p\sigma_u$ states. The

agreement of the summed intensity to the experimental measurements is generally very good over the full binding energy range. At higher energies (48-60 eV), the fit would likely be improved by accounting for the (e,2e) intensity above the double ionization threshold. The areas of the BES peaks for the $2p\sigma_u$ and $2s\sigma_g$ transitions are particularly important for the normalization of the experimental momentum profiles for these ion states to the $1s\sigma_g$ XMP. From the binding energy spectrum in figure 6.4, the areas of the peaks have been determined to an estimated accuracy of $\pm 5\%$.

The experimental momentum profiles for the transitions to the ground and excited final ion states were obtained by measuring the angular distribution of (e,2e) coincidence events for a number of binding energies, at a target gas pressure of 3.0×10^{-6} . The XMP for the transition to the $1s\sigma_g$ state is presented in figure 6.5a, and is in good agreement with the shape of the DJ theoretical profile. The sum of measurements obtained in a narrow range of binding energies about an average value of 32.5 eV is shown in figure 6.5b, while the XMP acquired at an average binding energy of 40.2 eV is presented in figure 6.5c. Although small contributions from the double collision process and from transitions to the $2s\sigma_g$ state are expected in the XMP measurement at 32.5 eV, greater than 90% of the intensity at this energy arises from the $2p\sigma_u$ transition, and the additional transition process at this energy should have only a small influence on the shape of the XMP. Similarly, greater than 90% of the intensity at 40.2 eV is due to the $2s\sigma_g$ transition, with small contributions arising from the $2p\sigma_u$ and $3s\sigma_g$ transitions. As the shapes of the $2s\sigma_g$ and $3s\sigma_g$ theoretical cross sections are very similar [66], the influence of the $3s\sigma_g$ transition on the XMP should be especially small. Hence, the XMPs in

figures 6.5b and 6.5c are labeled by the primary components, $2p\sigma_u$ and $2s\sigma_g$. The profiles for these two transitions have been normalized to the intensity of the $1s\sigma_g$ XMP, by the areas of the transitions in the BES, shown in figures 6.3 and 6.4. The theoretical momentum profiles obtained using the correlated wavefunction of Davidson and Jones [159] are also shown in figure 6.5. The agreement between the experimental and theoretical profiles is clearly very poor.

The measurement at 32.5 eV was corrected for the overlap of the double scattering events, and for the small intensity from the $2s\sigma_g$ transition, by removing the appropriate contribution of the $1s\sigma_g$ and $2s\sigma_g$ XMPs. The corrected and renormalized $2p\sigma_u$ XMP is shown in figure 6.6b. The effect of the correction is small, and acts to slightly lower the intensity in the low momentum region. A similar correction procedure to remove the contributions from the $2p\sigma_u$ transitions from the measurements at 40.2 eV has a negligible effect on the XMP. The corrected $2s\sigma_g$ XMP is presented in figure 6.6c. As in the previous figure, the discrepancy in the shapes and intensities of the theoretical and experimental profiles is quite dramatic.

The theoretical profile of the $2s\sigma_g$ transition significantly overestimates the experimental intensity at low momentum, and underestimates the intensity at higher (>0.7 a.u.) momenta. The theoretical profile of the $2p\sigma_u$ transition greatly underestimates the experimental intensity,

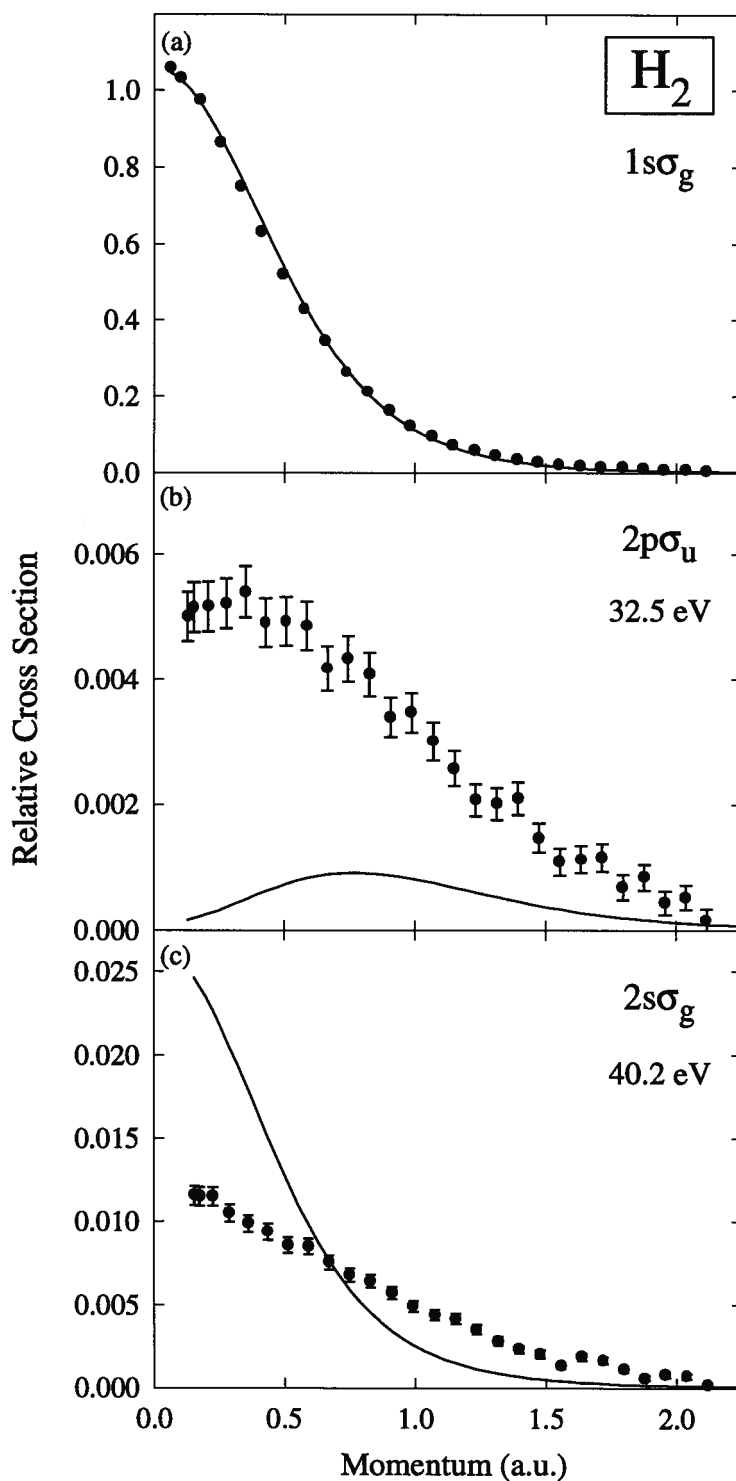


Figure 6.5: The XMPs (solid circles) for the transition to the $1s\sigma_g$, $2p\sigma_u$, and $2s\sigma_g$ H_2^+ ion states. The XMPs have been normalized to the areas of the line profiles in the BES of figure 6.4. The solid lines are theoretical profiles calculated by Liu and Smith [66] using the correlated wavefunction of Davidson and Jones [159], as shown in figure 6.1.

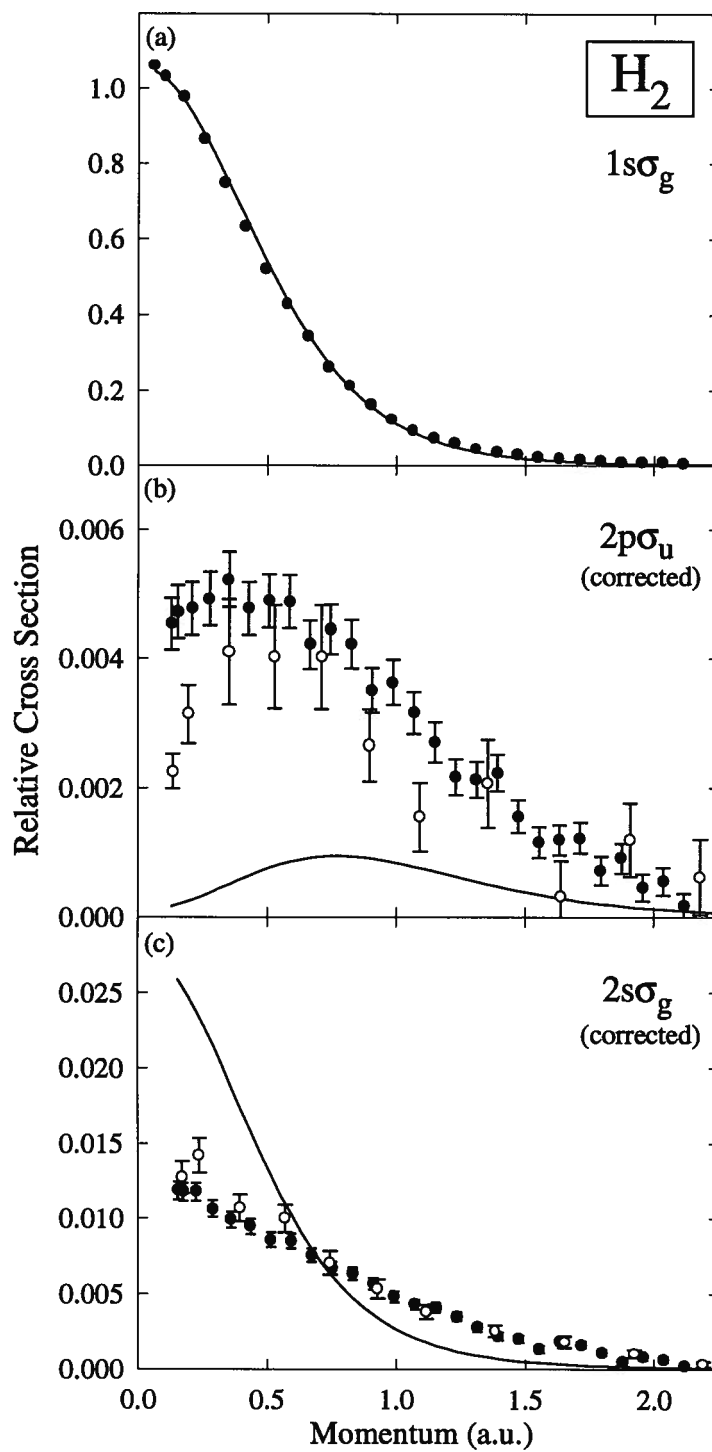


Figure 6.6: The $1s\sigma_g$, $2p\sigma_u$, and $2s\sigma_g$ XMPs (solid circles) corrected for the small contributions from overlapping transitions. The open circles are the energy dispersive measurements of Bharathi *et al.* [158].

and while the TMPs drop close to zero at low momentum (due to the symmetry of the $2p\sigma_u$ state), very little decrease is exhibited by the XMP.

The unpublished multichannel energy dispersive measurements of Bharathi *et al.* [158] are represented as open circles in figure 6.6, for comparison with the present measurements. The two multichannel measurements of the $2s\sigma_g$ XMPs are in excellent agreement. The $2p\sigma_u$ XMP reported by Bharathi *et al.* [158] is slightly lower, and exhibits a greater decrease in the cross section at low momentum than the present momentum dispersive XMP. Importantly, the large discrepancies with the theoretical profiles for the excited ion transitions are reproduced, providing strong independent support for the accuracy of the present measurements.

6.4 Multichannel BES Spectra and Momentum Profiles of D₂

In the evaluation of the H₂ theoretical momentum profiles, it was assumed that the range of internuclear separations resulting from the vibrational motion of the ground state molecule may be approximated by using the electronic wavefunctions at the equilibrium bond distance. This approximation is generally employed in EMS studies on molecular systems. The viability of the approximation has been investigated by Dey *et al.* [170], through the measurement of the XMPs of H₂ and D₂. No variation in the profiles for the transition to the $1s\sigma_g$ ground state ion were observed, indicating that the EMS cross section is not strongly influenced by the vibrational motion of the target. Similarly, isotopic substitution measurements of H₂O and

D₂O were performed by Bawagan *et al.* [37] to investigate the possible contribution of molecular vibration to the discrepancies observed between XMPs and high quality theoretical profiles (see section 1.3). Again, no variation with isotopic substitution was observed. Additionally, explicit calculation of the TMPs of H₂O at a range of nuclear coordinates was evaluated by Leung *et al.* [171]. While the XMPs were shown to vary with nuclear geometry, the vibrationally averaged profiles were found to be quite well described by the XMP at the equilibrium bond distance. These studies suggest that vibrational effects should be small in the present measurements on H₂ and D₂ for the transition to the 1s σ_g final ion state. However the role of molecular vibration in the cross section for the transitions to the repulsive excited ion states is unclear. To investigate the possible contributions from molecular vibration, the measurements for H₂ were repeated using D₂ as the target gas species.

The angle integrated (0 - $\pm 26^\circ$) BES of D₂ is shown in figure 6.7. The energy scale of this spectrum was set by positioning the 1s σ_g peak to the curve obtained from the energy calibrated [172] vibrationally resolved PES measurement of D₂ reported by Cornford *et al.* [173]. In figure 6.7b, the BES in the energy region of the excited state transitions is expanded. The solid and open circles in this figure represent measurements at target gas pressures of 5.8×10^{-6} torr and 2.4×10^{-6} torr, respectively. As in the hydrogen binding energy spectrum, the influence of the double scattering process (from two D₂ molecules) is apparent in the region below the 2p σ_u transition peak. The theoretical line profiles displayed in this figure were evaluated from the overlap of the ground state D₂ vibrational wavefunction and excited ion continuum wavefunctions, using the computer code of R. Le Roy [167]. Relative

to the area of the $1s\sigma_g$ peak, the areas of the BES peaks for the excited ion state transitions have been fixed to the relative areas of the H₂ BES transitions (figures 6.3 and 6.4). The BES line profiles, constrained in this manner, are in reasonable agreement with the experimental data. The restriction on the areas of the D₂ line profiles was imposed to emphasize any variation in the shapes of the D₂ $2p\sigma_u$ and $2s\sigma_g$ XMPs relative to the shapes of the H₂ XMPs, independent of any (small) variation in the BES areas, which are used to normalize the experimental profiles to the $1s\sigma_g$ XMP.

The momentum profiles for the transition from the ground state of D₂ to the $1s\sigma_g$ state and the $2p\sigma_u$ and $2s\sigma_g$ excited ion states (obtained at average energies of 32.9 eV and 40.4 eV respectively), are shown in figure 6.8. The (uncorrected - i.e. fig 6.5) momentum profiles for H₂ are also presented (open circles). In the case of the $2p\sigma_u$ transition (figure 6.8b), the D₂ experimental profile is marginally higher than the H₂ measurement at low momentum. This is likely due to a slightly greater contribution of the double scattering process at the transition energy of the D₂ $2p\sigma_u$ XMP. Except for this small discrepancy, the agreement between the H₂ and D₂ experimental momentum profiles is generally excellent. This strongly suggests that the evaluation of the theoretical profiles at the equilibrium bond distance is a reasonable approximation, and eliminates vibrational effects as a source of the discrepancy between experimental and theoretical momentum profiles.

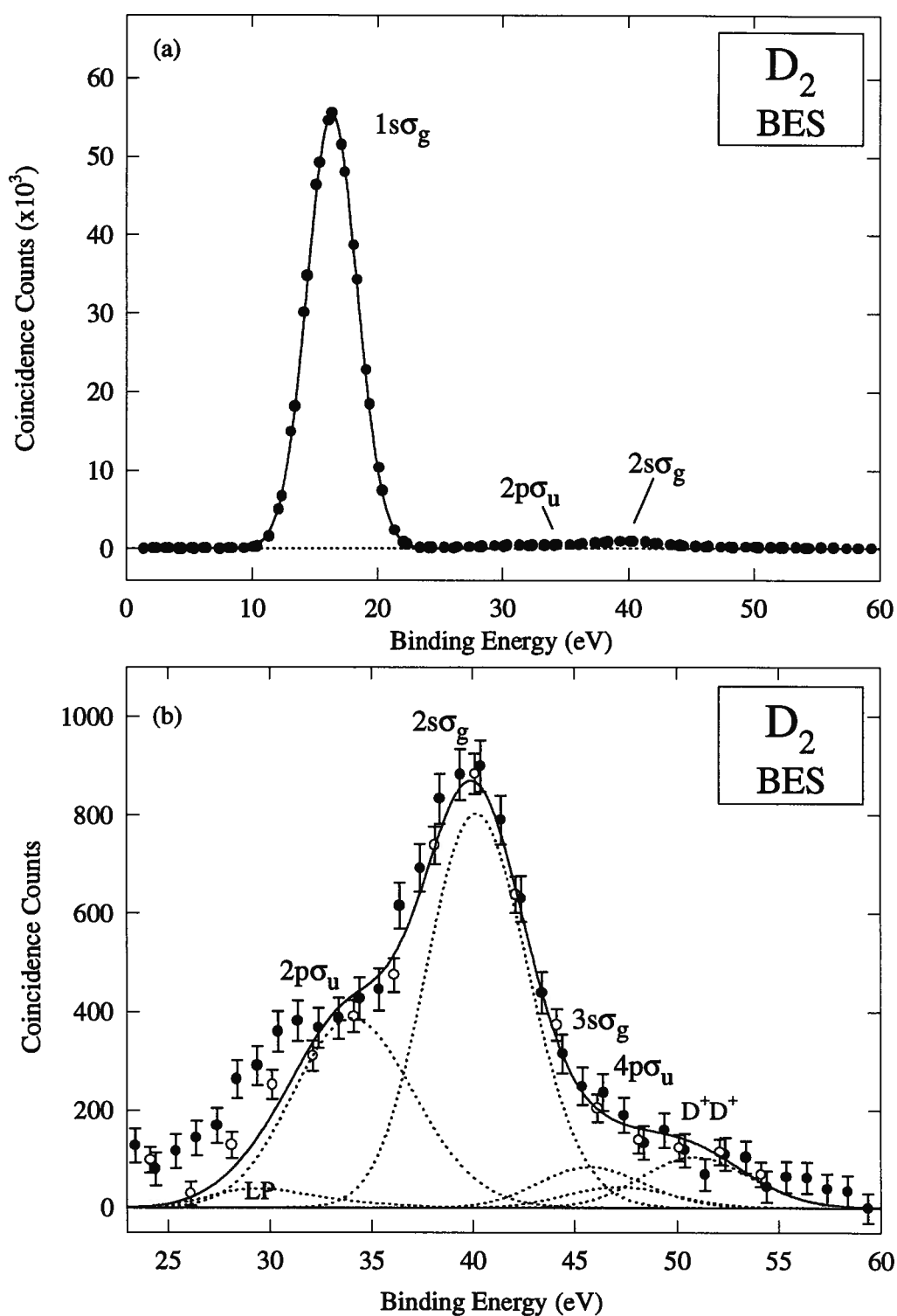


Figure 6.7: a) The angle integrated ($0 - \pm 26^\circ$) binding energy spectrum of D_2 . b) An expanded view of the BES about the transitions to the excited ion states. The solid and open circles represent measurements at gas pressures of 5.8×10^{-6} and 2.4×10^{-6} torr respectively.

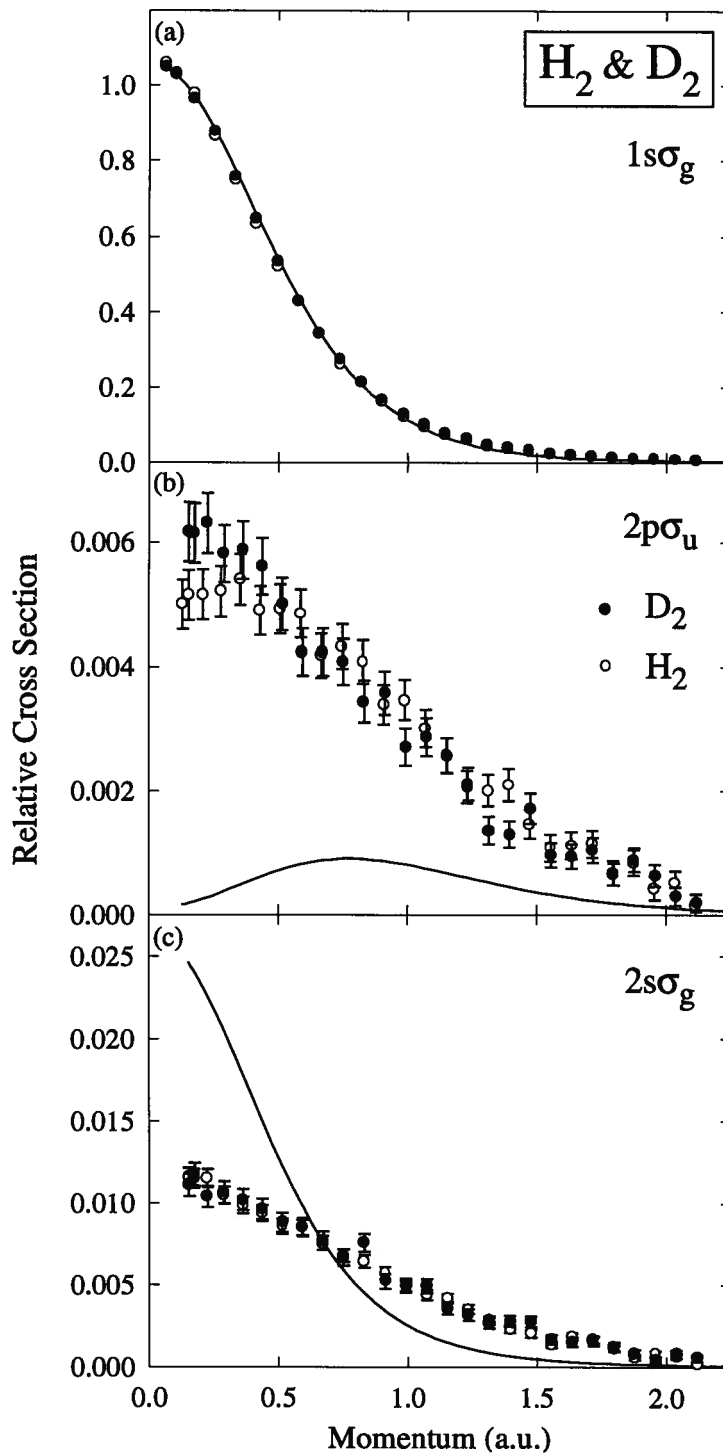


Figure 6.8: The $1s\sigma_g$, $2p\sigma_u$, and $2s\sigma_g$ XMPs of H₂ (open circles) and D₂ (filled circles). The profiles have been normalized to the areas of the line profiles in the BES of figure 6.4 (and figure 6.7), and have not been corrected for the small contribution of neighbouring transitions at the binding energy of each XMP measurement.

6.5 Discussion

The momentum dispersive multichannel measurements of the EMS cross section for the (e,2e) ionization to excited ion states of molecular hydrogen are significantly different, both in shape and magnitude, from the theoretical profiles calculated with highly correlated wavefunctions and based on the plane wave impulse approximation. The possible influence of the vibrational motion of the molecule on the experimental cross sections has been addressed through the measurement of the XMPs of D₂. These profiles were found to be in good agreement with the XMPs for H₂, and hence also exhibit large differences from the theoretical profiles. Bharathi *et al.* [158] have suggested that the poor agreement with theory results from deficiencies in the Davidson and Jones (DJ) [159] molecular ground state wavefunction. However, the TMPs based on the DJ wavefunction are in good agreement with the TMPs calculated with the correlated wavefunction of Hagstrom and Shull [160] (figure 6.1). In addition, the TMPs for the 2s σ_g transition using the correlated wavefunctions (HS and DJ), are very well matched by the TMP using an SCF wavefunction (figure 6.1). Hence, the use of a more accurate ground state wavefunction (in terms of its energy) in the calculation of the TMPs would likely exhibit little change from the profiles displayed in figure 6.1, particularly for the 2s σ_g transition.

The possibility for the observed discrepancies to result from an instrumental effect is also remote. As discussed in chapter 3, the response of the multichannel instrument has been well characterized and has been shown to be linear over a very wide range of operating conditions.

The series of measurements presented in chapter 4 confirms the quantitative accuracy of the multichannel measurements. Additionally, the deviations observed between the theoretical and experimental profiles are quite different for the transitions to the $2p\sigma_u$ and $2s\sigma_g$ final ion states. While the $2p\sigma_u$ XMP is significantly higher in intensity than the TMP, particularly at low momentum values, the $2s\sigma_g$ XMP underestimates the TMP in the low momentum region, and overestimates the TMP in the higher momentum region. If an unknown instrumental effect were manifested in the experimental profiles, the discrepancy with the theoretical profiles would be expected to be similar for the two final ion state transitions. Finally, the agreement observed between the unpublished measurements of Bharathi *et al.* [158] and the present experimental results provides independent support for the present work.

The differences observed between the TMPs and XMPs for H₂ (and D₂) are even more striking than those exhibited by the $n=2$ and $n=3$ cross sections of helium, presented in the chapter 5. The influence of second order collision processes¹, not considered in a PWIA analysis, was demonstrated in chapter 5 to be a likely cause of the enhanced experimental cross sections for the ionizing transitions to the excited helium ion states. The possible second order processes include the two-step TS-1 mechanism, in which the projectile interacts with both target electrons, and the TS-2 mechanism, in which, following a collision with the projectile, the outgoing target electron interacts with the second target electron. In the

¹ As in chapter five, it must be noted that the double (second order) *collision* processes should not be confused with the double *scattering* processes. The double scattering mechanism involves two separate first order collisions with two target atoms or molecules, while the double collision mechanism involves a second order interaction with a single target species.

present measurements of the (e,2e) cross sections for H₂ and D₂, these two-step mechanisms are a likely source of the discrepancy with the (PWIA) theoretical cross sections.

Scattering experiments involving the transition of two electrons are much more numerous for helium target species than for molecular hydrogen. However, Edwards, Ezell, Wood and colleagues have recently reported a series of measurements of the double excitation, ionization plus excitation, and double ionization cross sections for electron and proton impact of hydrogen [174 - 178]. The final ion states of the collision events were identified by the analysis of the kinetic energy of the H⁺ fragments. Initial measurements investigated the dissociation of H₂ into angles perpendicular to the direction of the incident projectile beam [174,175]. As observed in helium [140], the double ionization cross section of hydrogen was shown to be significantly higher for electron impact than for proton impact at equal projectile velocities [174,175]. A similar projectile charge dependence (proton / electron) was observed in the cross sections for the ionization to the H₂⁺ excited ion states (2pσ_u, 2pπ_u, 2sσ_g) [175]. These findings are believed to be the result of an interference between the two-step TS-2 term and both the first Born shake-up or shake-off and the TS-1 terms [175]. The influence of the two-step terms in these measurements offers strong support for the suggested role of these scattering processes in the present EMS cross section measurements.

In the EMS scattering kinematics, the two-step TS-1 and TS-2 terms involve the interaction of either the incident or scattered electron with the remaining H₂ target electron,

following a binary (e,2e) collision. If the second collision event involved a reasonable momentum transfer, the azimuthal angular relationship of the two outgoing electrons may be modified. This process would likely result in a more homogeneous angular distribution of electrons over the azimuthal range detected by the MCP/RAE detector. In accord with this analysis, the present measurements of the experimental profiles for the excited ion transitions are much more uniform across the momentum (angular) range than the theoretical profiles. The $2s\sigma_g$ experimental profile presented in figure 6.6 is much flatter than the TMP, while the $2p\sigma_u$, XMP does not exhibit the clear maximum at ~ 7 a.u. or the deep minimum at low momentum, displayed by the theoretical profile. While this picture of the two-step scattering process in EMS is rather simple, a qualitative description of the experimental measurements is provided.

6.6 Conclusions

The EMS experimental momentum profiles for the (e,2e) ionization of molecular hydrogen to the $1s\sigma_g$, $2p\sigma_u$, and $2s\sigma_g$ final ion states have been measured using the momentum dispersive multichannel spectrometer. While the momentum profile of $1s\sigma_g$ transition is very well described by theoretical profiles, the experimental profiles for the excited ion transitions are in poor agreement with TMPs based on highly correlated H₂ wavefunctions. The discrepancies between the experimental profiles and the theoretical profiles calculated in the PWIA are likely caused by two-step second order collision processes. These processes were also proposed to give an enhanced cross section in EMS transitions to

the excited ion states of helium (chapter 5). The present (e,2e) measurements of hydrogen complement the measurements on helium (chapter 5), and it is hoped that they will initiate a theoretical reinvestigation of the (e,2e) scattering process. The well defined final state and the large incident and outgoing electron energies of the EMS measurements should be a favorable kinematical arrangement for the theoretical description of the second order processes. The calculation of the H_2 cross sections will likely be complicated by the multicenter character of the molecule. However, for the transition to the $2s\sigma_g$ ion state the calculation may be simplified by the use of an (uncorrelated) SCF molecular wavefunction, which has been shown to give an accurate prediction of the $2s\sigma_g$ theoretical profile in the PWIA compared to TMPs calculated with correlated wavefunctions. The differences between the experimental cross sections and the (first order) theoretical profiles are quite dramatic, and the EMS measurements should provide a sensitive test for the theoretical description of the second order two-step processes.

Chapter Seven

Closing Remarks

A brief review of historical developments in chemistry, or for that matter in natural science as a whole, will convincingly show that methodological developments ...that is, the emergence of new theoretical or experimental tools or substantial improvement of old ones...often have had an enormous and sometimes quite dramatic impact on the progress of science.

Professor Sture Forsén [179]

The development, characterization, and application of a new multichannel spectrometer for the electron scattering coincidence technique of electron momentum spectroscopy has been presented in this thesis. Incorporating some aspects of previous single-channel and multichannel designs, together with many original approaches, the new instrument has been shown to provide a significant improvement in the detection efficiency over conventional single channel spectrometers. A channel electron multiplier and a microchannel plate/resistive anode position sensitive detector are situated on opposite sides of the exit circle of a cylindrical mirror analyzer to permit detection of coincident pairs of (e,2e) electrons over an azimuthal range of ± 26 degrees. Departing from a conventional TAC based system, the coincident arrival of electrons at the two detectors is recognized by the pile-up of pulses from each detector. The implementation of the PPU technique using ECL circuitry and rf-power

combiners has provided the ability for very fast detection of coincidence events, which in turn has permitted the gating of the RAE position computer. Of the many electrons striking the detector, only the positions of electrons coincident with an electron at the CEM are determined and recorded, significantly reducing the dead time of the detection system and optimizing the performance of the new spectrometer.

The new instrument has been fully characterized through measurements of a number of systems including: Ne, Ar, Kr, Xe, CH₄, and SiH₄. A comparison of a 15-minute multichannel measurement and a 46.5-hour single channel measurement of the XMP of the Ar 3p electron has provided a dramatic example of the capabilities of the momentum dispersive spectrometer. A more precise multichannel measurement of the Ar 3p XMP exhibited very good agreement with a theoretical profile calculated with a very high quality CI wavefunction. Similarly good agreement was exhibited in the XMPs of the outer valence orbitals of Kr and Xe with theoretical profiles based on near-Hartree-Fock limit wavefunctions. Less influenced by distorted wave effects, the measurements on the molecular species CH₄ and SiH₄ have permitted an evaluation of the spectrometer over a range of binding energies. Very good agreement of the XMPs and high quality TMPs for both the outer and inner valence electrons of these systems, and consistency with earlier single channel measurements, have confirmed the quantitative response of the instrument.

The enhanced capabilities of the multichannel spectrometer have been exploited in the application to the measurement of the (e,2e) transitions from the ground states of helium and molecular hydrogen (and D₂) to excited, singly charged, final ion states. On the basis of earlier published studies with much less sensitive instrumentation, it was anticipated that the present measurements would permit a very detailed investigation of the influence of electron correlation in the ground state of each target species. However, the experimental cross sections for the (e,2e) transitions of helium to the n=2 and n=3 final He⁺ ion states, as well as the transitions of hydrogen (and deuterium) to the 2pσ_u and 2sσ_g ion H₂⁺ (D₂⁺) states, have displayed significant differences in both shape and intensity relative to the theoretical profiles calculated using high quality correlated wavefunctions. Citing studies involving double photoionization, as well as double ionization and ionization plus excitations by electron and proton impact, the findings of the present measurements have been rationalized in terms of second order two-step collision processes, which are not accounted for in the two-body PWIA description of (e,2e) scattering typically used in EMS studies. Such processes involving two-electron transitions have been of much interest and debate in recent years. The well defined, high energy scattering kinematics of the present measurements should prove to be a valuable aid in the theoretical analysis of the two-step mechanism, and it is hoped that the results will precipitate an in-depth theoretical investigation of the second order (e,2e) cross sections for these transitions. Confirmation of the present hypothesis may, in turn, instigate further experimental studies of these systems at different impact energies, and involving transitions to higher final ion states.

With the improvements in sensitivity provided by the present instrument, as well as the recently reported instrument of Storer *et al.* [60] for the study of EMS of solids, the field of EMS is entering a new era. Over the past twenty-two years, EMS studies of small atomic and molecular gas phase systems have identified the general experimental and theoretical requirements for an accurate description of the momentum profiles of target electrons. Many of these studies have led directly to the development of improved electronic wavefunctions for the target species. The present measurements for hydrogen and helium notwithstanding, it has been established that for typical EMS scattering kinematics (impact energies ≥ 1200 eV), the application of the binary encounter plane wave impulse approximation is sound. Hence, the past investigations have laid the groundwork for the future application of the EMS scattering technique to explore the electronic structure of larger and more complex systems. Future directions in gas phase systems will likely be towards the study of large biomolecules, van der Waals complexes, and oriented molecules, as well as excited molecules, radicals and ions. Additional gains in sensitivity will be required to investigate these systems, although the developments and design of the present instrument offer great hope and insight for the achievement of such sensitivity. It is important to note that, even with the present multichannel detection, only a fraction of the total number of valid (e,2e) scattering events are measured. However, the extension of the momentum dispersive architecture of the present instrument, leads to an instrumental design in which coincidence events may be detected around the full 2π azimuth with all possible angular correlations. Such an instrument will incorporate a cylindrically symmetric energy analyzer, with microchannel plate electron

multipliers located at the exit plane. For full 2π detection, the convenience of large-area position sensitive resistive anodes will have to be sacrificed, and discrete anodes (on one- or two-degree centers) are likely to be employed. In light of this, the application of a TAC-based system for coincidence detection, requiring start and stop signals from the detectors, will be problematic. However, the PPU system, employed to great effect in the present spectrometer, may be readily extended to detect coincidences between any two of a number of discrete detectors. Developments along these lines promise additional gains of approximately two orders of magnitude. The ability to extend the range of EMS measurements to more exotic and challenging species looms on the not-too-distant horizon.

Bibliography

- [1] J.W.M. DuMond and H.A. Kirkpatrick, Phys. Rev. **37** (1931) 136.
- [2] J.W.M. DuMond and H.A. Kirkpatrick, Phys. Rev. **38** (1931) 1094.
- [3] R.H. Stuewer and M.J. Cooper, in: *Compton Scattering*, ed. B. Williams (McGraw-Hill, Toronto, 1977) pp. 1.
- [4] J.W.M. DuMond and H.A. Kirkpatrick, Rev. Sci. Instrum. **1** (1930) 88.
- [5] I.E. McCarthy and E. Weigold, Phys. Rep. **27C** (1976) 275.
- [6] C.E. Brion, Int. J. Quantum Chem. **29** (1986) 1397.
- [7] I.E. McCarthy and E. Weigold, Rep. Prog. Phys. **54** (1991) 789.
- [8] H. Ehrhardt, M. Schulz, T. Tekaatt and K. Willmann, Phys. Rev. Lett. **22** (1969) 89.
- [9] U. Amaldi Jr., A. Egidi, R. Marconero and G. Pizzella, Rev. Sci. Instrum. **40** (1969) 1001.
- [10] R. Camilloni, A. Giardini Guidoni, R. Tiribelli and G. Stefani, Phys. Rev. Lett. **29** (1972) 618.
- [11] E. Weigold, S.T. Hood and P.J.O. Teubner, Phys. Rev. Lett. **301** (1973) 475.
- [12] S.T. Hood, E. Weigold, I.E. McCarthy and P.J.O. Teubner, Nature **245** (1973) 65.
- [13] S.T. Hood, A. Hamnett and C.E. Brion, Chem. Phys. Lett. **39** (1976) 252.
- [14] D.S. Evans, Rev. Sci. Instrum. **36** (1965) 375.
- [15] M.P. Seah, J. Electron Spectry. Relat. Phenom. **50** (1990) 137.
- [16] Yu.F. Smirnov and V.G. Neudachin, JETP Lett. **3** (1966) 192.
- [17] V.G. Neudachin, G.A. Novoskol'tseva and Yu.F. Smirnov, JETP **28** (1969) 540.
- [18] A.E. Glassgold and G. Ialongo, Phys. Rev. **175** (1968) 151.
- [19] E. Weigold, S.T. Hood, I.E. McCarthy and P.J.O. Teubner, Phys. Lett. **44A** (1973) 531.

- [20] C.E. Brion, in: *The Physics of Electronic and Atomic Collisions*, eds. T. Andersen *et al.*, (American Institute of Physics Press, New York, 1993) pp. 350.
- [21] K.T. Leung, in: *Theoretical Models of Chemical Bonding part 3 of Molecular Spectroscopy, Electronic Structure and Intramolecular Interactions*, ed. Z.B. Maksic (Springer-Verlag, New York, 1990)
- [22] M.A. Coplan, J.H. Moore and J.P. Doering, *Rev. Mod. Phys.* **66** (1994) 985.
- [23] B. Lohmann and E. Weigold, *Phys. Lett.* **86A** (1981) 139.
- [24] S.T. Hood, I.E. McCarthy, P.J.O. Teubner and E. Weigold, *Phys. Rev. A* **8** (1973) 2494
- [25] K.T. Leung and C.E. Brion, *Chem. Phys.* **82** (1983) 87.
- [26] J.P.D. Cook, I.E. McCarthy, A.T. Stelbovics and Weigold E., *J. Phys. B* **17** (1984) 2339.
- [27] A.J. Dixon, I.E. McCarthy, C.J. Noble and E. Weigold, *Phys. Rev. A* **17** (1978) 597.
- [28] F.P. Larkins, *J. Phys. B* **14** (1981) 1477.
- [29] F.P. Larkins and J.A. Richards, *Chem. Phys.* **81** (1983) 329.
- [30] A.D. Smith, M.A. Coplan, D.J. Chornay, J.H. Moore, J.A. Tossell, J. Mrozek, V.H. Smith Jr. and N.S. Chant, *J. Phys. B* **19** (1986) 969.
- [31] Lahmam-Bennani, Duguet, Dupré and Dal Cappello, *J. Electron Spectry. Relat. Phenom.* **58** (1992) 17.
- [32] S.A.C. Clark, T.J. Reddish, C.E. Brion, E.R. Davidson and Frey R.F., *Chem. Phys.* **143** (1990) 1.
- [33] R. Camilloni, G. Stefani, A. Giardini-Guidoni, R. Tiribelli and D. Vinciguera, *Chem. Phys. Lett.* **41** (1976) 17.
- [34] A.O. Bawagan, R. Müller-Fiedler, C.E. Brion, E.R. Davidson and C. Boyle, *Chem. Phys.* **120** (1988) 335.
- [35] S.T. Hood, A. Hamnett and C.E. Brion, *J. Electron Spectry. Relat. Phenom.* **11** (1977) 205.
- [36] A.O. Bawagan, C.E. Brion, E.R. Davidson and D. Feller, *Chem. Phys.* **113** (1987) 19.
- [37] A.O. Bawagan, C.E. Brion, E.R. Davidson and D. Feller, *Chem. Phys.* **99** (1985) 367.

- [38] S.A.C. Clark, E. Weigold, C.E. Brion, E.R. Davidson, R.F. Frey, C.M. Boyle, W. von Niessen and J. Schirmer, *Chem. Phys.* **134** (1989) 229.
- [39] S.A.C. Clark, C.E. Brion, E.R. Davidson and C. Boyle, *Chem. Phys.* **136** (1989) 55.
- [40] C.L. French, C.E. Brion and E.R. Davidson, *Chem. Phys.* **122** (1988) 247.
- [41] C.E. Brion, I.E. McCarthy, I.H. Suzuki and E. Weigold, *Chem. Phys. Lett.* **67** (1979) 115.
- [42] C.E. Brion, S.T. Hood, I.H. Suzuki, E. Weigold and G.R.J. Williams, *J. Electron Spectry. Relat. Phenom.* **21** (1980) 71.
- [43] E.R. Davidson, D. Feller, C. Boyle, L. Adamowicz, S.A.C. Clark and C.E. Brion, *Chem. Phys.* **147** (1990) 45.
- [44] B.P. Hollebone, Y. Zheng, C.E. Brion, E.R. Davidson and D. Feller, *Chem. Phys.* **171** (1993) 303.
- [45] B.P. Hollebone, C.E. Brion, E.R. Davidson and C. Boyle, *Chem. Phys.* **173** (1993) 193.
- [46] J.P.D. Cook, C.E. Brion and A. Hamnett, *Chem. Phys.* **45** (1980) 1.
- [47] A. Hamnett, S.T. Hood and C.E. Brion, *J. Electron Spectry. Relat. Phenom.* **11** (1977) 263.
- [48] A.O. Bawagan and C.E. Brion, *Chem. Phys.* **144** (1990) 167.
- [49] P. Duffy, M.E. Casida, C.E. Brion and D.P. Chong, *Chem. Phys.* **159** (1992) 347.
- [50] D. Feller, C.M. Boyle and E.R. Davidson, *J. Chem. Phys.* **86** (1987) 3424.
- [51] I.N. Levine, *Quantum Chemistry* (Prentice-Hall, Englewood Cliffs, 1991)
- [52] Y. Zheng, I.E. McCarthy, E. Weigold and D. Zhang, *Phys. Rev. Lett.* **64** (1990) 1358.
- [53] J.H. Moore, M.A. Coplan, T.L. Skillman Jr. and E.D. Brooks, *Rev. Sci. Instrum.* **49** (1978) 463.
- [54] R.R. Goruganthu, M.A. Coplan, J.H. Moore and J.A. Tossell, *J. Chem. Phys.* **89** (1988) 25.
- [55] A. Egidi, R. Marconero, G. Pizzella and F. Sperli, *Rev. Sci. Instrum.* **40** (1969) 88.
- [56] W.G. Wolber, B.D. Klettke and F. Sperli, *Rev. Sci. Instrum.* **40** (1969) 1364.

- [57] J. Lower and E. Weigold, *J. Phys. E* **22** (1989) 421.
- [58] A.L. Ritter, J.R. Dennison and J. Dunn, *Rev. Sci. Instrum.* **53** (1984) 1280.
- [59] P. Hayes, M.A. Bennett, J. Flexman and J.F. Williams, *Rev. Sci. Instrum.* **59** (1988) 2445.
- [60] P. Storer, R.S. Caprari, S.A.C. Clark and Weigold E., *Rev. Sci. Instrum.* **65** (1994) 2214.
- [61] L. Avaldi, R. Camilloni, E. Fainelli and G. Stefani, *J. Phys. B* **20** (1987) 4163.
- [62] R. Camilloni, G. Stefani, R. Fantoni and A. Giardini-Guidoni, *J. Electron Spectry. Relat. Phenom.* **17** (1979) 209.
- [63] L. Frost, in: *(e,2e) & related processes*, eds. C.T. Whelan *et al.* (Kluwer Academic Publishers, Netherlands, 1993) pp. 185.
- [64] I.E. McCarthy and E. Weigold, *Rep. Prog. Phys.* **51** (1988) 299.
- [65] F.W. Byron Jr and C.J. Joachain, *Phys. Rep.* **179** (1989) 211.
- [66] J.W. Liu and V.J. Smith Jr, *Phys. Rev. A* **31** (1985) 3003.
- [67] C.J. Joachain, in: *The Physics of Electronic and Atomic Collisions*, A. Delgarno, R.S. Freund, P.M. Koch, M.S. Lubell and T.B. Lucatorto (American Institute of Physics, AIP Conference Proceedings 205, 1990) pp. 68.
- [68] E.W. McDaniel, *Atomic Collisions : Electron and Photon Projectiles* (John Wiley & Sons, Toronto, 1989).
- [69] M. Inokuti and S.T. Manson, *Electron Beam Interactions with Solids* (1985) 1.
- [70] E. Weigold and I.E. McCarthy, *Adv. At. and Mol. Phys.* **14** (1978) 127.
- [71] P.J.O. Teubner, in: *Electron Impact Ionization*, eds. T.D. Märk and G.H. Dunn (Springer-Verlag, New York, 1985) pp. 89.
- [72] K.A. Hall, J.F. Reading and A.L. Ford, *J. Phys. B* **26** (1993) 1697.
- [73] D.H. Madison, I.E. McCarthy and X. Zhang, *J. Phys. B* **22** (1989) 2041.
- [74] A. Lahmam-Bennani, A. Duguet and C. Dal Cappello, *J. Electron Spectry. Relat. Phenom.* **40** (1986) 141.
- [75] E. Weigold, *J. Electron Spectry. Relat. Phenom.* **51** (1990) 629.
- [76] I.E. McCarthy, R. Pascual, P. Storer and E. Weigold, *Phys. Rev. A* **40** (1989) 3041.

- [77] L. Frost and E. Weigold, *J. Phys. B* **15** (1982) 2531.
- [78] C.A. Coulson, *Rev. Mod. Phys.* **32** (1960) 170.
- [79] I. Shavitt, in: *Methods of Electronics Structure Theory*, Vol. 3 of *Modern Theoretical Chemistry*, ed. Henry Schaefer III (Plenum Press, New York, 1977) pp. 189.
- [80] A. Szabo and N.S. Ostlund, *Modern Quantum Chemistry* (McGraw-Hill, Toronto, 1989).
- [81] E. Clementi and R. Roetti, *At. Data Nucl. Data Tables* **14** (1974) 177.
- [82] E.R. Davidson and D. Feller, *Chem. Rev.* **86** (1986) 681.
- [83] P. Kaijser and V.H. Smith Jr., *Adv. Quantum Chem.* **10** (1977) 37.
- [84] P.O. Löwdin, *Adv. Chem. Phys.* **2** (1959) 207.
- [85] H.Z. Sar-El, *Rev. Sci. Instrum.* **38** (1967) 1210.
- [86] J.S. Risley, *Rev. Sci. Instrum.* **43** (1972) 95.
- [87] D. Halliday and R. Resnick, *Fundamentals of Physics* (John Wiley & Sons, Toronto, 1981).
- [88] L.J. Richter and W. Ho, *Rev. Sci. Instrum.* **57** (1986) 1469.
- [89] Philips Data Handbook T9, (1985)
- [90] J.L. Wiza, *Nucl. Instrum. and Meth.* **162** (1979) 587.
- [91] M.P. Seah and G.C. Smith, *Rev. Sci. Instrum.* **62** (1991) 62.
- [92] M.P. Seah, C.S. Lim and K.L. Tong, *J. Electron Spectry. Relat. Phenom.* **48** (1989) 209.
- [93] M.I. Green, P.F. Kenealy and G.B. Beard, *Nucl. Instrum. and Meth.* **126** (1975) 175.
- [94] R.C.G. Leckey, *J. Electron Spectry. Relat. Phenom.* **43** (1987) 183.
- [95] D. Rogers and R.F. Malina, *Rev. Sci. Instrum.* **53** (1982) 1238.
- [96] M. Lampton and C.W. Carlson, *Rev. Sci. Instrum.* **50** (1979) 1093.
- [97] S.H. Courtney and W.L. Wilson, *Rev. Sci. Instrum.* **62** (1991) 2100.
- [98] D.P. de Bruijn and J. Los, *Rev. Sci. Instrum.* **53** (1982) 1020.

- [99] M. Volkel and W. Sandner, *J. Phys. E* **16** (1983) 456.
- [100] EG&G Ortec Inc. Applications note AN-41
- [101] Motorola MECL Device Data Book (1989).
- [102] J.A. Simpson and C.E. Kuyatt, *J. Appl. Phys.* **37** (1966) 3805.
- [103] R.L. Arnoldy, P.O. Isaacson, D.F. Gats and L.W. Choy, *Rev. Sci. Instrum.* **44** (1973) 172.
- [104] M.P. Seah and M.W. Holbourn, *J. Electron Spectry. Relat. Phenom.* **42** (1987) 255.
- [105] R.H. Brigham, R.J. Bleiler, P.J. McNitt, D.A. Reed and R.H. Fleming, *Rev. Sci. Instrum.* **64** (1993) 420.
- [106] S.W. Braidwood, M.J. Brunger, D.A. Konovalov and E. Weigold, *J. Phys. B* **26** (1993) 1655.
- [107] J.P.D. Cook, I.E. McCarthy, J. Mitroy and E. Weigold, *Phys. Rev. A* **33** (1986) 211.
- [108] J. Mitroy, I.E. McCarthy and E. Weigold, *J. Phys. B* **18** (1985) L91.
- [109] M.J. Brunger and E. Weigold, *J. Phys. B* **25** (1992) L481.
- [110] O. Samardzic, S.W. Braidwood, E. Weigold and M.J. Brunger, *Phys. Rev. A* **48** (1993) 4390.
- [111] S. Braidwood, M. Brunger and E. Weigold, *Phys. Rev. A* **47** (1993) 2927.
- [112] S. Svensson, B. Eriksson, N. Mårtensson, G. Wendin and U. Gelius, *J. Electron Spectry. Relat. Phenom.* **47** (1988) 327.
- [113] E.R. Davidson, private communication.
- [114] M.S. Banna, B.E. Mills, D.W. Davis and D.A. Shirley, *J. Chem. Phys.* **61** (1974) 4780.
- [115] M.S. Banna and D.A. Shirley, *Chem. Phys. Lett.* **33** (1975) 441.
- [116] E. Hylleraas, *Z. Physik.* **54** (1929) 347.
- [117] I.E. McCarthy, A. Ugbabe, E. Weigold and P.J.O. Teubner, *Phys. Rev. Lett.* **33** (1974) 459.
- [118] A.J. Dixon, I.E. McCarthy and E. Weigold, *J. Phys. B* **14** (1976) 3277.
- [119] R. Taylor and R.G. Parr, *Proc. Natl. Acad. Sci. U.S.A.* **38** (1952) 154.

- [120] R.K. Nesbet and R.E. Watson, Phys. Rev. **110** (1958) 1073.
- [121] C.J. Joachain and R. Vanderpoorten, Physica **46** (1970) 333.
- [122] I.E. McCarthy and Mitroy J., Phys. Rev. A **34** (1986) 4426.
- [123] R.J. Tweed and J. Langlois, J. Phys. B **20** (1987) 5213.
- [124] A.W. Weiss, Phys. Rev. **122** (1961) 1826.
- [125] N.M. Cann and A.J. Thakkar, Phys. Rev. A **46** (1992) 5397.
- [126] D.E. Freund, B.D. Huxtable and J.D. Morgan III, Phys. Rev. A **29** (1984) 980.
- [127] T. Kinoshita, Phys. Rev. **105** (1957) 1490.
- [128] E.R. Davidson, Int. J. Quantum Chem. **37** (1990) 811.
- [129] S. Chakravorty and E.R. Davidson, private communication.
- [130] C.E. Brion and A. Hamnett, in: *The Excited State in Chemical Physics, Part 2*, Adv. Chem. Phys. **45**, ed. J. W. McGowan (John Wiley, New York, 1981) pp.1.
- [131] A. Hamnett, W. Stoll, W. Branton, M.J. Van der Wiel and C.E. Brion, J. Phys. B. **9** (1976) 945.
- [132] W.R. Chan, G. Cooper and C.E. Brion, Phys. Rev. A **44** (1991) 186.
- [133] J.W. Gallagher, C.E. Brion, J.A.R. Samson and P.W. Langhoff, J. Phys. Chem. Ref. Data **17** (1988) 9.
- [134] A.R. Stringanov and R.S. Sventitskii, *Tables of Spectral Lines of Neutral and Ionized Atoms* (Plenum, New York, 1968).
- [135] P.A. Heimann, U. Becker, H.G. Kerkhoff, B. Langer, D. Szostak, R. Wehlitz, D.W. Lindle, T.A. Ferrett and D.A. Shirley, Phys. Rev. A **34** (1986) 3782.
- [136] Y. Zheng, J.J. Neville, C.E. Brion, private communication.
- [137] Y. Zheng, J.J. Neville, C. E. Brion, Y. Wang, E. R. Davidson, Chem. Phys. **188** (1994) 109.
- [138] C. Dupré, A. Lahmam-Bennani, A. Duguet, F. Mota-Furtado, P.F. O'Mahony and C. Dal Cappello, J. Phys. B **24** (1991)
- [139] R.J. Tweed, Z. Phys. D **23** (1992) 309.
- [140] J.H. McGuire, Phys. Rev. Lett. **49** (1982) 1153.

- [141] L.H. Andersen, P. Hvelplund, H. Knudsen, S.P. Møller, K. Elsner, K.-G. Rensfelt and E. Uggerhøj, *Phys. Rev. Lett.* **57** (1986) 2147.
- [142] H. Knudsen and J.F. Reading, *Phys. Rep.* **212** (1992) 107.
- [143] T.A. Carlson and M.O. Krause, *Phys. Rev.* **140** (1965) 1057.
- [144] L.R. Andersson and J. Burgdörfer, *Phys. Rev. Lett.* **71** (1993) 50.
- [145] H.K. Haugen, L.P. Anderson, P. Hvelplund and H. Knudsen, *Phys. Rev. A* **26** (1982) 1950.
- [146] L.H. Andersen, P. Hvelplund, H. Knudsen, S.P. Møller, A. H. Sørensen, K. Elsner, K.-G. Rensfelt and E. Uggerhøj, *Phys. Rev.* **36** (1987) 3612.
- [147] J.F. Reading and A.L. Ford, *Phys. Rev. Lett.* **58** (1987) 543.
- [148] J.F. Reading and A.L. Ford, *J. Phys. B* **20** (1987) 3747.
- [149] R.E. Olson, *Phys. Rev. A* **36** (1987) 1519.
- [150] J.H. McGuire, *Phys. Rev. A* **36** (1987) 1114.
- [151] J.H. McGuire, *Adv. At. Mol. Opt. Phys.* **29** (1992) 7.
- [152] J.O.P. Pedersen and F. Folkmann, *J. Phys. B* **23** (1990) 441.
- [153] S. Füelling, R. Bruch, E.A. Rauscher, E. Träbert and P.H. Heckmann, *Nucl. Instrum. Meth. Phys. Res. B* **56/57** (1991) 275.
- [154] S. Füelling, R. Bruch, E.A. Rauscher, P.A. Neill, E. Träbert, P.H. Heckmann and J.H. McGuire, *Phys. Rev. Lett.* **68** (1992) 3152.
- [155] A. Lahmam-Bennani, *J. Phys. B* **24** (1991) 2401.
- [156] A.D. McLean, A. Weiss and M. Yoshimine, *Rev. Mod. Phys.* **32** (1960) 211.
- [157] E. Weigold, I.E. McCarthy, A.J. Dixon and S. Dey, *Chem. Phys. Lett.* **47** (1977) 209.
- [158] S. M. Bharathi, S. Braidwood, A. M. Grisogono, N. Persiantseva, and E. Weigold, ICPEAC XVII, Abstracts of Contributed Papers, eds. I.E. McCarthy *et. al.* (Brisbane, Australia, 1991,) pp. 243.
- [159] E.R. Davidson and L.L. Jones, *J. Chem. Phys.* **37** (1962) 2966.
- [160] S. Hagstrom and H. Shull, *Rev. Mod. Phys.* **35** (1963) 624.

- [161] J.A.R. Samson, Chem. Phys. Lett. **12** (1972) 625.
- [162] D.R. Bates, K. Ledsham and A.L. Stewart, Phil. Trans. Roy. Soc. London **A246** (1953) 215.
- [163] T.E. Sharp, At. Data **2** (1971) 119.
- [164] J.A.R. Samson, Phys. Rep. **28** (1976) 303.
- [165] J.L. Gardner and J.A.R. Samson, Phys. Rev. A **12** (1975) 1404.
- [166] J.L. Dunham, Phys. Rev. **34** (1929) 438.
- [167] R.J. Le Roy, Comput. Phys. Commun. **52** (1989) 383.
- [168] R.J. Le Roy, private communication.
- [169] W.F. Chan, G. Cooper and C.E. Brion, Chem. Phys. **168** (1992) 375.
- [170] S. Dey, I.E. McCarthy, P.J.O. Teubner and E. Weigold, Phys. Rev. Lett. **34** (1975) 782.
- [171] K.T. Leung, J.A. Sheehy and P.W. Langhoff, Chem. Phys. Lett. **157** (1989) 135.
- [172] J.M. Gilligan and E. E. Eyler, Phys. Rev. A **46** (1992) 3676.
- [173] A.B. Cornford, D.C. Frost, C.A. McDowell, J.L. Ragle and I.A. Stenhouse, Chem. Phys. Lett. **5** (1976) 486.
- [174] A.K. Edwards, R.M. Wood, A.S. Beard and R.L. Ezell, Phys. Rev. A **37** (1988) 3697.
- [175] A.K. Edwards, R.M. Wood, J.L. Davis and R.L. Ezell, Phys. Rev. A **42** (1990) 1367.
- [176] R.L. Ezell, A.K. Edwards, R.M. Wood, M.W. Dittmann, J.F. Browning and M.A. Mangan, Nucl. Instrum. Methods Phys. Res. B **56/57** (1991) 292.
- [177] A.K. Edwards, R.M. Wood, M.W. Dittmann, J.F. Browning, M.A. Mangan and R.L. Ezell, Nucl. Instrum. Methods Phys. Res. B **53** (1991) 472.
- [178] A.K. Edwards, R.M. Wood, M.A. Mangan and R.L. Ezell, Phys. Rev. A **46** (1992) 6970.
- [179] Sture Forsén, in: *Les Prix Nobel 1991*, ed. Tore Frängsmyr (Almqvist & Wiksell Int., Stockholm, 1992) pp. 21.
- [180] G.A. Baker Jr., I.E. McCarthy and C.E. Porter, Phys. Rev. **120** (1960) 254.

- [181] C.A. Coulson, Proc. Camb. Phil. Soc. **37** (1941) 55.
- [182] C.A. Coulson and W.E. Duncanson, Proc. Camb. Phil. Soc. **37** (1941) 67.
- [183] C.A. Coulson, Proc. Camb. Phil. Soc. **37** (1941) 397.
- [184] W.E. Duncanson, Proc. Camb. Phil. Soc. **37** (1941) 397.
- [185] W.E. Duncanson and C.A. Coulson, Proc. Camb. Phil. Soc. **37** (1941) 406.
- [186] C.A. Coulson and W.E. Duncanson, Proc. Camb. Phil. Soc. **38** (1942) 100.
- [187] R. Goodman, *Introduction to Stochastic Models* (Benjamin/Cummings, California, 1988)
- [188] B.P. Hollebone and C.E. Brion, private communication.